DOI: 10.2478/sspjce-2023-0001

Use of Recycled Polyethylene in Asphalt Mixture

Róbert Kovács[1], Eva Lukáčová[2], Adriana Czímerová[3*], Marcela Csölle[3], Ján Mandula[1]

[1]Technical University of Kosice, Slovakia, Faculty of Civil Engineering, Department of Geotechnics and Traffic Engineering
[2]VÚRUP, Ltd., Vlčie hrdlo 1, 820 03 Bratislava, Slovakia
[3]VUIS – CESTY, Ltd., Vlčie hrdlo 1, 821 07 Bratislava, Slovakia
*e-mail: Adriana.czimerova@gmail.com

Abstract

Plastics and plastic products have become part of our lives extremely quickly. Although, they make our lives easier in many aspects, at the end of their useful life, especially thanks to the thoughtless actions of people, they are becoming a serious environmental problem. Even though the laws and legislation are still forcing limits of using the plastic products and thus prevent waste, the concept of plastic-free living is probably not going to be reached easily and quickly. Using the recycling technology, we can prepare the recycled material, which represents a new raw material resource. With the right choice of physical-chemical parameters of recycled materials and using a suitable reaction condition we can incorporate them into the asphalt mixtures. Since their introduction the polymer-modified asphalt mixtures have gained in importance during the second half of the twentieth century, and they now play a fundamental role in the field of road paving. Moreover, the use of recycled plastic in such a product will contribute to the technical and economic recovery of secondary raw materials. The use of various recycled material in paving industry is a common practice but needs further research work. Thus, this study aims to the incorporation of recycled plastics into asphalt mixture. The main objective of our work was to find a suitable recycled plastic, which with its physico-chemical and technical parameters is suitable for incorporation into the asphalt mixture. In our study the recycled low-density polyethylene granulate was used, taken from films and various packaging materials. Our preliminary laboratory experiments were based on the possibilities to prepare and characterized the asphalt mixtures containing recycled plastic at different percentage, i.e., 4 %, 6 %, 8 % and 10 % by weight of bitumen. The experimental tests performed in the study were bitumen content, intergranularity, maximum bulk density, water sensitivity and resistance to permanent deformations. The results showed that the mix containing 6 % by weight of recycled plastic has ideal properties and meets most of the criteria that have been set for asphalt mixes. A commercially available polymer of similar chemical composition to the recycled material was used as a reference sample.

Keywords: low-density polyethylene, recyclate, asphalt mixture, reaction conditions, polymers

1 Introduction

A few decades ago, we could not have imagined that polymers and materials made from them, would become part of our lives that we would have to restrict and regulate their use, neither their production, distribution nor reuse. Can we even imagine our current way of living without plastic products? The answer is that it is certainly very difficult, if not impossible. Plastics are everywhere around us and have become common in our everyday life. For example, vast amount of food is packed in plastic to preserve its quality for maximum time. Even the textiles we wear are made from man-made fibres, which can fulfil a variety of functional properties. A family of four produces up to 150 kg of plastic waste per year [1]. The average Slovak uses 466 plastic bags a year. Slovaks belong to the most plastic bags users among European Union countries, with up to 89 % of these bags are being used only once. The average annual consumption in the EU is 198 single-use plastic bags, which represents a daily consumption of 1 bag per household [1].

Plastics, or in other words polymers, are macromolecular compounds that can vary greatly from one to another depending on their chemical composition (the basic backbone of most polymers is composed of carbon atoms, hydrogen in possible combination with oxygen, nitrogen, chlorine, or sulphur). Polymers are formed by polymerization from monomers (repeating, interlinked molecules). In their structure, they contain various characteristic groups that are either directly involved in the formation of the polymer chain or are simply bonded to it. In addition, other substances (called additives or fillers) can be added to improve selected properties and polymer becomes a composite material. It is the variability in properties (e.g., heat resistance, hardness or resistance to chemicals) combined with the basic property of plastics, plasticity, uniformity of composition and relatively low weight (in large volume), that allows for use in all industries [2]. The development of plastics can be dated back to the time when natural polymeric materials such as natural rubber in the form of chewing gum or various tree resins in the form of adhesives were firstly used. This was followed using chemically modified natural materials and it is continued today with the production of synthetic macromolecules produced by a variety of specific technologies.

Almost 90 % of produced plastics is thrown away immediately or within a few days (bags, packaging materials, bottles, wrappers, lighters, etc.). This leads to the global plastic/garbage problem. Hence, the following two main facts can be considered when we used the polymers:

- Plastics are mainly made from petroleum, which is a renewable natural resource.
- Plastics can only be recycled to a limited extent, but in nature plastics are almost indestructible - they are lightweight, durable, flexible and can withstand water, sunlight (and UV rays if they contain additives) and mechanical damage.

Recycling of the plastics is of high importance. To recycle plastics, one sorts them in recycling companies on sorting lines - the waste components that do not belong in the sorted plastics or are contaminated are sorted out. The sorting into different types depends on the processor or processing method. Sorted plastics are prepared for further processing [3].

Plastics are milled into various crumb stones or small pellets, which are used by melting and extrusion in the production of new products - they are treated as secondary raw material in the form of agglomerates or granulates for a specific product. Such recyclates are given a second chance and are reusable in a variety of industrial applications.

One possible use of such recycled plastics is for incorporation into asphalt mixes. On the other, it should be pointed out that not every plastic is suitable for such applications. Based on late research such granulates made from low-density polyethylene (LDPE) can be used very efficiently as an additive in asphalt mixtures.

At the very beginning we need to understand what such a multicomponent system consists of and by what possible force they are connected.

Basically, the asphalt mixture is a mixture of aggregates, binder, and fillers, used for constructing and maintaining roads, parking areas, ports, airport runways, bicycle lanes, sidewalks and also playgrounds and sport areas. It is produced in a plant that heats, dries, and mixes initial materials (aggregate, sand and bitumen) into a composite mixture. It should be pointed out, that the term asphalt is often mistakenly used to describe bitumen. According to the European specification (EN 12597), bitumen is a practically non-volatile, adhesive, and waterproof material obtained from petroleum or present in natural asphalt, which is completely or almost completely soluble in toluene and it is very viscous, or almost solid at ambient temperature [4]. Elemental analysis shows that the properties of the bitumen binder are primarily determined depending on the source of oil, properties of crude oil and distillation refining process, respectively. From a chemical point of view, bitumen is a complex mixture of approximately 300 to 2000 chemical compounds. The most and important are two groups of species: asphaltenes and maltenes [5].

Asphaltenes are amorphous brown, and/or black solids which contain oxygen, sulfur and transition metal atoms in the form of porphyrin rings of different length of aliphatic chains, pyrrole and pyridine rings. These large aromatic systems form large agglomerates / aggregates that are connected by intermolecular forces and π - π interactions. The resulting molecular aggregates form the so-called sandwich clusters and cause lower mobility of asphaltene molecules and thus significantly affect the viscoelastic properties and especially flexibility of bitumen. The proportion of asphaltenes in the bitumen ranges from 5 % to 25 % [6]. Due to the permanent electric charge and the presence of polar groups, together with polycyclic aromatic rings and metal complexes, asphaltenes contribute to the surface activity and adhesion of bitumen to aggregates.

Maltenes, which are responsible for adhesive properties, flexibility, and stiffness, form the second important fraction of bitumen structure. They contain lower molecular weight compounds, including resins, aromatic oils, saturated paraffins, respectively. Maltenes are soluble in low molecular n-alkane (n-pentane, n-heptane) [7].

Due to the good physico-chemical, rheological and thermal properties the net bitumen can be mixed with a wide range of chemical entities. According to their action the modifiers can be divided into adhesion, plasticizing, structuring and complex ones. A common feature of all such additives is that they must be compatible with the asphalt and can in no way impair the properties of the resulting mixtures.

Scientific research into the incorporation of various additives into asphalt has been growing steadily in recent decades and there are a number of materials that have been investigated.

They have been investigated for example nanomaterials [8], crushed rock, masonry and concrete [9, 10], bio-mass based product, such as bio-char, bio-oil, and bio-ash, etc. [11]

However, the most studied and already used in technical applications are plastics/polymers [12 – 17]. Regarding the use of plastic wastes for bitumen modification, those mentioned in the literature review are the low-density polyethylene [18], high density polyethylene [19], polypropylene [20] ethylene-vinyl acetate (EVA) [21, 22], acrylonitrile-butadiene-styrene [23], polyethylene terephthalate [24]. The recycled rubber from truck tires has also found great applications [25 – 28].

As it was demonstrated above many types of polymers are typically used in bitumen modification in different forms such as plastics, elastomers and reclaimed rubbers. On the other there are several limitations that must be fulfilled to prepare a good asphalt mixture with polymers. The produced polymer-modified asphalt mixture (PMAs)should satisfy a long list of requirements including appropriate mechanical properties, storage stability, high-temperature viscosity compatible with the traditional road-building processes and apparatus, and reasonable

cost, which remains of primary importance [13]. Given all these limitations only a very small number of polymers are currently used in industrial applications. A special criterion - especially in industrial applications in Slovakia - that such an application should be suitable for current asphalt mix plants in Slovakia. For above mentioned reason over research is oriented to the preparation of asphalt mixture with recycled polymer by so-called dry process. The dry process allows coating of plastics to the aggregates at high temperature followed by addition of bitumen to prepare the modified mix. The process seems to be very simple. On the other hand, the right chose of plastics – especially in case of recycled plastics – and the right chose of the reaction condition are of very high importance.
For that reason, the main objective of the presented research work was to demonstrate under laboratory conditions the effective use of recycled waste plastic by incorporating it into asphalt mixtures. Of course, to achieve our goal we had to fulfill some basic sub-objectives. One of the main criteria was to find a natural "one-component" polymer which should have a good miscibility in bitumen (blank sample). After this step we needed to find a suitable "recycled copy" of this material, which will have a very similar physical-chemical properties. The most common problem when a recycled plastic is used is the physical-chemical properties may differ from those of commercial, natural/virgin polymers. These quality differences add even more variables to the overall process mechanism and can have a major impact on the use of recycled plastic, the process technology, and the quality of the resulting asphalt mixture. The reaction conditions, such as the amount of plastic, temperature, mixing time, had to be set so that the mixture was completely mixed to completely coat the aggregate. The quantity and chemical nature of the recycled plastic must be very sensitively adjusted so that the recycled plastic is not completely dissolved during mixing and the quantity is such that the rheological properties are not ultimately compromised. If this were to happen the resulting properties would not meet the criteria for conventional asphalt mixture. The presented research work describes a very efficient way of incorporating recycled plastic into the asphalt mix.

2 Experimental Section

2.1 Materials and its Basic Characterization Methods

The bitumen with a penetration grade 50/70 from the Mol Hungarian Oil and Gas, Hungary has been procured and used (abbr. CA 50/70). This is the most used asphalt binder and meets the criteria for this type of research. All basic parameters of the bitumen were measured to make sure that the bitumen was of satisfactory quality for mix design. The measured parameters were penetration (according to EN 1426), softening point (according to EN 1427) and kinematic viscosity at 135 °C (according to EN 12 595), respectively. To assess the internal microstructure of the asphalt binder, a microscopic method using a scanning electron microscope (SEM, Tabletop Scanning Electron Microscope TM4000Plus (Hitachi High-Tech Corp., Japan) and an energy dispersive X-ray spectrometer (EDX) attached to SEM, AZtecOne (Hitachi High-Tech Corp., Japan) were used.
Aggregate from the Horný Tisovník deposit was used. The aggregate meets the requirements of the departmental regulation [29].
A commercially available low-density polyethylene (abbr. as LDPE) from SLOVNAFT, a. s. Slovakia was obtained.

Waste recycled plastics - the so-called low-density polyethylene recyclate - was obtained from RE-PLAST, s r. o., Zvončín (abbr. in the text LDPEre).
In case of LDPE and LDPEre sample the basic thermal and viscosity parameters were analyzed according to the required test methods used for the characterization of polymers.

2.2 Methods

In the actual design of the asphalt mixtures, the requirements of the departmental regulations KLAZ (Catalogue sheets for asphalt mixtures) [30] and TKP 6 (Technical-qualitative conditions for compacted asphalt mixtures) [31] were respected.

2.3 Laboratory Preparation of Asphalt Mixtures and Evaluation of Measured Results

A total of 3 asphalt mixes were prepared and characterized in this work, namely:
- Asphalt mixture: AC 16 loading 50/70 (designation in the text AC 16 L)
- Asphalt mixture: AC 16 loading 50/70 with 6 wt. % LDPE (designation in text AC 16 L-LDPE)
- Asphalt mixture: AC 16 loading 50/70 with 6 % by weight recycled plastics (designation in text AC 16 L -LDPEre)

For the procedure and conditions to produce the asphalt mixture in the laboratory the conditions in EN 12697-35 were used. The asphalt mixture shall be prepared at the required temperature, within the prescribed time interval. This required temperature being dependent on the gradation of the asphalt binder and related to the temperature of the subsequent compaction of the asphalt mixture during the production of the samples. A laboratory mixer equipped with thermostatically controlled heating and mechanically controlled speed was used to produce the asphalt mixtures. The mixer used to have a beater agitator, which is necessary to ensure that no damage to the aggregate or the mixer vessel can occur during mixing.
The aggregate (set of fractions according to Table 3) was dried to a steady weight in a ventilated drying oven at (110 ± 5 °C) prior to mixing with the desired grading lines along with the stone flour. Subsequently, the aggregate together with the stone fluor was weighed to an accuracy of 0.1 %. The net bitumen was also heated in a metal container (150 ± 20 °C) during preparation. After heating the initial samples, we proceeded to mix the asphalt mixture. Before mixing, we heated the container to the desired temperature and poured the weighed fractions of aggregate with stone flour into the mixing container. The aggregate grains were premixed for thorough mixing. After weighing the hot binder, we added the binder to the aggregate. The ingredients were thoroughly mixed, continuing mixing until a homogeneous mixture was obtained, and the aggregate was completely coated with the binder. The homogeneity of the mixture was checked visually. Mixing was stopped after four minutes. In case of the preparation of the asphalt mixture with added LDPEre, we followed a similar procedure, whereby the recyclate was added on top of the aggregate and after thorough mixing we added the hot bitumen. However, it should be noted that in this case, after visual inspection, we proceeded to increase the mixing time up to 5-6 minutes. After this time, we obtained a homogeneous asphalt mixture without any incompletely homogenized recycled granulates. It is important to remember that the added polymer - regardless of whether it is recycled or commercial ones – the equal amount of binder is replaced. This is very important due to the comparability of mixtures. We tried to keep the content of the components.

All empirical parameters of asphalt according to the respective catalogue sheets were analyzed in labrotory.

3 Results and Discussion

3.1 Basic Characteristics of Used Bitumen

At the beginning of the experimental work, we focused on the basic characterization of the initial samples. Table 1 shows the basic parameters of the bitumen sample CA 50/70 (STN EN 12591).

Table 1: Composition of the envelope structures of the assessed room

Tested characteristics	**Measured value**	**Test method**	**Requirement KLAZ**
Penetration at 25 °C; 0.1 mm	54.5	STN EN 1426	50 – 70
Softening point KG; [°C]	50.6	STN EN 1427	46 – 54
Kinematic viscosity at 135 °C; [mm^2/s]	539.1	STN EN 12595	≥ 295

The measured values clearly show that the bitumen sample CA 50/70 meets all the requirements for bitumen, used as a binder of the production of this type of asphalt mixture according to the asphalt catalogue sheets.

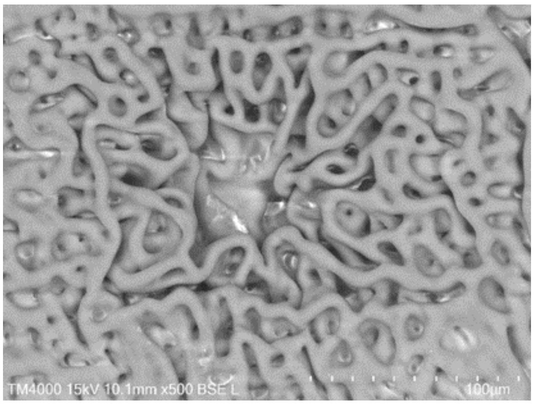

Figure 1: SEM micrograph of used bitumen sample CA 50/70

The SEM micrographs refers to the standard inner structure of bitumen (Figure 1). The structure was homogeneous, and no impurities in the binder have been identified. Elemental chemical analysis showed that used bitumen contains more than 97 % carbon atoms and approximately 2 – 3 % of sulphur atoms (as indicated on Figure 2).

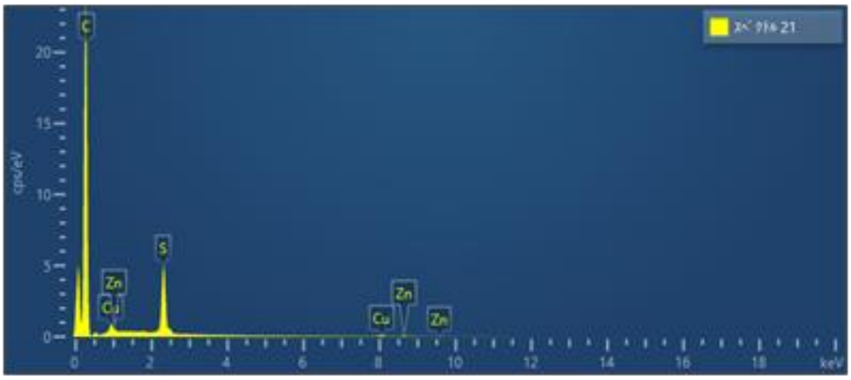

Figure 2: The EDX analysis of used bitumen sample CA 50/70

3.2 Basic Characteristics of the LDPEre

We received the material from RE-PLAST, Ltd. in two plastic 25 kg bags (LDPEre (1.bag) and LDPEre (2.bag). To guarantee the conformity of the two delivered samples, thermal and rheological tests (not shown here) were carried out on samples taken from both bags. Thermal analysis of the supplied recyclate confirmed the assumption that it contains other types of polyethylene (most likely a mixture of PE-LD and PE-HD in the presence of a slip agent, based on present peaks of melting temperatures). However, the composition of the recyclate does not negatively affect its use as an asphalt mixture modifier. Rheological curves can be observed in Figure 3.
Table 2 shows the basic thermal parameters together with the method used for the two LDPEre samples. As a reference sample the commercially available LDPE was used. The sample was tested using the same methods as recyclate samples.

Table 2: Basic thermal parameters of LDPEre (1.bag and 2.bag) and commercial LDPE sample

Property			**LDPEre**	**LDPEre**	**LDPE**
Parameter	**Unit**	**Test method**	1. bag	2. bag	
Melt mass flow rate (90 °C/2.16 kg)	g/10 min	STN EN ISO 1133-1	0.76	0.78	1.95
Melting point	°C		108.8/123.7	108.4/123.3	110.6
Crystallisation temperature	°C	STN EN ISO11357-3	111.7/97.8/ 61.9	111.5/97.8/ 61.9	95.6
5 % weight loss	°C		409.9	410.5	417.8
10 % weight loss	°C	PP SIV 0216	426.5	426.1	435.1
Temperature of decomposition	°C		447.4	445.9	452.9
Ash content	% (m/m)	PP SIV 0202	1.66	1.85	-

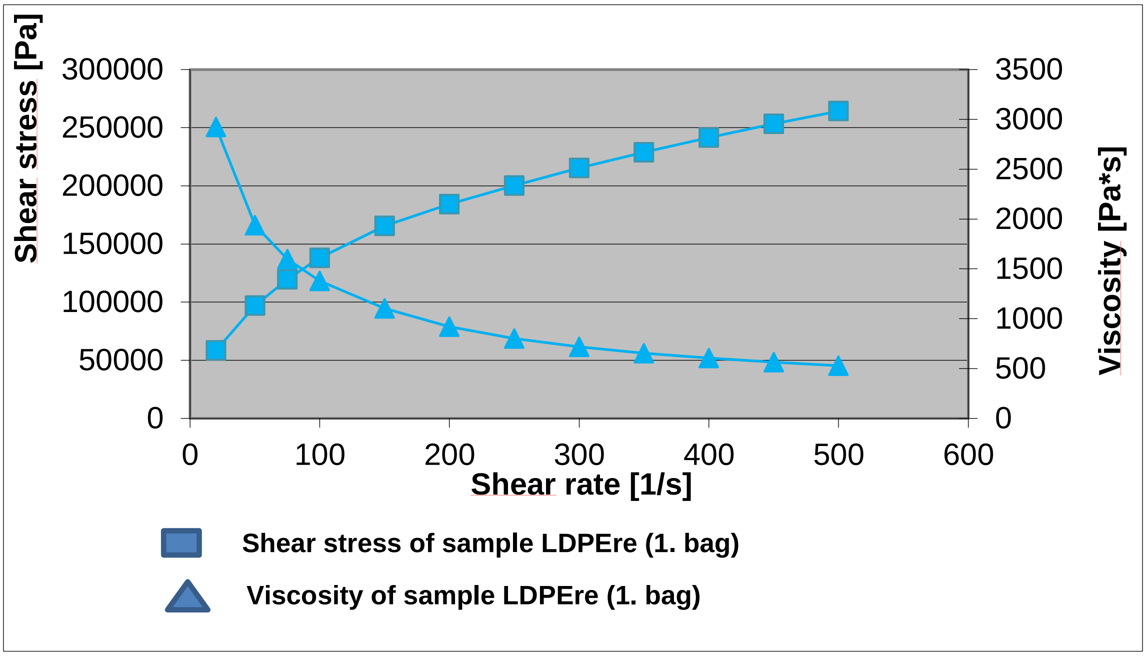

Figure 3: Rheological curves of used LDPEre (1.bag)

Design of the basic composition of asphalt mixtures for asphalt overlays and processing of mix recipes in accordance with the requirements of KLAZ and TKP 6.

In the next part of our study, we proceeded to design the basic composition of asphalt mixtures for the base course AC 16 L. The requirements of the departmental regulations KLAZ (Catalogue sheets for asphalt mixtures) and TKP 6 (Technical-qualitative conditions for compacted asphalt mixtures) were respected in the design mixture. The composition is described in Table 3.

Table 3: Composition of asphalt mixtures AC 16 L

Aggregate	**Fraction**	**% (by mass in AC 16 L mixture)**
Mýtna	0/4	35.00
Horný Tisovník	4/8	22.00
Horný Tisovník	8/11	10.00
Horný Tisovník	11/16	30.00
Žirany	stone flour	3.00
TOTAL		100.00

In case of use of LDPEre, the 6 % LDPEre per weight of bitumen content was used. The percentage recyclate in asphalt mixture was calculated by our previous experiments and based on most common literature evidence [10, 13 – 24 and references therein]. At the very beginning of our research, we start to understand how the polymer is incorporated to the asphalt mixture. We have investigated the various loadings of LDPE to asphalt mixture, i.e., i.e. 4 %, 6 %, 8 % and 10 % by weight of bitumen. The results of tour test showed that the mix containing 6 % by weight of recycled plastic has ideal properties and meets most of the criteria that have been set for asphalt mixes.

The aggregate mixture as shown in Table 3 is composed of individual fractions and stone flour so that the resulting grain size line conforms to the grain size limit lines specified in the respective asphalt mix catalogue list. The resulting cumulative percent passing through the sieve meet the requirements for aggregate gradation and quality according to the applicable technical notes. After successful preparation of the asphalt mixtures at laboratory conditions the set of empirical parameters were investigated. The results are listed in Table 4.

Table 4: The tested empirical parameters of asphalt mixtures

Measured Parameter	**Unit**	**AC 16 L**	**AC 16 L - LDPE**	**AC 16 L - LDPEre**	**Requirements [30]**
Grain size	22.4	100	100	100	100
	16	100	100	98	90 - 100
	8	69	60	52	50 -75
	2	32	27	25	20 - 45
	0,5	15	13	12	7 - 26
	0,063	9.0	8.2	7.4	3 - 11
Bitumen content	B_{min}	4.2	4.2	4.0	4.4
Intergranularity	V	5.0	5.9	6.2	3.5 – 6.0
Maximum bulk density	ρ_{vm}	2.532	2.509	2.512	-
Bulk density	ρ_{bssd}	2.406	2.361	2.356	-
Water sensitivity	ITSR	96	98	95	70
Resistance to permanent deformations	PRD_{AIR}	5	3.4	3.1	3
	WTS_{AIR}	0.048	0.032	0.025	0.07

According to the measured results, it can be pointed out that the laboratory prepared and investigated asphalt mixtures shows very similar properties. Small deviations were measured in the case of intergranularity, resistance to permanent deformations. The small deviation was also confirmed in bitumen content. This can be explained in a simple way. Although in the experiment we follow the so-called wet process, we still try to add individual components to the mixing container by pouring granules on the hot bitumen. This means that the recylate immediately meets the hot bitumen and undergoes chemical decomposition, which is then further aided by the mixing and mixing time. Ideal modification is obtained when the polymer conserves its internal structure after mixing with bitumen, the molecules of which determine only a macroscopic swelling of the network. If the network becomes a continuum that involves

the entire material, the overall mechanical properties of the polymer-modified mixture markedly reflect those of the polymer [13]. Whether this can be realized or not depends on the interactions among the asphalt components and the polymer. Such interactions obviously depend on the chemical affinity of the inner structure, which is characterized by different polarities. Therefore, it seems to be that during the first contact usually the selectively swelling occurred. For our opinion the part of the polymer – the melted small fragments – become the part of the bitumen and thus increasing the volume of asphalt.
The conclusion of this reflection is that the success of the preparation of polymer-modified asphalt mixture comes from the ability of some compatible polymers to significantly influence and improve the rheological properties of bitumen, even when added in relatively small quantities. But, on the other hand the number of chemical entities that are dissolved during mixing and the temperature cannot exceed so much that the rheological properties are ultimately impaired. The other entities are swollen between the aggregates but being fully compatible they do not cause a change in properties.
It should be also noted that he preparation of asphalt mixtures with plastic recyclate - but also with any other type of modifier - can be carried out in two ways. According to the literature and also to practical results, the most ideal solution is the pre-modification of the asphalt binder [32]. As it was mentioned before his method is called the "wet route", where the modifier or, additives (plastic, rubber, etc.) are mixed under given reaction conditions (temperature, pressure, mixing time) to the asphalt binder. This can be done in additional equipment, called mixers or "blenders". The problem is that such equipment does not exist in Slovakia. This means that we have tried to adapt fully to the requirements of the practice. Because of this, our research and subsequent validation has been set up so that the technological procedure could be applicable to current asphalt mix plants in Slovakia.
However, even when modifying the mix itself, both the asphalt and the asphalt with the modifier (in our case LDPE and LDPEre) must meet the adhesion criteria of EN 12697-11. In our research, this is a very important criterion because the LDPEre is used the first time. This type of recyclates for such purposes have been investigated in Slovakia first time. Therefore, we have already carried out affinity tests in the laboratory prior to the actual preparation. We repeated the test with net bitumen type: CA 50/70 and with bitumen CA 50/70 modified with commercially available LDPE. The results were approximately 70 – 80 % for the conventional asphalt, very similar for the adhesion between aggregate with asphalt binder modified with commercially available LDPE, but results were as high as 90 – 95 % when LDPEre was used. This test was decisive for us and confirmed that the recyclate was suitable for its intended use [32]. To illustrate, in Figure 4 are the photographs of the measured results.
The measured values clearly show that the bitumen sample CA 50/70 meets all the requirements for bitumen, used as a binder of the production of this type of asphalt mixture according to the asphalt catalogue sheets.

Even so, we consider these results very promising and by a small change of the reaction conditions we will be able to adjust the whole reaction mechanism in the future to respect the values given in the KLAZ. It should be noted that in the case of using recycled polymer, we must consider many factors that may affect the sample, and these may be since we need to know exactly the source of the waste plastic, the separation of the different components and of course the resulting properties of the recyclate.

Figure 4: Affinity tests between aggregate and net bitumen type CA 50/70 (left), net bitumen type CA 50/70 modified with commercially available LDPE (centre) and net bitumen type CA 50/70 modified with LDPEre (right)

Even if the basic rheological and thermal properties of the sample did not show large variations, obviously even a small change in the physical-chemical properties can cause variations in the final mixture. In further experiments, we must also adjust the entire reaction time and mixing procedure so that the sample is indeed completely homogeneously mixed.

4 Conclusion

The use of recycled low-density polyethylene in asphalt mixtures was demonstrated in this study. Based on our laboratory experiments and results modified asphalt mixture with 6 weights % of recycled LDPE added exhibits properties very similar to conventional asphalt mixtures. From the measured results, it can be pointed out that the asphalt mixture with PE-LD shows very similar properties to that without recyclates. Small deviations were measured in the case of intergranularity which has in overall no effect on the final mixture. Moreover, the mixing time needs to be extended in case of use of recycled LDPE. On the other hand we can conclude that the mixture with recyclate showed a very similar feature as a conventional asphalt mixture. All results and observations must be considered in the production of asphalt mixtures in a plant in a future. The results to date will serve as a basis to produce asphalte mixture in a plant.
However, it is important to be aware of some important facts arising from such multidisciplinary research. The use and therefore the production of plastic products is still increasing all around the world. This is happening even though humanity is still trying to do its best to prevent plastic waste. However, to understand the whole value of the input of plastics to the environment we must consider not only the production/ distribution but also the waste management chain. This is very important feature, because this is the starting line to implement the effective ways and technological procedures for reduction the waste or for its recycling. Incorporation of waste plastic in this scale, as it is described in our study, will not solve the global environmental problem with the accumulation of the garbage. On the other hand, it opens the way to reduce of the environmental impact of reducing the plastic waste. Our effort in this research-oriented paper was to show that how many factors must be taken into consideration to obtain the asphalt mixture that meets all the requirements placed on it. However, by gradually removing all the undesirable properties and by setting up the right mechanism, it will be possible to set up the technological procedures so clearly that the technology of adding waste plastics to asphalt mixtures can be used in common practice in Slovakia soon.

Acknowledgments

This work was supported by the Slovak Research and Development Agency under the contract No. APVV-19-0520.

References

[1] Online, www.naturpack.sk

[2] Mikulášová, D. (2002). Makromolekulová chémia, STU Bratislava.

[3] Hopewell. J., Dvorak, R., & Kosior, E. (2009) Plastic Recycling: Challenges and Opportunities. *Philosophical Transactions of The Royal Society B Biological Sciences*, 364, 2115 – 2126.

[4] European Committee for Standardization (2000) EN 12597: Bitumen and Bituminous Binders-Terminology; European Committee for Standardization: Brussels, Belgium.

[5] D´Melo, R. Taylor (2015) Constitution and structure of bitumens. In: The Shell Bitumen Handbook, 6th ed.; R. N. Hunter, S. Self, J. Read (eds.); ICE Publishing: London, UK (ISBN: 978-0727758378).

[6] Speight, J. C. (2004). Petroleum Asphaltenes. Part 1. Asphaltenes, resins and the structure of petroleum. *Oil&GasScience and Technology*, *59*, 467 – 477.

[7] Corbett, L. W. (1969). Composition of asphalt based on generic fractionation, using solvent deasphaltening, elution-adsorption chromatography and densimetric characterization. *Analytical Chemistry*, 41, 576 – 579.

[8] Jahromi, S. G., Khodaii, A. (2009). Effects of nanoclay on rheological properties of bitumen binder. *Construction and Building Materials*, *23*(8), 2894- 2904. doi: 10.1016/j.conbiuldmat.2009.02.027.

[9] Azizian, M. F., Nelson, P. O., et al. (2003). Environmental impact of highway construction and repair materials on surface and ground waters: Case study: crumb rubber asphalt concrete. *Waste management*, *23*(8), 719-728.

[10] Paranavithana, S, Mohajerani, A. (2006). Effects of recycled concrete aggregates on properties of asphalt concrete. *Resources Conservation and Recycling*, *48*(1), 1-12.

[11] Xuefei, Z., Kun, Z., Wu, Ch., Kefei, L., Kan, J. (2020). Preparation of bio-oil and its application in asphalt modification and rejuvenation: a review of the properties, practical application and life cycle assessment. *Construction and Building Materials*, *262*, 120528, https://doi.org/10.1016/j.conbuildmat.2020.120528.

[12] Giavarini, C. (1994). Polymer-Modified Bitumen. In: Apshaltenes and Asphalts 1. Developments in Petroleum Science (T. F. Yen, G. V. Chilingarianeds.) Elsevier, New York, 381 – 400.

[13] Polacco, G., Filippi, S. (2015). A review of the fundamentals of polymer-modified asphalts: Asphalt/polymer interactions and principles of compatibility. *Adv. Colloid Interface Sci*, *224*, 72–112. doi: http://dx.doi.org/10.1016/j.cis.2015.07.010

[14] Zhu, J., Birgisson, B., Kringos, N. (2014). Polymer modification of bitumen: Advances and challenges. *Eur. Polym. J.*, *54*, 18–58.

[15] Kalantar, Z. N., Karim, M. R., Mahrez, A. (2012). A review of using waste and virgin polymer in pavement. *Constr Build Mater.*, *33.* 55–62.

[16] Bouldin, M. G., Collins, M. J. H., Berker, A. (1990). Rheology and microstructure of polymer/asphlat blends. *Rubber Chem. Technol.*, *64*, 577–600.

[17] Dalhat, M. A., Wahhab, A. A. (2017). Performance of recycled plastic waste modified asphalt binder in Saudi Arabia. *Int. J. Pavement Eng.*, *18*, 349 – 357.

[18] García-Morales, M., Partal, P., Navarro, F.J. & Gallegos, C. (2006). Effect of waste polymer addition on the rheology of modified bitumen. *Fuel*, *85*(7-8), 936-943.

[19] S. Hınıslıoğlu and E. Ağar (2004) Use of waste high density polyethylene as bitumen modifier in asphalt concrete mix, Materials Letters, 58(3-4), pp. 267-271.

[20] Casey, D., McNally, C., Gibney, A. & Gilchrist, M.D. (2008). Development of a recycled polymer modified binder for use in stone mastic asphalt. *Resources Conservation and Recycling*, *52*(10), 1167-1174.

[21] García-Morales, M., Partal, P., Navarro, F.J., Martínez-Boza, F., Gallegos, C., González, N., González, O. & Muñoz, M.E. (2004). Viscous properties and microstructure of recycled eva modified bitumen. *Fuel*, *83*(1), 31-38.

[22] Isacsson, U. & Lu, X. (1999). Characterization of bitumens modified with SEBS, EVA and EBA polymers. *Journal of Materials Science*, *34*, 3737-3745.

[23] Isacsson, U. & Lu, X. (1999). Characterization of bitumens modified with SEBS, EVA and EBA polymers. *Journal of Materials Science*, *34*, 3737-3745.

[24] Ahmadinia, E., Zargar, M., Karim, M.R., Abdelaziz, M. & Ahmadinia, E. (2012). Performance evaluation of utilization of waste Polyethylene Terephthalate (PET) in stone mastic asphalt. *Construction and Building Materials*, *36*, 984-989.

[25] Lewandowski, L. H. (1994). Polymer modification of paving asphalt binders. *Rubber Chem Technol 1994*, *67*(3), 447–80.

[26] Legge, N. R. (1987) Thermoplastic elastomers. *Rubber Chem Technol*., *60*(3), 83–117.

[27] Cao, W. (2007) Study on properties of recycled tire rubber modified asphalt mixtures using dry process. *Construction and Building Materials*, *21*, 1011-1015.

[28] Issa, M. (2020). The impact of adding waste tire rubber on asphalt mix design. Proceedings of International Structural Engineering and Construction Emerging Technologies and Sustainability Principles, Edited by Hossein Askarinejad, Amarjit Singh, and Siamak Yazdani ASEA SEC 5, Christchurch, New Zealand.

[29] KLK 1/2021 Aggregates catalogue list, MDV SR: 2021.

[30] KLAZ 1/2019, Asphalt catalogue list, MDV SR: 2019.

[31] TKP 6 Dense asphalt mixtures, MDV SR: 2019.

[32] EN 12697-11:2020 Bituminous mixtures – Test methods – Part 11: Determination of the affinity between aggregate and bitumen

[33] Czímerová, A., Takáčová, A., Sasai, R., Lukáčová, E. (2023). Bitumen modified by virgin and waste low-density polyethylene. *Petroleum and Coal*, *65*, 363 – 375.

DOI: 10.2478/sspjce-2023-0002

Impact of Takt-Time Planning on Plastering Work Productivity: A Case Study

Mária Kozlovská[1], Daria Kempecova[1*]

[1]Technical university of Kosice, Slovakia
Faculty of Civil Engineering, Department of Technology, Economics and Management in Civil Engineering
*e-mail: daria.kempecova@tuke.sk

Abstract

This article aims to analyze productivity issues during the implementation of plastering works on the case study of a residential complex. The results of the study revealed that establishing a proper work schedule and adhering to the Takt schedule resulted in a 19% increase in plastering productivity compared to non-Takt schedules. Furthermore, the study identified the existence of waste, which had a negative impact on the progress of the plastering work and could have been prevented through better project planning during the initial project phases.

Keywords: takt-time planning, productivity, project management, construction, plastering works.

1 Introduction

Productivity in construction is an important factor that can greatly impact the success of a project. It refers to the amount of output or work completed in a given time period and can be influenced by various factors such as the quality of materials and equipment used, the efficiency of workers, the effectiveness of management and planning, and the overall project design [1]. Improving productivity in construction can lead to cost savings, increased profitability, and timely project completion. However, it can be a complex challenge, requiring careful analysis and implementation of various strategies and tools to optimize processes and resources [2].
Construction productivity specifically pertains to the measure of output or work completed per unit of labor, materials, and resources employed in construction projects. It evaluates the efficiency and effectiveness of the construction process and is essential for project managers and stakeholders to ensure timely project delivery and cost-effectiveness. Labor productivity refers to the measure of output or work accomplished per unit of labor input. It assesses the efficiency and effectiveness of workers in each timeframe. Labor productivity is a crucial metric for evaluating the performance of a workforce and identifying opportunities for improvement in various industries, including construction [3].
Construction projects are often complex, involving multiple tasks and resources that must be carefully coordinated to ensure successful completion. Lean construction can be very helpful in improving construction processes and reducing waste. Lean construction is a methodology that

aims to eliminate waste and improve efficiency in construction projects by focusing on continuous improvement, value creation, and collaboration among all stakeholders [4], [5], [6]. One lean tools that can help with improving productivity is Takt time planning, a method that originated in manufacturing but has been adapted for use in construction [7], [8], [9].
Takt time planning is a method of scheduling work that is based on the time available for production and the rate at which work must be completed. In manufacturing, takt time refers to the rate at which a product must be produced in order to meet customer demand. In construction, takt time planning involves breaking down the construction schedule into smaller tasks and then scheduling those tasks based on the available time and resources [10], [11]. A construction schedule is a detailed and time-bound plan that outlines the sequence of activities, tasks, and milestones required to complete a construction project. It includes start and finish dates for each activity and helps project managers and stakeholders monitor progress, allocate resources, and manage the overall timeline of the construction project. The construction schedule is a vital tool for ensuring that the project is completed on time and within the allocated budget [3].
To begin the Takt time planning process, the construction team must first establish the overall project timeline and identify the key milestones that must be met along the way, this can be usually done by the last planner. The team must also determine the total number of working hours available for the project, as well as any other constraints, such as limited access to the site or the availability of materials and equipment. Once these parameters have been established, the team can begin to divide the project into smaller tasks that can be completed within the available time. The next step would be to divide the workstations into work areas that have similar work volumes. The takt time planning process also involves identifying the resources that will be needed to complete each task, such as labor, materials, and equipment. The team must ensure that these resources are available when needed and that they are used efficiently to minimize waste and maximize productivity. One key benefit of takt time planning is that it can help to identify potential bottlenecks and other issues that could delay the project. For example, if a particular task is scheduled to take longer than the available time, the team may need to allocate additional resources or adjust the schedule to ensure that the project stays on track. Another benefit of takt time planning is that it can help to improve communication and collaboration among the construction team. By breaking the project down into smaller tasks and establishing clear timelines and resource requirements for each task, the team can work together more effectively to ensure that the project is completed on time and within budget [10], [12], [13].
Signs of effective work practices often include [14]:

- Fluidity of work: This refers to the smooth flow of work, where work crews are able to move from one work area to another without unnecessary breaks. It also includes the efficient utilization of production resources, such as materials, machines, workers, and finances, without delays or bottlenecks.
- Uniformity of work: Uniformity of work refers to the consistent and planned level of productivity maintained by workers within designated workspaces over a specific period of time. It encompasses not only the equal distribution of working hours but also the deliberate effort to ensure that each worker performs their tasks with a standardized level of productivity. By adhering to this principle, work crews aim to achieve a sense of regularity and stability in their output, thereby minimizing disruptions or variations in the work process.

- Rhythmicity of work: This refers to the repetition of work in certain or consistent rhythms. This can include having a set pace or rhythm for completing tasks, which can help maintain productivity and avoid unnecessary delays.

The main goal of this article is to analyze the productivity issues during the implementation of plastering works on the case study of residential complex Popradská. The purpose of this study can be categorized into two main objectives: i) to map the process of performing plastering works by manually monitoring workers at least once a week; ii) to design an improved work schedule by utilizing Takt time planning to enhance workers productivity.
The result of the mapping will be a time-space display of the duration of the work and the location of the workers. After the mapping, the takt time will be determined and an analysis of the real productivity that workers could achieve will be made.

2 Methods

This article aims to analyze productivity issues during the implementation of plastering works on the case study of residential complex Popradská. Building SO 104 - Apartment building "B" is designed as a separate rectangular building with overall dimensions of 81.58 x 20.71 m. It consists of three sections (Figure 1), which are connected on 2 underground floors within a shared garage, which is also connected on the 2nd floor by a tunnel to parking facility G (building site SO 106 G). The building is designed as a 3-section, detached 9-storey building (2 underground and 7 above-ground floors) [15].

Figure 1: Case study residential complex Popradská: apartment building "B", divided into three sections with marked work zones: (a) 2.th Floor plan, (b) section C-C [15]

In order to fulfill the goal of the study, three main research steps were established:
1. Initial analysis and evaluation of existing literature.

In order to prepare a relevant and up-to-date article on the impact of Takt-time planning on plastering performance, an initial analysis and evaluation of existing literature and practice was carried out. Two sources, namely the Web of Science and SCOPUS databases, were utilized to obtain up-to-date information. The search engine was utilized with keyword combinations such as "Construction productivity" and "Takt-time planning" as well as "Construction schedule" and "Takt-time planning." This made it possible to create a theoretical basis for the study.

2. On-site data collection through manual observation, photo documentation and interviews with workers.

The next step after the initial literature review is to create a methodology for gathering and examining data from a case study. The case study residential complex Popradská is located in Kosice, Slovakia. Plastering work was chosen as the main process for the data gathering as it is an important part of interior construction. Three teams that perform plastering work were selected for productivity measurement. Each team consisted of three workers with the same work skills. At this stage, the progress of the plastering work will be mapped by manually monitoring the performance of workers using Excel forms on mobile on a weekly basis. The data used in this article were collected over a period of five months. The mapping will result in a spatio-temporal display of work duration and workers' location.

3. Design an improved work schedule using Takt-time to improve productivity.

At this stage, an analysis of the actual performance will be carried out to determine the required takt time. A takted work schedule will be prepared based on actual performance with better use of spatio-temporal management principles. One working zone is equal to one floor in one section. Underground floors were not taken into account, since work was not executed there, therefore the total number of working areas is 21. In Figure 1, it can be seen that section number 2 is smaller in area than sections number 1 and 3, which are equal. The difference in the areas of the working zones should be taken into account when determining the duration of the takt.

3 Results and Discussion

Mobile forms of monitoring were used to document the execution of plastering work. The forms were prepared in Excel and placed on Google Drive in order to enable editing this file through phone and computer without having to download it. The used form consisted of date, work zone, section number, number of the apartment, completion indicator for each construction for the plastering (ceiling and walls), number of work team, and the number of workers in subsequent team. For the ease of documenting each work zone in the form was named according to its floor and section, for example 1.1 work zone represents (1.NP, section B1). The evaluation of the level of completion of the construction was made in percentage and based on the subjective opinion of the author during the visual screening. The example of the used spreadsheet is presented in Figure 2.

Plastering work monitoring form					**Date:**	
Work zone	**Section**	**Apartment**	**Completion indicator for ceiling**	**Completion indicator for walls**	**Work team**	**Number of workers**
2.1	B1	201	100%	100%	1	3
2.1	B1	202	100%	50%	1	3

Figure 2: Example of output from monitored data of plastering works

Since it was important to reflect the true production process, the work status had to be documented at least once a week, with a re-creation of the movement of workers through personal interviews with workers. The results of mapping the direction of the work of individual work teams are depicted in Figure 3.

From picture 3, it can be observed that the work process is disorganized, irregular, and unnecessary breaks occur. Teams work at different speeds without smoothness, uniformity, and rhythm, which are three fundamental characteristics of an effective construction process. Additionally, it is evident that the direction of process organization was not controlled since the teams initially worked in a horizontal-ascending direction, but subsequently, the direction of plastering started to show a chaotic nature. Such inconsistent organization can have a negative impact on the efficiency and flow of the work process.

Figure 3: The results of mapping the direction of the plastering work of individual work teams on a typical plan of the 3rd floor and in section (- team № 1, - team № 2, - team № 3)

The data collected is a detailed record of the progress of work over a period of five months, with daily updates. However, to make it easier to visualize and analyze the data, it was decided to group the daily progress updates into working weeks instead and create a simplified form of a table that shows the progress made during each week. This type of data aggregation can be helpful for identifying patterns and trends in the progress of work overtime and can make it easier to spot areas where progress is lagging or where adjustments may need to be made. The results of the data collection are depicted in Figure 4.

The completion indicator column is used to track the progress of construction, where each floor is divided into sections that need to be completed. The green color indicates that the section has been fully completed (100%), the red color indicates that the section has not been started yet (0%), and the yellow color indicates that the section has been started but is not yet complete, with an approximate percentage of completion being assigned. This system allows for a quick visual representation of the progress being made on the project.

As it was mentioned before, three teams that perform plastering work were selected for productivity measurement and each team consisted of three workers. However, the number of workers is not a constant value and could change, so this value should also be monitored. Teams are depicted in different colors in Figure 4 with the number of workers in each team is shown. This type of visual representation can be helpful for quickly identifying which teams are working on the project, how many workers are in each team, and potentially how the workload is being distributed among the teams.

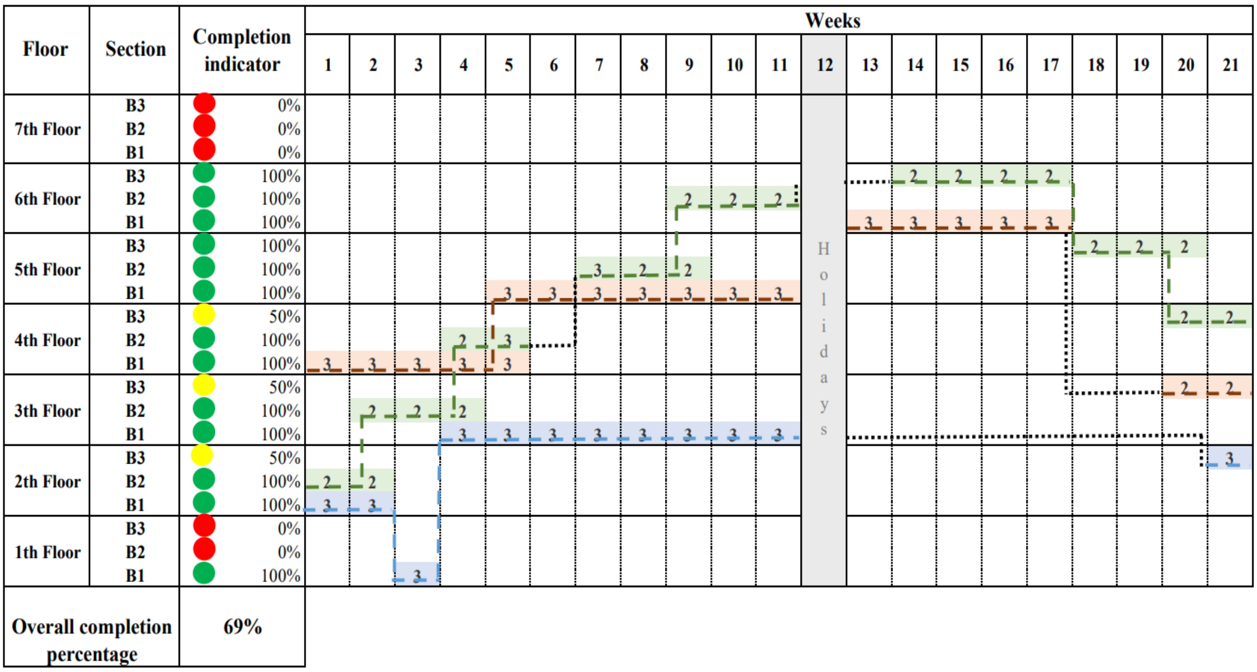

Figure 4: Spatio-temporal representation of the execution of plastering works by 3 work groups

(- *color display of work teams, with the number of the workers in each team;*

- *spatio-temporal movements of each team;* - *unproductive time;*

- *work has not started;* - *work in progress;* - *work completed).*

In addition, the overall plastering work completion percentage was calculated as the average of each section's completion rate (1).

According to Figure 4, the overall completion percentage is 69%.

$$y = \frac{\sum_{i=1}^{n} x_i}{\mathrm{n}} \tag{1}$$

y - overall completion percentage; *x* - completion indicator; *n* – total number of work zones.

From Figure 4, it can be seen that workflow is chaotic, not smooth, there are unnecessary breaks, teams work at different speeds without consistency. During data collection, several cases of inefficient use of production resources such as materials, machines, workers were noted, which led to delays. For example, the lack of adequate water supply and electricity has been identified as critical issues that could be mitigated by improved project planning during the construction organization phase.

Takt time planning principles were used to optimize the plastering workflow. At first, the direction of the progress of work was designed. The implementation of an organized work process successfully addressed deficiencies in work organization (Figure 5), which were previously evident through the chaotic progression of individual teams within the workspace (Figure 3). By having each team follow a unified horizontal-ascending direction, they were able to transition seamlessly between floors. This streamlined approach optimizes workflow, ensuring tasks are carried out sequentially and efficiently, thereby increasing productivity and minimizing redundancy. The consistent direction assigned to each floor facilitates easy orientation for individual trades in the work environment, promoting standardized production procedures. This clear guidance fosters improved coordination, cooperation, and performance among the various trades, enhancing overall project efficiency.

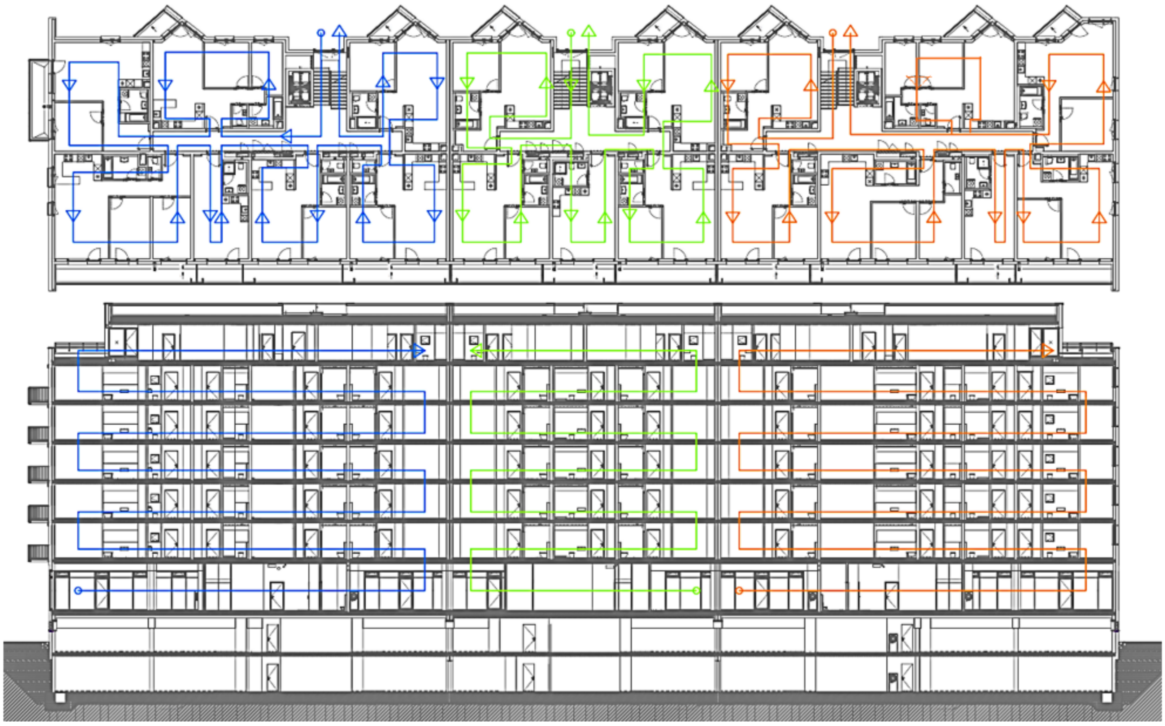

Figure 5: The designed direction of the progress of work on the example of a typical plan of the 3rd floor and in section (__ - team № 1, __ - team № 2, __ - team № 3)

In the next step the length of the takt time was defined based on analysis of the spatio-temporal representation of the execution of plastering works, were the duration of the work at work zone weren't set. The real work rate was defined. It should be noted that the work rate was found not to measure how much square meters were done within 1 hour, but to determine how many days it takes to complete the work in one working zone. The green team (number 2) was chosen as a sample for the work rate calculation because it demonstrated the most effective execution of work with no significant waste occurrences. Selecting a sample group, such as the green team, that represents a high level of efficiency and effectiveness in executing work can be useful for determining work rates or productivity benchmarks. According to the results the average duration of work for the 2 workers in section B2 is three weeks, whereas in section B3 is four weeks. Therefore, the production takt time was set at four weeks for each section, but with different number of workers. Sections B1 and B3 were assigned three workers, while section

B2 required two workers due to its smaller square footage. It is assumed that the workers are not working at 100% capacity in order to provide time buffers necessary to eliminate possible wastes. The designed takt schedule of the execution of plastering works is presented in Figure 6.

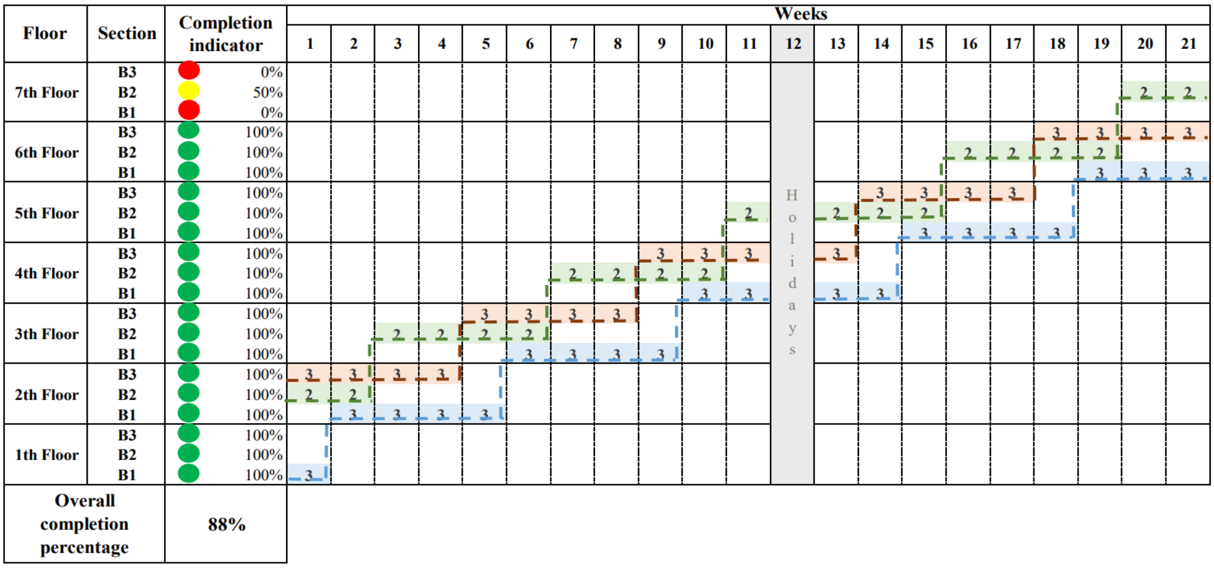

Figure 6: Designed takt schedule of the execution of plastering works by 3 work groups with 4 weeks takt (*- color display of work teams, with the number of the workers in each team; - spatio-temporal movements of each team; - work has not started; - work in progress; - work completed).*

As shown in Figure 6, the overall completion rate after implementing takt time principles is 88%, indicating a 19% increase in productivity. Designed schedule is fluid, it means that there are no unnecessary interruptions or delays in the work process, and resources are being used efficiently. It is uniform, it means that there is consistency in the work process, which helps prevent disruptions or inconsistencies. And work is rhythmic, it means that there is a set pace or rhythm for completing tasks, which helps maintain productivity and avoid unnecessary delays. All of these factors contribute to a more efficient and effective work environment. In addition, the workflow is smooth, paced, standardized, there is no unproductive time, therefore it can be considered efficient.

4 Conclusion

The article's findings are based on plastering work performed on the Popradská residential complex construction project, which was the subject of the case study.

According to the study findings, it was observed that a correctly established work schedule and adherence to the Takt schedule led to an increase in plastering workers productivity in 19% compared to non-Takt schedules. Additionally, the study identified the presence of waste, which adversely impacted the progress of the plastering work. Specifically, the lack of adequate water supply and electricity were identified as critical issues that could have been mitigated through improved project planning during the construction organization phase.

In conclusion, takt time planning is a valuable tool for construction project planning and scheduling. By breaking the project down into smaller tasks and establishing clear timelines and resource requirements for each task, the construction teams can work together more efficiently and effectively to ensure successful project completion. While takt time planning may require some additional effort upfront, the benefits in terms of improved productivity, reduced waste, and greater project success make it well worth the investment.

Acknowledgments

The activity presented in the article is part of the VEGA research grant No. 1/0336/22 “Research on the effects of Lean Production/Lean Construction methods on increasing the efficiency of on-site and off-site construction technologies”.

References

[1] Hossain A., Bissenova A. & Kim J. R. (2019). Investigation of Wasteful Activities Using Lean Methodology: In Perspective of Kazakhstan’s Construction Industry. *Buildings 9*(5), 113. DOI: 10.3390/buildings9050113.

[2] Rajkumar K. B. & Biswas A. P. (2016). Identification of Non-Value Adding Activities using Lean Technology in Construction. *Int. J. of Engineering Research & Technology (IJERT) 5*(3), pp. 640-643. Retrieved date of access 11.04.2023 from https://www.ijert.org/.

[3] Chamulová B. (2013). Dynamický časový plán v procese riadenia výstavby. 1. vyd. Brno: Tribun EU, 97.

[4] Issa Us. H. & Alqurashi M. (2020). A Model for Evaluating Causes of Wastes and Lean Implementation in Construction Projects, *Jour. of Civ. Eng. and Man. 26 (4),* 331.

[5] Mughees, A., Zhili, G. & Gary, S. (2020). Framework for selection of lean construction tools based on lean objectives and functionalities. *International Journal of Construction Management*, DOI:10.1080/15623599.2020.1729933.

[6] Zhanga, L. & Chenb, X. (2016). Role of lean tools in supporting knowledge creation and performance in lean construction. International Conference on Sustainable Design, Engineering and Construction. *Procedia Engineering, 145*, pp. 1267 – 1274. DOI: 10.1016/j.proeng.2016.04.163.

[7] Brioso X., Murguia D. & Urbina A. (2017). Teaching Takt-Time, Flowline, and Point-to-Point Precedence Relations: A Peruvian Case Study. In Creative Construction Conference, 19-22 June 2017, Primosten, Croatia.

[8] Yassine T., Bacha M. B. Sa, Fayek F. & Hamzeh F. (2014). Implementing Takt-Time Planning in Construction to Improve Workflow. In IGLC-22 Production Planning and Control 22, June (pp. 787–798). Oslo.

[9] Fabian A., & Adel F. (2020). Spatiotemporal Planning of Construction Projects: A Literature Review and Assessment of the State of the Art. *Front. Built Environ. 6.* DOI: 10.3389/fbuil.2020.00128.

[10] Keskiniva K., Saari A. & Junnonen J.-M. (2021). Takt Production Monitoring and Control in Apartment Renovation Projects. *Buildings, 11,* 92. DOI: 10.3390/buildings11030092.

[11] Keskiniva K., Saari A. & Junnonen J.-M. (2020). Takt Planning in Apartment Building Renovation Projects. *Buildings, 10,* 226; DOI:10.3390/buildings10120226.

[12] Frandson A., Berghede K. & Tommelein I. (2013). Takt Time Planning for Construction of Exterior Cladding. In 21st annual conference of the International Group for Lean Construction, 31-2 Aug (pp. 527–536). Fortaleza, Brazil.

[13] Brioso X., Murguia D. & Urbina A. (2017). Comparing three scheduling methods using BIM models in the Last Planner System. *Organization, Technology and Management in Construction: An International Journal,9*(1) 1604-1614. DOI: 10.1515/otmcj-2016-0024.

[14] Gašparík, J., Motyčka, V., Šťastný, P., & Szalayová, S. (2021). Multi-Criteria Optimization of Mechanized Earth Processes and Its Impact on Economic and Environmental Sustainability. *Sustainability, 14*(1), 78. DOI: 10.3390/su14010078.

[15] Gonos R. & Kušnírik M. (2021). Polyfunkčný súbor "Popradská" I.etapa. Realizačný projekt, 1-22.

DOI: 10.2478/sspjce-2023-0003

Optimization of a Self-Compacting Paste Based on Glass Powder Using Mixture Design and the Desirability Function

Messaouda Ch. Boulkhiout[1*], Ryad Amdoun[2], El Hadi Benyoussef[1], Abderrahim Bali[1]

[1] Laboratory of Civil Engineering Materials and Environment, Ecole Nationale Polytechnique, Algiers, Algeria
[2] Institut National de la Recherche Forestière (INRF), Baïnem - BP 37, Cheraga, Algiers, Algeria
*e-mail: messaouda.cherrak@g.enp.edu.dz

Abstract

The partial replacement of cement by supplementary cementitious materials is an opportunity for reducing fossil energy consumption and greenhouse gas emissions. In this study, forty (40) pastes were formulated by applying a 4-factor mixture plan, consisting of cement, glass powder (GP), superplasticizer and water. Third order models "special cubic" established for the flow time, spreading diameter, and flow velocity, responses were statistically significant. The analysis of the models allowed the study of the individual and combined effects of the different factors, highlighting the predominant effect of the superplasticizer on the dispersion GP fines. The multi-criteria optimization allowed the development of two optimal pastes SCP1 and SCP2 incorporating 25 and 7% GP, respectively. SCP1 was chosen because at this GP amount, unlike at 28 days, the paste presents the best strengths at 90 days with 4.5% increase for flexural tensile strength and 15.69% increase for compressive strength while maintaining satisfactory workability.

Keywords: desirability function, self-compacting paste, mixture design, glass powder, fresh properties, recycling, environment, compressive strength

1 Introduction

Glass waste produced in urban areas causes major environmental problems with low recycling rates. The annual global production of glass is about 130 million tons. Despite efforts to recover glass, only 27 million tons have been recovered worldwide, representing 1/5 of the total glass waste produced [1]. These figures show that efforts still need to be made to recycle this non-biodegradable waste. It takes a million years to decompose. In order to reduce urban environmental problems, glass waste is recycled and valorized in the construction industry, notably cement and concrete [2].
Self-compacting concrete (SCC) is an innovative workable material that is characterized by its high capacity to set up under its own weight without vibration or compaction. SCC made of only with cement can lead to high costs and other technical problems such as higher hydration heat. Therefore, Supplementary Cementitious Materials (SCMs) are frequently used as a partial cement replacement, reducing heat of hydration, increasing compactness, and reducing

segregation while maintaining appreciable workability [3, 4]. In addition, using these cementitious materials helps save on cement quantities and reduces the carbon footprint.

In this context, since the 2000s, several researchers have worked on the valorization of glass in concrete industry and SCC in general, and in pastes in particular, notably by using it either as a supplementary cementitious material or as an addition [5 - 7]. More extensive research is needed to overcome the barrier of the specific percentage of GP contribution in fresh and hardened properties [8].

The research focused on the study of the effect of Glass Powder (GP) on the various performances of concrete, mortar or paste. Up to 30% cement, replacement by GP shows no major effect on mechanical performance. In fact, 30% GP could be incorporated into the concrete without any harmful long-term effect. Examination of the mortar samples at 270 days showed a dense microstructure thanks to the pozzolanic reaction of the fine glass particles. Despite the lower initial strengths, the concrete samples continued to develop strength over time and approached the strength of the control mix [9, 10]. Regarding rheological behavior, different opinions are put forward. Hence, the increase in workability as a function of the percentage of GP has been investigated, in particular, for SCC. An increase was observed up to 20% substitution, then the trend reversed and a drop in fresh state performance was recorded. This trend was attributed to the low water absorption and smooth surface of GP [11, 12]. In addition, other research has shown the opposite effect with a loss of fluidity. This loss, which was accentuated by the in the percentage of GP substitution, was attributed to the low density of GP which is less important than that of cement. An equal mass substitution of cement by GP increases the friction between solid particles in the paste by increasing the solid/water volume ratio [13, 14].

The complexity of incorporating crushed glass in concrete technology requires further research to confirm the effectiveness and conditions of use of this material as an alternative cementitious material [15]. Clear answers are needed in the near future to clear up the existing ambiguities caused by unclear trends in the effect of GP on the fluidity especially of cementitious mixes. With regard to future research trends in this area of glass waste recovery, they are moving towards high substitution dosages with possible recourse to activators in order to achieve the expected performance with low quantities of cement. Efforts are still being made to protect the environment and manufacture low-carbon materials.

The present study is a part of this area of research where the aim is to investigate the effect of recycled GP from bottles on the workability of self-compacting pastes (SCP). The main objective is to study the influence of PV on cement paste fluidity, focusing on the individual effects and possible interaction of the various inputs. To carry out this study, the mixing experiments plans, thanks to a reduced number of experiments, allow the construction of mathematical models explaining the variation of the responses according to the materials proportions in the mix. The adopted plan was built by considering the various components of the paste as factors: cement, glass powder, superplasticizer, and water. The third-order "special cubic" models established for the responses flow time, *T*(s); spreading diameter, *D*(cm) and fluidity velocity *D*/*T* (cm/s), are established and analyzed.

The determination of the optimal mix proportions with complex responses requires the simultaneous consideration of several responses. It is therefore a case of a problem based on multi-criteria decision making [16-18]. Satisfactory solutions can be obtained by applying the desirability function [19, 16].

The combined application of a mixture design and the desirability function results in a more powerful approach to design an optimal GP-based self-placing paste.

2 Materials and Methods

2.1 Materials Used

Self-compacting pastes are prepared using 42.5 N Portland cement (Type II), a superplasticizer (SP) and a glass powder (GP) whose physical characteristics are summarized in Table 1. The GP is obtained from recycled bottles, crushed for 15 hours, and then sieved.

Table 1: Physical characteristics of the materials used

Portland cement CEM II	**Superplasticizer**	**Glass powder**
Standard : NF EN 197-1 [16]	Type : polycarboxylate	Bulk density : 2500 kg/m^3
Bulk density : 3060 kg/m^3	Aspect : Liquid	Fineness (BSS) : 2800 cm^2/g
Fineness (BSS) : 3700 cm^2/g	Color : Brown	Size grading $\leq$ 63µm
Setting time : 60 mn	PH : 9.5-10.5	
Compressive strength: 50 MPa	Density : 1.19 ± 0.01	

Glass powder (GP) which is rich in silica as shown in (Table 2), constitutes a main element in the improvement of the pozzolanic reaction.

Table 2: Chemical characteristics of cement and glass powder (GP)

Constituents	**SiO_2**	**Al_2O_3**	**Fe_2O_3**	**CaO**	**MgO**	**SO_3**	**K_2O**	**Na_2O**	**CrO_3**
Cement	21.31	3.00	3.29	65.39	3.74	0.66	0.72	0.18	-
GP	71.12	1.71	0.24	10.02	3.01	0.25	0.19	13.1	0.23

2.2 Mixing Procedure

The preparation of self-compacting pastes consists of mixing first the liquids, water, and SP at low speed for 1 min. Then, the paste is elaborated by adding solid suspensions from cement and GP which were beforehand dry homogenized. The solid fraction is introduced gradually for 2 mn mixing at low speed then for 1 mn at high-speed meeting the recommendations of Maher [21].

2.3 Mixture Design

Preliminary tests were carried out to delimit the study domain for obtaining workable pastes, neither too firm nor too liquid and not showing obvious signs of segregation [21]. The defined study domain is a 4-dimensional space, and the levels of variation of the studied factors (constituents) and the position of the candidate points for the determination of the experiment matrix are reported in Table 3.

Table 3: Levels of the studied factors, position, and number of points in the experiment matrix

Mixture design factors			**Mixture design points**	
	Min	**Max**	**Position**	**Number**
C : Cement	0.43	0.550	Center	5
GP : Glass powder	0.00	0.130	Edge	8
SP : Superplasticizer	0.00	0.026	Interior	8
W : Water	0.38	0.500	Plane	14
			Vertex	5
			Total (matrix)	40

The generated mixture plan consists of 40 points (mixtures or experiments). The results from the application of this plan will be used to fit the third order models for each measured response.

2.4 Measured Responses

A self-compacting paste must be stable, homogeneous, and fluid. To characterize the rheological activity of the self-compacting paste, four responses are measured: flow time *T*(s), paste spreading diameter *D*(cm), paste segregation Seg and flow velocity *D/T* (cm/s).

2.4.1 Flow Time *T* (s)

The flow time in seconds, *T* (s), is evaluated by the standardized Marsh cone test according to the (NF P18 507) standard [22]. Its purpose is to characterize the flow of self-compacting paste and its ability to fill a fixed volume by measuring the time required in seconds, *T* (s), to fill a one-liter container. It is a simple and practical method for obtaining a relative measure of the flowability of a paste.

2.4.2 The Paste Spreading *D* (cm)

The paste spreading diameter *D* (cm), is measured by the mini-slump cone which is first filled and then lifted allowing the cement paste mass to spread. Once stable, the average diameter of the cake is recorded. The mini-cone test or spreading test is inspired from the Abrams cone test but with its appropriate dimensions as shown in Figure 1 [23]. This test consists of filling the mini-cone placed on a horizontal surface and measuring the diameter of the obtained spread paste in both directions. After raising the cone and waiting for 1 minute, the diameter value will be the average of the two recorded measurements. Thus, it gives an indication on the workability of the elaborated flowing paste.

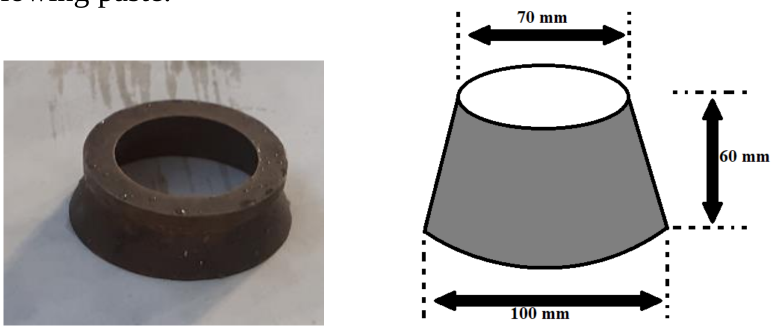

Figure 1: Mini cone for spreading test

2.4.3 Segregation of the Pastes

The segregation of the pastes has been also assessed by considering the visual aspect and the bleeding water on the surface after a settling time of 2 hours. Pastes with a risen water level not exceeding 2 mm are considered stable without segregation and designated by the value 0. However, when an excessive bleeding water level occurs and exceeds a height of 2 mm, the pastes are considered unstable and result in segregation. In this case the value of 1 is assigned to the Seg response.

2.4.4 The Flow Velocity *D/T* (cm/s)

This last parameter is the ratio between the first two responses (*D/T*) in order to characterize the rheology in terms of the flow velocity of the self-locking paste (cm/s).

2.5 Statistical Modeling

In the case of mixture, the constituents (factors) are dependent on each other. Classical experimental design methods such as factorial design are based on the independence of the factors. For this reason, they are not applicable for the development of cement paste formulation model performed at constant volume where the sum of the proportions of all constituents is equal to 1 or 100%. Thus, the mixture design is chosen. The measured responses depend on the proportions of the components [24, 25]. The mixture is composed of q components where x_i represents the proportion of the i^{th} component. The following equation can be written as follows:

$$0 \leq x_i \leq 1 \quad , i = 1, 2, \ldots q \tag{1}$$

$$\sum_{i=1}^{q} x_i = 1 \tag{2}$$

In the case of stresses on the variables, Equation (1) becomes:

$$0 \leq L_i \leq x_i \leq Ui \leq 1 \quad , \quad i = 1, 2, \ldots q \tag{3}$$

where, Li and Ui are the lower and upper stresses of the i^{th} component respectively. The applied stresses reduce the experimental domain to an irregular dimensional space $(q - 1)$ called irregular hyper-polyhedron.

The third order polynomial model "special cubic" is chosen for this study (Equation 4).

$$Y = \sum_{i=1}^{q} \beta_i x_i + \sum_{i<j} \sum \beta_{ij} x_i x_j + \sum_{i<j} \sum_{j<k} \sum \beta_{ijk} x_i x_i \, x_k \tag{4}$$

where β_i, β_{ij} ,β_{ijk} are the coefficients of the regression equation calculated by the least squares method (Goupy and Creighton 2006). x_i, x_j and x_k are the proportions of the i^{th}, j^{th} and k^{th} component of the mixture respectively.

2.6 Statistical Analysis and Diagnosis

In order to assess the relevance of the model to perfectly describe the studied domain, it is necessary to calculate the fit statistics, to make a diagnosis and an ANOVA of the model.
The fit statistics that will be taken into account are the coefficient of determination R^2, the R^2adj and the R^2pred. Values of R^2 close to 1 indicate the adequacy of the model with the variability of the data collected. R^2 increases with the number of variables even if they are not statistically significant [18], so it is necessary to consider the R^2adj which decreases when the number of non-significant terms in the model increases. The R^2pred measures the amount of variation in the new data predicted by the model and should not differ from R^2 by more than 0.2. A large deviation would indicate a problem in the data or in the model. In this case, several possibilities can be taken into account in the diagnosis of the regression: - verification by graphical methods of the Normal Plot of Residuals, - the possibility of the Box-Cox Plot for Power Transforms, - the search for outliers, - the choice of another model or its modification by deleting statistically non-significant terms.
The statistical significance of the model, the factors and their interactions is determined by analysis of variance (ANOVA, Fisher F-value test).
If the fit statistics, ANOVA and diagnosis are satisfactory, the resulting model can be used in the study and the optimization. These statistical analyses were carried out using the Design Expert 13 software demonstration version to draw the different diagrams and proceed with the optimization.

2.7 Multiresponse Optimization by Desirability Function

Desirability is based on the transformation of all obtained responses *Yi* into a desirability function *di(Yi)* from different scales into a scale-free value ranging from 0 to 1 [16, 19]. The value 0 is assigned when the factors give an undesirable response and the value 1 to the optimal performance for the factors under consideration. Two types of transformations are considered according to the objectives: the unilateral transformation in the case of maximization or minimization of *Yi*, and the bilateral transformation to reach a target value t_i for *Yi* (Equation 5).

$$d_i(Y_i) = \begin{cases} 0, \ \ Y_i < l_i \\ \left(\frac{Y_i - l_i}{t_i - l_i}\right)^s, l_i \le Y_i \le t_i \\ \left(\frac{Y_i - u_i}{t_i - u_i}\right)^t, t_i \le Y_i \le u_i \\ 0, \ \ Y_i > u_i \end{cases} \tag{5}$$

where, l_i and u_i are respectively the lower and upper bounds of the studied response ($l_i < t_i < u_i$). The *s* and *t* correspond to the weighting of the factor depending on the user according to the sought degree of desirability for a given response between l_i and u_i. The overall desirability function (D) is the geometric mean of the individual desirability values of each response $d_i(Y_i)$ calculated by Equation 6:

$$D = \left(\prod_{i=1}^{n} d_i(Y_i)\right)^{\frac{1}{n}} \quad (6)$$

In order to achieve the desired workability, the *T*(s) response is minimized, and the spread *D*(cm) and *D/T* (cm/s) responses are maximized to obtain pastes with good workability and zero segregation (Seg).

2.8 Validation of Model

The comparison between the predicted and measured values by the *t-test* has been conducted in order to judge the validity of the multi-response optimization. The t-test compares the experimental mean m with the calculated theoretical mean μ according to Equation 7 [26].

$$|t| = \frac{m-\mu}{s/\sqrt{n}} \quad \text{n} \quad (7)$$

where, m is the observed mean, μ the theoretical mean, s is the estimated standard deviation of the sample and n the number of repetitions. If $|t| < 4.303$ at 5% risk, the difference is not significant then the model is validated. If $|t| > 4.303$, the difference is significant, so the model is non-validated.

2.9 Mechanical Strength of Optimal Pastes

Compressive and flexural strengths have been assessed only for the optimal pastes, in order to decide on the final formula to be used which should meet all the workability and strength criteria.
The strength measurements were carried out on 40 × 40 × 160 mm prismatic specimens meeting the (EN 1015-11) standard [27]. The tests were conducted at 28 days and 90 days of curing. Three specimens were prepared for each mix to monitor the variability of the different cement paste design. Each test result reported represented the average strength of three test samples.

3 Results and Discussion

3.1 Mixture Design Results and Responses Modeling

The results of application of the mixture design are summarized in Table 4.
For each response, a special cubic model was fitted to the mixture design results (Table 4). The coefficients of the fitted models for the four responses are summarized in Table 5.
Prior to the exploitation of these models, a diagnosis of the regression should be made to check the normal distribution assumptions of the residues and to detect possible "outliers". After ANOVA, the modification of the models by deleting insignificant terms is also considered in order to improve the relevance of the models. The deletion of these terms should lead to an improvement in the values of *R^2*, *Adjusted R^2*, *Predicted R^2* and *Adeq Precision*.

Table 4: Mixture design results

Run	**Factors**					**Responses**			
	C	**GP**	**SP**	**W**	**%GP**	***T*(s)**	***D*(cm)**	***Se***	***D*/*T***
1	0.467	0.036	0.02	0.476	6	9.45	42.38	1	4.48
2	0.430	0.103	0.00	0.460	16	39.5	32.88	0	0.83
3	0.550	0.044	0.02	0.380	6	242.	35.13	0	0.15
4	0.487	0.062	0.01	0.437	9	27.8	39.00	0	1.40
5	0.462	0.101	0.02	0.415	15	31.6	42.38	0	1.34
6	0.453	0.073	0.00	0.467	12	20.6	31.13	0	1.51
7	0.461	0.099	0.00	0.440	15	100	10.00	0	0.01
8	0.549	0.071	0.00	0.380	10	100	10.00	0	0.01
9	0.430	0.083	0.02	0.461	14	10.3	41.00	1	3.97
10	0.467	0.036	0.02	0.476	6	8.46	44.25	1	5.23
11	0.430	0.130	0.01	0.422	20	30.0	41.50	0	1.38
12	0.453	0.073	0.00	0.467	12	19.6	31.75	0	1.62
13	0.487	0.062	0.01	0.437	9	22.6	39.50	0	1.75
14	0.492	0.120	0.00	0.380	17	100	14.00	0	0.01
15	0.487	0.062	0.01	0.437	9	23.0	39.50	0	1.72
16	0.501	0.068	0.02	0.405	10	34.8	45.00	1	1.29
17	0.519	0.000	0.01	0.462	0	15.3	42.00	1	2.74
18	0.487	0.062	0.01	0.437	9	23.9	38.50	0	1.61
19	0.430	0.070	0.00	0.500	12	100	10.00	0	0.01
20	0.487	0.062	0.01	0.437	9	24.1	40.00	0	1.66
21	0.550	0.030	0.01	0.408	4	67.0	31.50	0	0.47
22	0.456	0.077	0.02	0.441	12	17.7	40.50	1	2.28
23	0.550	0.000	0.02	0.424	0	27.3	40.00	1	1.46
24	0.519	0.000	0.01	0.462	0	13.3	46.00	1	3.46
25	0.550	0.000	0.00	0.450	0	100	10.00	0	0.01
26	0.527	0.050	0.00	0.419	7	100	13.50	0	0.01
27	0.511	0.040	0.02	0.423	6	25.3	40.75	1	1.61
28	0.517	0.083	0.02	0.380	12	50.5	37.50	1	0.74
29	0.464	0.102	0.01	0.414	15	32.5	40.50	1	1.24
30	0.464	0.130	0.02	0.380	19	48.4	39.00	0	0.81
31	0.454	0.130	0.00	0.416	19	100	10.00	0	0.01
32	0.491	0.032	0.00	0.477	5	100	10.00	0	0.01
33	0.492	0.120	0.00	0.380	17	100	12.00	0	0.01
34	0.460	0.039	0.00	0.500	6	9.38	32.50	0	3.46
35	0.470	0.004	0.02	0.500	1	4.82	43.00	1	8.92
36	0.527	0.050	0.00	0.419	7	100	13.00	0	0.01
37	0.499	0.088	0.00	0.413	13	100	10.00	0	0.01
38	0.446	0.028	0.02	0.500	5	4.88	44.50	1	9.12
39	0.430	0.054	0.01	0.500	9	5.72	45.50	1	7.95
40	0.493	0.000	0.00	0.500	0	8.20	34.50	0	4.21

Table 5: Estimated coefficients of fitted models

Full model terms	**Responses**			
	***T*(s)**	***D*(cm)**	**Seg**	***D*/*T*(cm/s)**
Cement	499.93	20.41	-0.29	2.34
GP	1159.72	6.89	0.21	3.21
SP	59516.04	-1468.75	63.66	-96.26
Water	-524.24	45.44	0.31	11.15
Cement – GP	2455.52	-56.13	1.10	-12.86
Cement – SP	-73340.42	1879.87	-74.20	114.49
Cement - Water	3718.79	-85.83	0.18	-25.08
GP – SP	-78639.86	2016.45	-80.11	105.30
GP – Water	1561.91	-43.69	-0.82	-30.69
SP – Water	-64337.30	1723.24	-73.27	186.14
Cement - GP - SP	-2644.89	160.16	19.97	6.03
Cement - GP - Water	-8650.25	202.41	-8.94	52.86
Cement - SP - Water	-24877.91	727.66	53.75	-82.41
GP - SP - Water	-9172.96	325.12	54.26	-9.29

3.2 Regression Diagnostic and Model Modification

Two graphic diagnoses are considered: the "Normal Plot of Residuals" (Figure 2) and the "Residuals vs. Runs" (Figure 3) to detect possible “outliers” values.

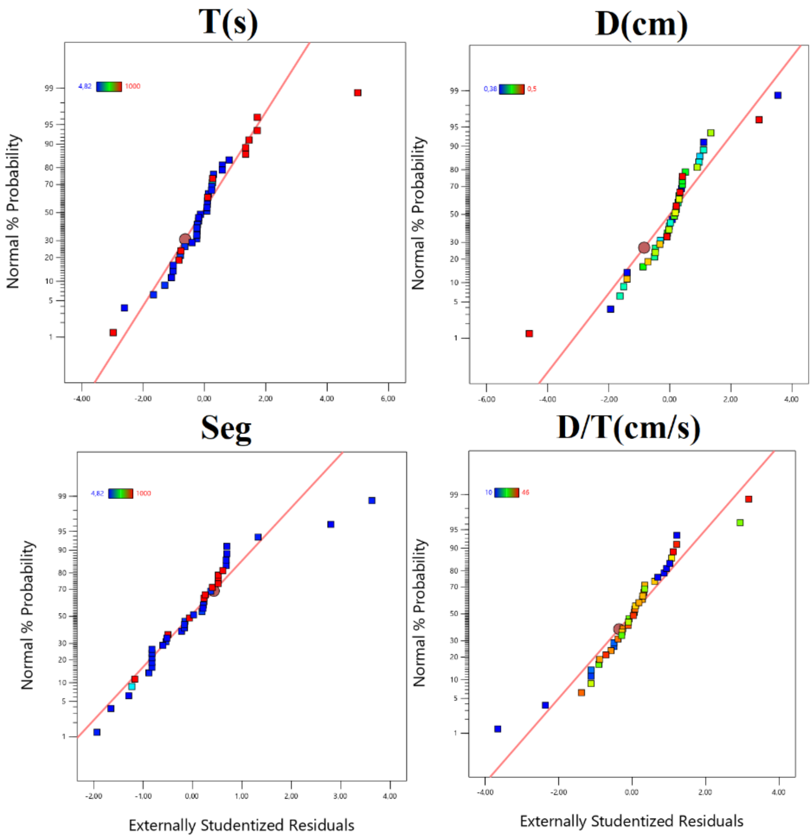

Figure 2: Normal Plot of Residuals. *T*(s): flow time. *D*(cm): spread of paste. Seg: segregation of the pastes. *D*/*T*(cm/s): Flow speed.

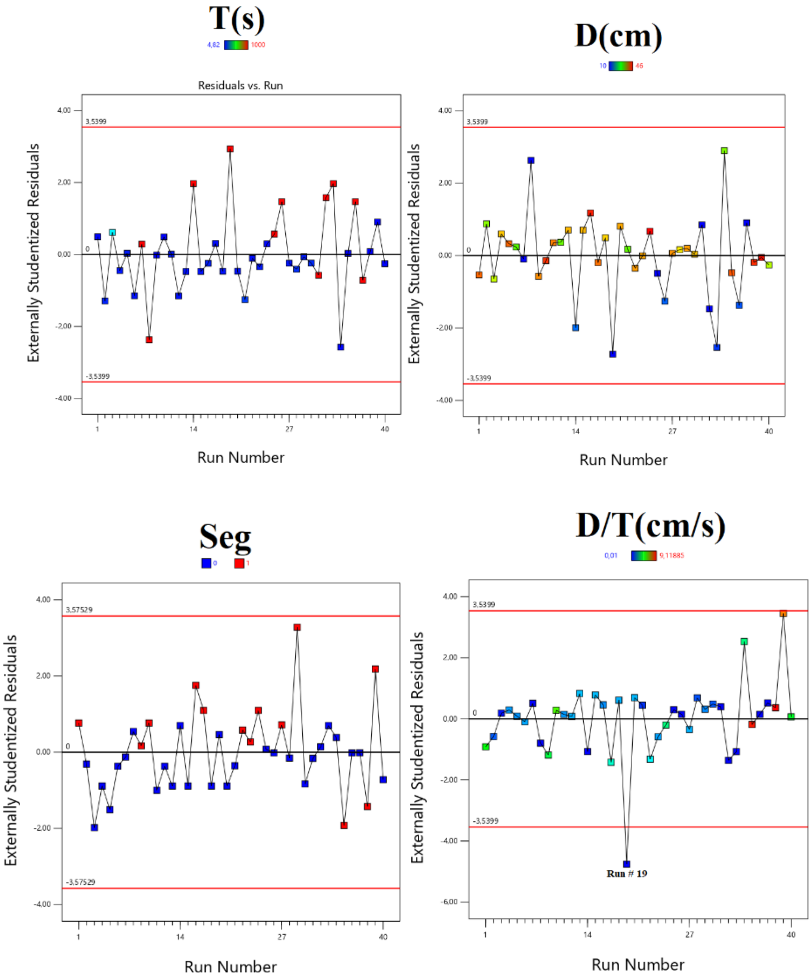

Figure 3: Residuals vs. Run. T(s): flow time. D(cm): spread of paste. Seg: segregation of the pastes. D/T(cm/s): Flow speed.

According to Figure 2, it can be seen that the normal distribution is acceptable. Figure 3 shows good residuals values as a function of the experiments except for the result of experiment 19 concerning the *D/T* (cm/s) response. This obtained value could be explained by the absence of SP in the paste making it less fluid, thus hindering the measurement of T and amplifying the error of the *D/T* (cm/s) response. In addition, this paste contains a high proportion of GP compared to similar pastes (e.g., Run 34) with the highest Water/Cement+GP ratio (equal to 1) for this category of pastes where SP = 0.

ANOVA was used to determine the statistical significance of the terms in the fitted models. Non-significant terms are removed from the model, which is noted as the "modified model". Table 6 presents the estimated coefficients of the significant terms for each response. It should be noticed that the segregation model (Seg) is not significant.

Table 6: Estimated Coefficients, ANOVA of models *T*(s), *D*(cm), Seg and *D/T* (cm/s) and factors percentages contribution (only significant models and factors are presented)

Models	**Factors**	**Estimated Coefficient**	**ANOVA**						**% of contribution**
				SS	***Df***	**MS**	***F* value**	**Probability *p***	
T(s)	C- SP	-82311.37		9.870E+05	1	9.870E+05	19.34	0.0001***	13.34
	GP- SP	-82399.34		1.007E+06	1	1.007E+06	19.73	< 0.0001***	13.10
	SP-W	-73655.18		8.119E+05	1	8.119E+05	15.91	0.0003***	10.76
			Res.	1.684E+06	33	51039.02			
			Tot. (co.)	7.541E+06	39				
D(cm)	C-SP	2207.85		710.16	1	710.16	29.44	< 0.0001***	10.59
	GP- SP	2223.26		733.13	1	733.13	30.39	< 0.0001***	10.25
	SP- W	2071.37		642.14	1	642.14	26.62	< 0.0001***	9.27
			Res.	796.03	33	24.12			
			Tot. (co.)	6920.22	39				
D/T(cm/s)	C- W	-14.82		9.34	1	9.34	22.15	< 0.0001***	4.22
	GP- W	-17.89		14.47	1	14.47	34.29	< 0.0001***	6.53
	SP- W	66.42		18.98	1	18.98	45.00	< 0.0001***	8.57
			Res.	13.92	33	0.4219			
			Tot. (co.)	221.42	39				

T(s): flow time, *D*(cm): spread diameter, Seg: segregation, *D*/*T*(cm/s): flow speed, *SS:* Sums of squares, *Df*: degrees of freedom, *S* : mean squares; Res: residual; Tot. (co.): total (corrected). The differences were considered significant at $p = 0.01$ to 0.05 (*), highly significant at $p = 0.001$ to 0.01(**) and very highly significant at $p \leq 0.001$ (***)

To determine the order of effectiveness of input factors, the absolute values of estimated coefficients in each tested response are examined (Table 6). The higher the absolute value of the coefficient, the more effective the factor. The order of effectiveness of input factors for each tested response, based on the absolute values of estimated coefficients, is as follows: GP-SP followed by C-SP, and finally SP-W for the response *T*(s); GP-SP followed by C-SP, and finally P-W for the response *D*(cm); SP-W followed by GP-W, and finally C-W for the response *D/T* (cm/s).

The percentages of contribution indicate the proportion of total variation in the response that can be attributed to each factor, which can be calculated using the sums of squares (SS) for each factor relative to the total sum of squares (Tot. (co.)) in each tested response. The percentages of contribution for each factor are reported in Table 6.

From Table 7, it can be seen that R^2 values are improved after modification of the models. The predicted R^2 values are in reasonable agreement with the *adjusted* R^2 since their difference is less than 0.2. The *predicted* R^2 which measures the predictive ability of the model shows a clear improvement for the modified models. The *Adeq Precision* measures the signal to noise ratio. Thus, a ratio higher than 4 is desirable. The ratio is 16.7 for T, 21.98 for *D* and 34.34 for *D/T* which indicates an adequate signal. All fit statistics improved with the modification of the models (Table 7).

Table 7: Fit Statistics for full and modified model.

Responses	**Model**	**Fit Statistics**			
		R²	***Adjusted R²***	***Predicted R²***	***Adeq Precision***
T(s)	Full	0.80	0.70	0.19	10.33
	Modified*	0.78	0.74	0.63	16.72
D(cm)	Full	0.90	0.85	0.58	14.30
	Modified*	0.89	0.86	0.81	21.98
D/T(cm/s)	Full	0.96	0.94	0.86	29.08
	Modified*	0.94	0.93	0.88	34.34

* The insignificant model terms are removed.

The modified models can therefore be used to explore experimental space which can be presented as ternary curves.

3.3 Effects of Constituents on Responses

3.3.1 Effects of Constituents on *T* (s)

Cement-SP, GP-SP and SP-Water interactions are the most significant terms on the variation of the T(s) response. The superplasticizer (SP) has therefore an important influence on the flow time of the pastes. This predominant role of SP on the flow of mixtures has already been observed [28]. Thus, the increase of SP in the mix reduces the flow time resulting in a more fluid paste, thus a gain in workability (Figure 4). These results are in agreement with other studies [29, 30].

The effects of cement and GP are almost identical (Figure 4). Indeed, fines in a mixture lead to a loss of workability due to the increase of the specific surface area of the mixture which requires more water to achieve the same workability. Cement and GP have generally the same negative effect on the rheology of mixtures and require more water or the use of a deflocculating agent such as SP to achieve the desired workability [14, 31]. Furthermore, SP and water play the same role, and both produce workable materials.

The interaction of SP with cement and GP highlights the importance of its role in fines deflocculating, promoting their movement in the mixture, thus allowing the expected rheological performance to be achieved. Studies from the literature have underlined the important effect of GP, specifically, on the fluidity of mixes. This effect, which may be either favourable or the opposite, is closely related to the type of SP used. Indeed, it has been reported that the fluidity decreases with increasing GP content in the presence of polycarboxylate type

SP similar to the one used in the present case. The opposite occurs in the case of the use of PNS type SP [31]. In addition to providing possible explanations for the existing opinion differences, these results confirm the strong interaction between GP and SP.

It has been noticed that SP has little influence on *T*(s) when the interaction of SP with water is beyond 0.02 (Figure 5). Indeed, superplasticizer is generally characterized by an optimum content called saturation dosage, beyond which their increase has no influence on the fluidity of the mixtures [32, 31].

The positive effect of water is not very pronounced, as shown in Figure 5, due to the restricted range in which this component varies.

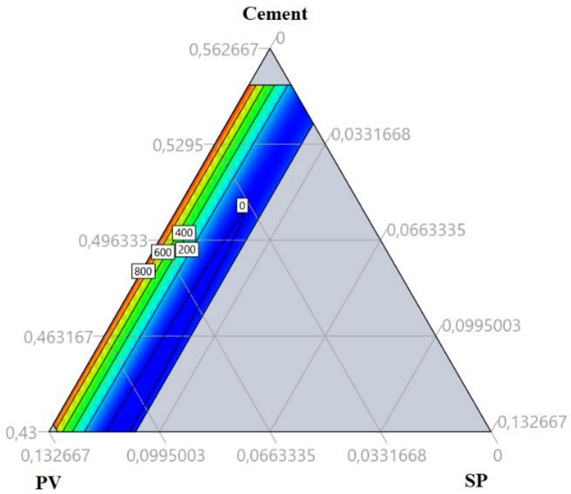

Figure 4: Ternary response diagram
T(s) at Water = 0.473

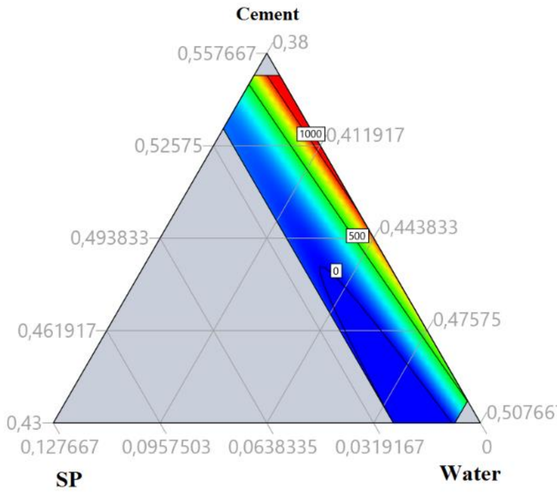

Figure 5: Ternary response diagram
T(s) at GP = 0.062

3.3.2 Effect of Constituents on *D*(cm)

The significant interactions effects on the variation of the *D*(cm) response are: Cement-SP, GP-SP and GP-Water where SP remains the most influential constituent (Table 6). According to Figure 6, increasing the percentage of SP in the mix leads to an increase in *D*(cm). The same is true for the proportion of water in the mix (Figure 7). Cement and GP have the same influence on the paste spread, but it is less important than the influence of SP. Unlike the latter, which has a positive effect on workability, cement and GP produce a negative effect. Increasing their dosage leads to a drop in workability [33]. Overall, the spreading results are in agreement with the results of *T* where SP positively influences the flowability [31].

The addition of GP to the mix causes the spread diameter to be reduced and thus decreases the workability. This loss of workability has been attributed to the increase in fines in the mix which increases the cohesion of the mix and hinders their flow [33].

Solimane and Tagnit-Hamou [34] also noted the loss of fluidity with the incorporation of GP. They attributed this loss to the lower density of GP (2500 kg/m^3) than that of cement (3060 kg/m^3). With the partial replacement of cement by GP, the volume ratio of solid particles to water becomes larger with an increasing substitution rate. Thus, the friction between the solid particles in the paste increases.

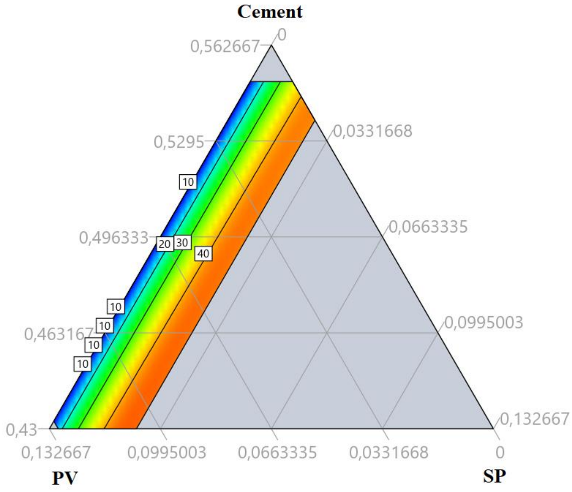

Figure 6: Ternary response diagram
D(cm) at water = 0.473

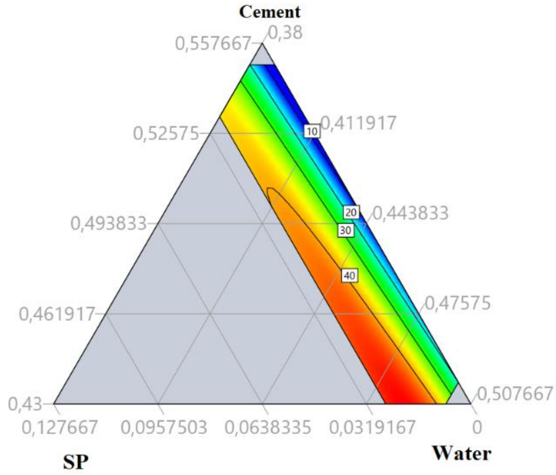

Figure 7: Ternary response diagram
D(cm) at GP = 0.062

3.3.3 Effects of Constituents on *D/T*(cm/s)

The interest of this response lies in the fact that it combines *T*(s) and *D*(cm) into a single response that reflects the flow velocity. The latter is high for the more workable pastes.
The influential terms differ from those observed for *T* and *D*. Cement-Water, GP-Water and SP-Water interactions are the most significant terms highlighting the importance of water on the paste flow velocity (Table 6). Figure 8 shows clearly that *D/T* increases with increasing water content in the paste.

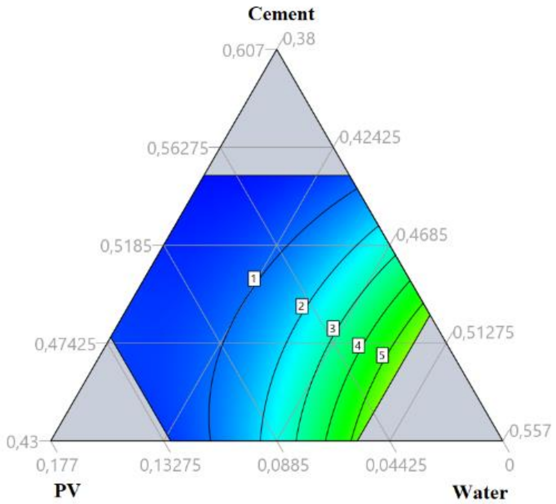

Figure 8: Ternary response diagram
D/T(cm/s) at SP = 0.013

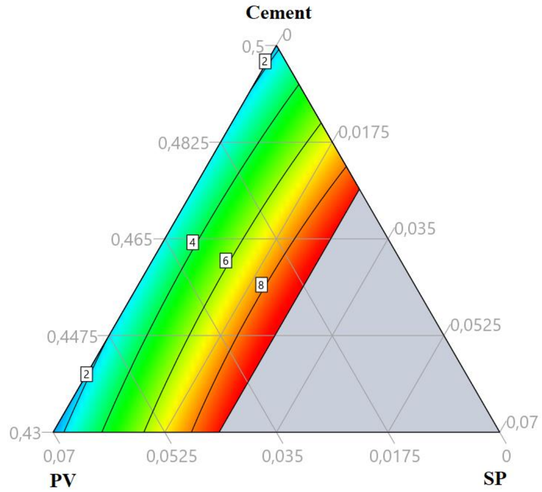

Figure 9: Ternary response diagram
D/T (cm/s) at water = 0.5

The variation of the *D/T*(cm/s) response also depends on the proportion of SP in the paste. Indeed, when it increases the *D/T* response increases too (Figure 9).

The ratio of the *D*(cm) to *T*(s) response is relevant as a response because it shows the importance of the proportion of water on the workability of the paste which has not been shown by analyzing independently each response. It should also be noted that the *D/T*(cm/s) ratio model has better fit statistics (R^2, R^2_{adj}, R^2_{pre}, *Adeq Precision*) compared to the *T*(s) and *D*(cm) models (Table 6). This new variable, not yet considered in current research, is a promising one and could constitute a reference parameter for self-placing pastes and even fluid concretes, such as the water/cement ratio for cementitious mixes in general. Further studies to examine this parameter are recommended.

3.4 Optimization and Model Validation

Multi-objective optimization results in several optimal solutions of different desirability. Solutions with high desirability indicate that the objective can be easily achieved. For this purpose, two optimal solutions with a desirability value of 0.84 are selected for validation. The optimal compositions and predicted responses of the SCP1 and SCP2 mixtures are summarized in Table 8.

Table 8: Optimal composition of the two pastes minimizing *T*, maximizing *D* and *D/T* for Desirability = 0.845

	C	**GP**	**SP**	**W**
SCP1	0.430	0.130	0.018	0.422
SCP2	0.452	0.039	0.008	0.500

The predictive accuracy of the model has been examined by conducting additional experiments under optimal conditions and comparing the predicted values to the measured values obtained with the SCP1 and SCP2 pastes. For each point, the experiment was repeated 3 times.
The measured and predicted results are grouped in Table 9. The t-test shows that the measured results are not statistically different from the predicted values. The predicted optimal solutions are therefore validated.

Table 9: Multi-response optimization validation responses

	Responses	**Predicted Response** μ	**Experimental Mean** *m*	$\lvert t \rvert$*	**signification**
SCP1	*T* (s)	39.88	36.32 ± 3.53	1.75	N.S
	D (cm)	40.08	38.92 ± 1.04	1.94	N.S
	D/*T* (cm/s)	1.01	1.08 ± 0.13	1.67	N.S
SCP2	*T* (s)	7.69	7.71 ± 0.41	0.07	N.S
	D (cm)	37.81	39.56 ± 2.08	1.46	N.S
	D/*T* (cm/s)	4.87	5.14 ± 0.47	1.73	N.S

3.5 Mechanical Strength of Optimal Pastes

The comparison of the mechanical strength results of the two optimal pastes as reported in Table 10, allows to note that the performances obtained at 28 days for SCP1, containing 25 % of partial substitution of cement by GP, are lower than those obtained for SCP2 which contains only 7 % GP for cement substitution. Indeed, the flexural tensile strength of SCP1 is -5.4% lower than that of SCP2. As for the compressive strength, it goes from 37.60 MPa for SCP2 to 32.50 MPa for SCP1, i.e. a reduction of -13.56 %. This drop in mechanical performance is explained by the reduction in the quantity of cement which is replaced by GP. Therefore, SCP1, with a higher substitution rate, develops lower strengths at 28 days.

Table 10. Mechanical strength of optimal pastes

	Flexion (MPa)		**Compression (MPa)**	
	28 days	**90 days**	**28 days**	**90 days**
SCP1 (25%GP)	3.30	4.60	32.50	43.87
SCP2 (7 % GP)	3.49	4.40	37.60	37.92
Difference %	-5.40	+4.50	-13.56	+15.69

On the other hand, a reversal of this trend is observed at 90 days where the strength values are higher for SCP1. Indeed, the flexural tensile strength increases from 4.40 MPa for SCP2 to 4.60 MPa for SCP1 with a gain of +4.5%. As for the compressive strength, it increases from 37.92 MPa for SCP2 to 43.87 MPa for SCP1, which represents an increase of +15.69%. Overall, at 90 days, the strengths are higher in the case of the highest GP substitution rate, especially for SCP1 which contains more GP at a rate of 25% of cement replacement.

These results are very interesting and allow to retain the single optimal formula SCP1. Also, they show the long-term effectiveness of GP, because although the performances were reduced at 28 days because of the reduction of the quantity of cement compared to the elevated GP content, then the tendency was completely reversed at 90 days with significant gains in strength. This increase in mechanical performance is justified by the pozzolanic effect of GP due to the reaction of its silica with the lime released from the hydration of cement [35]. This reaction is similar to that of cement to form hydrated calcium silicates, C-S-H; but is slower and only occurs in the long term [36]. Several studies have obtained similar results where the focus has been on the GP pozzolanic activity which improves cement hydration. Its addition to cementitious mixtures by partial substitution of cement has been successfully used by achieving long-term strength gains compared to 28-day strengths [37, 36].

4 Conclusion

A mixture design was applied to investigate the workability of GP-based pastes as a function of the proportions of cement, GP, SP and water.

The models for the variation of *T*(s) and *D*(cm) are statistically significant and highlight the importance of the SP-GP interaction where the SP would act on the fines deflocculating of the GP to achieve the expected rheological performance.

The *D/T* (cm/s) ratio is a new approach to analyze the results of *T*(s) and *D*(cm) by combining the two. The model reflecting the variation of this response has the best fit statistics. The *D/T*(cm/s) response allowed to highlight the effect of water contrary to the analysis carried out on each response separately despite its important role in the rheology of mixtures. This response requires further work to make it a reference in the study of self-compacting mixtures as is the water/cement ratio for the mechanical performance of concretes, pastes, and mortars.

The proportions for two optimal pastes have been predicted: SCP1 and SCP2 containing 7 and 25% GP respectively. The validation of the optimal solutions by experiments shows the predictive accuracy of the models fitted for flow time *T*(s), spreading diameter *D*(cm) and flow velocity *D/T*(cm/s).

Evaluation of the flexural tensile and compressive strengths of the optimal pastes showed the positive effect of GP on long-term mechanical performance. SCP1 with 25% GP has higher strengths at 90 days than SCP2 with 7% cement replacement by GP. In addition, it offers an economic gain because the quantity of cement in the mix is reduced, thus leading to an ecological gain by reducing the emission of CO_2 gas due to the manufacture of cement. The pozzolanic character of GP has allowed the long-term mechanical performance to be achieved and even exceeded. By comparing the strengths of SCP2 with a lower substitution GP content and therefore with more cement, it has been noticed that the loss of mechanical performance due to the high substitution rate is largely recovered with time.

The present work allowed the determination of the optimal GP dosage of 25% as partial substitution of cement, leading thus to a self-compacting paste with the best mechanical performance.

References

[1] Statista, Key figures on glass recycling worldwide, (2018). Google Scholar https://www.statista.com/statistics/1055604/key-figures-glass-recycling-globally/.

[2] Jiang, Y., Ling, T.-C., Mo K.H., Shi C. (2019). A critical review of waste glass powder – Multiple roles of utilization in cement-based materials and construction products. *Journal of Environmental Management*, *242*, pp. 440-449.

[3] Nepomuceno, M.C.S., Pereira-De-Oliveira, L.A., Lopes, S.M.R. (2014). Methodology for the mix design of self-compacting concrete using different mineral additions in binary blends of powders. *Construction and Building Materials*, *64*, pp. 82-94.

[4] Yang, S., Zhang, J., An, X., Qi, B., Shen, D., Lv, M. (2021) Effects of fly ash and limestone powder on the paste rheological thresholds of self-compacting concrete, *Construction and Building Materials*, Volume *281*, 122560, ISSN 0950-0618, https://doi.org/10.1016/j.conbuildmat.2021.122560.

[5] Khudair, Y. A., Mohammed, M. K., & Hama, S. M. (2020). Optimization of glass powder content in self-compacting concrete as partial replacement of cement. *IOP Conference Series: Materials Science and Engineering*. 022140. doi:10.1088/1757-899X/928/2/022140

[6] Wang, Y.,Li, J., He, X., Zheng, Z., Su, Y., Zhao, H., Yang, J., Strnadel, B. (2020). Effects of wet-grinded superfine waste glass on the fresh properties and reaction characteristic of cement pastes, *Construction and Building Materials*, Volume *247*, 118593, https://doi.org/10.1016/j.conbuildmat.2020.118593.

[7] Paul, S.CH., Šavija, B., Babafemi, A.J. (2018). A comprehensive review on mechanical and durability properties of cement-based materials containing waste recycled glass, *Journal of Cleaner Production*, Volume *198*, Pages 891-906, https://doi.org/10.1016/j.jclepro.2018.07.095.

[8] Ahmed, K.S. & Rana, L.R. (2023). Fresh and hardened properties of concrete containing recycled waste glass: A review. *Journal of Building Engineering*, Volume *70*, 106327, ISSN 2352-7102, https://doi.org/10.1016/j.jobe.2023.106327.

[9] Shayan, A & Xu, A. (2004). Value-added utilisation of waste glass in concrete. *Cement and concrete Research*, vol.*34*, pp.81 - 89. https://doi.org/10.1016/S0008-8846(03)00251-5.

[10] Idir, R., Cyr, M. & Tagnit-Hamou, A. (2011). Pozzolanic Properties of Fine and Coarse Color-Mixed Glass Cullet. *Cement and Concrete Composites*, *33*, 19-29.

[11] Matos, A. M., Ramos, T., Nunes, S., & Sousa-Coutinho, J. (2016). Durability enhancement of SCC with waste glass powder. *Materials Research*, *19*, 67-74. https://doi.org/10.1590/1980-5373-MR-2015-0288.

[12] Sharifi Y., I. Afshoon, Z. Firoozjai & A.Momeni. (2016). Utilization of waste glass micro-particles in producing self-consolidation concrete mixtures. *International Journal of Concrete Structures and Materials*; vol. *10*, 337-353.

[13] Shayan A, Xu A. (2006). Performance of glass powder as a pozzolanic material in concrete: a field trial on concrete slabs. *Cem Concr Res*; *36*: 457–68. https://doi.org/10.1016/j.cemconres.2005.12.012.

[14] Lu, J. X., Duan, Z. H., & Poon, C. S. (2017). Fresh properties of cement pastes or mortars incorporating waste glass powder and cullet. *Construction and Building Materials. 131*, 793-799. https://doi.org/10.1016/j.conbuildmat.2016.11.011.

[15] Dong, W., Li, W., Tao, Z. (2021). A comprehensive review on performance of cementitious and geopolymeric concretes with recycled waste glass as powder, sand or cullet. *Resources, Conservation and Recycling*. Volume *172*, 105664, ISSN 0921-3449, https://doi.org/10.1016/j.resconrec.2021.105664.

[16] Derringer G, Suich R. (1980). Simultaneous optimization of several response variables. *J Qual Tech 12*(4):214–219. https://doi.org/10.1080/00224065.1980.11980968.

[17] Jeong, I.J, Kim, K.J. (2009). An interactive desirability function method to multiresponse optimization. *Eur J Oper Res.,195*(2):412- 426. doi: 10.1016/j.ejor.2008.02.018.

[18] Myers, R.H.; Montgomery, D.C. (2009). Response Surface Methodology: Process and Product Optimization Using Designed Experiments; John Wiley & Sons, Inc.: New York, NY, USA,.

[19] Harrington EC (1965) The desirability function. *Ind Qual Control 21*(10):494–498.

[20] EN 197-1:2011: Cement Composition, specifications and conformity criteria for common cements.

[21] Barrak, M.E. (2005). Contribution to the study of the flowability of self-compacting concrete in the fresh state. PhD thesis.

[22] NF P18-507. November 1992: Additions for concrete. Water retention. Method for measurement of fluidity by flowing with the “cone de marsh”.

[23] NF P18-358. July 1985: Admixtures for concretes, mortars and grouts - Routine grouts for prestressing ducts - Measurement of fluidity and water reduction.

[24] Eriksson, L., Johansson, E., Wikström, C. (1998). Mixture design—design generation, PLS analysis, and model usage, *Chemometrics and Intelligent Laboratory Systems*, Volume *43*, Issues 1–2, Pages 1-24.

[25] Goupy, J. (2000). Experimental designs: mixtures. DUNOD,

[26] Schwartz, D. (1992). Méthodes statistiques à l’usage des médecins et des biologistes. Collection Statistique en biologie et en médecine. Ed Flammarion Medecine-Sciences, Paris.

[27] EN 1015-11 (2019).Test methods for masonry mortar. Determination of flexural and compressive strength of hardened mortar.

[28] Ali Mardani-Aghabaglou, Hasan Tahsin Öztürk, Murat Kankal, Kambiz Ramyar. (2021). Assessment and prediction of cement paste flow behavior; Marsh-funnel flow time and mini-slump values. *Construction and Building Materials*, Volume *301*, 124072, ISSN 0950-0618, https://doi.org/10.1016/j.conbuildmat.2021.124072.

[29] Hiroshi Uchikawa, Shunsuke Hanehara, Tokuhiko Shirasaka, Daisuke Sawaki. (1992). Effect of admixture on hydration of cement, adsorptive behavior of admixture and fluidity and setting of fresh cement paste. *Cement and Concrete Research*. Volume *22*, Issue 6, Pages 1115-1129, ISSN 0008-8846, https://doi.org/10.1016/0008-8846(92)90041-S.

[30] Weisong Yin, X. Li, T. Sun, Y. Chen, F. Xu, G. Yan, M. Xu, K. Tian. (2021). Utilization of waste glass powder as partial replacement of cement for the cementitious grouts with superplasticizer and viscosity modifying agent binary mixtures: rheological and mechanical performances. *Construct. Build. Mater. 286* , p. 122953. 10.1016/j.conbuildmat.2021.122953

[31] Saber Ibrahim, Amr Meawad. (2022). Towards green concrete: Study the role of waste glass powder on cement/superplasticizer compatibility. *Journal of Building Engineering*. Volume *47*, 103751, ISSN 2352-7102, https://doi.org/10.1016/j.jobe.2021.103751.

[32] Agulló, L., Toralles-Carbonari, B., Gettu, R. et al. (1999). Fluidity of cement pastes with mineral admixtures and superplasticizer—A study based on the Marsh cone test. *Mat. Struct. 32*, 479–485. https://doi.org/10.1007/BF02481631

[33] Ali A. Aliabdo, Abd Elmoaty M. Abd Elmoaty, Ahmed Y. Aboshama (2016) Utilization of waste glass powder in the production of cement and concrete. *Construction and Building Materials*. Volume *124*, Pages 866-877, ISSN 0950-0618. https://doi.org/10.1016/j.conbuildmat.2016.08.016.

[34] Soliman, N.A., Tagnit-Hamou, A. (2016). Development of Ultra-Hight-Performance concret using powder– towards ecofriendly concrete, *Construction and Building Materials*. *125*: 600-612.

[35] Zheng, K. (2016). Pozzolanic reaction of glass powder and its role in controlling alkali–silica reaction. *Cement and Concrete Composites*. Volume *67*, Pages 30-38, ISSN 0958-9465. https://doi.org/10.1016/j.cemconcomp.2015.12.008.

[36] Lee, H., Hanif, A., Usman, M., Sim, J., Oh, H. (2018) Performance evaluation of concrete incorporating glass powder and glass sludge wastes as supplementary cementing material, *Journal of Cleaner Production*, Volume *170*, Pages 683-693, ISSN 0959-6526, https://doi.org/10.1016/j.jclepro.2017.09.133.

[37] Mahsa, K., Ghahremaninezhad, A. (2016). An investigation into the hydration and microstructure of cement pastes modified with glass powders. *Construction and Building Materials*. Volume *112*, Pages 915-924, ISSN 0950-0618, https://doi.org/10.1016/j.conbuildmat.2016.02.085.

DOI: 10.2478/sspjce-2023-0004

The Use of Seismic Isolators to Improve Building Performance

Madi Rafik[1], Bordjiba Abdelhak[2*]

[1]Université 8 Mai 1945, Guelma, Algérie-
[2]Université Badji Mokhtar, Annaba, Algérie
*e-mail: bordjibaabdelhak@gmail.com

Abstract

The use of seismic isolators is a design method that involves inserting a flexible element at the base of the structure to decouple its movement from that of the ground to reduce vulnerability to earthquakes. They also make it possible to reduce the demand for force and deformation on the various structural elements. The aim of this research is to evaluate the contribution of HDRB high damping elastomeric seismic isolators in the reduction of seismic forces. It also consists in comparing the results of the dynamic analysis of the two fixed base structures in frames or frames braced by shear walls with the isolated structure mounted on an HDRB elastomer system and subjected to the same seismic excitation using the SAP 2000 calculation software. The results obtained showed an attenuation in the accelerations, a lengthening of the period, strong reduction in displacements and a reduction in the shearing force at the base of the isolated structure compared to fixed base structures.

Keywords: building, seismic, energy dissipation, modelization, dynamic analysis

1 Introduction

The conventional approach to protecting buildings against earthquakes is to increase resistance and or ductility by reinforcing the structure or repairing damaged elements, in order to withstand significant loads by developing plastic hinges at well-determined places to dissipate energy by inelastic deformations. This approach is not entirely effective because of the amplification of the seismic solicitations transmitted to the buildings. The reduction of seismic forces is the most effective approach because it aims to partially shield the structure from the seismic action rather than reinforce it so that it can withstand high loads. To this end, the use of seismic protection and isolation systems makes it possible to decouple the structure from ground movements induced by an earthquake in order to prevent the occurrence of damage. The insulation at the base consists in putting between the foundation and the superstructure seismic isolators which absorb the seismic energy due to their nonlinear responses and they have a very important horizontal deformability to be able to dissipate the deformation transmitted to the construction and a very high vertical rigidity to support the weight of the structure. It also makes it possible to increase the fundamental period (Figure 1) and reduce the vibration frequency of the structure in order to avoid the phenomenon of resonance [1]. Many variables may have different effects on the performance of the buildings particularly the ones with irregularities such as torsion. Force-based method (FBD) and displacement-based method (DBD) have been commonly used to evaluate the performance of the structures. The DBD method may give more realistic prediction of damage levels where this method directly provides plastic hinge deformations for the target displacement. Through combining this method to the capacity design principles, nonductile formations can be avoided and more economical outcomes can be achieved [12]. With seismic insulators, a potentially high level of protection of buildings compared to conventional techniques can be achieved with in addition, the realization of savings on project costs [2]. The insulation technique is not reserved for new structures; on the contrary, one of its main advantages is that it can be applied very well to the seismic rehabilitation of existing constructions [3].

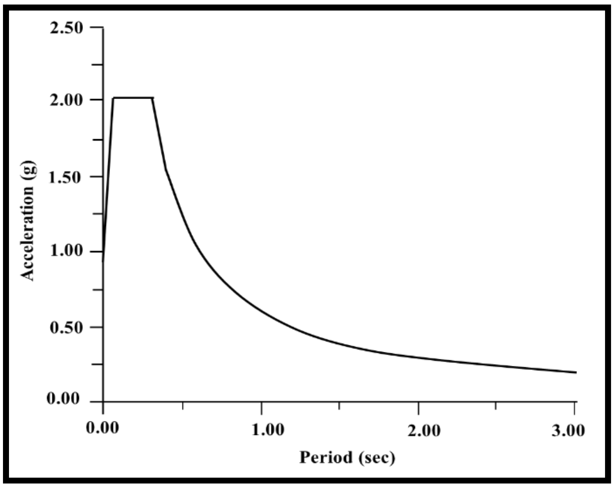

Figure 1: UBC 97 design spectrum [3]

2 Behavior of Seismic Isolators

Seismic isolation is about providing a discontinuity between the foundation and the superstructure, so that the seismic energy cannot be fully transmitted to the superstructure. It induces a significant reduction in the acceleration of the upper floors and inter-floor movements. Therefore, it ensures the protection of the structure. According to their mode of operation, seismic supports can be classified into several categories [4]:

- Deformation supports: in lead low damping rubber bearing (LDRB), lead rubber bearing (LRB) and in high damping rubber bearing (HDRB).
- Deformation and sliding supports.
- Bearing supports.

2.1 Deformation Supports

They are made of hooped elastomer: alternating layers of elastomer, natural rubber, or synthetic elastomer and of hoops in the form of metal plates.

The horizontal deformability is ensured by the elastomer layers and the vertical rigidity of the supports is ensured by the presence of the hoops. They allow horizontal flexibility and greatly reduce the relative displacement of floors.
In case of the more flexible of elastomers, a lower seismic load felt by the building. But too much flexibility of the supports considerably reduces the stability of the structure in normal times [5].
We distinguish:

- Support in lead low damping rubber bearing (LDRB): these isolators consist of two thick steel end plates and many thick steel shims. The behavior of the material in shear is completely linear up to shear stresses greater than 100%, with damping of around 2% to 3% of critical damping [6].
- Support in lead rubber bearing (LRB): the elastomer base isolator with lead bar is rather flexible in the horizontal direction, but quite rigid in the vertical direction (Figure 2). It prolongs the period of the structure and allows energy dissipation**.** The normal recommended period for optimal performance is between 1.5 and 2.5 sec [7].
- Support in high damping rubber bearing (HDRB): In this type supports, the elastomer used provides a significant amount of damping, usually from 8% to 15% of critical damping. It is vertically rigid, capable of supporting vertical gravity loads while being laterally flexible and capable of allowing large horizontal displacements (Figure 3).

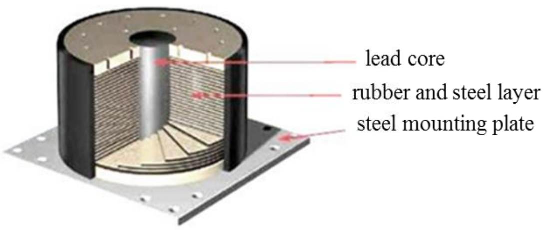

Figure 2: Lead rubber bearing isolator (LRB) [6]

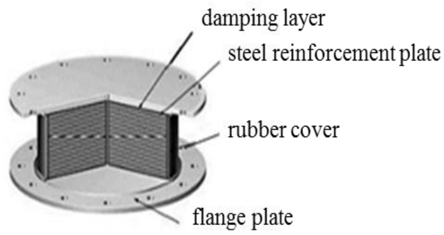

Figure 3: High damping rubber bearing isolator (HDRB) [6]

2.2 Sliding Supports

These are two separate blocks that slide relative to each other and allow the decoupling of the movements of the superstructure from those of the foundation elements by means of a sliding interface which dissipates seismic energy by friction (Figure 4). They can be used with both light and massive structures, because their period depends only on the radius of curvature. They can also support a high vertical load and provide more than 30% damping [8]. Slip-based isolator systems are frequently applied in constructions and walkways because of its advantages, listed below, compared to conventional rubber bearings:

- The non-influence of the input frequency on this system.
- The torsional effects produced by asymmetric construction are reduced due to the coincidence of the center of mass of the structure and that of the sliding supports.

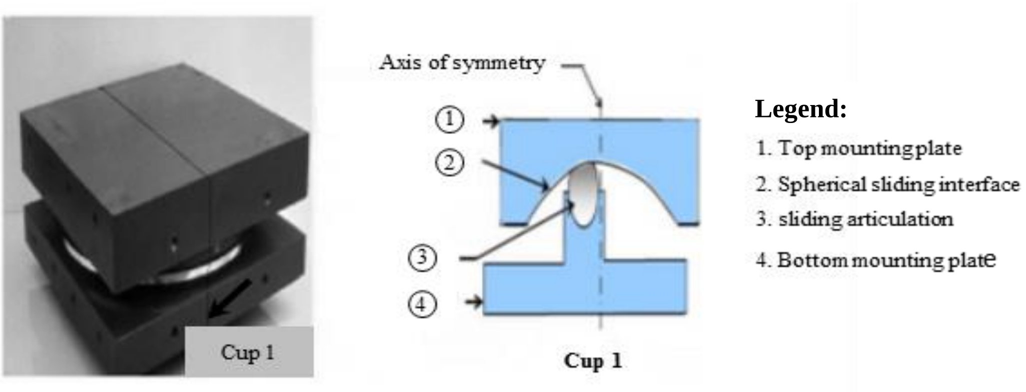

Figure 4: Sliding support [8]

2.3 Deformation and Sliding Supports

It is formed by the association of sliding plates and deformation supports. This system leads to a reduction in both acceleration and displacement of the Superstructure and thus leads to a significant decrease in shear forces at the base. This is particularly advantageous in the case of constructions on deep foundations, more sensitive to shear than superficial foundations.

2.4 Rolling Supports

To allow movement in two directions, spherical balls or two orthogonal layers of cylindrical rollers are used. The main disadvantages of this system are the seizure after a prolonged period without solicitation and their low damping (Figure 5).

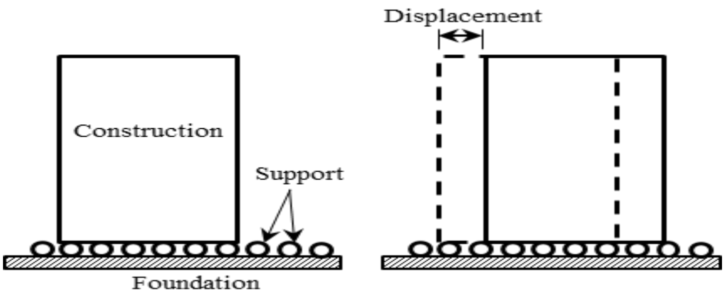

Figure 5: Rolling supports

3 Modeling of Seismic Isolator Based on Elastomer

Fretted elastomers have the ability to both increase the natural period of the structure and dissipate energy so as to limit displacement. These devices can withstand very high shear strains.

The various parameters which characterize the behavior law of the isolator are (Figure 6): elastic rigidity K_e, horizontal elastoplastic rigidity K_d, the effective stiffness at maximum displacement K_{eff}, plasticization resistance Q_d, plasticizing displacement D_y and design displacement D_u.

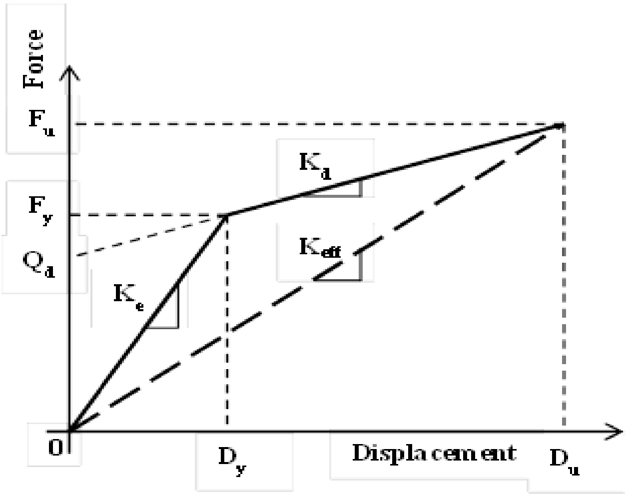

Figure 6: LRB behavior law [9]

The seismic isolators will be modeled in the SAP2000 software, using "Link Element" with hysteretic behavior of an elastomeric isolator. The bidirectional hysteritic model adopted with a bilinear behavior coupled in shear (Figure 7) is based on the model of Wen [9].

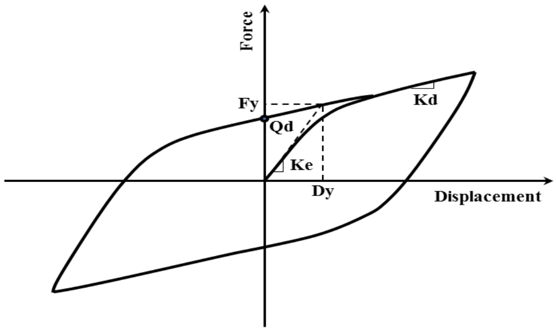

Figure 7: Hysteretic behavior of an elastomeric isolator [9]

4 Presentation of the Structure

It is a reinforced concrete structure (ground floor + 5 floors). The floor of the various stages is hollow body of 20 cm thick. The dimensions are (30x35) cm for the beams, (30x30) for chaining and (30x40) for columns. The floor height is 3.15 m. The structure is located in a class IIa seismic zone. The foundation soil is of the loose type. The characteristics of the materials are as follows:

- Concrete: F_C28 = 25 MPa, E_C = 32164 MPa.
- Steels: FeE400 for longitudinal reinforcement: E_S = 2.105 MPa, f_Y = 400 MPa
  FeE235 for transverse reinforcement: E_S = 2.105 MPa, f_Y = 235 MPa.
- Permanent loads G and overloads Q are as follows:
  $G_{TERRACE}$ = 0.57 tf/m², $Q_{TERRACE}$ = 0.10 tf/m², G_{FLOOR} = 0.50 tf/m², Q_{FLOOR} = 0.10 tf/m².

Structure 1 is in autostable frame with fixed supports (Figure 8). Structure 2 is made of autostable frame braced by shear walls of 15 cm thick, with fixed supports (Figure 9). Structure 3 (Figure 8) is made of autostable frame on isolated supports (seismic isolators).

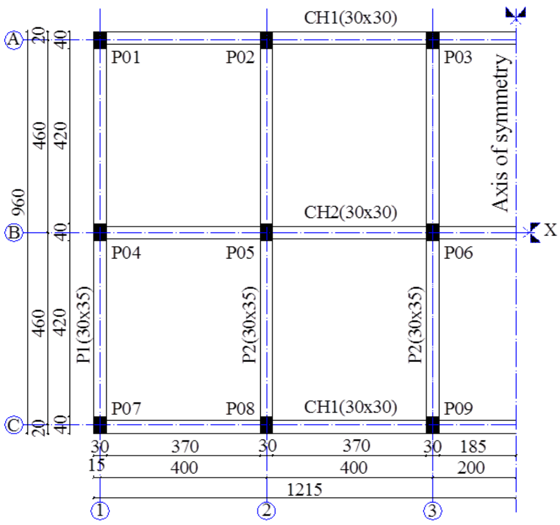

Figure 8: Formwork floor, structure 1 and 3

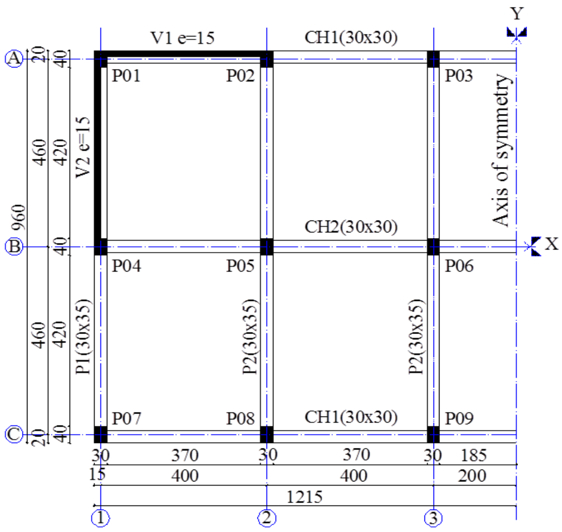

Figure 9: Formwork floor, structure 2

5 Sizing of the Isolator

The Algerian Code RPA 99, version 2003, provides no guidance on the calculation of structures on seismic supports. For this reason, we will use the code UBC 97 [10]. The characteristics of the chosen isolator HDRB (Figure 10), are the following: Elasticity modulus E = 1800 kN/m^2, Shear modulus G = 540 kN/m^2, maximum shear stress γ_{max} = 150%.

According to UBC 97, the seismic data is:

seismic zone factor (2a)	z = 0.15
zone seismic coefficients	C_A = 0.3 and C_V = 0.5
maximum capable earthquake response coefficient	M_M = 2
amortization β_{eff} = 15%	B_D = 1.35 and B_M = 1.35
periods : T_D	2 sec and T_M = 2.5 sec.
soil profile type S_E	C_{VM} = 0.50 and $_{VD}$ = 0.50
type of fault A, proximity to the fault 10 km	N_v = 1.2 and N_a = 1

The sizing steps are as follows:

A. Calculation of the values of the minimum and maximum total rigidities K_D and K_M.
The periods T_D and T_M, are defined by:

$$T_D = 2\pi\sqrt{\frac{W}{K_D}} \quad \text{and} \quad T_M = 2\pi\sqrt{\frac{W}{K_M}} \tag{1}$$

This gives:

$$K_D = \frac{4\pi^2 W}{T_D^2\, g} \quad \text{and} \quad K_M = \frac{4\pi^2 W}{T_M^2\, g} \tag{2}$$

with W = 12500 kN, we find:
K_D = 12563.20 kN/m and K_M = 8040.45 kN/m.
This gives for each of the 18 shock absorbers:
$K_{D/absorber}$ = 697.95 kN/m and $K_{M/absorber}$ = 446.69 kN/m.

B. Design displacement calculations D_U and maximum D_M

$$D_U = \frac{\left(\frac{g}{4\pi^2}\right) C_{VD}\, T_D}{B_D} \quad \text{and} \quad D_M = \frac{\left(\frac{g}{4\pi^2}\right) C_{VM}\, T_D}{B_M} \tag{3}$$

Which gives: D_U = 0.18 m and D_M = 0.23 m

C. Calculation of rubber thickness t_r

$$t_r = \frac{D_U}{\gamma_{\max}} = 0.12\, m$$

we take t_r = 0.15 m

D. Calculation of the support section A

Horizontal rigidity K_H of a shock absorber is given by: $K_H = \frac{G\,A}{t_r}$

Taking $K_H = K_{D/asorber}$, we find: $A = \frac{K_H\, t_r}{G} = 0.19\, m^2$

for a circular isolator: $A = \pi D^2/4$ = 0.19 m^2 Which gives D = 0.50 m.

E. Calculation of the rubber thickness between two steel frets t_c

The form factor S is given by: $S = \frac{D}{4 t_c}$

either: $t_c = \frac{D}{4 s}$

The form factor varies between 5 and 30. We take S = 10.
Which gives t_c = 12.50 mm. We take t_c = 12 mm.

F. Calculation of the number of steel frets n_a

$n_a = \frac{t_r}{t_c} - 1$, either 11 steel frets 2 mm thick.

G. Calculation of the total height H of the isolator

H = 12x12+11x2+2x25 = 216 mm

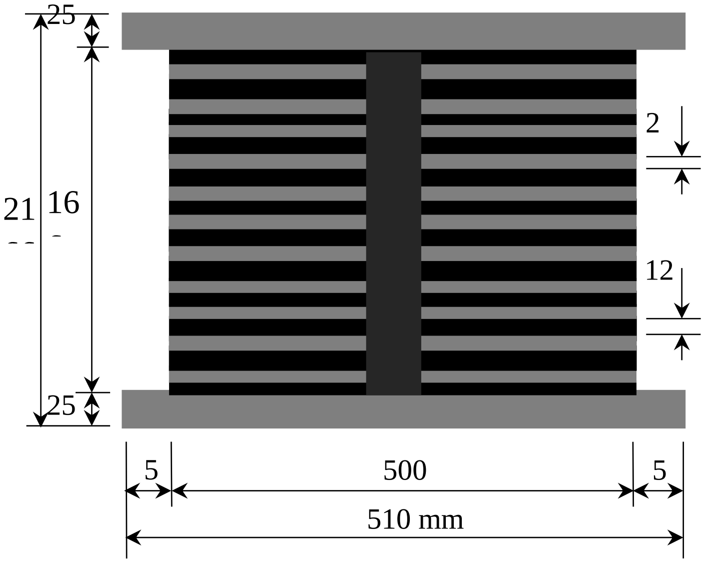

Figure 10: HDRB Isolator characteristics

5.1 Description of the Seismic Excitation

The two horizontal components of accelerograms used in the analysis are (N-S) and (E-W). They are applied respectively in the transverse and the longitudinal direction of each structure. The accelerograms of these two components are shown in Figures: 11 and 12. A_{max} = 0.134 g at t = 0.695 sec.

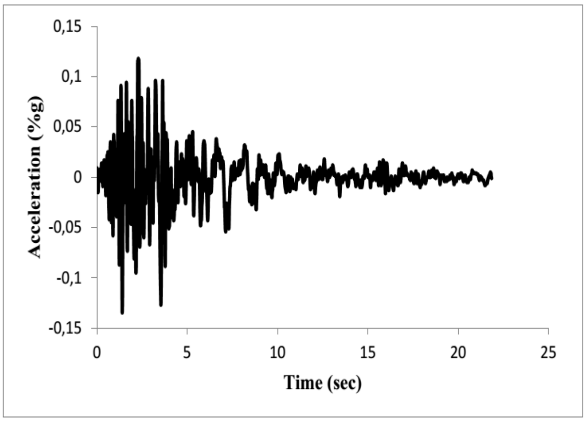

Figure 11: Transverse component [11]

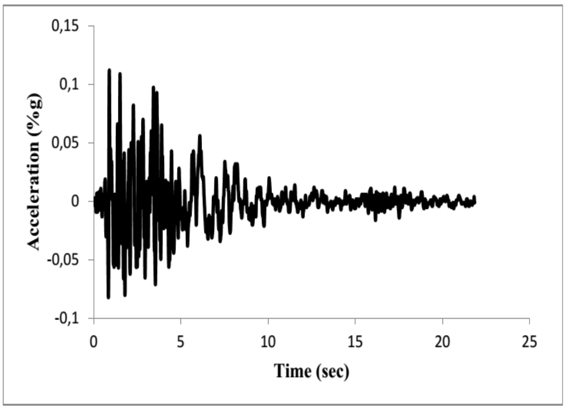

Figure 12: Longitudinal component [11]

The modeling of the different structures is mentioned in Figure 13.

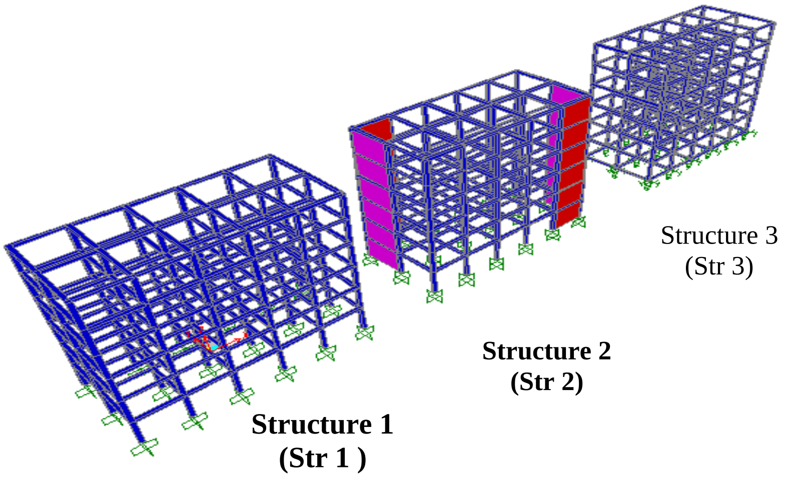

Figure 13: Modeling of the structures by SAP2000, V14

6 Results Analysis

The periods obtained for each type of structure are given in Table 1.

Table 1: Comparison of periods

Mode	Period (sec)		
	Fixed base structure (Frame)	**Fixed base structure (Frame + Shear wall)**	**Isolated Structure**
1	1.32	0.51	2.71
2	1.21	0.33	1.86
3	0.43	0.21	1.39
4	0.38	0.11	0.72
5	0.24	0.09	0.51
6	0.21	0.08	0.48
7	0.15	0.06	0.42
8	0.12	0.05	0.39
9	0.08	0.05	0.43
10	0.07	0.04	0.32
11	0.06	0.03	0.30
12	0.06	0.02	0.25

These results show an increase in the period of the isolated structure compared to fixed base structures. The maximum displacements and accelerations obtained for each type of structure are given in Table 2.

Table 2: Comparison of displacements and acceleration

Level	Maximum displacement (cm)			Maximum acceleration (m/s^2)		
	Str 1	**Str 2**	**Str 3**	**Str 1**	**Str 2**	**Str3**
6	4.43	0.45	5.5	1.95	2.54	0.95
5	4.18	0.38	4.9	1.65	1.99	1.06

4	3.71	0.30	4.2	2.03	1.77	1.26
3	2.97	0.21	3.4	1.83	1.80	1.36
2	1.97	0.12	2.4	1.85	1.84	1.25
1	0.80	0.05	1.4	1.51	1.37	0.91
0	0.00	0.00	0.5	0.00	0.00	0.46

One notices an increase in displacements and a reduction of accelerations in the various levels of the structure isolated compared to the fixed base structures.
The inter-story displacements obtained for each type of structure are mentioned in Table 3.

Table 3: Inter-story displacements

Niv.	**Inter-story displacements (cm)**		
	Str 1	**Str 2**	**Str 3**
6	0.25	0.07	0.60
5	0.47	0.08	0.70
4	0.74	0.09	0.80
3	1.00	0.09	1.00
2	1.17	0.07	1.00
1	0.80	0.05	0.90

One notices an increase in the inter-story displacements of the isolated structure compared to the fixed base structures. The shear forces at the base for each type of structure are given in Table 4.

Table 4: Comparison of shear forces at the base

Sens	**Shear force at the base (t_f)**		
	Str 1	**Str 2**	**Str 3**
Transversal	180.51	273.66	31.86

According to the results obtained, the insulation system reduces the shearing forces at the base.

7 Conclusion

During an earthquake, the majority of victims are due to the collapse of buildings on their occupants. The best response to this risk is to build structures that comply with earthquake-resistant codes, the objective of which is to use design techniques that make it possible to create resistant structures. It is about saving as many human lives as possible by avoiding the collapse of structures. The seismic isolator is one of the techniques used to reduce the dynamic effect of vibration. For this research we used an isolator type elastomer with high damping HDRB. After pre-dimensioning of the seismic isolator according to code UBC97, and the dynamic study by SAP2000, a comparison was made between the different calculation results. The results of the dynamic study show: an increase in the period and displacements, attenuation in acceleration, a reduction in the shearing force at the base of the isolated structure compared to fixed base structures. The isolated structure moved like a rigid body because the displacements are located mainly at the levels of the supports. Therefore, the insulation of structures increases the performance of buildings by reducing the dynamic response. It is more efficient to minimize structural damage and save lives during and immediately after an earthquake. We conclude that the seismic isolator technique is an accepted design alternative for reducing seismic risks and improving the performance of structures. In the future, it aims to study the seismic performance of an existing high-rise building exhibiting torsional irregularity. This building rests on lead rubber bearings designed taking into account the force in the shear walls whose main objective is to improve the seismic performance of the building by eliminating the harmful torsional effects and decreasing the seismic forces.

References

[1] Abdollahzadeh, G., & Sadeghi, A, (2018). Earthquake recurrence effect on the response reduction factor of steel moment frame. Asian journal of Civil Engineering, 19, 993–1008.

[2] Faroughi, A., Moghadam, A. S., & Hosseini, M, (2017). Seismic progressive collapse of MRF–EBF dual steel systems. *Proceedings of the Institution of Civil Engineers Structures and Buildings, 170,* 67–75.

[3] Hakim, R. A., Alama, M. S., & Ashour, S. A, (2014). Seismic assessment of RC building according to ATC-40, FEMA-356 and FEMA-440. *Arabian Journal for Science and Engineering, 39,* 7691–7699.

[4] Hosseini, M., Fanaie, N., & Yousefi, A. M. (2014). Studying the vulnerability of steel moment resistant frames subjected to progressive collapse. *Indian Journal of Science and Technology, 7*(3), 335–342.

[5] Kiakojouri, F., & Sheidaii, M. (2018). Effects of finite element modeling and analysis techniques on response of steel moment-resisting frame in dynamic column removal scenarios. *Asian Journal of Civil Engineering, 19*, 295–307.

[6] Kordbagh, B., & Mohammadi, M. (2017). Influence of seismicity level and height of the building on progressive collapse resistance of steel frames. *The Structural Design of Tall and Special Buildings, 26*(2), e1305.

[7] Manasa M. S., Mathai A., 2017. Performance of Lead Rubber Bearing as a Base Isolator. *International Journal of Science Technology & Engineering* 3(1).

[8] Mazloom, M., Gholipour, M., & Ghasemi, M. (2019). Evaluating inelastic performance of mega-scale bracing systems in low- and medium-rise structures. *Asian Journal of Civil Engineering, 20*, 383–393.

[9] Salmasi, A. C., & Sheidaii, M. R. (2017). Assessment of eccentrically braced frames strength against progressive collapse. *International Journal of Steel Structures, 17*(2), 543–551.

[10] Vara Lakshmi, T. V. S., & Adiseshu, S. (2016). A study on preparing of high performance concrete using silica fume and fly ash. *The International Journal of Engineering and Science, 5*, 29–35

[11] Xu, J.-G., Wu, G., & Feng, (2019). D.-CNear fault ground motion effects on seismic resilience of frame structures damaged in wenchuan earthquake. *Structure and Infrastructure Engineering*, *16*, 1347–1363.

[12] Saritas, F. (2022). Seismic Performance Assessment of an Isolated Multispan Bridge. *Arab. J. Sci. Eng., 47*, 12993–13008.

DOI: 10.2478/sspjce-2023-0005

Improvement of Productivity in Buildings Construction

Chemseddine Dehchar[1*], Khaled Boudjellal[1], Mohamed Bouabaz[1]

[1]Faculty of Technology, Department of Civil Engineering, LMGHU Laboratory, University of 20 August 1955, Skikda, Algeria
*e-mail: ch.dehchar@univ-skikda.dz / dehcharchemseddine@hotmail.com

Abstract

Improving productivity in construction projects has long been a major concern, and much research has been carried out to try to ameliorate construction productivity. To this end, this study aims to improve and increase the productivity rate of flat slab formwork used in residential construction projects. A survey consisting of 150 questionnaires was undertaken to identify the factors that influence on the productivity. Based on the relative Importance Index (RII), data on eleven factors deemed to affect productivity were selected. A collection of 100 data points from various sites were utilized to develop two models. Firstly, an Artificial Neural Network (ANN) model was employed, and secondly, a parametric approach was investigated. The data were divided into two sets, with 70% of the data used for training and the remaining 30% used for testing. The models' performance was evaluated using the Mean Squared Error (MSE) and Mean Absolute Percentage Error (MAPE) values. In the test phase, the artificial neural network model yielded an MSE value of $2.6610e^{-4}$ and a MAPE value of 4.9227, whereas the parametric model produced an MSE of 0.040 and a MAPE of 9.525. It was found that the artificial neural network model provided reliable prediction accuracy compared to the parametric model. However, the artificial neural network approach can be selected as a robust model in predicting and controlling the productivity rate in local construction projects by using the developed model based on the identified factors.

Keywords: Artificial Intelligence, Construction Industry, Artificial Neural Network, Labour Productivity, Parametric Approach

1 Introduction

In the construction industry, productivity can be defined as the quantity of production work per corresponding input [1]. This relationship can take different forms, defining labour productivity when using work-hour as an input or cost productivity when cost input is taken into account [2, 3]; however, this simple definition of factors does not seem realistic and cannot give robust and accurate results, as omitting the influence of other factors can affect productivity. Various research studies have been conducted over many years to estimate, predict and improve the productivity rate in the construction industry, taking into account the effect of different influencing factors.

The review of the literature in the area of construction and specifically productivity improvement can be divided into two main parts, the first focuses on the identification of factors affecting productivity, and the second deals with applications of artificial intelligent.

The pace of labour productivity is a critical factor that directly influences the outcome of projects, ultimately determining their success or failure [4, 5]. According to [6], factors affecting labour productivity may vary from country to country and from site to site, and may also vary within a site. [7] Stated that, labour productivity is influenced by various factors, including external conditions, site conditions, and workers' characteristics. The combined influence of these factors determines the overall level of efficiency and effectiveness attained in construction tasks. [8] Invited 180 Kuwaiti companies to participate in a sample survey that included 45 factors grouped into four groups, to identify the factors most influencing Kuwaiti projects, the result of the statistical analysis determined that the total project cost could be reduced by focusing on the design phase. The influence of several factors on labour productivity in Malaysian construction sector was examined in [9], the authors found that project management skills were the factors that had the greatest impact on productivity, and also stated that the implementation of new technologies in construction sector has positive effects on labour productivity. Another study by [10] highlights that the management group ranks first in three categories, which includes 30 factors studied for their effects on labour productivity in Egyptian construction firms, the authors also found that workers experience and skills were the most important factor. A questionnaire survey conducted in Trinidad and Tobago by [11], to identify the influencing factors on construction projects, were investigated on 30 contractors who are members of the Contractors Association. The survey included 42 factors categorized into four groups: Management, Technological, Human/Labour, and External. Both close-ended and open-ended queries were used, and the respondents were asked to score each factor based on a Likert Scale, ranging from 1 to 4, indicating the effect level. To determine the rank of each factor, the researchers calculated the Relative Importance Index (RII%) and ranked the factors accordingly. The top three influencing factors identified were: the lack of labour supervision, unrealistic scheduling and expectation of labour performance, shortage of experienced labour. In [12], 52 factors, were used to investigate their influence on productivity in Yemen, by calculating the relative importance index, the authors found that workers experience and skills were the most significant factors. [13] Proposed a fuzzy fault tree-based approach to identify factors influencing labour productivity in Lithuania. Initially, they gathered data from 15 experts who evaluated 27 factors using a Likert scale, ranging from 1 to 5, to indicate the degree of severity. After this step, 18 factors with a Relative Importance Index (RII) greater than 0.7 were selected for the subsequent analysis. In the next phase, the authors constructed a fault tree structure through multiple sessions and expert interviews to define the interrelations among the selected factors. Finally, the fuzzy approach was employed to evaluate the contribution of each factor. The results of their analysis indicated that two factors, namely "inflation in the cost of execution" and "improper project financing," were identified as the most influencing factors impacting labour productivity in Lithuania. Another study conducted by [14] aimed to identify the factors affecting labour productivity in the South Africa construction industry based on contractors' perceptions. A questionnaire survey consisting of 41 factors was randomly distributed to 96 contractors. The obtained responses were then analysed using descriptive and inferential statistics. The factors were ranked according to their P-values, and the most significant influencing factors on labour productivity were found to be: excessive bureaucracy, late delivery of materials, industrial action resulting from political activities. Authors in [15] identified factors affecting labour productivity in Australian construction projects by following a three-step approach. In the first step, they conducted a questionnaire to gather data on various factors related to labour productivity in construction projects. The second step involved drawing a cause-and-effect feedback loop to identify the complicated interrelated links between the 38 factors. Lastly, the authors used the Decision-Making Trial and Evaluation Laboratory (DEMATEL) method to prioritize the factors. The results of the study revealed that project size, level of skill and experience, and communication problems with foreign workers were the most significant factors affecting labour productivity in Australian multi-storey building construction projects. In another research conducted by [16], authors examined the influence of weather conditions on labour productivity in the United Kingdom. The study involved collecting data over a span of 5 years, from September 2017 to August 2022. To gather information, the researchers administered 28 online questionnaire surveys to relevant participants. Based on their findings, the authors proposed implementing modular techniques in construction, wherein certain elements are produced in factory settings with controlled environments. This approach is expected to mitigate the adverse effects of weather on construction projects, consequently reducing overall costs.

In the second half of the 1980s, Artificial Neural Networks were developed and used to solve various construction problems such as cost estimation, duration and productivity. Numerous models were produced [17–19],and are still in progress to this day. [20] Examined the influence of ten factors, on Turkish formworkers' productivity. A three-layer feed-forward back propagation neural network was used, using these factors as input variables, a hidden layer containing five hidden neurons and an output neuron to estimate the labourers' productivity rate, compared to the estimate of the Turkish Ministry of Public Works and Settlement, the simulation results indicate that the model developed accurately predicted the total man-hours required. In another approach, [21], also formulated a multi-layer ANN with the backpropagation algorithm using ten influencing factors, as input variables to assess the labour productivity rate for finishing work on marble floors. The architecture of the model used was a three-layer neural network with one hidden node in the hidden layer and used the hyperbolic tangent sigmoid function as a transfer function, a degree of accuracy of 90.9% was recorded, which proved that Network, the Backpropagation Neural Network, the Radial Base Function Neural Network and the Adaptive Neuro-Fuzzy Inference System, and compared their results to choose the best model the developed model can reliably predict the productivity rate, it was also found that the most influential factors on productivity were age, number of workers and experience. Two ANNs models with different architectures were developed by [22], using three categories of influencing factors, the capabilities of a Feed-Forward neural network and a Radial-Based NN to predict masonry crew productivity were compared; the results showed that the RBNN technique predicted productivity better than the FFNN. Authors in [23] took thirteen factors that were found to have a negative effect on labour productivity and considered them as inputs for developing an ANN model to estimate bricklayer productivity, a gradient descent momentum backpropagation was used as a training algorithm for the model which has three hidden layers and a hyperbolic tangent sigmoid transfer function; accurate results were obtained using this architecture, in addition, the results of the sensitivity analyses led to the conclusion that the wall thickness was the factor that most influenced the labour productivity rate. [24] Developed four ANN models based on different techniques, including the General Regression Neural for predicting the productivity rate of formwork labours, the performance results show that the Backpropagation NN is the best model among the four techniques developed in the study.Authors in[25]stated that labour productivity in Saudi construction projects is affected by a number of factors and can be quantified using mathematical models. For this purpose, the author developed four different models based on multilayer perceptron neural network

(MLPNN), general regression neural network (GRNN), support vector machine (SVM), and multiple additive regression trees (MART) to assess the productivity rate of concrete construction activities and compared the results of the developed models. The GRNN model was found to be the best estimator model for labour productivity of steel fixing and concrete pouring, while the MART model provided better results than the others for formwork assembly productivity. In order to ensure effective and efficient project delivery,[26] utilized an artificial neural network (ANN) to assess the relationships between various factors and bricklaying productivity during the pre-planning phase. The developed model included 7 input factors, 5 hidden neurons, and one output. The results showed good performance, indicating that the ANN model can be utilized to enhance project delivery by providing a more realistic estimation of productivity rates. This, in turn, leads to better planning, cost estimation, and resource allocation. In a study conducted by [27], authors used sets of five Artificial Neural Network models to develop a single model capable of estimating steel reinforcement works. They collected 145 data points from construction sites in Poland, which were then divided into 90% for training and 10% for testing purposes. The proposed model demonstrated satisfactory performance, indicating its robustness in estimating steel reinforcement works. [28] Developed an Artificial Neural Network (ANN) model to assess the productivity rate of piping assembly activities in Brazilian projects. They tested 108 different Feedforward Neural Network (FFNN) architectures, each with 14 input neurons, to select the best model. The research results indicated that the Mean Square Error (MSE) of the chosen model reached the value of 9.67E-04, demonstrating satisfactory performance and accuracy. A hybrid model combining artificial neural network (ANN) and Grasshopper Optimisation Algorithm (GOA) was developed by[29]. The objective was to identify the factors with the greatest impact on labour productivity in Iranian construction projects and improve the accuracy of labour productivity prediction. Out of the 19 factors initially considered, only 6 factors were identified as influential and utilized to develop the predictive ANN model. [30] Employed Artificial Neural Networks (ANN) to predict the productivity rate for brick masonry work. The authors conducted a questionnaire survey that initially included forty-four factors. However, based on the Relative Importance Index (RII) analysis, only the top 13 ranking factors were considered as inputs for the model. The developed model utilized a three-layer backpropagation-feedforward neural network with one hidden layer consisting of 30 hidden neurons. The Mean Squared Error (MSE) was used as a measure of accuracy for the model. The results indicated that the developed model effectively estimated brick masonry productivity by considering the impact of the selected 13 factors.
Parametric model was developed in the early 1960s, it has been used to find the relationship between the response and one or more factors, usually by applying regression analysis to the parameters [31]. [32] Developed a parametric equation based on multiple linear regression (MLR) analysis to model the labour productivity of marble floor finishing works in Iraq.100 data including 10 influencing factors were collected and used to predict productivity, good performance, and a high correlation was obtained, indicating a good relationship between the response and the factors, and the model can be reliably used to estimate productivity. In another study conducted by [33] to estimate the percentage loss or increase in construction labour productivity, 14 influencing factors were defined and used to develop a regression model, the author argued that the proposed model can accurately predict construction labour productivity. [34] Examined the influence of various buildability factors on the labour productivity of structural elements, by developing a MLR model to assess the relationship between design characteristics and labour productivity. The results show that the model can provide information

for designers to adapt their designs to achieve the best labour productivity performance.Authors in [35] conducted a study to examine the impact of worker experience and skill level on masonry construction productivity in Vietnam. They developed a logistic regression model to estimate productivity and found that there was no difference in average productivity between different worker experience groups. However, they did observe a significant difference in productivity between worker skill groups. [36] Employed a multiple linear regression method to analyse the impact of three factors on labour productivity in lightweight brick wall installation and lightweight brick wall plastering in Indonesia. The researchers achieved an impressive accuracy of 99.43% and 99.04% for the two respective models, indicating the robustness and reliability of the developed models. In their study conducted at eight construction sites in Niš, Serbia, [37] Focused on analysing concreting processes, particularly those related to columns and walls. They gathered 60 data points to develop regression analysis and Simulation models aimed at improving the accuracy of forecasting productivity rates for concrete works. The findings of the study indicated that these proposed models have the potential to enhance decision-making and improve the accuracy of planning in construction projects involving residential buildings in Niš, Serbia.

The Algerian construction industry is currently facing a major problem in accurately measuring construction labor productivity. This issue is mainly attributed to the continued utilisation of traditional technologies, which has significantly hindered progress in the construction sector. The challenges are particularly evident in the execution of flat slab formwork activities, resulting in excessive resource consumption in terms of manpower, time, and cost. To enhance construction efficiency, time management, and cost control, it is crucial to address the productivity issues related to flat slab formwork. By optimizing the flat slab formwork productivity in Algerian building projects, it becomes possible to achieve faster construction cycles, lower labor costs, and improve overall project performance. This, in turn, leads to more efficient resource utilization and successful project outcomes.

While previous studies have examined construction productivity in a general context, however, there appears to be a noticeable gap in the existing research regarding comprehensive investigations into the factors influencing productivity, particularly in Algerian construction projects. Additionally, there is a lack of intelligent methods that specifically concentrate on accurately measuring and estimating labor productivity rates for flat slab formwork within the context of the local construction industry. Since our study focuses on a local problem with specific characteristics compared to other world regions, we are faced with the following issues:

- What are the key factors that influence productivity in Algerian construction projects?
- How do the identified factors influence the productivity rate of flat slab formwork in Algerian construction projects?
- How can we estimate this productivity?

This paper aims to address two primary objectives: identifying the key factors that affect productivity in Algerian construction projects and developing intelligent models capable of estimating the labour productivity rate of flat slab formwork. By conducting research on this topic, the study intends to fill the existing knowledge gap and contribute valuable insights to both academia and industry practitioners. The findings of this research will provide valuable guidance for productivity improvement and decision-making in the management of construction projects in Algeria.

2 Methodology

This study aims to improve the labour productivity rate of flat slab formwork in Algerian building projects. To achieve the objective mentioned, the methodology presented in this section was adopted.

2.1 Questionnaire Survey Analysis

Identifying factors that negatively affect labour productivity in construction projects has been a major concern for managers [32, 38]. After careful analysis of the top influential factors cited by researchers [10, 12], [21-23], [39–43], the factors that appeared repeatedly were identified and extracted. Moreover, by considering on-site observations of construction projects, a questionnaire survey was designed including 16influencing factors classified into three main groups as shown in Table 1.The survey consisted of closed-ended questions that were sent by email to local expert, who were asked to rate the impact of each factor on labour productivity using a five-point Likert scale, ranging from 1 (indicating the least impact) to 5 (indicating the greatest impact). Respondents were specifically asked to indicate the extent to which a specific factor affected labour productivity according to their own perception. The designed questionnaire survey was divided into three sections:

1. The first shows the respondents' personal information (position and professional experience)
2. The second section consists of three groups with 16 influencing factors, the respondents rank the importance of each of them based on a five-point Likert scale, where 1 indicates the least impact while 5 represents the greatest impact.
3. The last section represents a space dedicated to the respondents' opinions.

Table 1: Questionnaire survey factors

Questions (Factors)		
Group 01: Management	**Group 02: Factors related to workers**	**Group 03: External factors**
Small crew size Low wages Formwork condition Delay in payment of the company by the project owner Congestion in the workspace Poor control Low workers motivation	Work-hour/absenteeism Worker’s experience Quantity of installed work Worker’s age	Weather condition Humidity High temperature Low temperature Shortage of building materials

2.1.1 Sample Size

For a more diverse and precise analysis, we specifically targeted project managers, technical managers, site managers, civil engineers, and architects working in the public and private sectors to gather their perceptions and viewpoints on the various factors that influence labour productivity in the Algerian construction industry. A statically representative sample of the population was obtained using a formulae developed by [12, 44], as expressed bellow:

$$n = \frac{m}{1 + \frac{(m-1)}{N}} \quad (1)$$

where, *n* is the sample size of the limited population, m is the sample size of the unlimited population, and *N* is the sample size of the available population. *m* is estimated as follows:

$$m = \frac{z^2 \times p(1-p)}{\varepsilon^2} \quad (2)$$

z represents the statistic value for the confidence level used (*z* = 1.645 for 90% confidence level), *ε* is the sampling error of the point estimate, and *p* is the value of the population proportion that is being estimated, for which [45], proposed using a conservative value of *p* = 0.50 to obtain a sample size at least as large as needed. The value of *m* can be obtained than:

$$m = \frac{(1.645)^2 \times 0.50(1-0.50)}{0.1^2} = 67.65 \simeq 68 \quad (3)$$

In this study, a total number of 150 available samples were selected, based on this; the required representative sample size of the population is obtained as follows:

$$n = \frac{68}{1 + \frac{(68-1)}{150}} \simeq 47 \quad (4)$$

A total of 150 samples were distributed by email and only 56 feedbacks were received, this number of completed questionnaires met and exceeded the required sample size. The respondents in the samples are project managers, technical managers, site managers, civil engineers, and architects, working in Algerian construction industry. 48.22% of them having an experience of 1 to 4 years, while 44.64% have an experience of 05 to 09 years, and the remaining 7.14% have 10 or more years of experience.

2.1.2 Defining the Influencing Factors

The Relative Importance Index (RII) technique was used to define the most influential factors; this index was calculated according to equation (6).

$$RII(\%) = \left(\frac{\sum_{i=1}^{5} n_i \times x_i}{5\sum_{i=1}^{5} x_i}\right) \times 100 \quad (6)$$

where, n_i indicates the Likert scale from 1 to 5, and x_i denotes the frequency of each n_i.
The results of the RII show that three factors had an RII greater than 80%, whereas nine factors have an RII between 70 and 80%, while the RII of the other four factors is in the range of 60% and 70%. Table 2 summarizes the results of RII and the rank of each factor.

Table 2: RII (%) Results and rank of each factor

Factors	**RII (%)**	**Rank**
Small crew size	78.21	07
Low wages	89.64	01
Formwork condition	84.29	03
Congestion in the workspace.	71.79	12

Poor control	74.64	09
Delay in payment of the company by the project owner	74.29	10
Low workers motivation	86.07	02
Work-hour /absenteeism	78.93	04
Worker’s experience	78.57	05
Quantity of installed work	78.57	05
Worker’s age	68.57	13
Weather condition	68.57	13
Humidity	65.00	16
High temperature	75.36	08
Low temperature	67.14	15
Shortage of building materials	73.93	11

In this study, factors with an RII (%) greater than 75% were taken into account. On this basis, the most relevant factors deemed to affect the productivity rate are: workers' wages, workers' motivation, formwork condition, number of working hours, workers' experience, crew size, quantity of installed work, and temperature. Table 3 summarises all the factors considered.

Table 3: The selected influential factors

Factors	Categories	Classification
Number of working hours	Quantitative	Numerical
Number of formworkers	Quantitative	Numerical
Number of unskilled workers	Quantitative	Numerical
Minimum workers' experience	Quantitative	Numerical
Maximum workers' experience	Quantitative	Numerical
Formwork condition	Qualitative	Mediocre Average Good
Type of workers' motivation	Qualitative	Extra money Recuperation days Piecework
Temperature	Quantitative	Numerical
Wage of formworkers	Quantitative	Numerical
Wage of unskilled workers	Quantitative	Numerical
Surface area of the slab formed	Quantitative	Numerical

2.2 Data Collection

The data for this study were collected daily, based on in site observations on the flat slab formwork task, a number of 100 data samples, comprising 11 quantitative and qualitative influencing factors, were compiled from construction projects in different regions of Algeria, the qualitative factors used in this study were transformed into numerical values for use in the models (Table 4). As indicated in the previous sections, productivity can be calculated in different ways (total or partial factor productivity) [46], the type of labour productivity, which is of interest in this study, is defined as the ratio of output to worker-hour (Equation 7), noting that the output presents the surface area of the slab that was carried out in square metres.

$$productivity\ rate = \frac{output}{man \times work\ hour} \quad (7)$$

Table: 4 Transformation of qualitative factors into numerical form

Qualitative factors		**Numerical transformation**
Formwork state	Mediocre	-0.50
	Average	0.00
	Good	0.50
Type of motivation	Extra money	0.10
	Recuperation days	0.15
	Piecework	0.20

2.3 Artificial Neural Network Model Development

2.3.1 Data Preprocessing

The preprocessing phase consists of preparing the data before introducing them into the model, which gives the network the capacity to converge more quickly and to better generalise the results obtained. In this phase the input and target data were normalised to be within the range of [0 to 1] both for the training and the test phase using equation (8).

$$X_n = \frac{X_i - X_{i_{min}}}{Xi_{min_{i_{max}}}} \tag{8}$$

where: X_n: the value of the variable (x_i) after normalization. And X_i: the value of the variable before normalization. X_i min; X_i max are the minimum and maximum value of (X_i).

2.3.2 Data Processing

Is the process by which the collected data is organised and introduces into the ANN model, to obtain better generalisation of the results, for this purpose, the designed set was divided into training and test subsets, the training subset is used to initialise the weights and biases of the network. According to [47], each network starts training from arbitrary initial weights and biases, while the test subset is used to verify the network design, testing the efficiency of the model on the new data. During the modelling phase, a phenomenon can occur when errors begin to increase in front of the test data after providing very small values in the training sets, this phenomenon is known as over fitting, in this case, the model adjusted its parameters well and stored all the training courses, but when new data was introduced into the network, the model failed to adapt and generalise the new situation. Different methods have been used to avoid this phenomenon; in this study the Bayesıan regularisation technique was used.
Simulation software was utilized to create, train and test the networks, with random division of the designed set into 70% training, and 30% into test sets.

2.3.3 Model Architecture and Adapted Algorithm

The model architecture represents the number of appropriate layers, and the way these layers are connected, as well as the type of algorithm chosen. In this study, several architectures were tested to obtain better accuracy, the model with three layers having 11 input neurons, two hidden layers having 15 and 10 hidden neurons in the first and second hidden layers respectively, and one output neuron as presented in Figure 1. Backpropagation was used as a learning algorithm with Bayesian regulation.

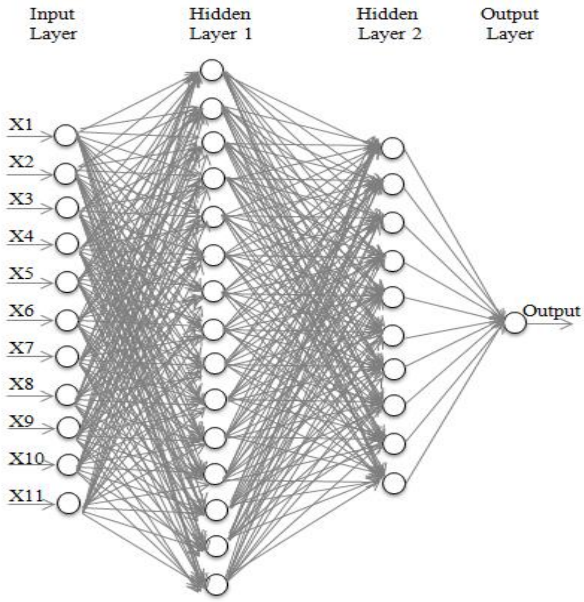

Figure 1: The architecture of the ANN model developed

2.3.1 Transfer Function

The transfer function is a monotonic, continuous, increasing and differentiable function applied to the sum of the weighted inputs of the model to produce their resulting outputs. This function consists of two sub-functions used by the neurons in the different layers. Firstly, the neuron in each layer receives a linear combination of weighted inputs, determining the sum of the information collected, using the activation function A(x) which is given as follows:

$$A_i(x) = \sum_{j=1}^{N} \left(W_{ij} \times X_j\right) - \theta_i \tag{9}$$

where: X_j: the inputs, and W_{ij}: the weights and θ_i is the threshold (bias).
In the next step, the neurons use an O(A) output function, to keep the output values within a specified range, operating it on the activation function which has a scalar format and returns the scalar output neurons. Thus, the transfer function O(A(x)) is the combination of the two previous functions (activation and output function), which is used to produce the final output neurons [48]. Different transfer functions are available in the Artificial Neural Network model used to pass information from one layer to the other [47], the most commonly used are log-sigmoid, tan-sigmoid, and linear (purelin). Each function of the latter has its own range that generates output results within it. The logsig produces results between 0 and 1 while tansig returns outputs in the range of -1 and 1, however, the specific range of purelin is: [-∞ + ∞].
The transfer functions adopted in this study for the implementation of the ANN model were the log-sigmoid transfer function (logsig) and the hyperbolic tangent sigmoid (tansig) which were used in the first and second hidden layers, respectively, while the pureline linear transfer function was used in the output layer equation (10), equation (11) and equation (12).

$$Log\,sig(A) = \frac{1}{(1 + exp(-A))} \tag{10}$$

$$Tansig(A) = \frac{2}{(1 + exp(-2A))} - 1 \tag{11}$$

$$F(A) = A \tag{12}$$

2.3.2 Training and Testing Phase

Network training is the first process carried out by the model to select its parameters, it consists of adjusting the values of weights and biases until a minimum error value is reached and the best performance is obtained. The Bayesıan regularization training algorithm was used in this study to obtain better results. This algorithm consists of adding an additional term (penalty term), which represents the sum of the squares weights to the equation error, and then propagating the resulting errors back to readjust the weights and biases, and minimizing the errors to obtain the best prediction of the output.
Out of the 100 datasets collected, a number of 70 datasets were used for training in the first phase, while the remaining 30 datasets were retained to test the model in order to generalize the model to the new data, and to obtain better performance in predicting the results.
The Mean Square Error (MSE) and the Mean Absolute Percentage Error (MAPE) were used in this study to calculate the performance of the model, as follows:

$$MSE = \frac{\sum_{i=1}^{n}(x_i - E_i)^2}{n} \tag{13}$$

$$MAPE = \frac{100}{n} \times \sum_{i=1}^{n} \left|\frac{x_i - E_i}{x_i}\right| \tag{14}$$

where, n is the number of the data, E is the model outputs, and x_i is the actual value.

2.4 Parametric Analysis

Parametric analysis is a method that links a variable to be estimated (labour productivity) and the different factors that influence it through a mathematical relationship. The technique most commonly used to develop the parametric equation is Multiple Linear Regression (MLR).

2.4.1 Development of Multiple Linear Regression Model

At this stage, 70% of the total data collected, were used to develop the model using Statistical Product and Solutions Services (SPSS) software. The correlation test was carried out to check the relationship between the response and the explanatory variables. The results of the correlation coefficient (R) and determination coefficient (R2) presented in Table 5 show a strong correlation between the response (flat slab formwork productivity rate) and the explanatory variables, indicating that they have a good relationship. A significant value for the model was found to be less than 0.05, meaning that the regression line fits the data well.

Table 5: Model Results Summary

Coefficient of correlation (R)	**Coefficient of determination (R2)**	**Significance of the model**
0.958	0.917	0.000

Table 6 summarises the results of MLR coefficients and the resulting equation for estimating the productivity rate of flat slab formwork in construction projects takes the form below:

$$\begin{aligned} Y = {} & 3,239 - 0,304X_1 - 0,088X_2 - 0,139X_3 - 0,021X_4 \\ & +0,007X_5 - 0,015X_6 - 1,356X_7 + 0,011X_8 \\ & -0,004X_9 + 0,000103\,X_{10} - 0,000053X_{11} \end{aligned} \tag{15}$$

Table 6: Coefficients of Multiple Linear Regression

Model	**Unstandardized Coefficients**	
	ß	**Std. Error**
(Constant)	3.239	0.716
X1	-0.304	0.024
X2	-0.088	0.035
X3	-0.139	0.014
X4	-0.021	0.024
X5	0.007	0.010
X6	-0.015	0.047
X7	-1.356	1.302
X8	0.011	0.001
X9	-0.004	0.006
X10	0.000103	0.000046
X11	-0.000053	0.000039

2.4.2 Validation of the Developed Model

Model validation is the stage during which the new data was used on the explanatory variables (factors) to test the ability of the parametric equation developed in equation (15), to estimate and predict the productivity rate of the flat slab formwork. In this respect, a set of 30 data was applied to the developed parametric equation, and the results of the predicted productivity rate were compared with the actual productivity rate. The MSE and MAPE measures were calculated to verify the performance of the model with the new data.

3 Results and Discussion

This paper aims to develop a machine learning model capable of predicting and estimating the labour productivity rate for flat slab formwork assembly. In this respect, an Artificial Neural Network was first trained using 70% of the data sets and tested using 30% of the data sets. Various ANN architectures were tested with different combinations in the number of hidden layers and hidden neurons as well as in the learning algorithm, and in the different ANN parameters, to choose the best model that gives the best performance, the final structure adopted in this study was a three-layer feed-forward back-propagation neural network having two hidden layers with 15 hidden neurons and 10 hidden neurons in the first and second hidden layers respectively. The Bayesian regularization technique was adopted as the learning algorithm. The modelling phase consists of training the network first; in this step, the model shows its ability to predict the results of the labour productivity rate with lower values of the MSE and the MAPE, as shown in Figure 2. Testing the network is the next step carried out by the model to examine its ability to handle unseen data. Good results from MSE and MAPE were obtained at this stage as well, showing the model's ability to predict the labour productivity rates of flat slab formwork, as shown in Figure 3. In line with the results from the MSE and MAPE, it can be said that the model developed performs well and that no significant difference could be observed between the predicted and actual labour productivity rates. Table 7 summarises the overall results of the measures. The regression analysis in the developed ANN model was carried out to examine the relationship between actual targets and estimated output, a correlation coefficient of 0.9994 was obtained indicating a good linear correlation between forecasted and actual labour productivity (Figure 4).

In the second part of the study, a parametric analysis of the collected data was carried out by developing a Multiple Linear Regression model. The results of the correlation coefficient and the determination coefficient rather than the significant value of the developed equation show a strong correlation between the response (labour productivity rate) and the explanatory variables (factors). A good result from MSE and MAPE was obtained, indicating that the parametric equation developed has the capacity to estimate and predict the labour productivity rates of flat slab formwork (Figure 2). A set of 30 data was applied to the developed parametric equation to validate it and the results of the predicted labour productivity rates were compared to the actual labour productivity rates. Based on the MSE and MAPE results obtained during the validation phase, it can be stated that the parametric equation developed works well and can be used reliably to predict the labour productivity rates of flat slab formwork (Figure 3). Table 8 lists the results of the performance of the parametric model.

Finally, from the results of the two methods above, it can be seen that both the ANN model and the parametric model can be reliably used to estimate and predict the labour productivity rate. However, significant differences between the performances of the two models developed were observed, so we can conclude that the ANN model gives better results and predicts the labour productivity rates of flat slab formwork better than the parametric model.

Table 7: Results of the Artificial Neural Network performance

Phase \ **Performance**	**MSE**	**MAPE %**
Training phase	8.0796e-05	0.82832
Test phase	2.6610e-04	4.9227

Table 8: Results of the parametric equation performance

Phase \ **Performance**	**MSE**	**MAPE %**
Development phase	0.048	9.395
Validation phase	0.040	9.525

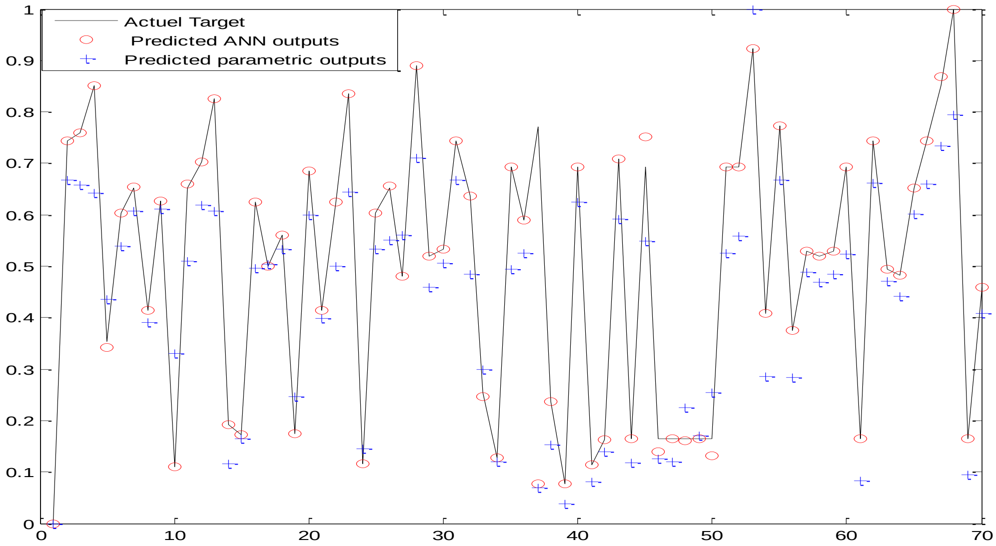

Figure 2: Predicted Neural Network and parametric outputs versus actual targets in the training phase

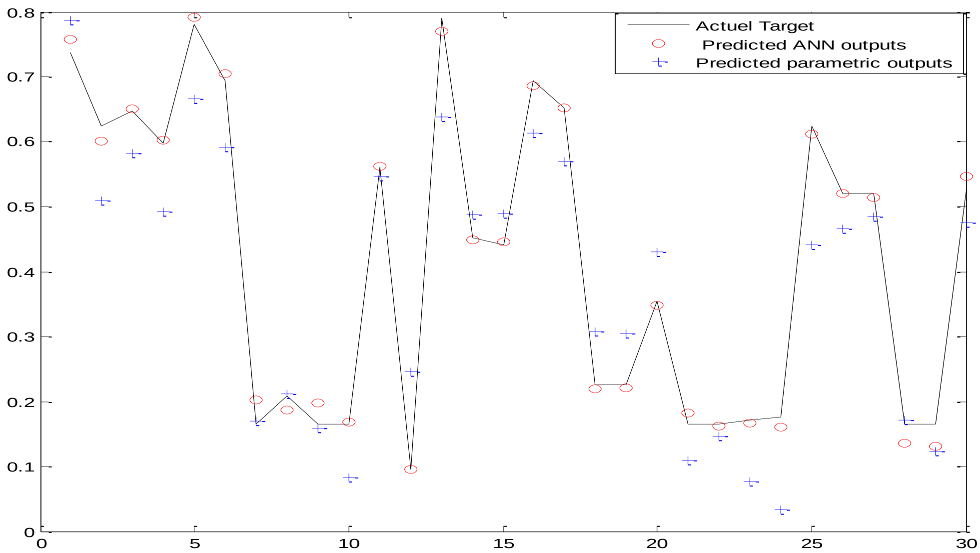

Figure 3: Predicted Neural Network and parametric outputs versus actual targets in the test phase

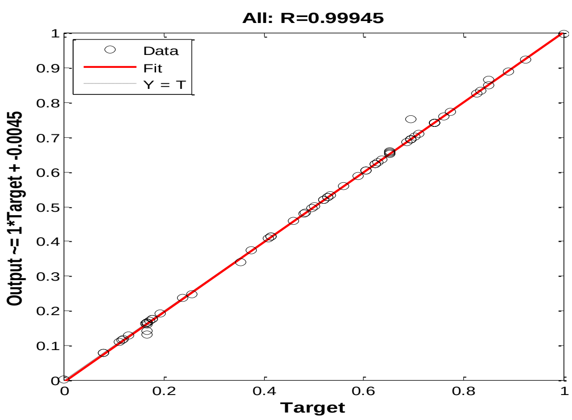

Figure 4: The regression analysis and correlation coefficient R in ANN model

Additionally, we investigated samples of previous studies conducted by many researchers on formwork productivity modelling. Results were reported regarding the performance of each model. For instance, [49] obtained a MAPE of 14.55% and 17.69% for the ANN and MLR models, respectively, for column formwork productivity. In another study by [25], the MART model was found to be the best among the four developed models, with an MSE of 0.0937. Furthermore, [24] developed four models for slabs, walls, and columns formwork productivity, it was found that Backpropagation Neural Network was the best model which achieved an MSE of 0.018.
Table 9 describes a comparison study conducted on existing models versus the developed models.

Table 9: Results comparison among existing models

Existing Research	**The used model**	**Performances results in the test phase**
Developed research study	Artificial Neural Network	MSE = 2.6610e-04 MAPE = 4.9227 %
	Multiple Linear Regression	MSE = 0.040 MAPE = 9.525 %
S. Nassar and A. Khaleel. (2019)	Artificial Neural Network	MAPE = 14.55 %
	Multiple Linear Regression	MAPE = 17.69 %
E. A. Mlybari. (2020)	MART	MSE = 0.0937
Golnaraghi et al. (2019)	Backpropagation Artificial Neural Network	MSE = 0.018

By comparing the outcomes of the mentioned models with models developed in this study, it can be observed that the latter exhibits significantly higher performance accuracy. The achieved MSE and MAPE values suggest that our ANN and MLR models are better in predicting formwork productivity and providing more accurate results. This confirms the reliability and efficiency of the methods used in this study, which leading to a significant advancement in the field of formwork productivity modelling.

4 Conclusion

This study presented a development of a multilayer Artificial Neural Network and a parametric equation based on MLR models aimed at predicting and increasing the labour productivity rate of the flat slab formwork in Algerian construction projects. A survey of 150 questionnaires was distributed to define the most influential factors. The total number of data collected on the 11 influencing factors defined in this study was 100, which were then randomly divided into two main subsets. An Artificial Neural Network model was first developed using 70% of the data set, to train the network to update weights and biases, and the remaining 30% was used to test

the network for better generalisation on the new data. The model architecture used was a three-layer feed-forward ANN with a backpropagation algorithm and Bayesian regularisation as a learning function. A parametric equation was developed in the second part of this study, also using the same 70% of the dataset to establish a mathematical equation based on the multiple linear regression method. The remaining 30% of the dataset was used to validate the equation against the new data.
The results of this study clearly show that the ANN model developed is more efficient and gives more accurate prediction results than the parametric equation. However, it can be noticed that both developed models have a good relationship between the predicted results and the actual targets. Moreover, a high performance was recorded, indicating that both models behave well with the unseen data and produce results reasonably close to the actual targets. The results of this research study allow concluding that the ANN model and the parametric equation developed can be reliably used to predict the measurement of the productivity rate with the incorporation of influencing factors deemed to affect the labour productivity of the flat slab formwork task.

References

[1] Gerek, I. H., Erdis, E., Mistikoglu, G. & Usmen, M. A. (2014). Evaluation of plastering crew performance in building projects using data envelopment analysis. *Technological and Economic Development of Economy*, *22*(6), 926–940.

[2] Thomas, H. R., Maloney, W. F., Horner, R. M. W., Smith, G. R., Handa, V. K. & Sanders, S. R. (1990). Modeling construction labor productivity. *Journal of Construction Engineering and Management*, *116*(4), 705–726.

[3] Yi, W. & Chan, A. P. C. (2014). Critical review of labor productivity research in construction journals. *Journal of Management in Engineering*, *30*(2), 214–225.

[4] Boughaba, A. & Bouabaz, M. (2020). Identification and risk management related to construction projects. *Advances in Computational Design*, *5*(4), 445–465.

[5] Boulkenafet, N., Boudjellal, K. & Bouabaz, M. (2023). Optimization of productivity in the rehabilitation of building linked to BIM. *Advances in Computational Design*, *8*(2), 179–190.

[6] Olomolaiye, P. O., Jayawardane, A. K. W. & Harris, F. C. (1998). *Construction Productivity Management*. England: Addison Wesley Longman.

[7] Florez-Perez, L. Song, Z. & Cortissoz, J. C. (2022). Predicting construction productivity with machine learning approaches. Proceedings of the International Symposium on Automation and Robotics in Construction. 2022-July, (107–114).

[8] Jarkas, A. M. & Bitar, C. G. (2012). Factors affecting construction labor productivity in Kuwait. *Journal of Construction Engineering and Management*. *138*(7), 811–820.

[9] Karim, N. A., Hassan, S., Yunus, J. & Hashim, M. (2013). Factors Influence Labour Productivity and the Impacts on Construction Industry. *Caspian Journal of Applied Sciences Research*, *2*(August), 349–354.

[10] El-Gohary, K. M. & Aziz, R. F. (2013). Factors influencing construction labor productivity in Egypt. *Journal of Management in Engineering*, *30*(1), 1–9.

[11] Hickson, B. G. & Ellis, L. A. (2014). Factors affecting Construction Labour Productivity in Trinidad and Tobago. *The Journal of the Association of Professional Engineers of Trinidad and Tobago*, *42*(1), 4–11.

[12] Alaghbari, W., Al-Sakkaf, A. A. & Sultan. B., (2019). Factors affecting construction labour productivity in Yemen. *International Journal of Construction Management*, *19*(1), 79–91.

[13] Shoar, S. & Banaitis, A. (2018). Application of fuzzy fault tree analysis to identify factors influencing construction labor productivity: A high-rise building case study. *Journal of Civil*

Engineering and Management, *25*(1), 41–52.
[14] Adebowale, O. & Smallwood, J. (2020). Contractors' perceptions of factors affecting construction labour productivity in South Africa. *Journal of Contemporary Managemen*, *17*(2), 326–346.
[15] Nasirzadeh, F., Rostamnezhad, M., Carmichael, D. G., Khosravi, A. & Aisbett, B. (2022). Labour productivity in Australian building construction projects: a roadmap for improvement. *International Journal of Construction Management*, *22*(11), 2079–2088.
[16] Roberts, D., Park, K., Ankrah, N. & Kim, K. P. (2023). The effect on cost when utilising modular construction techniques-The impact of weather on labour productivity. *International Journal of Sustainable Building Technology and Urban Development*, *14*(1), 77–95.
[17] Bouabaz, M. & Hamami, M. (2008). A cost estimation model for repair bridges based on artificial neural network. *American Journal of Applied Sciences*, *5*(4), 334–339.
[18] Otmani, A., Bouabaz, M. & Al-Hajj, A. (2020). Predicting Maintenance and Rehabilitation Cost for Buildings Based on Artificial Neural Network and Fuzzy Logic. *International Journal of Computational Intelligence and Applications*, *19*(1), 1–13.
[19] Peško, I. *et al.* (2017). Estimation of costs and durations of construction of urban roads using ANN and SVM. *Complexity*. 2450370.
[20] Umit Dikmen, S. & Sonmez, M. (2011). An artificial neural networks model for the estimation of formwork labour. *Journal of Civil Engineering and Management*, *17*(3), 340–347.
[21] Al-Zwainy, F. M. S., Rasheed, H. A. & Ibraheem, H. F. (2012). Development of the construction productivity estimation model using artificial neural network for finishing works for floors with marble. *ARPN Journal of Engineering and Applied Sciences*, *7*(6), 714–722.
[22] Gerek, I. H., Erdis, E., Mistikoglu, G. & Usmen, M. (2015). Modelling masonry crew productivity using two artificial neural network techniques. *Journal of Civil Engineering and Management*, *21*(2), 231–238.
[23] Aswed, G. K. (2016). Productivity Estimation Model for Bracklayer in Construction Projects Using Neural Network. *Al-Qadisiyah Journal For Engineering Sciences*, *9*(2), 183–199.
[24] Golnaraghi, S., Zangenehmadar, Z., Moselhi, O. & Alkass, S. (2019). Application of Artificial Neural Network (s) in Predicting Formwork Labour Productivity. *Advances in Civil Engineering*, *2019*, 1–11.
[25] Mlybari, E. A. (2020). Application of soft computing techniques to predict construction labour productivity in Saudi Arabia. *International Journal of GEOMATE*, *19*(71), 203–210.
[26] Bokor, O., Florez-Perez, L., Pesce, G. & Gerami Seresht, N. (2021). Using Artificial Neural Networks to Model Bricklaying Productivity. Proceedings of the 2021 European Conference on Computing in Construction, 2021, July (52–58).
[27] Juszczyk, M. (2020). Analysis of labour efficiency supported by the ensembles of neural networks on the example of steel reinforcement works. *Archives of Civil Engineering*, *66*(1), 97–111.
[28] Sarmento, M., Sc, M., Luiz, M., Ferreira, R. & Sc, D. (2021). Sizing an Artificial Neural Network for Modelling Piping Assembly Labor Productivity Under Different Conditions. *International Journal of Engineering Research and Applications*, *11*(2), 16–22.
[29] Goodarzizad, PP., Mohammadi Golafshani, E. & Arashpour, M. (2021). Predicting the construction labour productivity using artificial neural network and grasshopper optimisation algorithm. *International Journal of Construction Management*, 1–28.
[30] Lawaju, N., Parajuli, N. & Shrestha, S. K. (2021). Analysis of Labor Productivity of Brick Masonry Work in Building Construction in Kathmandu Valley. *Journal of Advanced College of Engineering and Management*, *6*, 159–175.
[31] Phaobunjong, K. (2002). *Parametric Cost Estimating Model for Conceptual Cost Estimating of Building Construction Projects*. University of Texas at Austin.
[32] Al-Zwainy, F., Abed - Alla Eiada, A. & Abed - Almajed Khaleel, T. (2016). Application

Intelligent Predicting Technologies in Construction Productivity. *American Journal of Engineering and Technology Management*, *1*(3), 39–48.

[33] El-Kholy, A. M. (2010). Productivity performance estimation in Egyptian construction projects based on regression analysis. *Mansoura Engineering Journal (MEJ)*, *35*(01), 44–54.

[34] Narayanan, K. M. A. & Aswathi, M. P. (2018). Labour Productivity Model for Structural Elements By Varying Buildability Factors using Multiple Regression Analysis. *International Journal of Advance Research, Ideas and Innovations in Technology*, *4*(2), 139–146.

[35] Khanh, H. D., Kim, S. Y., Van Khoa, N. & Tu, N. T. (2021). The relationship between workers' experience and productivity: a case study of brick masonry construction. *International Journal of Construction Management*, 1–10.

[36] Paikun, P., Fatimah, C., Nugroho, N. S. & Kusmana, D. (2021). Labor Productivity Rating Model for Light Brick Wall Installation in Residential Projects. *ASTONJADRO*, *10*(2), 260–270.

[37] Matejević-Nikolić, B. & Živković, L. (2022). Comparative Representation of Two Models for Predicting the Productivity of Column and Wall Concreting Process. *Buildings*, *12*(11), 1809.

[38] Al-Zwainy, F. M. S., Abdulmajeed, M. H. & Aljumaily, H. S. M. (2013). Using Multivariable Linear Regression Technique for Modeling Productivity Construction in Iraq. *Open Journal of Civil Engineering*, *03*(03), 127–135.

[39] Enshassi, A., Mohamed, S., Mustafa, Z. A. & Mayer, P. E. (2007). Factors affecting labour productivity in building projects in the Gaza strip. *Journal of Civil Engineering and Management*. *13*(4), 245–254.

[40] Fagbenle Olabosipo, I., Ogunde Ayodeji, O. & Owolabi James, D. (2011). Factors Affecting the Performance of Labour in Nigerian Construction Sites. *Mediterranean Journal of Social Sciences*, *2*(2), 251–257.

[41] El-Gohary, K. M., Aziz, R. F. & Abdel-Khalek, H. A. (2017). Engineering Approach Using ANN to Improve and Predict Construction Labor Productivity under Different Influences. *Journal of Construction Engineering and Management*, *143*(8), 1–10.

[42] Hafez, S. M. (2014). Critical Factors Affecting Construction Labor Productivity in Egypt. *American Journal of Civil Engineering*, *2*(2), 35.

[43] Kaming, P. F., Olomolaiye, P. O., Holt, G. D. & Harris, F. C. (1997). Factors influencing craftsmen's productivity in Indonesia. *International Journal of Project Management*, *15*(1), 21–30.

[44] Hogg, R. V. & Tanis, E. a. (2009). *Instructor ' s Solutions Manual Probability and Statistical Inference Eighth Edition*. Upper Saddle River, NJ(USA): Prentice Hall.

[45] Sincich, T., Stephan, D. & Levine, D. M. (2002). *Practical statistics by example using Microsoft Excel and Minitab*. Prentice Hall Professional Technical Reference.

[46] Gopal, T. G. S. R. & Murali, K. (2015). A Critical Review on Factors Influencing Labour Productivity in Construction. *Journal of Mechanical and Civil Engineering (IOSR-JMCE)*, *12*(5), 47–51.

[47] Heravi, G. & Eslamdoost, E. (2015). Applying Artificial Neural Networks for Measuring and Predicting Construction-Labor Productivity. *American Society of Civil Engineers*, *141*(10), 04015032.

[48] Duch, W. & Jankowski, N. (1999). Survey of neural transfer functions," *Neural Computing Surveys*, *2*, 163–212.

[49] Nassar, Y. S. & Khaleel, T. A. (2019). Building Model to Predict Labour Productivity Using Multiple Linear Regression Technique for " Formwork Concrete Columns ". *Kufa Journal of Engineering*, *10*(2), 12–26.

DOI: 10.2478/sspjce-2023-0006

Use of Electrical Resistivity Tomography for Joint Geophysical and Geotechnical Landslide Characterization: A Case Study

Hassiba Kherrouba [1], Mohammed Lamara [2], Riad Benzaid [3*]

[1,3] Geological Engineering Research Laboratory (LGG), Jijel University, Algeria
[2]Laboratory of Civil Engineering and Environment, Jijel University, Algeria
*e-mail: r_benzaid@univ-jijel.dz / benzaid.riad@gmail.com

Abstract

Slope movement processes include complex soil and rock failure mechanisms. Their study benefits from a multidisciplinary approach based on a wide range of information including geological and geomorphological mapping, and geotechnical and geophysical investigations. This research paper focuses on the characterization of the Tamentout landslide that occurs in the southeast of Jijel province. The study area belongs to the Tellian domain in which the geological outcrops are dominated by Senonian formations, composed of marl deposits overlain by Numidian flysch of Aquitano-Burdigalian age, with a sloping topography ranging from 20° to 30°. The geophysical approach consists of processing the available geophysical data of resistivity, obtained by the Electrical Resistivity Tomography (ERT). This study aims to characterize the internal structure, and the changes in water saturation within the unstable mass and locate the depth of slip surface associated with this landslide. Through this work, we combined geological and geotechnical investigations with electrical resistivity tomography (ERT). This combination gave a more detailed image of the substrate geology and structure of the landslide zone. The 2D resistivity results show that the basement consists of two main formations. The first one is a highly conductive formation with a resistivity range between 2 and 25 Ωm, a depth of 0-8 m, and is interpreted as a saturated marl-clay overlaying. The second, a hard and compact formation with a resistivity range between 50 and 200 Ωm and a depth range of 8 to 40 m, was interpreted as a substrate of tellian marls. The presence of boulders of Numidian sandstone within the two formations is materialized by a very high resistivity value ranging from 500 to 1000 Ωm. The slip surface was located on the layer with low resistivity (2-25 Ωm). The precise determination of the depth of the shear zone is of vital use in implementing mitigation measures and carrying out the stabilization work of this unstable zone. Through this work, we will highlight the advantage of the combination of available results of the geological, geotechnical investigations and electrical resistivity tomography (ERT) carried out in the study area.

Keywords: Tamentout, landslide, electrical resistivity tomography (ERT), resistivity, slip surface.

1 Introduction

Landslides are complex geological phenomena that can have disastrous consequences [1, 2]. The study of this damaging phenomenon involves the application of a combined approach based on a wide range of data including geological and topographical investigations combined with geotechnical and geophysical measurements [3, 4]. In recent years, the application of

geophysical methods to landslide studies has evolved considerably [5, 6]. Due to the rugged terrain and abrupt topographic changes in the landslide areas, it was difficult to conduct such investigations. Recently, some geophysical imaging techniques based on tomography are commonly used in shallow surveys [5, 7, 8], the purpose of geophysical prospecting applied to ground movements is mainly to identify the lateral limits of the mass in motion, the slip surface in depth, as well as the imaging of the internal structure of the moving body [6, 9].
Landslides are among the most, widespread and damaging natural hazards in northern Algeria. They represent a major threat to the population, buildings, and various infrastructures in most mountainous regions [1, 10, 11]. These phenomena are frequent in the Jijel region, due to the high relief and the lithological complexity of its soils, as well as climatic conditions, which it is considered among the rainiest areas in Algeria. Among landslides in the Jijel region, there are those of Tamentout.
This study aims to the contribution of Electrical Resistivity Tomography (ERT) for the Tamentout landslide (located between the PK 42 + 260 and 43 + 050) characterization, and how geophysical information can improve our knowledge about the geometry of this sliding zone portion. This work highlights the advantage of using geological, geotechnical investigations, and those acquired from the use of electrical resistivity tomography at the study area.

2 Geographic Location and Geological Context

Djimla is a mountainous region covering an area of 65.28 km² located 45 km southeast of Jijel province (northeast Algeria). With its elongated shape, it is characterized by a steep topography, and altitudes vary from 209 m to 1548 m (Figure 1). Tamentout region is a mountain group belonging to the reliefs of Djimla. The geological, topographical, and climatological features of the region are particularly favorable for ground movements.

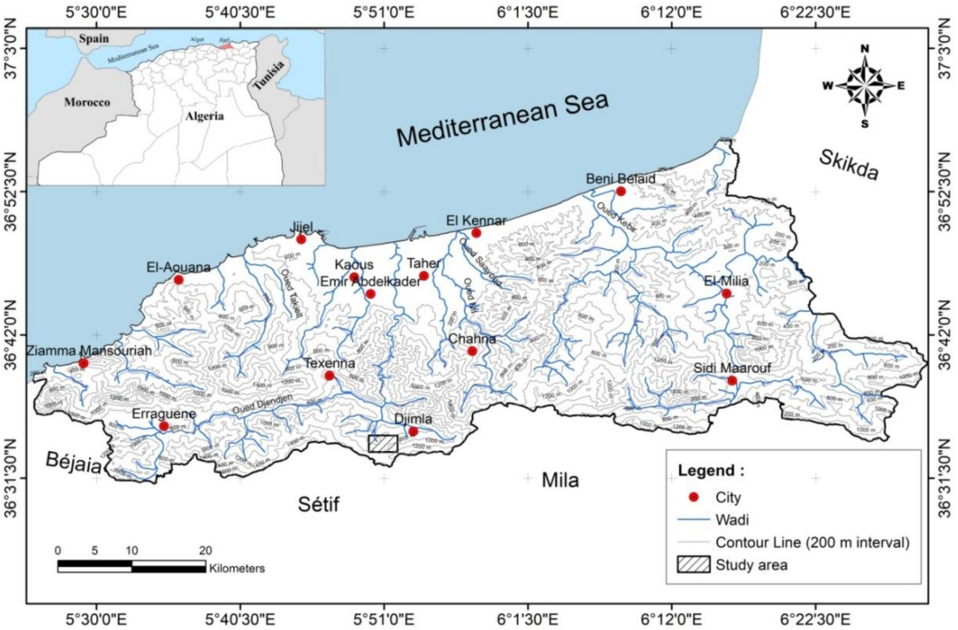

Figure 1: Geographic location map of the Tamentout landslide (Northeast Algeria)

The landslide targeted by our study is located at 5.5 km southwest of Djimla village, and 2 km northwest of the Tamentout col. Its geographical coordinates are: 5 ° 49 '26 "East and 36 ° 33' 51" North (Figure 1).
The study region had long attracted the attention of geologists. Indeed, this mountainous region is characterized by an important geological contrast (Figure 2), which became a subject of research conducted by several geologists. The Djimla region, which includes the study area, is located in the contact zone between internal and outer domain formations “crystallophyllian basement, tellian formations” [12, 13, 14].

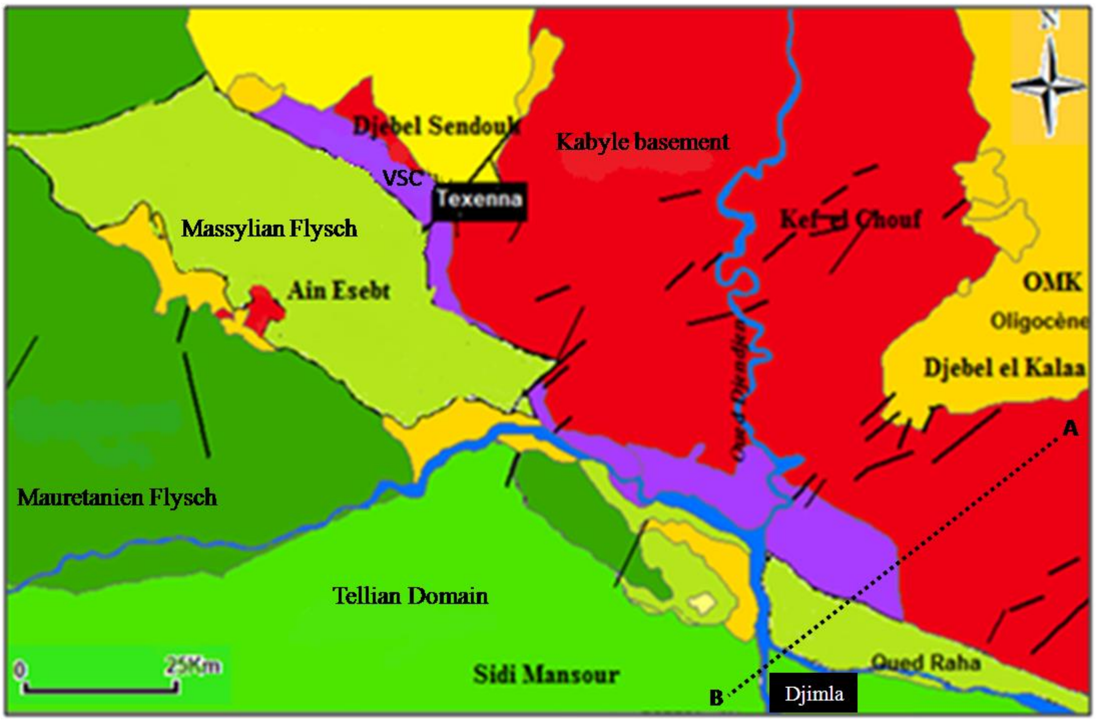

Figure 2: Geological map showing the alpine units of Petite Kabylie-Jijel region, slightly modified [13]. AB: Cross-section

The geological formations that are outcropping in the study region (Figure 3 and 4) are mainly characterized from top to bottom as follows:
- The Numidian flysch occupies the highest structural position in the Alpine structure. It is composed of three terms that are in stratigraphic continuity from top to bottom: (1) A higher term with selexites, the upper part of which reaches basal Burdigalian [12, 13]; (2) A median term formed by Numidian sandstones in thick benches, with heterometric grains and a quartz dragees, dated Aquitanian to lower Burdigalian [13, 14]; (3) A basic term consisting sub-Numidian clays, sometimes varicolored, green, red or purplish to Tubotomaculum. The Numidian formations lie in discordance on tellian formations (Figure 3) [12, 13].

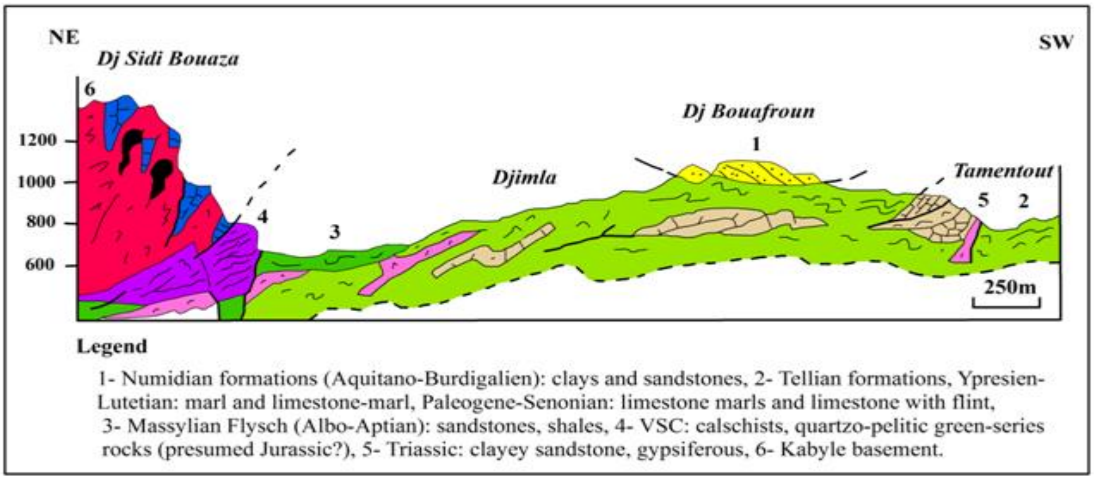

Figure 3: Geological cross-section NE-SW shows the structural feature of the Tamentout region where the landslide occurred [6]

The Tellian formations are represented in Tamentout by a group (about 100 m) of the Campanian- Maestrichtian (term1), a term from the Paleocene (term2), (term3) admitting to their summit of "Suessonian" facies limestones with flint (term4). The terms 2, 3, and 4 are between 250 and 300 m thick. On the term (4) that is attached to the Ypresian finally arrive about 80 to 100 m of black marl is observed (term 5) past lime, locally shaped yellow balls are observed and the Lutetian terminates this lithological series [13, 14].

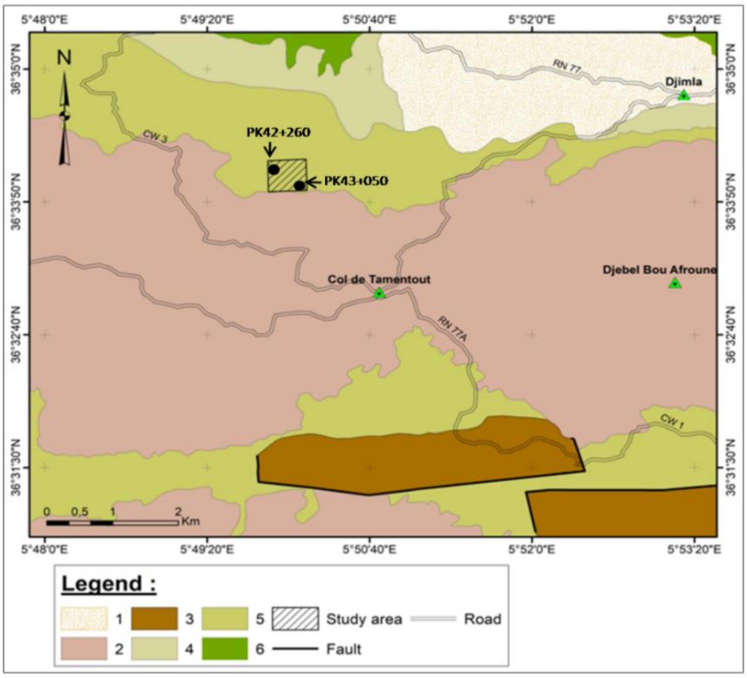

Figure 4: Geological map of the study area (Extracted from "Tamesguida" geological map at the scale 1/50.000, slightly modified [28]. 1-Quaternary: slope scree consisting, 2-Numidian formations (Aquitano-Burdigalien): clays and sandstones, 3-4-5 and 6-Tellian formations (Maastrichtian-Danian to Eocene): schistose marls and clays, schistose marls, marls, and limestone with flint

3 Causes and Landslide-Related Disorders

This slope extends in the direction of N-NE. Disorders observed in the study area are induced by the combination of several geological, hydrogeological, and geotechnical dynamics. Among the degradations observed on-site, we can cite:

- The presence of instability indices materialized by slumping bulges and cracks, also the lining trees and electrical poles down the slope.
- Very significant damage to the pavement with fissures and ground breaks, especially at the level of tectonic weakness zones.

Landslides do not usually occur as a result of a single cause. They are often observed after the occurrence of several harmful factors that initiate instabilities. This combination is at the origin of the triggering ground movement such as:

- Slope: the stability conditions of terrain being directly linked to its slope; in the study site we observed moderate to steep slopes.
- Lithology: marl-clay nature of the grounds and their permeability rate and sensitivity in the presence of water.
- Hydroclimatological and hydrological characteristics of the study region: The region of Tamentout is characterized by a mild and rainy Mediterranean climate in winter with hot and dry summer. It receives a height of rainfall ranging from 1000 to 1200 mm/year; during the cold season, hail and snow are observed mainly on reliefs exceeding 800 m altitude. The study area is well watered; due to the frequency and intensity of these precipitations, and the occasional occurrence of hail and snow on the Djimla Mountains, which is feedings potential landslide areas [6, 10, 15].
- Geologic structures: Main axes of unstable zones (presence of regional faults).
- Anthropogenic factors: Following earthworks (overload at the head of the already unstable slope, discharge in the foot removing a stabilizing stop, etc.).
- Earthquakes: According to the Algerian seismic regulation, the region of Jijel is characterized by medium seismicity (Zone IIa) with acceleration in order of 0.25 g [16].

4 Methodology

4.1 Geotechnical Investigation

In order to obtain more complete interpretation and to analyze the correlation between the lithology of the landslides and determined the distribution of electrical resistivity on the profiles; results of geotechnical tests carried out in 2016 were used [17]. The description of soil lithology is presented in Table 1 and Figure 5. These boreholes were accompanied by piezometric measurements.

Table 1: Lithological description of borehole's and piezometric measurements

Borehole N°	Depth in meter	Lithology	Water level in meter
SC1	0.00 – 08.30	marl-clay	
	08.30– 20.50	Sand-gravel clay with sandstone blocks	

PK 42+200			16.87
	20.50– 40.00	marl compact	
	0.00 – 04.20	marl-clay	
SC2 PK 42+560	04.20 – 30.00	Marl compact	18.77
	0.00 – 7.50	Sand-gravel clay with sandstone blocks	
SC3 PK 43+020	6.00 – 30.00	Marl compact	02.80

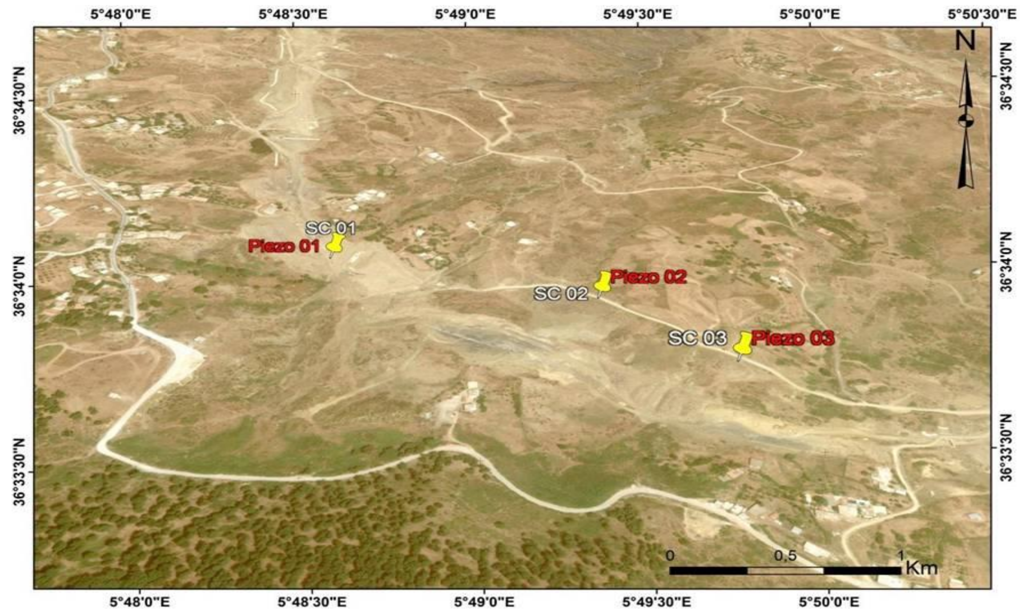

Figure 5: Location of boreholes and piezometric surveys carried out in the study area

4.2 Electrical Resistivity Tomography for Landslide Investigation

Electrical Resistivity Tomography or Electrical Resistivity Imaging is a geophysical technique derived from conventional resistivity methods used to identify subsurface soil [18, 19, 20, 21]. Electrical tomography provides high-resolution 2D, 3D, and 4D images of the basement [6, 22], [23, 24].

A set of electrical resistivity tomography profiles was carried out in the study area by the company GEOEXPLO in 2018 [25], four (4) lines of 2D resistivity surveys called RL1 to RL4 because are considered representative of the field in question was chosen for this study. These profiles were produced using a Saris / Scintrex instrument with a Wenner-Schlumberger measuring device composed of 30 steel electrodes with an electrode spacing of about 5 (m) (RL1-RL2) and 2.5 meters (RL3 and RL4) [25]. The lines RL1-RL3 were positioned northwest-southeast, while the lines RL3-RL4 were oriented northeast-southwest. The total length of profiles was varying between 130 m and 450 m and reaching around 25 m in depth (Figure 6).

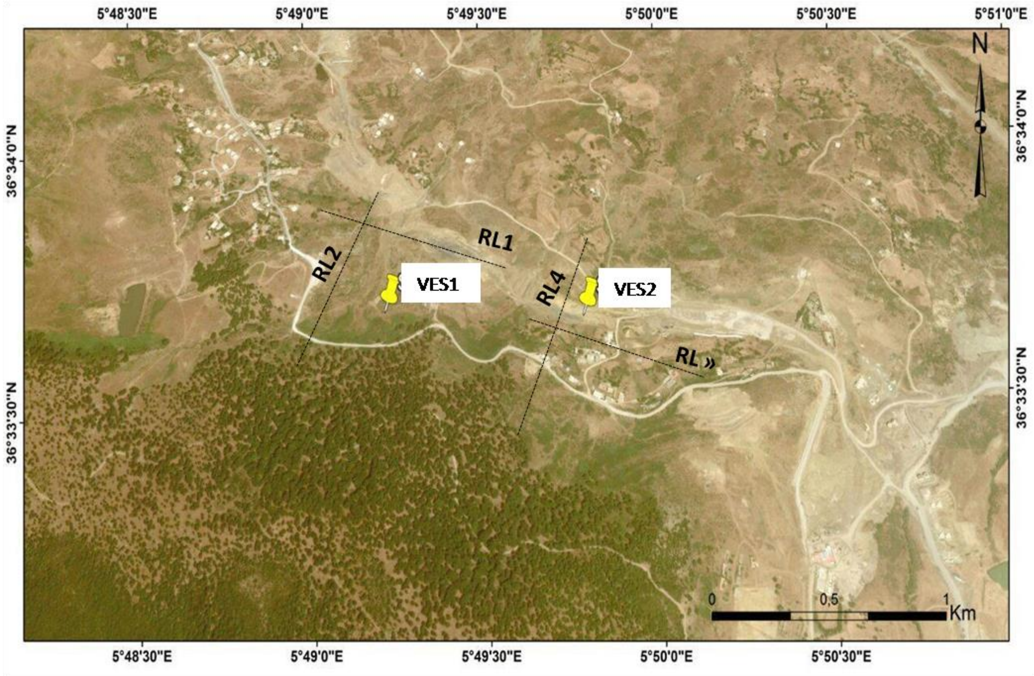

Figure 6: Locations of resistivity lines (RL) and vertical electrical soundings (VES) at the study area

5 Results and Discussion

5.1 Geotechnical Characteristics

Based on the results obtained from boreholes (Table 1 and Figure 7) show that the soil of the study area is mainly composed of a first layer represented by a friable marl-clay and/or a second layer marked by a clay with blocks of sandstone. The ensemble overlaying bedrock composed by tellian compact marls.

Table 2 lists the values of basic parameters of soils. For the type of soil encountered, the values of dry and wet densities range between 1.89-2.20 g/cm^3 and 2.18-2.42 g/cm^3, which gives dense-state formations, the water content (W) range between 6.85% and 15.20% which is characteristic of slightly wet to moist soils. The piezometric readings carried out indicated the presence of water at varying levels (Table 1). Understanding the hydrological functioning of an unstable mass is a major objective in the study of ground movements. The infiltration and circulation of water within an unstable ground can generate a progressive deterioration of the materials which will decrease the mechanical characteristics and increase the risk of triggering the phenomena of landslides.

The results of Atterberg limits tests are grouped in Table 3.

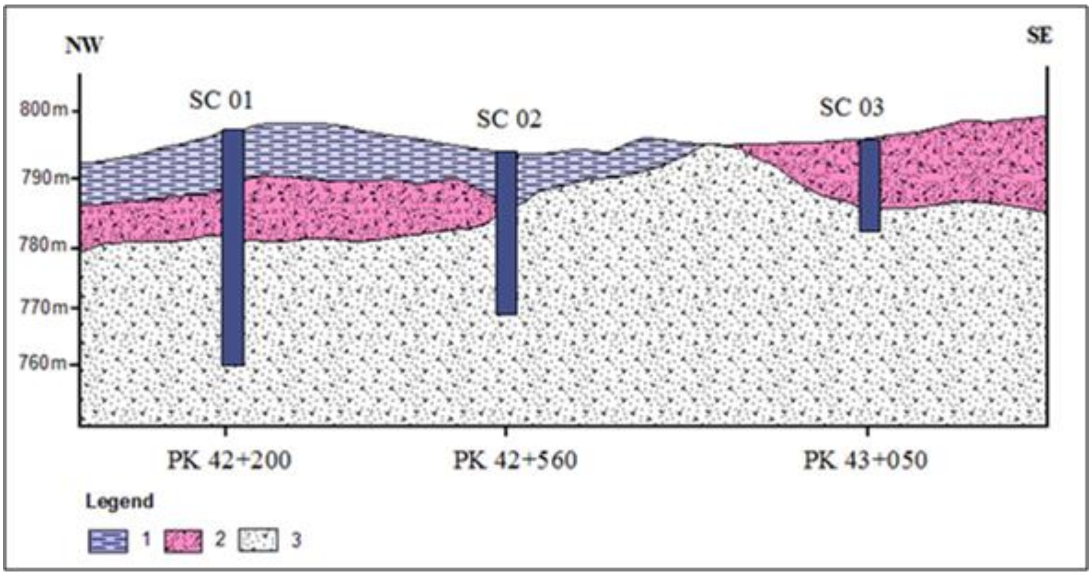

Figure 7: Lithological cross-section of the study area.1- Marl-clay, 2- gravel-clay with blocks sandstone, 3- compact marls "bedrock"

Table 2: Values on the physical parameters of soils

Borehole N°	**Depth in meter**	**Water content in %**	**Dry bulk density ρ_d in g/cm^3**	**Wet bulk density ρ_h in g/cm^3**
SC PK 42+200	35.1-35.38	6.85	2.18	2.33
	35.6-36	10.78	2.07	2.30
	36.44-36.75	8.86	2.12	2.30
	39.5-39.77	15.20	1.89	2.18
SC PK 42+560	1.30-1.57	12.20	2.16	2.42
	6.30-6.50	11.63	2.20	2.38

Table 3: Results of Atterberg limits

Borehole N°	**Depth in meter**	**Liquid Limit (WL) in %**	**Plastic Limit (WP) in %**	**Plasticity Index (PI)**	**Consistency Index (CI)**
SC PK 42+200	35.1-35.38	36	19	17	1.71
	35.6-36	32	18	14	1.52
	39.5-39.77	27	13	14	0.80
SC PK 42+560	1.30-1.57	33.81	22.06	11.75	1.84
	6.30-6.50	34.18	21.29	12.89	1.75

The liquid limits (WL) range between 27 and 36 percent, while the plastic limits (WP) range between 13 and 22 percent (Table 3). The plasticity index (PI) ranged from 11 to 17 and the

consistency index (CI) ranged from 0.80 to 1.84 percent. These results indicate that we are dealing with plastic low clay (CL) and very hard consistency.
Geotechnical tests revealed dense, slightly moist, moderately plastic and consistent soils. Marls and clays are the impermeable rocks; In other part, we note that the value of water content is very variable with depth which indicates the presence of pockets accumulation of underground water formed by gravelly-clays with boulders of sandstones which condition the setting in motion of the unstable mass. The landslide occurs in marl-clay when their water content increases significantly. Among the predominant factors for the occurrence of landslides are: 1) The low cohesion of soil, 2) The high degree of reworking, 3) Increased water content and pore pressures.

5.2 Geophysical Results

The pseudo-sections are represented at the same resistivity scale (Figure 8). The interpretation of the results was done based on resistivity ranges.
All pseudo-sections that we have selected as a part of our study show us the following:

- A change in the resistivity value indicates the change in facies; This is practically visible in all pseudo-sections.
- The appearance of saturated zones shows that the ground is very permeable in some places and shows that these areas present a preferential water circulation path.
- A line that distinguishes the boundary between two different resistivity environments. From a geological point of view, this boundary may also be a boundary between the Bed-Rock and the formations that have been displaced. The distribution of the resistivity on the different lines is as follows:

The pseudo-section ERT1 of the first profile RL1 (Figure 8a), shows the distribution of electrical resistivity at a depth of 25 meters. It shows good resistivity contrast, allowing better identification of the underground horizons and their state of stability. In this pseudo-section, the conductive formations are dominant with a high concentration in the center of the profile. These formations are characterized by a resistivity ranging between 5 and 30 Ωm, which can be attributed to saturated marl-clay, while the moderately resistant formations are scattered and located more at limits of the profile, whose resistivity values range between 50 and 100 Ωm. These resistant formations can be attributed to compact marls. The moderately resistant range located 750 m to the NW could correspond to a boulder of sandstone according to the borehole (SC01) carried out near the electrical panel.
In the pseudo-section ERT2 of the profile RL2 (Figure 8b), two lithological horizons are distinguished. A superficial horizon located at SW of the profile, and which shows a more resistant trend than the previous profile. The resistivity falls in a range between 75 Ωm and 500Ωm. This layer superimposes a second less resistant layer with a low resistivity (5-25 Ωm) on the side NE. In the center of RL2, a boulder of sandstone seems to come off and move from the SW towards NE, which can represent a slip surface on which the resistant formation outcrop in the surface can be slid.
Pseudo-section ERT3 of the profile RL3 (Figure 8c) corresponds to a conductive horizon with electrical resistivity ranging between 5 and 30 Ωm, which can be attributed to saturate marl-clay. This horizon is interspersed with moderately resistant formations, which electrical resistivity range between 50 and 250 Ωm and corresponds to compact marl. The configuration

of this resistant formation has a sliding potential on the conductive formation given the slope and shape of these two formations.

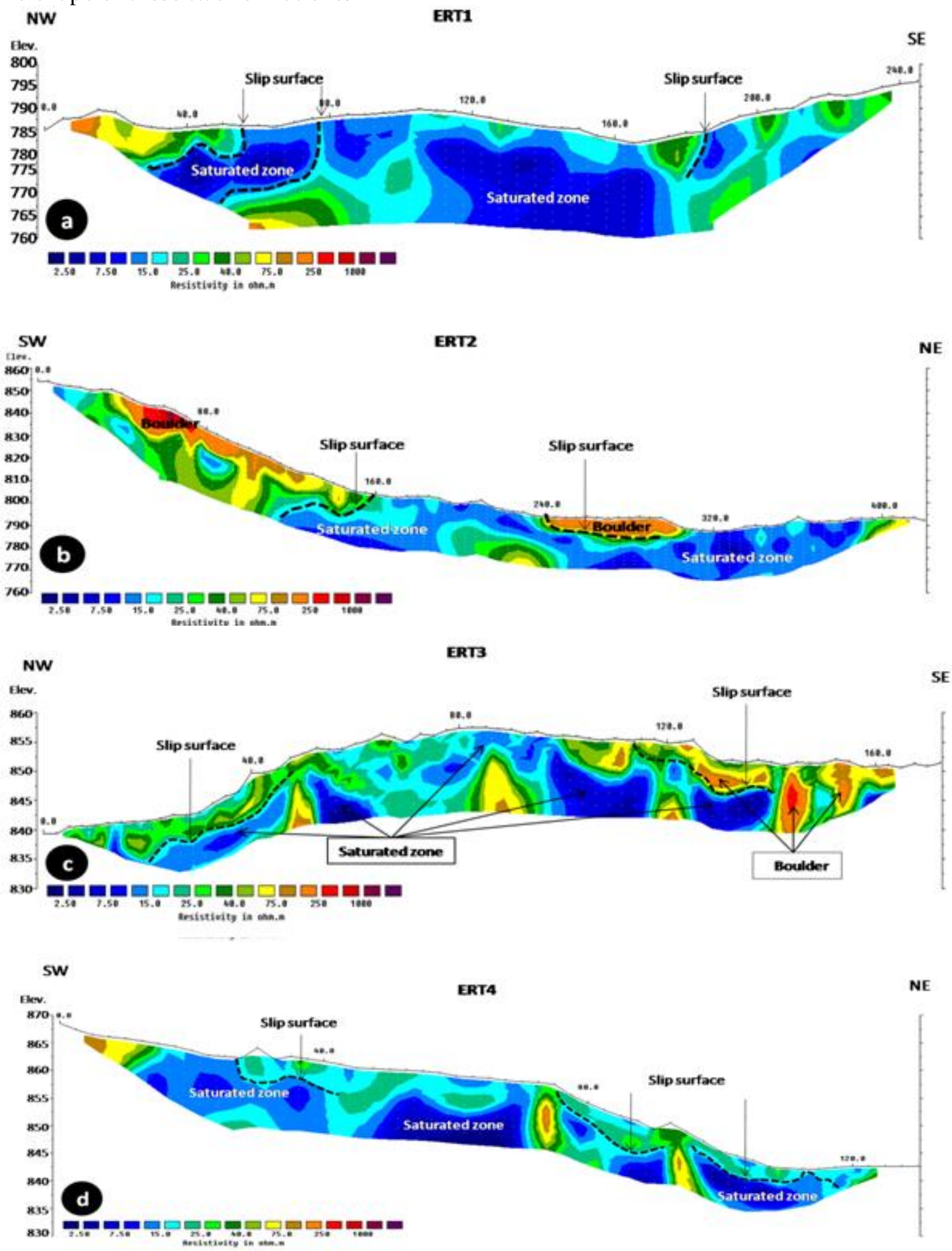

Figure 8: Pseudo-sections of RL1-RL4 lines

The pseudo-section ERT4 of the profile RL4 (Figure 8d), illustrates a large conductive horizon, its electrical resistivity ranging between 5 and 30 Ωm, which corresponds to saturate marl-clay. The resistant formation located in the SW part with electrical resistivity moderately oscillate between 50 to 100 Ωm can be attributed to compact marls, while in the NE part of the profile where the slope is presenting, a resistant formation can be attributed to compact marl-clay is highlighted with two sub-vertical intercalations separating the conductive formation, present a sliding potential of the conductive layer.

Electrical imaging made it possible to reach certain conclusions on the geometric configuration of the terrains as well as their resistivity values. In general, the sections show alternation of conductive ground interspersed with low resistant to resistant terrains with irregular shapes. Electrical resistivity values obtained were calibrated with logs of core drillings. The first resistivity range presents a conductive formation whose values of resistivity range between 5 to 20 Ωm, which can be attributed to saturate marl-clay. The second resistivity range is characterized by a resistivity ranging between 20 and 1000 Ωm. The weak resistance formations (20 to 100 Ωm) are attributed to compact marls, while the resistant formations (100 to 1000 Ωm) are attributed to boulder of Numidian sandstone. Fine soils such as clays and marls are very sensitive in the presence of water, and they are characterized by the possibility of flow due to the increase in water content. The consistency of soil varies on the water content when it increases, the soil passes successively from the solid to the plastic state, and then to the liquid state. The layer with resistivity values varying between 2-25 Ωm, is represented by clays. Layers in low values of resistivity, approximately 2 Ωm are related to higher water content. Based on data from core drill holes located near the tomography profiles, subnumidian clays are present; their thickness can reach 20 m at the level of SC1 and 7.5 m at the level of SC3. This formation covers compact tellian marl.

In particular, the active landslide material is characterized by electrical resistivity values ranging between 5 and 25 Ωm, which can be attributed to saturate zone. The slip surface is located in a depth range between 4meters (ERT3 and ERT4) and 7 m (ERT1 and ERT2). Despite varied resistivity contrasts, the ERT allowed us to define the geometry of the landslide object of our study, to identify the sub-vertical discontinuities, often corresponding to the failure surface, and to locate the zones characterized by a higher water content (saturated zones) (Figure 8).

The results obtained are correlated with the results of the research work of Bellanova et al. [26], Mezerreg et al. [20], and Pasierb [24]. We notice that the resistivity values obtained are similar, namely: the saturated zones, the values were between 3 and 20 Ωm and gradually increased in the unsaturated zones to reach values between20 and 100 Ωm. For sandstone blocks (boulder), resistivity values reach 1000 Ωm.

5.2.1 Identification of Shear (Slip) Surfaces

Generally, landslides that affect homogeneous formations can lead to variations in resistivity with mass movement in clayey layers. This can be explained by the presence of water, which is an important factor in the reduction of the mechanical characteristics of the soil, combined with the presence of a large percentage of the clay fraction [27]. For a first interpretation, the results obtained can be divided into two resistivity ranges: the first varies from 2.0 to 25 Ωm, the second range above 25 Ωm. Several authors associate this low resistivity (less than 25 Ωm) with the presence of a slip surface. In the electrical imaging profiles, a resistant formation is

shown with a resistivity varying from 50 to 200 Ωm near this formation and in places, a conductive formation is observed with a low resistivity between 2.0 and 25 Ωm, mainly due to the presence of water (saturated zone). This conductive layer with its curvilinear shape can represent the slip surface on which resistant formations can slide.
The preliminary results of this geophysical and geotechnical prospecting campaign in the study area have shown that: Electrical tomography appears to be a viable geophysical method to locate layers of low resistivity susceptible to trigger landslides. Tomography integrated with geological information has proven to be a powerful tool for the investigation of landslides.

6 Conclusion

This study is to characterize the internal structure, changes in water saturation, and the location of the slip surface of the Tamentout landslide. Analysis of the electrical tomography imaging allowed us to characterize the geometric configuration of the grounds as well as their resistivity values. The combination of slope with the morphology of conductive and resistant formations shows that the slip surface may be located at the surface of the layer with a resistivity ranging between 5 and 20 Ωm, corresponding to saturate formations.
The pseudo-section shows that the main cause of the instability is due to the presence of a saturated zone; hence drainage systems and evacuation of groundwater can be recommended as a remedy technique to stabilize this landslide. Finally, to follow the movement and its evolution, it is recommended to regularly conduct geophysical prospecting of the unstable sites. Electrical tomography should be combined with other geotechnical and geophysical methods to better identify the depth of the slip surface.
The resistivity of the 2D inversion model has been well correlated with the Tamesguida geological map. Thus, the 2D resistivity survey provided valuable information about the subsoil characteristics, in particular on slope instability.

Acknowledgments

The authors would like to thank the anonymous reviewers for their constructive suggestions. They are grateful to the Algerian National Highway Authority (ANA, Jijel) for providing the necessary data for this study.

References

[1] Achour, Y., Boumezbeur, A., Hadji, R., Chouabbi, A., Cavaleiro, V., & Bendaoud, E. (2017). Landslide susceptibility mapping using analytic hierarchy process and information value methods along a highway road section in Constantine, Algeria. *Arab J Geosci, 10*(194). https://doi.org/10.1007/s12517-017-2980-6.

[2] Bounemeur, N., Benzaid, R., Kherrouba, H. et al. (2022). Landslides in Mila town (northeast Algeria): causes and consequences. *Arab J Geosci, 15*(753). https://doi.org/10.1007/s12517-022-09959-7.

[3] Lapenna, V., Lorenzo, P., Perrone, A., Piscitelli, S., Rizzo, E., & Sdao, F. (2005). 2D electrical resistivity imaging of some complex landslides in Lucanian Apennine chain, southern Italy. *Geophysics, 70*, B11–B18.

[4] Perrone, A., Lappena, V., & Piscitelli, S. (2014). Electrical resistivity technique for landslide investigation: A review. *Earth Science Reviews, 135*, pp. 65-82.

[5] Husainy, S. N., Bery, A. A., Abir, I. A., Lestari, W., & Akingboye, A. S. (2023). Landslide susceptibilitymapping of Penang Island, Malaysia, using remotesensing and multi-geophysical methods. *Earth SciencesResearch Journal, 27*(2), pp. 93-107. https://doi.org/10.15446/esrj.v27n2.107274

[6] Kherrouba, H., Lamara, M., & Benzaid, R. (2022). Geological and Geophysical Characterization Using Electrical Resistivity Imaging of Certain Landslides at Djimla region (Jijel, Northeast Algeria). In: *Advances in Geophysics, Tectonics and Petroleum Geosciences.* CAJG 2019. Advances in Science, Technology & Innovation. Springer, Cham. https://doi.org/10.1007/978-3-030-73026-0_70.

[7] Hack, R., Havenith, H.B., Jongmans, D., Abdrakmatov, K., Trefois, P., Delvaux, D., & Torgoev, A. (2000). Geophysics for slope stability. *Surveys in Geophys, 21*, pp. 423-448.

[8] Jongmans, D., & Garambois, S. (2007). Geophysical investigation of landslides: A review. Bulletin de la Société Géologique de France. 178, pp. 101-112.

[9] Grandjean, G., Bitri, A., Pennetier, C., Meric, O., & Malet, J.P. (2006). Caractérisation de la structure interne et de l'état hydrique de glissements argilo-marneux par tomographie géophysique : l'exemple du terrain de Super-Sauze (Alpes du Sud,France).*C.R.Acad.Sci, 338*, pp. 587-595.https://doi.org/10.1016/j.crte.2006.03.013.

[10] Kherrouba, H. (2008). Etude géologique et géotechnique des zones instables de la région de Texenna-Djimla, wilaya de Jijel, (Algérie). Mém de Magister. UnivJijel. Algérie.

[11] Meziani, B., Machane, D., Bendaoud, D., CheikhLounis, G., Oubaiche, E., Chabane, S., Bensalem, R., & Moulouel, H. (2017). Geotechnical and geophysical characterization of the Bouira-Algiers Highway (AinTurck, Algeria) landslide. *Arab J Geosci, 10*(117). https://doi.org/10.1007/s12517-017-2926-z.

[12] Bouillin, J.P. (1979). La transversale de Collo et d'El Milia (Petite Kabylie) une région clef pour l'interprétation de la tectonique alpine de la chaîne littorale d'Algérie. ThèseDoct. Univ. P.M.C, Paris, France.

[13] Djellit, H. (1987). Evolution tectono-métamorphique du socle Kabyle et polarité demise en place des nappes de flyschs en Petite Kabylie occidentale (Algérie). Thèse Doct. Univ d'Orsay Paris.

[14] Durand Delga, M. (1955). Étude géologique de l'Ouest de la Chaine numidique. Bull. Serv.Carte Géol. Alger.2 (24).

[15] Maameri, R., & Tebboub, M. (2019). Apport de l'imagerie géophysique à l'étude des glissements de terrain. Pénétrante autoroutière 77-région de Tamentout -Jijel (Nord-Est Algérien). Mém de Master. UnivJijel.

[16] RPOA (2008). Règles parasismiques applicables au domaine des ouvrages d'art, Document Technique Règlementaire (DTR), Ministère des Travaux Publics, Algérie.

[17] Rizzani De Eccher (2016). Rapports de l'étude géotechnique, Annexe B, Campagne de reconnaissance d'EXE, p187; Annexe D, Essai in situ et enlaboratoire, Rapport géotechnique, pp18. Terrassement; Source: Agence Nationale des Autoroutes (ANA), Jijel, 2019.

[18] Friedel, S., Thielen, A., & Springman, S.M. (2006). Investigation of a slope endangered by rainfall-induced landslides using 3D resistivity tomography and geotechnical testing. *J Appl Geophys 60*, pp. 100-114. https://doi.org/10.1016/j.jappgeo.2006.01.001.

[19] Lebourg, T., Binet, S., Tric, E., Jomard, H., & El Bedoui, S. (2005). Geophysical survey to estimate the 3D sliding surface and the 4D evolution of the water pressure on part of a deep-seated landslide. *Terra Nova 17*, 399–406. https://doi.org/10.1111/j.1365-3121.2005.00623.x.

[20] Mezerreg, NEH, Kessasra, F., Bouftouha, Y., Bouabdallah, H., Bollot, N., Baghdad, A., & Bougdal, R. (2019). Integrated geotechnical and geophysical investigations in a landslide site at Jijel, Algeria. *J Afr Earth Sci*, *160*. 103633. https://doi.org/10.1016/j.jafrearsci.2019.103633.

[21] Wilkinson, P.B., Loke, M.H., Meldrum ,P.I., Chambers, J.E., Kuras, O., Gunn, D.A., & Ogilvy, R.D. (2012). Practical aspects of applied optimized survey design for electrical resistivity tomography. *Geophys. J. Int*, *189*, pp. 428-440.

[22] Kherrouba, H., Lamara, M., & Benzaid, R. (2019). Contribution of electrical tomography to the study of lanslides in Texenna region (Northeast Algeria). In Sundararajan N et al. (eds.), *On Significant Applications of Geophysical Methods*, Advances in Science, Technology & Innovation. https://doi.org/10.1007/978-3-030-01656-2_11.

[23] Mita, M., Glazer, M., Kaczmarzyk, R., Dąbrowski, M., & Mita, K. (2018). Case study of electrical resistivity tomography measurements used in landslides investigation, Southern Poland. *Contemp Trends Geosci*, *7*(1). pp.110–126. https://doi.org/10.2478/ctg-2018-0007.

[24] Pasierb, B., Grodecki, M. & Gwóźdź, R. (2019). Geophysical and geotechnical approach to a landslide stability assessment: a case study. *ActaGeophys*, *67*, pp. 1823–1834. 2019.https://doi.org/10.1007/s11600-019-00338-7.

[25] Rapport de l'étude géophysique des glissements de terrain de Tamentout. Bureau d'engineering, études et équipements en géosciences "GeoExplo", (2018). Alger. Source: Agence Nationale des Autoroutes (ANA).

[26] Bellanova, J., Giuseppe, G., Giocoli, A., Luongo, R., Macchiato, M., Perron, A., Uhlemann, S., & Piscitelli S. (2018). Electrical resistivity imaging for the characterization of the Montaguto landslide (southern Italy). *Eng.Geol 243*:272-281. https://doi.org/10.1016/j.enggeo.2018.07.014.

[27] Gueguen, P., Garambois, S., Cravoisier, S., & Jongmans, D. (2004). Geotechnical, geophysical, and seismological methods for surface sedimentary layers analysis. *13th World Conference on Earthquake Engineering Vancouver*, B.C., Canada, Paper No. 1777.

[28] Ehrmann, F. (1946). Carte Géologique Tamesguida au 1/50000. Bulletin du Service de la carte géologique de l'Algérie.

DOI: 10.2478/sspjce-2023-0007

Use of Waste Tire Chips and PET Plastic Flakes in Backfill Behind Retaining Walls

Benamara Fatima Zohra [1*], Kechkar Chiraz [1], Rouaiguia Ammar [1], Bencheikh Messaouda [1], Nigri Ghania [1], Feligha Marwa [2]

[1]Laboratory of Civil Engineering and Hydraulic (LGCH), Faculty of Science and Technology, Department of Civil Engineering and Hydraulics, University 8 Mai 1945, Guelma, Algeria
[2] LMGHU Laboratory, University of 20 August 1955, Skikda, 21000 Algeria
*e-mail: benamara_fati2003@yahoo.fr

Abstract

The use of waste in the field of civil engineering is one of the solutions to reduce the harmful impact of waste on the environment on the one hand and preserve natural resources on the other. This study aims to investigate the effect of using waste materials such as plastic and tire chips that can be used as backfill in retaining walls. A numerical study has been carried out by using PLAXIS 2D software version 8.6 to model three types of rigid retaining walls, namely: scale wall test, cantilever wall, and gravity wall. In addition, the backfills of those retaining walls are composed of two mixtures. The first is a mixture of sand and tire chips (TC) with different percentages (10%, 30%, 50%, and 70%). The second is a mixture of sand and PET plastic flakes at different percentages (12.5%, 22.5%, and 32.5%). The results obtained from this study confirmed that the use of PET plastic waste and tire chips waste mixed with sand in the backfills of rigid retaining walls contributes effectively to the reduction of horizontal and vertical displacements as well as the earth pressures behind the retaining walls, therefore improving the stability of the retaining walls.

Keywords: tire chips (TC), PET plastic flakes, rigid retaining walls, backfill, PLAXIS 8.6

1 Introduction

Some soils, due to their poor geotechnical properties, can be considered problematic soils that cannot support heavy loads. Therefore, these soils require some improvement to increase their mechanical stabilities and enhance their performance. Conventional soil reinforcement techniques involve vertical or horizontal reinforcement elements in the soil [1]. Soil reinforcement consists of combining the soil with fibers to form a composite material. The recovery of waste in the field of civil engineering is an important sector where several types of waste have found applications under the condition that they are not subject to very rigorous quality criteria. Among the waste affecting the environment are waste tires and plastic bottles left in nature. According to [2], scrap tire derived (STD) in the form of tire chips, granulated rubber, and powdered rubber, and plastic bottles (PET, PP) in the form of flakes or granules have experienced an increase in their application in the geotechnical field [3].

Several researchers have conducted studies on the use of additives such as scrap tire-derived (STD) and plastic bottle waste in geotechnical applications. Recycled tires are usually shredded or crushed, and they can be used as substitute aggregates in backfill in road embankments, retaining walls, foundations, landfills, and other applications [4, 5]. Cecich et al. [6] investigated the effect of using tire chips as lightweight backfill for retaining structures. They found a more than 60% gain in total construction cost, and that the wall is more stable. Hataf and Rahimi [7] carried out a series of laboratory tests to investigate the use of tire chips mixed with sand to increase the bearing capacity of the foundation. Yoon et al. [8] studied the compression behavior and performance of tire-derived aggregate (TDA) used in the construction of road embankments in Canada.

Reddy and Krishna [9] made a scale model of a retaining wall in order to determine the effect of using a light fill composed of a mixture of sand and tire chips on the mechanical behavior in terms of displacement and earth pressure.

Reinforcement of poor-quality soils with fiber materials such as PET plastic waste has been conducted by several researchers to improve their bearing capacities and reduce lateral deformation and settlement [10, 11]. The standard PET plastic soil-waste composite is defined by [12] as a composite with discrete and randomly distributed elements of PET plastic flakes, which can improve the mechanical behavior of the composite. Soils reinforced with PET plastic flakes are seamlessly integrated into a floor matrix [13].

In this work, a numerical study has been carried out for three retaining walls, namely: a scale model wall, a cantilever wall, and a gravity wall whose backfill is placed behind it and is composed of two types of mixture. The first one is made up of a mixture of "sand and PET plastic flakes", whereas the second one is made up of a mixture of "sand and tire chips (STC)" with different percentages, thus forming a backfill material for retaining walls to improve the stability on one side and the recovery of plastic and rubber waste. In addition, it will protect the environment and preserve the deposits of sandy materials.

2 Scale Wall Test

This numerical study used two types of backfill behind the retaining walls. The first type of backfill is sand alone, and the second is a mixture of sand and tire chips (STC) in different percentages (10%, 20%, 30%, 40%, and 50%), according to the work reported by [9]. The characteristics of the embankments (sand and tire chips) (STC) as well as the properties of the retaining wall model used in the numerical analysis are presented below.

2.1 Wall Materials Test

2.1.1 Sand

For this study, it would be of interest to use fine to medium sand. The properties of sand are presented in Table 1 [9].

Table 1: Properties of sand

Parameter (unit)	**Value**
Specific gravity G_s (-)	2.66

Unit weight (kN /m^3)	17.4
Effective diameter D_{10} (mm)	0.175
Uniformity Coefficient C_u (-)	2.314
Coefficient of curvature C_c (-)	0.99
Modulus of elasticity Es (MPa)	58
Poisson's ratio v (-)	0.3
Internal friction angle φ (°)	33.5
Cohesion C (kPa)	9.3

2.1.2 Backfill of Sand and Tire Chips (STC)

Laboratory characterization tests were carried out by using scrap tire chips (TC) of 10 x 10 mm size and about 20 mm length in different STC mixtures (10%, 20%, 30%, 40%, and 50%). The properties of the mixture of sand and tire chips (STC) are presented in Table 2 [9].

Table 2: Properties of the different STC mixtures for the backfill of the scale model wall

STC Mixture (%)	γ_{sec} **(kN/m^3)**	φ **(°)**	E**(kPa)**	υ
STC 0	16.1	48	50 000	0.330
STC 10	14.62	51	45 101	0.325
STC 20	14.12	52	40 202	0.320
STC 30	13.17	56	35 303	0.315
STC 40	12.29	51	30 404	0.310
STC 50	10.42	44	25 505	0.305

2.1.3 Wall Test

The wall test is made of steel of 25 cm thickness and 60 cm height with a density equal to 70 kN/m^3. Reddy and Krishna [9] reported the characteristics of the scale wall test.

3 Numerical Study of the Scale Wall Test

The numerical study was performed with PLAXIS 8.6 software, using the Finite Element Method. The backfill soil is modeled based on the drained Mohr-Coulomb model [14]. The soil is modeled into 15-node triangular elements. The boundaries are fixed horizontally and vertically at the bottom and on one of the side boundaries of the model, as shown in Figure 1. The dimensions of the model are (8 x 0.6) m. Overloads varying between 0 and 10 kN/m^2 are applied on the free horizontal face of the embankment (to investigate the impact of raising the overload in relation to the percentages of the TC and determine the maximum vertical displacements).

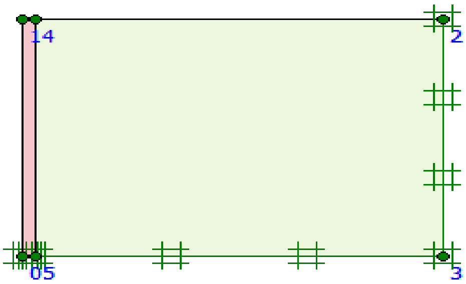

Figure 1: Modeling the test wall profile

A fine mesh is used for the model. The initial mesh of the test wall model is shown in Figure 2. The deformed mesh of the test wall model is shown in Figure 3.

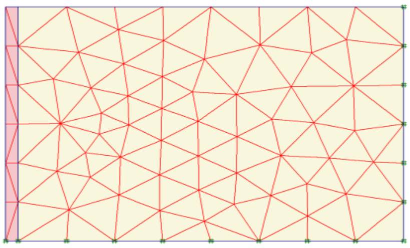

Figure 2: Initial mesh of test wall model

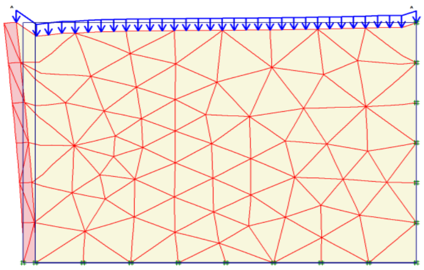

Figure 3: Deformed mesh of wall test model (STC 10%)

3.1 Results and Discussion

The backfill of the test wall is carried out with sand alone and with mixtures (sand and tire chips) with different percentages of tire chips, as presented in Tables 1 and 2. The response of the wall was determined after the application of surcharges that varied from (0 to 10) kN/m^2. It is worth discussing these interesting facts revealed by the results in terms of horizontal and vertical displacements along the height on the face of the wall (Figures 4 and 5), as well as the lateral earth pressures (Figure 6).

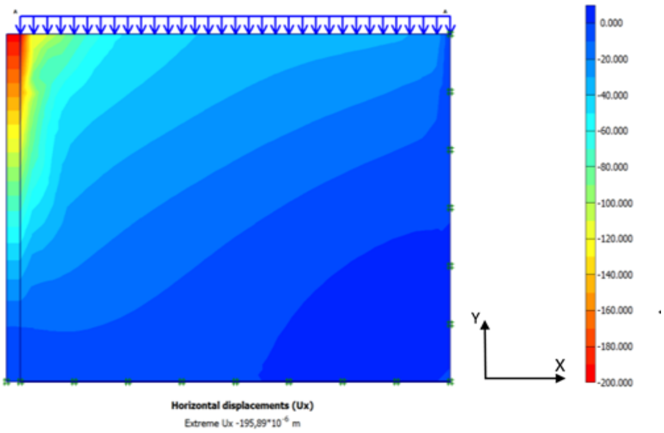

Figure 4: Horizontal displacements (U_X), the case STC 10 %

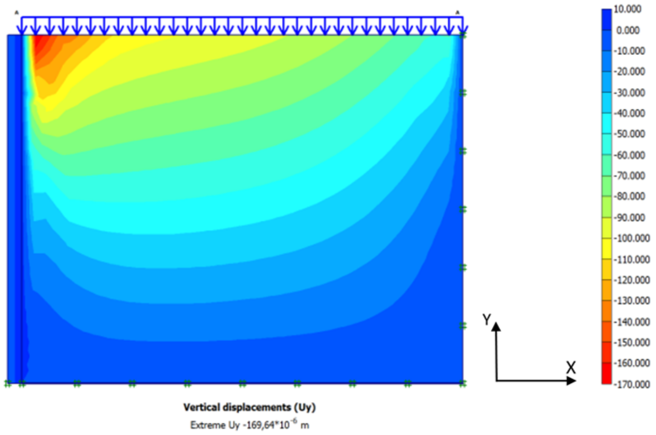

Figure 5: Vertical displacements (U_Y), the case STC10 %

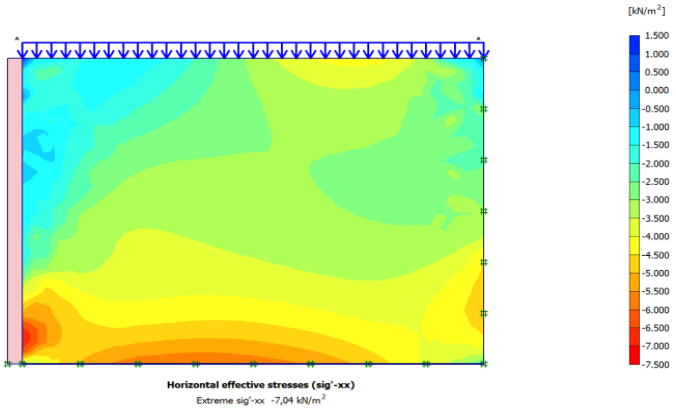

Figure 6: Horizontal restraints (σ_{xx}), case STC10 %

The most striking results emerge from the horizontal displacements computed behind the wall. It is apparent from Figure 7 that the Horizontal displacements decrease with the increase of the tire chips percentages (% TC) and minimum displacements are recorded at the 30 % level. For the STC 0 backfill and the surcharge (q = 10 kN/m^2), it is interesting to notice that the maximum displacement of the wall is about 0.22 mm.

The STC 30 backfill has the lowest displacements at the top of the wall (0.15 mm). However, the horizontal displacements showed an increase at the percentages of 40% and 50%. It has been observed that the vertical displacements showed a decrease for a percentage of 30% (Figure 9). From Figures 8 and 9, the horizontal and vertical displacements have increased with increasing the applied surcharge from (0 to 10) kN/m^2.

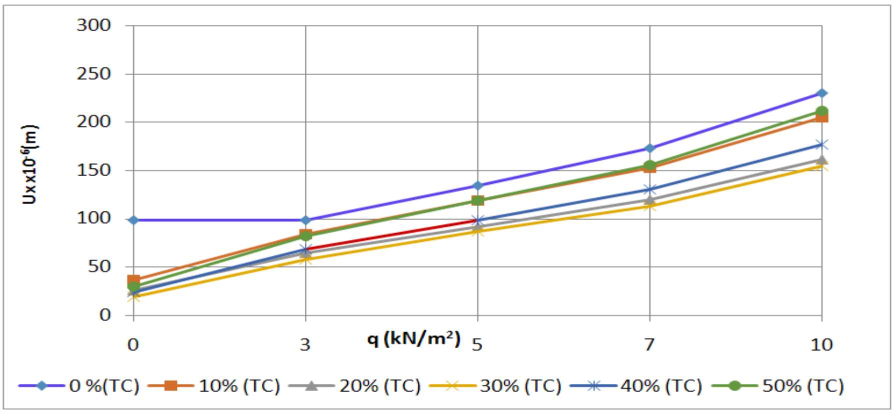

Figure 7: Horizontal displacements depending on the surcharge applied for different % (TC)

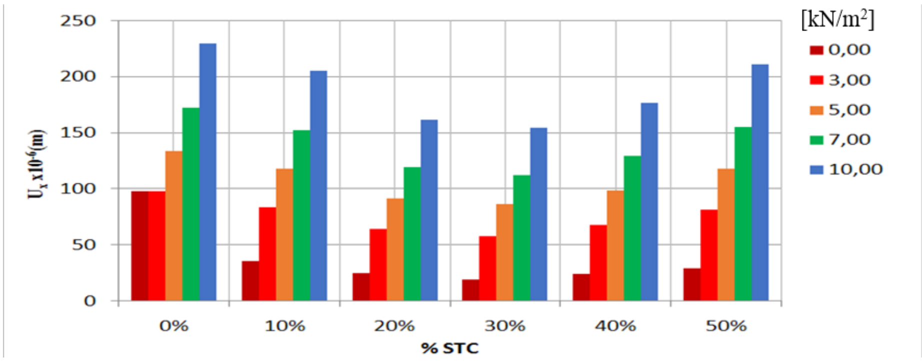

Figure 8: Horizontal displacements as a function of percentages (TC) for different applied surcharges

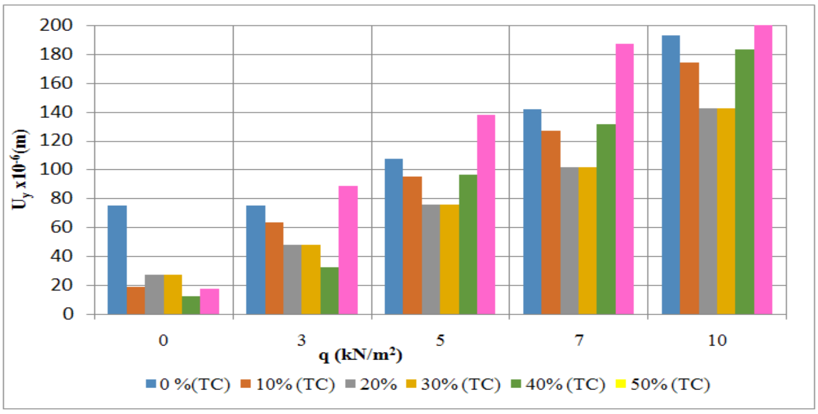

Figure 9: Vertical displacements as a function of percentages (TC) for different applied surcharges

The results obtained from the numerical study, which was performed on the wall test model, confirm that the percentage of 30% of tire chips is the ideal percentage that contributes to the reduction of horizontal and vertical displacements, whatever the surcharge applied. These results are in accordance with the experimental results reported by [9].

4 Numerical Study of Retaining Walls

To validate the results of the test wall on the rigid retaining walls in situ, a numerical Finite Element Analysis (FEM) is carried out by using the software PLAXIS 8.6. In addition, the effect of using sand PET-plastic mixtures and sand tire chips (STC) on the behavior of both retaining walls (cantilever wall and weight wall) has been studied.

4.1 Material Parameters of Retaining Wall Models

The materials used in this study are sand, PET plastic flakes, and tire chips (TC) as well as reinforced concrete retaining walls.

4.1.1 The Structure of Retaining Walls

Two types of retaining walls were used, namely, the gravity wall and the reinforced concrete cantilever wall, whose characteristics are illustrated in Table 3 [15].

Table 3: Properties of reinforced concrete retaining wall [15]

Model	γ **(kN/m^3)**	E **(MPa)**	υ
Elastic	25	34180	0.200

4.1.2 Sand-PET Plastic Mixture

PET Plastic flakes are used in percentages of 12.5%, 22.5%, and 32.5% of the dry weight of sand. The properties of the sand-PET plastic mixture are shown in Table 4 [16].

Table 4: The properties of the sand-PET plastic mixture

Parameter (unit)	**Sand-PET Plastic Mixture**		
	12.5%	**22.5%**	**32.5%**
Unit weight (kN/m^3)	16.3	15.47	14 .98
Modulus of elasticity $E_{p\text{-}s}$ (MPa)	394.50	663.7	932.9
Poisson's ratio v (-)	0.31	0.32	0.33
Angle of internal friction φ (°)	40.3	44.4	41.1
Cohesion C (kPa)	49.5	30.3	46.3

4.1.3 Tire Chip Sand Mixture (STC)

In this study, mixtures of sand and tire chips (STC) are considered lightweight backfill materials behind both cantilever retaining walls and weights for different percentages (STC 0, STC 10, STC 30, STC 50, STC 70) as shown in Table 5 [4].

Table 5: Tire chips sand mixture properties

STC %	***γ* (kN/m³)**	***φ* (°)**	***C* (kPa)**	***E* (kPa)**	***υ***
STC 0	18.15	41	0	47888	0.300
STC 10	16.30	37.2	1	32700	0.300
STC 30	16.11	38	13.98	45145	0.306
STC 50	14.89	35	31.21	42155	0.309
STC 70	11.41	27	22.11	36037	0.314

4.1.4 In-situ Soil Tests

The in-situ soil properties are presented in Table 6 [17].

Table 6: In situ soil properties

Model	***γ* (kN/m³)**	***φ* (°)**	***C* (kPa)**	***E* (kPa)**	***υ***
MC	18.0	28	5	50000	0.300

4.2 Numerical Analysis of Cantilever Wall

The soil is modeled into 15 node-triangular elements by using the drained Mohr-Coulomb model. The boundaries are fixed laterally on both sides and fixed horizontally and vertically at the lower boundary, as shown in Figure 10. The initial mesh is shown in Figure 11. The dimensions of the model are (80 m x 15 m). The cantilever wall is analyzed using both mixtures (STC) and PET plastic sand as lightweight backfill materials, whose characteristics are shown in Tables 4 and 5, respectively. The number of elements and nodes are respectively 162 and 1391 [16].

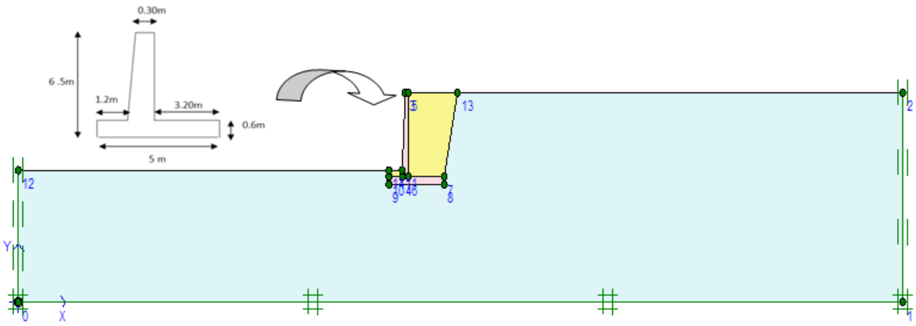

Figure 10: Cantilever retaining wall model

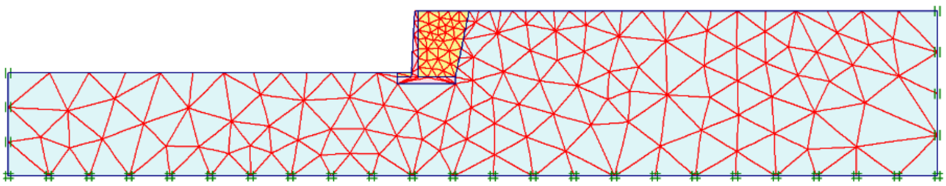

Figure 11: The initial mesh of the cantilever retaining wall model

4.2.1 Results and Discussion

Figures 12, 13, and 14 show the deformed mesh of the model, the vertical and horizontal displacements, the stresses, and the strains along X and Y respectively.

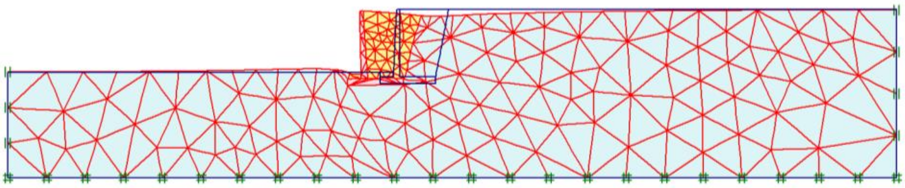

Figure 12: Deformed mesh of the cantilever retaining wall

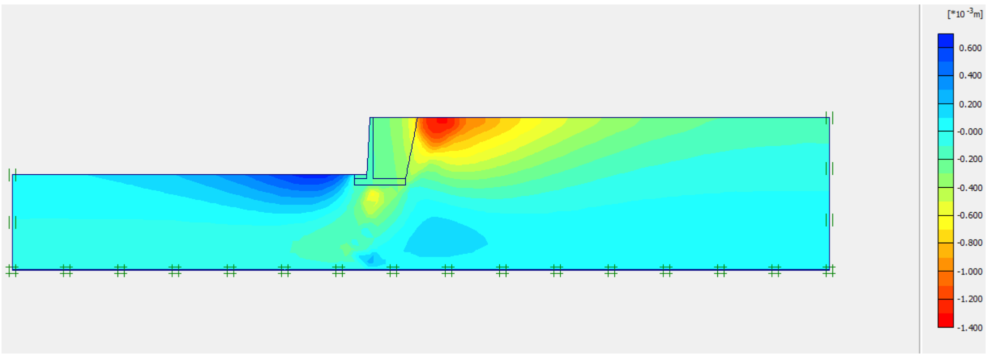

Figure 13: Vertical displacements (U_y) of the cantilever retaining wall

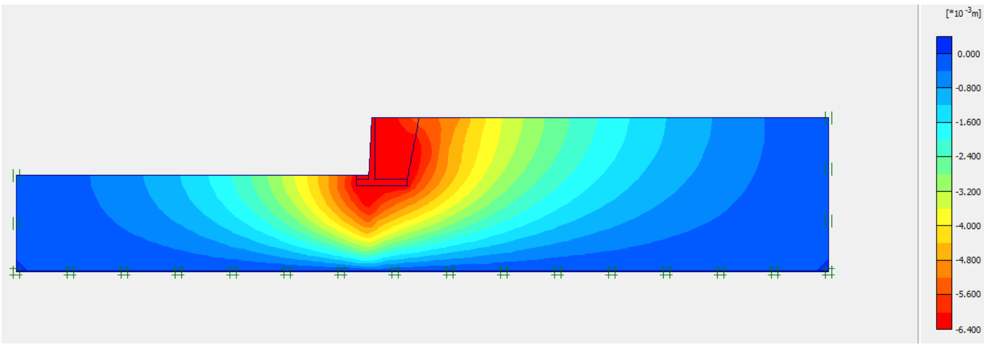

Figure 14: Horizontal displacements (U_x) of the cantilever retaining wall model

The main obtained results are shown in Tables 7 and 8.

Table 7: The main results for the case of cantilever wall with backfill (sand-plastic PET)

(%) PET	$U_{X(max)}$ **x10^{-3} (m)**	U_Y **x10^{-6} (m)**	σ_{xx} **(kN/m^2)**	F_s
0	7.52	1.35	29.31	1.993
12.5	6.35	1.32	44.20	2.079
22.5	6.32	1.28	31.18	2.082
32. 5	6.29	1.23	62.69	2.084

Table 8: The main results for the case of cantilever wall with backfill (STC)

(%) (TC)	$U_{X(max)}$ x10^{-3} (m)	U_Y x10^{-3} (m)	σ_{xx} (kN/m^2)	F_s
0	9.64	3.10	122.44	1.956
10	9.50	2.59	82.95	1.955
30	7.43	1.39	80.36	2.060
50	7.50	1.29	80.41	2.082
70	7.69	1.10	84.66	2.075

4.2 Numerical Study of the Gravity Wall

To study the effect of lightweight embankments on the stability of rigid walls, a gravity wall is modeled as a rigid element with the same elastic model as the cantilever wall whose geometry is presented in Figure 16, and with the same type of soil in situ. The wall is 4 m high and 1.5 m wide. Both backfills, STC and sand-PET plastic, are placed behind the gravity wall over a thickness of 0.50 m (Figure 15).

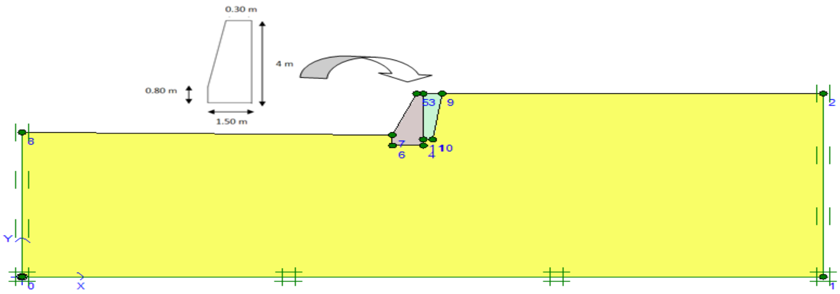

Figure 15: Gravity wall model

A refined mesh was chosen to obtain more reliable results. The number of elements and nodes are respectively 1132 and 9273. The generation of the mesh is given in Figure 16.

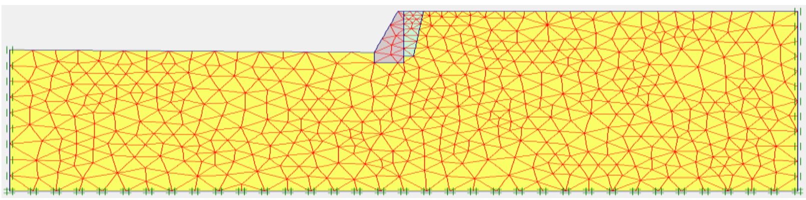

Figure 16: The initial mesh of the gravity wall

4.3.1 Results and Discussion

Figures 17, 18, and 19 show the deformed mesh of the model, the vertical and horizontal displacements, the stresses, and the strains along X and Y respectively.

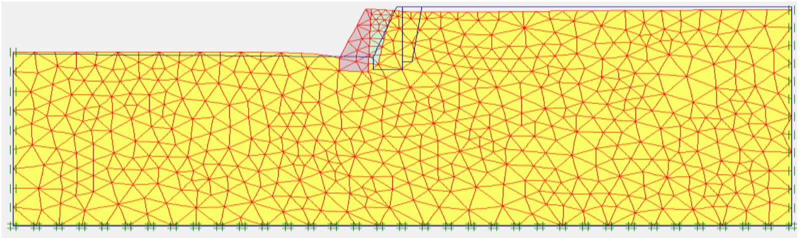

Figure 17: Deformed mesh of the gravity wall

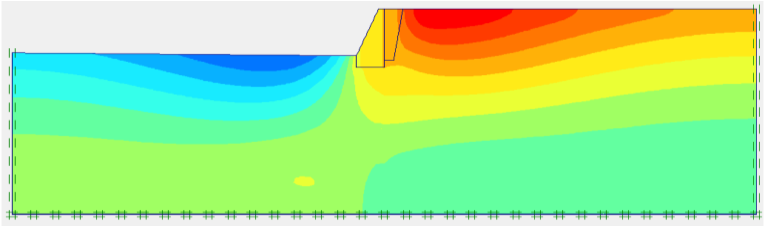

Figure 18: Vertical Displacements (Uy) of the gravity wall, case 22.5% PET Plastic

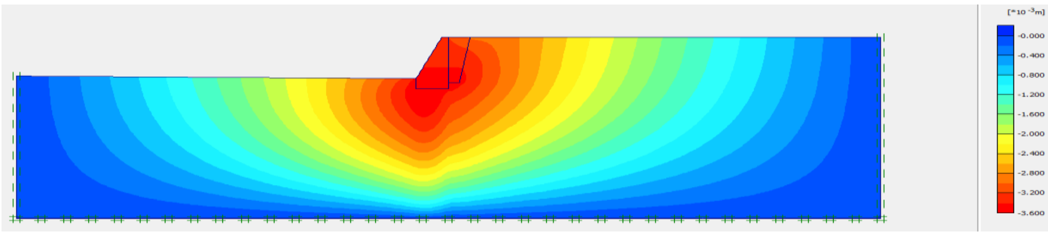

Figure 19: Horizontal displacements of the gravity wall (U_x), case 22.5% PET plastic

The results of the modeling of the gravity wall with both backfills, sand-plastic PET and STC, are shown in Tables 9 and 10.

Table 9: The main results of the gravity wall with sand-plastic PET backfill

PET plastic (%)	$U_{X(max)}$ **x10^{-3} (m)**	U_Y **x10^{-6} (m)**	σ_{xx} **(kN/m^3)**	F_s
0	3.61	685.61	36.77	1.834
12.5	3.59	683.97	30.99	1.976
22.5	3.58	675.34	26.58	1.988
32. 5	3.58	671.98	37.24	1.994

Table 10: The main results of gravity wall with STC backfill

TC (%)	$U_{x(max)}$ **x10^{-3} (m)**	U_Y **x10^{-6} (m)**	σ_{xx} **(kN/m^2)**	F_s
0	4.11	1.50	3282	1.356
10	3.78	888.57	2463	1.455
30	3.59	682.71	2811	2.670
50	3.58	672.59	1907	2.752
70	3.54	659.44	1702	2.545

As shown in Tables 7, 8, 9, and 10, the horizontal and vertical displacements decrease with increasing percentages of tire chips (TC) and PET plastic flakes. This decrease is observed for both the retaining walls (cantilever wall and weight wall). It has also been noticed that the earth pressures increased slightly with increasing percentages of recycled waste: PET plastic flakes and tire chips (TC) added to backfill behind retaining walls.

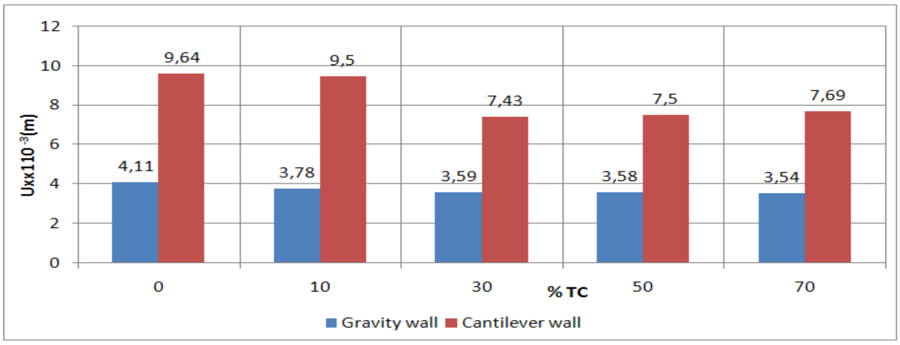

Figure 20: Comparison between cantilever wall and gravity wall displacements in the case of STC backfill

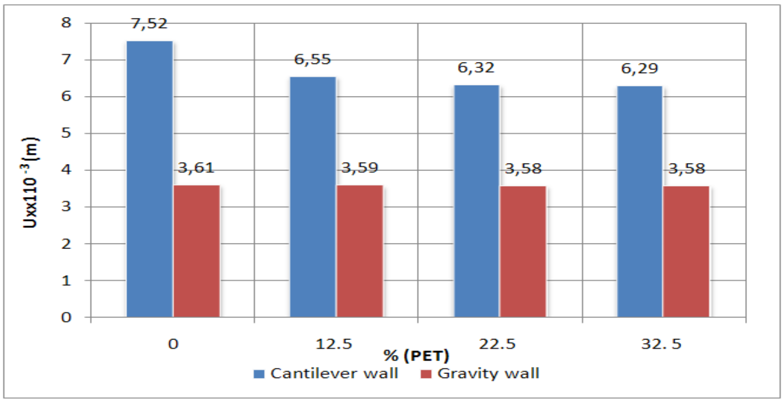

Figure 21: Comparison between the horizontal displacements of the cantilever wall and the gravity wall in the case of sand-plastic PET backfill

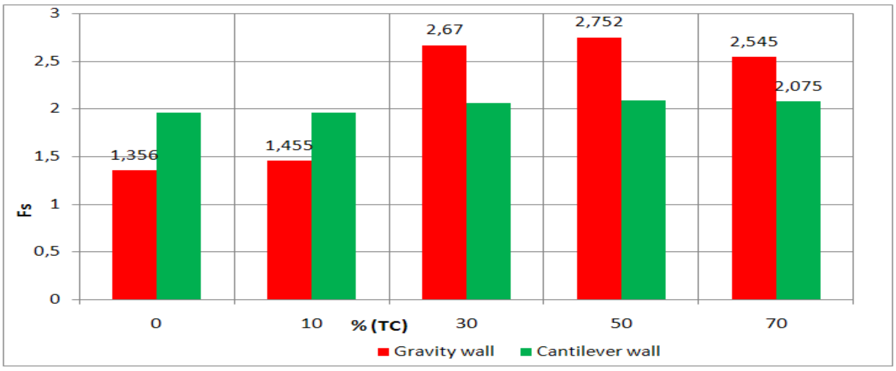

Figure 22: Comparison between safety factors of cantilever wall and weight wall in the case of STC backfill

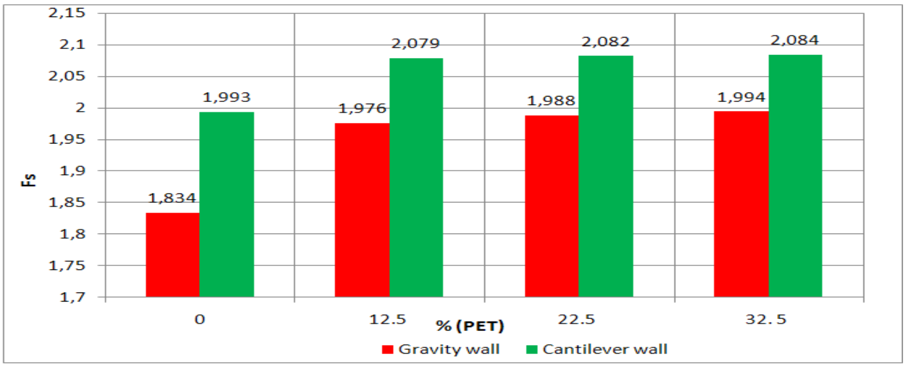

Figure 23: Comparison between safety factors of cantilever wall and weight wall reinforced in the case of sand-plastic PET backfill

Based on the results presented in Figures 20 and 21, the horizontal displacements developed behind the cantilever retaining wall are greater than those developed behind the gravity wall.
Referring to Figures 22 and 23, the safety factors showed an improvement with the increase in the percentages of both waste PET plastic flakes and tire shavings (TC).

5 Conclusion

To expand the field of use of inert waste materials such as used tires and plastic bottles in geotechnical structures, a numerical study using finite element software, PLAXIS 8.6, has been performed on a scale model retaining wall. The study was realized by considering a mixture of tire chips and sand as backfill for the retaining wall. The principal findings are derived from the horizontal displacements computed behind the scale model retaining wall.

- The minimal displacements are recorded at the 30% percent level, and the horizontal displacements decrease as the tire chips percentages (% TC) rise.
- It is significant to note that the maximum displacement of the wall for the STC 0 backfill and the surcharge (q = 10 kN/m^2) is around 0.22 mm.
- The lowest displacements at the top of the wall (0.15 mm) can be observed in the STC 30 backfill. However, at 40% and 50% of the percentage, there was an increase in the horizontal displacements.
- It has been stated that the vertical displacements decreased for the percentage of 30%.

In general, the numerical results are in accordance with those obtained from the experimental study, in which the percentage of 30% of tire chips is the ideal percentage that contributes to the reduction of horizontal and vertical displacements as well as active earth pressures, whatever the surcharge applied.
In order to apply these results to full-scale walls, a numerical study is carried out using PLAXIS software on rigid retaining walls. Two types of backfill are placed behind these walls, which are sand-tire chips (STC) and sand-PET plastic flakes mixtures.
The main finding of the mathematical study on rigid walls has a direct connection to their displacements and, as a result, their stability.

- The displacements, both horizontal and vertical, decrease as the percentage of tire chips (TC) and PET plastic flakes increases.
- This reduction has been observed for the weight wall and cantilever wall retaining walls.

- The percentage of 22.5% of PET plastic flakes and the percentages between 30% and 50% of tire chips (TC) reduce the horizontal and vertical displacements, which affect these structures, and contribute to the reduction of earth pressure behind the retaining walls.
- The safety factors showed an improvement with the increase in the percentages of both waste PET plastic flakes and tire chips (TC).
- The stability of retaining walls (cantilever and gravity walls) is improved by the efficient reduction of horizontal and vertical displacements achieved via the use of PET plastic waste and tire chips (TC) combined with sand as backfill behind rigid retaining structures.

In conclusion, this study suggests that the use of recycled waste mixed with sand with well-defined percentages is generally determined by laboratory tests.

Acknowledgments

This research work is supported by the Ministry of Higher Education and Research of Algeria.

References

[1] Sanjay KS. (2017). *Fundamentals of Fibre-Reinforced Soil Engineering, Developments in Geotechnical Engineering.* Series editors Braja M Das. Henderson. USA.

[2] ASTM. D 6270. (2004). *Standard Practice for Use of Scrap Tires in Civil Engineering Applications*. ASTM: West Conshohocken. PA, USA.

[3] Adhikari B & Maiti SD. (2000). Reclamation and recycling of waste rubber. *Progress in Polymer Science, Vol*.25, PP. 909-948

[4] Ahmed,I. (1993). Laboratory study on properties of rubber-soils. Report No. FHWA/IN/JHRP-93/4. West Lafayette, IN: Purdue University.

[5] Reddy SB, Krishna AM, Krishna, & Reddy R. (2017). Sustainable Utilization of Scrap Tire Derived Geomaterials for Geotechnical Applications. *Indian Geotechnical Journal 48*(3), 1-16, DOI. 10.1007/s40098-017-0273

[6] Cecich V, Gonzales L, Hoisaeter A, Williams, J, & Reddy, K. (1996). Use of shredded tires as lightweight backfill material for retaining structures. *Waste Management and Research. 14*, 433-451.

[7] Hataf N & Rahimi MM. (2005). Experimental investigation of bearing capacity of sand reinforced with randomly distributed tire shreds. *Construction and Building Materials. 20* (10), 910-916.

[8] Yoon S, Prezzi M, Siddiki NZ & Kim B. (2006). Construction of a test embankment using a sand–tire shred mixture as fill material. *Waste Management 26,* 1033–1044.

[9] Reddy SB, & Krishna AM. (2015). Recycled tire chips mixed with sand as lightweight backfill material in retaining wall applications: An experimental investigation. *International Journal of Geosynthetics and Ground Engineering*. https://doi.org/10.1007/s40891-015-0036-0.

[10] Consoli Smith J, Jones M Jr, Houghton L. (1999). Future of health insurance. *N Engl J Med 965*, 325–329

[11] Zaimoglu AS & Yetimoglu T. (2011). Strength Behavior of Fine Grained Soil Reinforced with Randomly Distributed Polypropylene Fibers. *Geotechnical and Geological Engineering. 30*(1), 197–203.

[12] Li C. (2005). *Mechanical response of fiber-reinforced soil*. PhD Dissertation, The University of Texas at Austin, U.S.A.

[13] Hejazi SM, Sheikhzadeh M, Abtahi SM & Zadhoush A. (2012). A simple review of soil reinforcement by using natural and synthetic fibers. *Construction and Building Materials. 30*, 100–116.

[14] Brinkgreve RBJ. (2003). Manuel de Référence de PLAXIS Version 8.6. [PLAXIS 8.6]. Delft University of Technology and PLAXIS BV. Pays-Bas.

[15] Saribas I & Ok B. (2019). Seismic performance of recycled aggregate–filled cantilever reinforced concrete retaining walls. *Advances in Mechanical Engineering. 11*(4) 1–11

[16] Luwalaga JG. (2016). *Analysing the Behaviour of Soil Reinforced with Polyethylene Terephthalate (PET) Plastic Waste.* A Research Thesis presented in partial fulfilment of the requirements for the degree of Master of Engineering (M Eng.), Faculty of Engineering at Stellenbosch University.

[17] Djadouni H, Trouzine H, Correia AG & Miranda TFS. (2019). 2D numerical analysis of a cantilever retaining wall backfilled with sand–tire chips mixtures. *European Journal of Environmental and Civil Engineering*. DOI:10.1080/19648189.2019.1570870.

[18] Vendruscolo MA NC, Fonini A & Rosa FD. (2009). Fiber reinforcement effects on sand considering a wide cementation range. *Geotextiles and Geomembranes. 27*(3), 196–203.

DOI: 10.2478/sspjce-2023-0008

Evaluation of Recycled Brick Waste Aggregates as a Sustainable Substitute in Cement Treated Base

Youcef Toumi [1*], Samy Mezhoud [1], Otmane Boukendakdji [2], Moussa Hadjadj [2]

[1]Department of Civil Engineering, Laboratory of Materials and Construction Durability (LMDC), University of Mentouri Brothers Constantine 1, Constantine, Algeria
[2]Department of Civil Engineering, LME laboratory, University Yahia fares, Medea, Algeria
*e-mail: youcef.toumi@doc.umc.edu.dz

Abstract

Recycling industrial waste to obtain secondary raw materials is a key focus of environmental policy and circular economy strategies. One such industrial waste, recycled brick waste (RBW), is characterized by high pollution and low recycling rates. This paper evaluates the effects of graded replacement of various RBW sizes as a substitute for coarse and fine natural aggregate (NA) on the mechanical properties and durability of cement treated base (CTB). The novelty of this study lies in the durability evaluation of four types of CTB, including natural, recycled, and mixed CTB. RBW and NA materials are characterized and compared, and the mechanical properties and durability of CTB with RBW materials are analyzed and compared to CTB with 100% NA. The results show that the mixes containing waste bricks exhibit comparable mechanical characteristics and could be used in layers of pavement foundations. Additionally, the durability of the mixes containing RBW yields better results compared to blends containing NA.

Keywords: cement treated base (CTB), recycled brick waste (RBW), mechanical properties, durability, abrasion test

1 Introduction

The building industry, which consumes over 3 billion tons of virgin materials annually, is the largest consumer of such materials worldwide [1]. In recent years, there has been a growing emphasis on sustainable pavements that utilize recycled materials to help conserve natural resources. Instead of discarding construction and demolition waste in landfills, it is being considered as a valuable source of recycled materials for replacing natural aggregates, thereby reducing potential environmental impacts and enhancing the economic value of recycling [2]. In many developing countries, brick construction is still prevalent alongside concrete construction, resulting in a significant amount of demolition waste comprised of brick aggregates. This presents an opportunity for utilizing recycled brick aggregates as a building material, particularly in countries like South Africa [3].

Several researchers have explored the idea of recycling brick waste. Hou et al. [4] investigated the effects of incorporating cement-stabilized crushed brick aggregates (CBA) in asphalt pavement base and subbase applications. The results have shown that as the content of CBA increases, the maximum dry density of the cement-stabilized CBA decreases, while the optimal water content increases. Additionally, the unconfined compressive strength, splitting strength, and resilient modulus at different ages all decrease with an increase in CBA content. Other studies have also examined the use of recycled concrete aggregates and crushed clay brick as substitutes for natural aggregates in unbound base materials, showing similar trends in terms of moisture content, dry density, and CBR values [5]. Furthermore, structural- and pavement-grade concrete mixtures using recycled brick aggregates have been developed, demonstrating comparable mechanical properties and durability performance to conventional concrete mixtures [6]. Additionally, investigations on the microstructure and durability of concrete with varying levels of replacement of sand aggregate with recycled brick aggregate have shown changes in water absorption, pozzolanic reactivity, and porous structure [7].

Atyia et al. [8] showed that the replacement of NA by RBW as coarse and fine aggregates in the concrete induce the compressive strength to be less. In addition, the total porosity is increased, and the thermal conductivity was less than the conventional concrete. Christen et al. [3] developed a more sustainable 3D printable concrete by the replacement of NA with RBW. An existing 3D printable concrete mix is used as reference and adjusted by replacing rate of 64%. The results show a decrease of compressive strength by 25%. Furthermore, studies have explored the use of waste clay bricks as substitutes for sand in roller-compacted concrete pavement, revealing that up to 25% substitution of brick waste for sand does not significantly affect the properties of concrete, but higher substitution ratios can result in increased water absorption [9]. Additionally, investigations on the pore structure and morphology characteristics of recycled fine aggregates from clay bricks as substitutes for sand in green concrete have shown a significant increment in porosity, pore volume, and pore size, indicating the impact of pozzolanic activity and internal curing [10]. SEM results showed that the mechanical interlocking of the interfacial transition zone and the compactness of reaction rim strengthened effectively with the incorporation of RBW.

Moreover, the use of crushed clay bricks as substitutes for natural fine or coarse aggregates in durable concrete has been shown to affect dry density and compressive strength [11]. Geotechnical applications of recycled brick aggregates have also shown favorable characteristics in terms of compaction and shear strength [12]. The values of maximum dry density (MDD) and optimum moisture content (OPM) are evaluated as 2.03 g/cm^3, 11.52 % respectively. Lastly, the design of cement-stabilized macadam mixtures with varying replacement ratios of recycled brick aggregates is being investigated to improve the content of recycled materials. Results showed that mixtures of recycled brick stabilized by cement with different replacement ratios had good mechanical properties, and the 7 days strength of the 55% replacement ratios mixtures reached 7.11 MPa, which exceeded the requirements of 3 MPa and 5 MPa for the pavement sub-base and base of the Chinese specification, respectively [13].
In this paper, we aim to further explore the potential of utilizing RBW in pavement construction, in the manufacture of CTB through providing a comparison of a several mechanical properties. The objective of this research is to analyze the effect of graded replacement of varying granular fractions of (0/3) mm and (3/8) mm, as well as 100% of RBW, on the durability properties in

road construction. Modified Proctor tests were conducted to evaluate the fresh state characteristics, while compressive strength, tensile strength, porosity, water absorption by immersion, thermal conductivity, and abrasion resistance were measured. The findings of this study could potentially have significant implications for sustainable construction practices, particularly in developing countries where brick construction is still prevalent.

2 Materials

The materials used in this study included Portland cement (CEM II 42.5) in accordance with EN 197-1, natural crushed aggregates (sand of size 0/3 mm and coarse gravels of fractions 3/8, 8/15, and 15/20 mm), and recycled brick waste (RBW) were obtained from the waste of fired bricks originating from the brick factory in Medea, located in the northern region of Algeria and included (sand of size 0/3 mm and coarse gravels of fractions 3/8, 8/15, and 15/20 mm). The physical and chemical properties of the cement and all aggregates are presented in Tables 1, 2 and 3. The recycled brick waste used in this study is shown in Figure 1. The grading curves of the aggregates used are shown in Figure 2.

Table 1: Chemical composition of Portland cement

SiO_2	**CaO**	**Al_2O_3**	**Fe_2O_3**	**MgO**	**SO_3**	**L.I**	**K_2O**	**CaO_{Free}**	**Na_2O**
23.83	56.35	6.06	4.66	2.44	2.37	2.23	0.83	0.66	0.58

Table 2: Physical properties of aggregates

Test items		**Fractions (mm)**			
		0/3	**3/8**	**8/15**	**15/20**
NA	Specific density (kg/m^3)	2690	2590	2610	2650
	Water absorption (%)	3.45	1.96	1	0.46
	Los Angeles (%)	/	32.4	25.95	24.88
	Sand equivalent (%)	78	/	/	/
	Fineness modulus	3.04	/	/	/
	Methylene blue value (%)	0.5	/	/	/
RA	Specific density (kg/m^3)	2340	2280	2150	2000
	Water absorption (%)	18.2	16.8	14.03	10.21
	Los Angeles (%)	/	34.16	23.72	30.23
	Sand equivalent (%)	69.11	/	/	/
	Fineness modulus	2.63	/	/	/
	Methylene blue value (%)	0.5	/	/	/

Table 3: Fluorescent Chemical analysis of aggregates

Component	**Al_2O_3 (%)**	**SiO_2 (%)**	**Fe_2O_3 (%)**	**CaO (%)**	**SO_3 (%)**
NA	6.77	0.59	2.50	90.14	/
RBW	18.73	49.28	9.56	20.08	2.45

Figure 1: Recycled brick waste used in this study

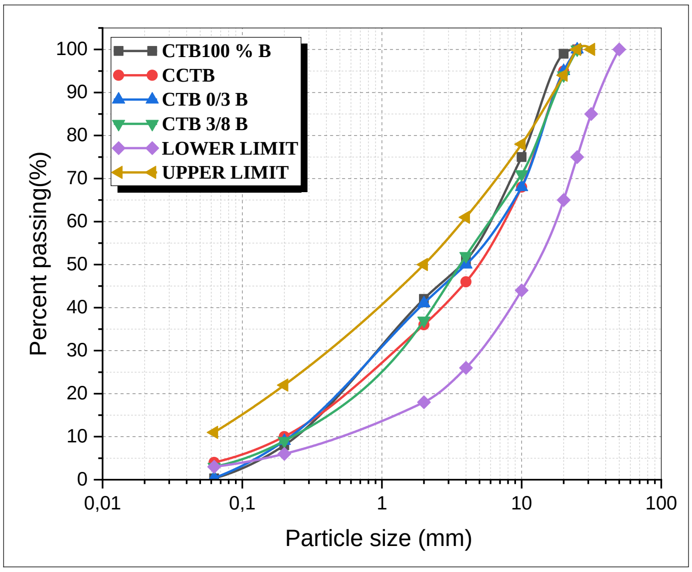

Figure 2: Gradation curves for the CTB

3 Experimental Program

The experimental program in this study aimed to investigate the impact of replacing recycled brick waste (RBW) as a fraction of fine and coarse (0/3 and 3/8 mm) and 100% RBW in CTB. The formulation of the control cement treated base (CCTB) followed the NF EN 14227-1 [14] standard, with a fixed cement percentage of 6% and optimal water quantity determined through proctor modifier tests. The variables in the study were the type of aggregate used. Four samples were produced for each CTB mixture, and the results were obtained as an average of three readings. The CTB samples included: CCTB, consisting of natural aggregate treated with cement; CTB 0/3 B, with a recycled fraction of 0/3 and the remaining fraction of natural aggregate; CTB 3/8 B, with a recycled fraction of 3/8 and the remaining fraction of natural aggregate; and CTB 100% B, which used cement-treated recycled brick waste as the aggregate. Table 4 presents the quantities of materials used in the mixtures for performance evaluation.

Table 4: Chemical composition and characteristics of the materials used

Abbreviation	**Grain size-nominal dimensions (mm)**	**Proportion of mixtures (%)**
	0/3	44
	3/8	21
CTB	8/15	17
	15/20	18

A mixer with a capacity of 150 liters was used to manufacture the CTB mixtures in a laboratory environment with a temperature of 20°C and 50% relative humidity. After placing the mixed materials into molds on the vibrating table, they were vibrated for 1 minute after each layer. The specimens were removed after 24 hours and kept in water at 20°C until the testing age. The method for preparing the mixtures is illustrated in Figure 3.

Figure 3: Method for preparing the mixtures of CTB

The experimental program in this study involved conducting tests for fresh and hardened properties in accordance with the standards listed in Table 5. The testing of fresh concrete included the dry density–water content relationships were determined by conducting modified compaction tests on CTB materials in accordance with the ASTM standard [15]. It is noted that the sample was compacted in five layers in a 102 mm diameter by 127 mm high mold with the application of 56 blows per layer for the compaction testing. The compaction was carried out with a 4.5 kg hammer dropped from a height of 450 mm.
The testing of hardened CTB included the compressive strength, tensile strength, water absorption, porosity, thermal conductivity, and abrasion test. The compressive strength was measured in cubic specimens of 10x10x10 cm^3 at 3, 7 and 28 days of curing, according with Standard EN 196-1 [16]. All CTB specimens are subjected to tensile strength test was measured on prismatic specimens of 7x7x28 cm^3 at 3, 7 and 28 days of curing, this test was performed in accordance with Standard EN 196-1 [16]. In regards to the porosity accessible to water test, three cubic specimens 7x7x7 cm^3 from the were used to evaluate their porosity in water up to 28 days, according to the NF P18-459 [17]. The water absorption by immersion test was determined on CTB prismatic specimens of 7x7x28 cm^3, as per ASTM C642 [18]. After 28 days of curing, the specimens were dried in 105± 5˚C. the specimens were cooled down by natural heat loss after 24 hours of oven drying period. For about 24 hours, the specimens were immersed in normal curing water. The water absorption of the mixes shows the difference between saturated mass and oven-dried mass. Thermal conductivity is one of the means that are generally used with the aim to assess with precision the thermal characteristics of CTB. The thermal conductivity test was performed using the technique of the hot wire by CT-meter on prismatic specimens of 7x7x28 cm^3 according to Standard (NF EN 933-15)[19]. The abrasion resistance of the CTB studied was measured using the Cantabro test. This test determines the mass loss of a cylindrical specimen of similar diameter and height ($D = H = 10$ cm). The test specimens are rotated in Los Angeles drum for 300 revolutions according to Standard (ASTM C1747) [20].

Table 5: Tests protocol

	Tests	**Specimen (mm)**	**Standards**
Aggregate	Grain size distribution	/	EN 933-1
	Density	/	EN 1097-3
	Water absorption	/	EN 1097-6
	Los Angeles (%)	/	EN 1097-2
	Sand equivalent	/	EN 933-8
	Methylene blue value	/	EN 933-9
CTB	Proctor compaction	Cylinder	ASTM
	Compressive strength	Cube (10*10*10 cm3)	EN 196-1
	Tensile strength	Prismatic (7*7*28 cm^3)	EN 196-1
	Water absorption	Prismatic (7*7*28 cm^3)	NBN B15-215
	Porosity	Cubic samples of (7*7*7)	NF P18-459
	Thermal conductivity	Prismatic (7*7*28 cm^3)	NF EN 933-15
	Abrasion test	Cylinder ($D = H = 10$ cm)	ASTM C1747

4 Results and Discussion

4.1 Proctor Compaction

The variation of the dry density and water content for estimation of optimum water content (OWC) and maximum dry density (MDD) of the different mixtures are presented in Figure 4.

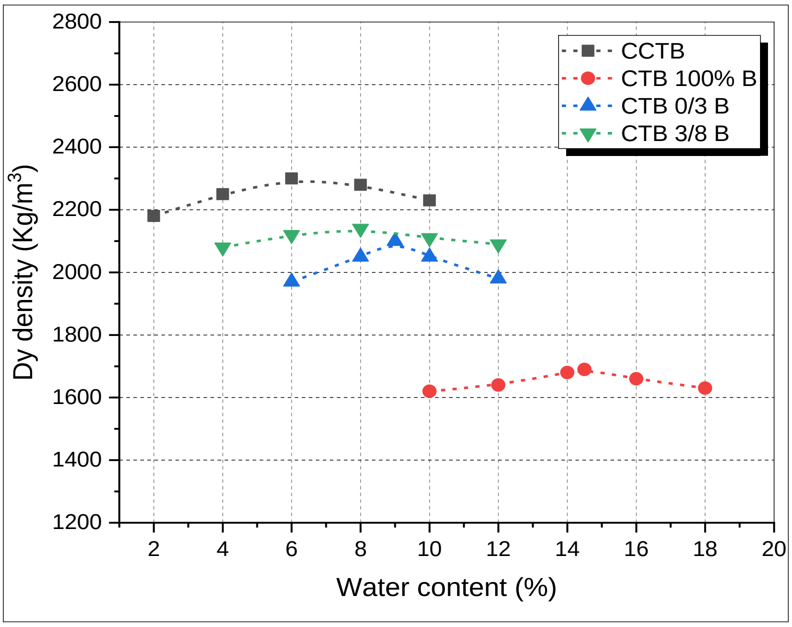

Figure 4: Variation of dry density with water content

The results of the compaction tests showed that the control mix (CCTB) had the highest MDD value of 2300 kg/m3 with the lowest OWC value of 6%. Partial replacement of NA with RBW resulted in a decrease in MDD, with CTB 3/8 B, CTB 0/3 B, and CTB 100% B showing approximately 7%, 9%, and 26% decrease in dry density, respectively, compared to CCTB. Conversely, the water content results showed an increase in OWC, with CTB 100% B showing the highest increase of about 59%, followed by CTB 0/3 B with a 33% increase, and CTB 3/8 B with a 25% increase, compared to CCTB. This suggests that the addition of crushed brick waste decreases MDD and increases OWC due to the lower density and higher water absorption capacity of crushed brick waste. Similar findings have been reported by other researchers [11, 12, 21], who have confirmed that the replacement of NA with RBW leads to an increase in OWC and a decrease in MDD. Additionally, Ajay et al. [22] showed that the incorporation of RBW content leads to the increase of porous crushed clay in the mixtures, which has significant water absorption capacity and may contribute to the slight increase in OWC with increased RBW content in the mixtures.

4.2 Compressive Strength

Figure 5 shows the variation on compressive strength of different CTB mixtures at 3, 7 and 28 days of curing.

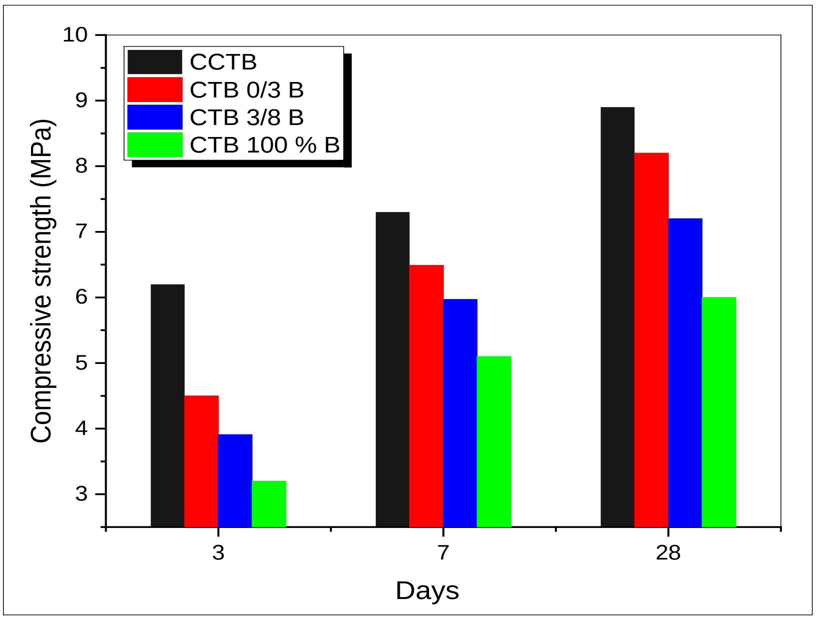

Figure 5: Compressive strength with CTB

The compressive strength results, as shown in Figure 4, revealed a decrease in strength for CTB 0/3 B, CTB 3/8 B, and CTB 100% B at all ages compared to CCTB. At 28 days, the decrease in compressive strength was approximately 8% for CTB 0/3 B, 19% for CTB 3/8 B, and 32% for CTB 100% B compared to CCTB. It was evident that the increase in size of recycled brick waste (RBW) materials had a negative effect on the strength values. This decrease in strength could be attributed to the higher porosity and water absorption of recycled aggregates, as reported by previous studies [23]. These findings are consistent also with other research [8]that showed a decrease in compressive strength of approximately 15% when RBW was used as a fine aggregate, 25% when used as a coarse aggregate, and 30% when used as both fine and coarse aggregate. According to the cement treated Base Guide [24], the minimum of the CTB compressive strength in 7 days is 2.1 MPa. The results indicate that all CTB mixtures achieved the minimum compressive strength, which allows them to be used.

The correlation between compressive strength values and porosity values was high ($R^2 = 0.99$) according to Figure 6, indicating that compressive strength of CTB mixtures was very sensitive to porosity, which increased with the use of RBW materials. This confirmed the relationship between porosity and compressive strength of CTB mixtures, with an increase in porosity leading to a decrease in compressive strength. This finding is consistent with the research by Christen et al. [3] that reported a decrease in resistance of concrete with increased porosity. The addition of highly porous RBW to the concrete mixture thus reduces its resistance, confirming the obtained results.

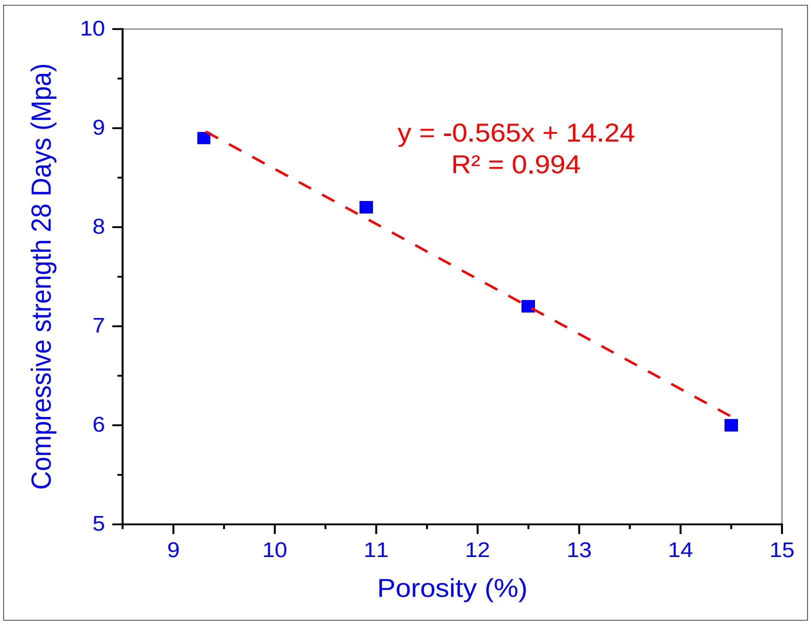

Figure 6: Correlation between compressive strength and porosity of CTB mixes

4.3 Tensile Strength

Figure 7 shows the variation on tensile strength of different CTB mixtures at 3, 7 and 28 days of curing.

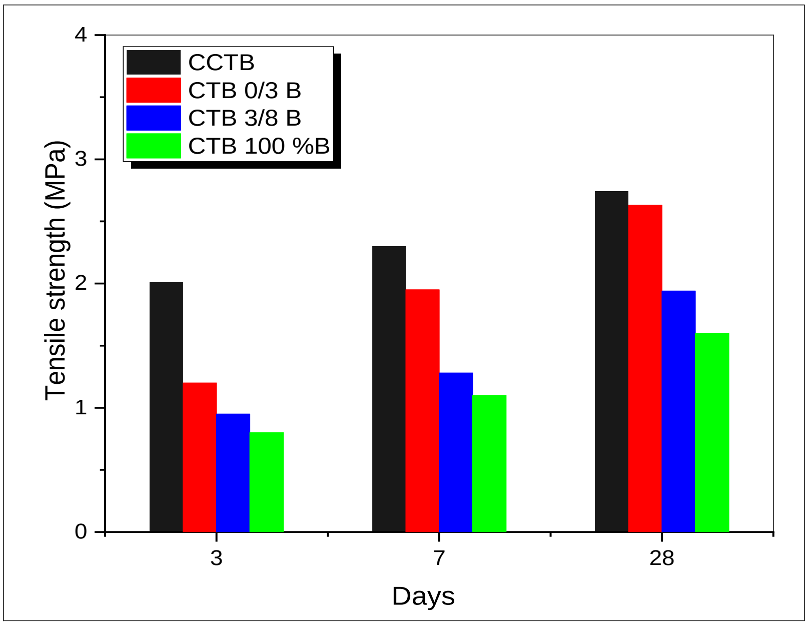

Figure 7: Tensile strength with CTB

The results of the tensile strength tests, as shown in Figure 7, revealed that CTB with 100% RAB materials experienced a significant decrease of approximately 42% compared to their reference CCTB. When RAB was used as a fine aggregate in the production of CTB 0/3 B, the

tensile strength decreased by about 5%. Similarly, when RAB was used as a coarse aggregate in the production of CTB 3/8 B, the tensile strength decreased by about 30%. Previous research [8] has attributed this degradation of resistance in mixtures with RBW to the low crushing resistance of RBW particles in comparison to natural aggregate particles.
The low resistance of RBW aggregates can be explained by their higher vacuum ratio and low solid ratio compared to natural aggregates, which weakens RBW aggregates in comparison to natural aggregates. According to the cement treated Base Guide [24], the minimum of the CTB tensile strength in 7 days is 0.7 MPa. The results indicate that all CTB mixtures achieved the minimum tensile strength, which allows them to be used.

4.4 Water Absorption by Immersion

Figure 8 illustrates the water absorption by immersion of various CTB mixtures after 28 days of curing.

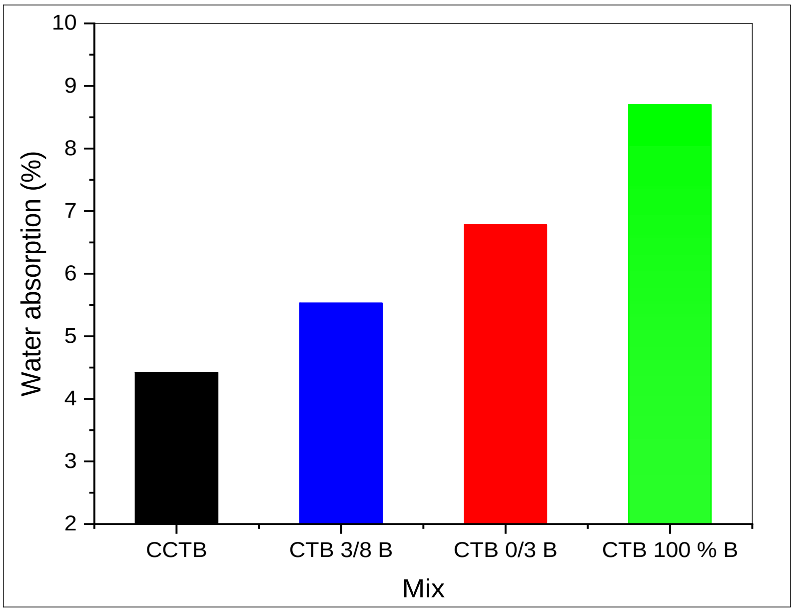

Figure 8: Water absorption by immersion of CTB at 28 days

The results show a gradual increase in absorption values with the use of RBW as gravel (3/8 mm), sand (0/3 mm), and total replacement of NA by RBW. The absorption values increased by 20%, 25%, and 45%, respectively, compared to the mixture using 100% natural aggregates. This trend can be explained by the increase in internal porosity caused by the use of RBW, which is characterized by its high porosity and greater water absorption compared to NA.
This finding is consistent with that of [7], who concluded that the porosity of RBW and its greater water retention will lead to greater water absorption in the RBW concrete.

4.5 Porosity

Figure 9 shows the effect of RBW on the porosity of all CTB mixtures.

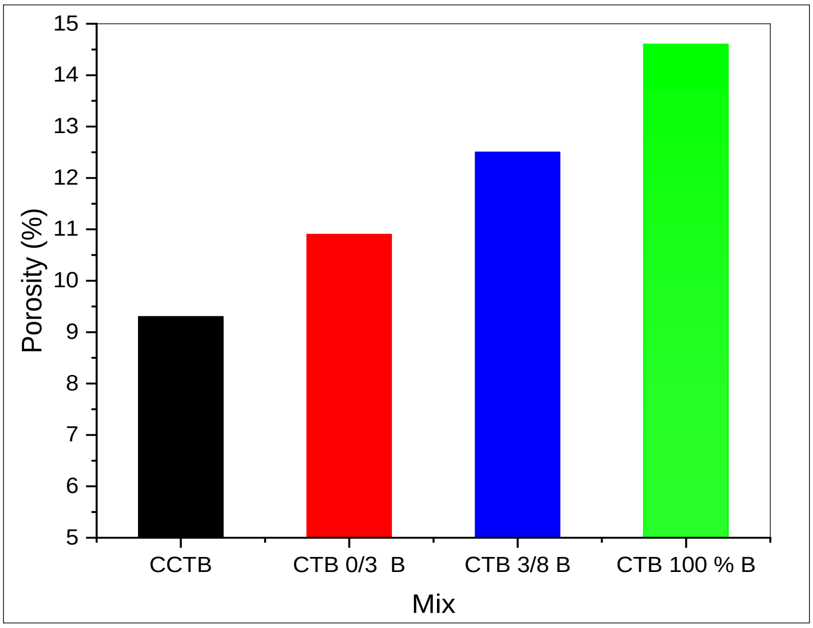

Figure 9: Porosity results of CTB samples at 28 days

The results indicate that porosity increased with the use of RBW. When RBW was used as sand (0/3mm) in CTB 0/3B, porosity increased by 17%. When RBW was used as gravel (3/8mm) in CTB 3/8B, porosity increased by 34%. The complete replacement of NA by RBA in CTB 100% B resulted in high porosity (about 56%) compared to the various mixtures of CTB. This increase in porosity occurred due to the use of recycled brick aggregates, which are characterized by a higher porosity than natural aggregates. This finding is consistent with the results reported by [3, 8] regarding the high porosity of RBW, which increases the overall porosity of the concrete mixture containing RBW.

Figure 10 shows Relationship between porosity and compressive strength of CTB mixtures.

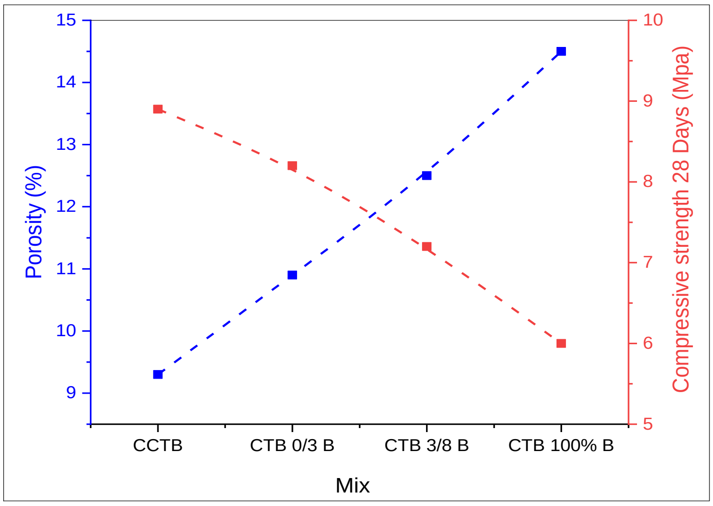

Figure 10: Relationship between porosity and compressive strength of CTB mixes

It can be observed that the compressive strength of CTB is highly sensitive to the porosity induced by the use of RBW materials. The tendency of compressive strength decreased as porosity increased.

4.6 Thermal Conductivity

The thermal conductivity results of the produced CTB are shown in Figure 11.

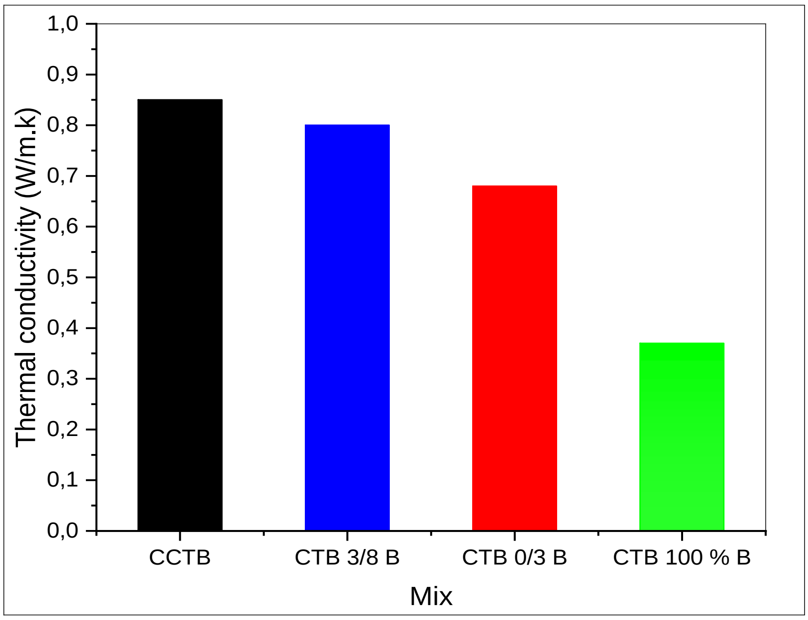

Figure 11: Thermal conductivity of CTB

The replacement of natural aggregates by recycled brick aggregates leads to a decrease in the thermal conductivity of CTB mixes, where when using RBW as gravel (3/8mm) and sand (0/3mm), the thermal conductivity values of CTB 3/8B and CTB 0/3B was less than CCTB by 6% and 20% respectively compared by CCTB, Thermal conductivity is reduced by more than 55% for a complete substitution of NA by RBW.

This result demonstrated that the type of aggregate has an important influence on the thermal conductivity of the CTB. This improvement in the thermal conductivity with the introduction of RBW is explained by low density and high porosity of RBA compared to NA [8, 25].

Atyia et al [8] reported the dry density and porosity is directly linked to the thermal conductivity of the concrete.

They are the main factors influencing the thermal properties of concrete. With increasing density, the porosity decreases, and thermal conductivity increases and vice versa.

Figure 12 shows the evolution of thermal conductivity and porosity as function of CTB mixtures.

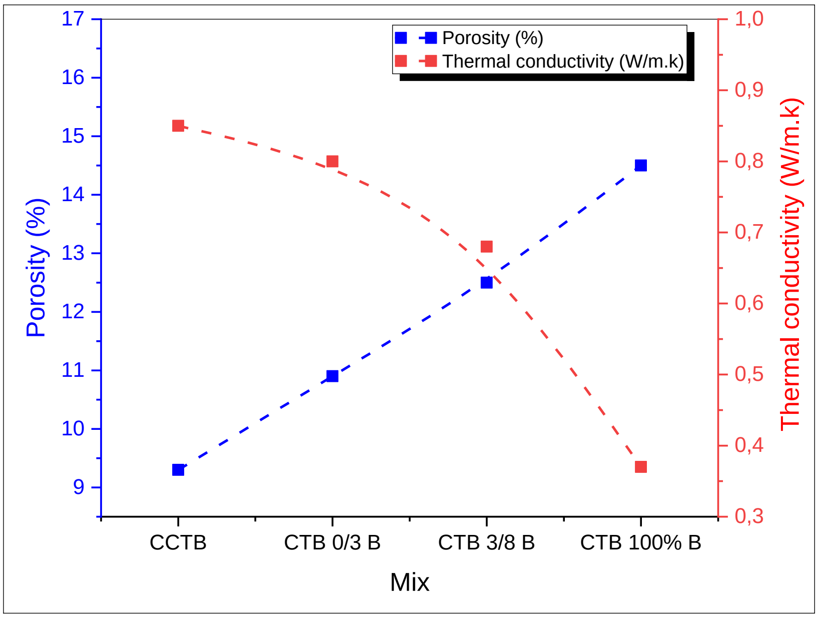

Figure 12: Relationship between porosity and Thermal conductivity of CTB mixes

Where the greater the porosity, the lower the thermal conductivity values and vice versa, which indicated that there is a direct relationship between them. The results also show that there is an equilibrium point between thermal conductivity and porosity for the CTB 3/8 B mixture.

4.7 Abrasion Tests (CANTABRO Loss)

The abrasion resistance test or Cantabro test was performed to estimate the internal cohesion among the particles. The samples were submitted to the Los Angeles drum without any balls, and the device was set to rotate for 200 cycles, in accordance with [20]. The variation in abrasion resistance evaluated by the Cantabro test of the different CTB mixtures studied is shown in Figure 13.

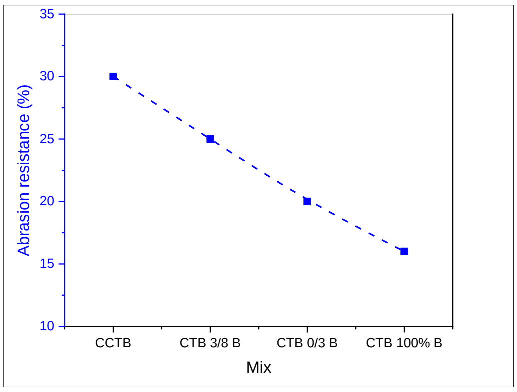

Figure 13: Abrasion test of CTB mixes

The CTB 3/8 B mix showed a reduction in abrasion loss of approximately 17% compared to the CCTB mix. However, the CTB 0/3 B and CTB 100% B mixes showed a reduction of 33% and 47%, respectively, in comparison to the CCTB mix. The abrasion resistance was affected in our case by the nature of the aggregates used. The mixes containing RBW showed higher abrasion resistance compared to the mixes containing NA. It can be concluded that good quality lightweight aggregates have better abrasion resistance.

4.8 SEM Analysis

To support the mechanical performance, scanning electron microscopy (SEM) analyses of CTB mixtures were performed, and the results are presented in Figure 14.

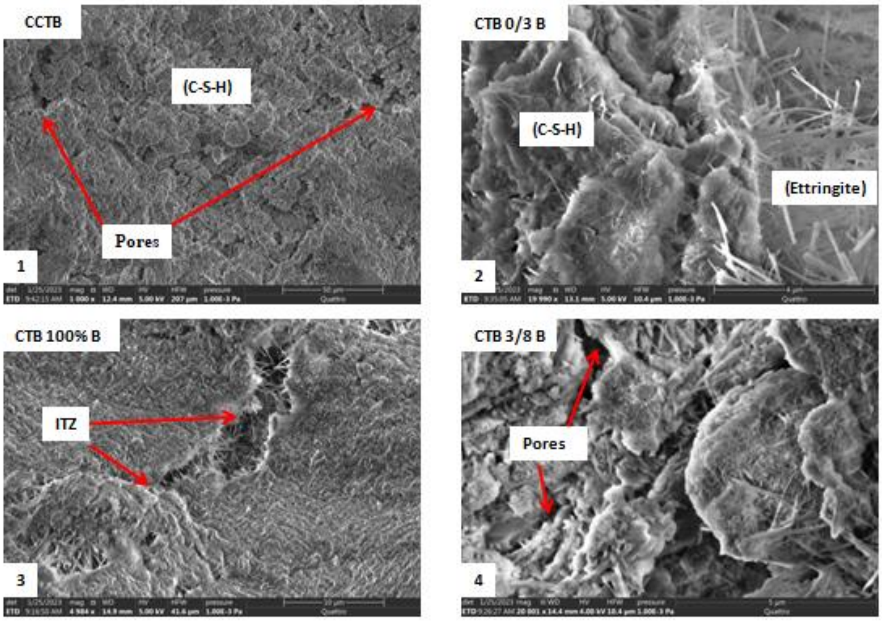

Figure 14: SEM images of CTB mixes : (1) CCTB; (2) CTB 0/3 B; (3) CTB 3/8 B; (4) CTB 100 % B

As shown in Figure 12 (1), the CCTB mix had a denser matrix with minimal porosity. However, when RBW was used as the fine aggregate (sand) in the CTB 0/3 B mix, as depicted in Figure 13 (2), new CSH hydrates were created due to the high pozzolanic impact of RBW particles. The use of RBW as a coarse aggregate in the CTB 3/8 B mix, as shown in Figure 13 (3), resulted in more pores compared to the CCTB mix due to RBW's effect on the internal bonding of particles. The CTB 100% B mix, produced by replacing NA entirely with RBW, revealed a smoother, looser surface and more pores in the microstructure, as depicted in Figure 14 (4).
These findings are consistent with the mechanical characteristics of the CTB mixtures and can be used to explain their performance. This result is in line with previous studies conducted by [4, 10, 26].

5 Conclusion

This study demonstrated that the use of recycled brick waste not only has a significant impact on road engineering but also contributes to global environmental protection. In addition, based on the analysis of the experimental results, the following conclusions can be drawn:

- The size of recycled brick waste particles significantly affects the characteristics and mechanical properties of the maximum dry density-optimum water content. The RBW (recycled brick waste) materials have lower densities and higher water absorption capacities than NA (natural aggregates).
- The compressive strength results indicate good performance for all CTB (cement treated base), highlighting the suitability of RBW to replace NA. The incorporation of recycled brick aggregates in the form of sand (0/3 mm) and gravel (3/8 mm) in CTB slightly decreases their mechanical performance.
- The use of RBW in the preparation of CTB considerably increases its ability to absorb water. CTB blends containing RBW are characterized by high porosities compared to CCTB.
- In addition, replacing natural aggregates with recycled aggregates improves thermal conductivity in the CTB.
- The incorporation of RBW significantly increases the porosity and total pore volume of CTB. The pozzolanic activity of fine RBW contributes to the improvement in the satisfactory compactness of ITZ between the fine RBW and cement matrix.
- CTB with RBW showed improvement in abrasion resistance compared to that in CTB made with 100% NA. Incorporating RBW in the form of gravel (3/8 mm), sand (0/3 mm), and 100% RBW in CTB led to increased abrasion resistance of 17%, 33%, and 47%, respectively.
- RBW is an interesting alternative as results indicate that all CTB mixtures containing RBW achieved minimum compressive and tensile strength, allowing them to be used in the field of road construction.

Overall, the results show that the mixes containing waste brick exhibit comparable mechanical characteristics and could be used in layers of pavement foundations. Additionally, the durability of these mixes yields better results compared to blends containing natural aggregates.

References

[1] Zheng, L., Wu, H., Zhang, H., Duan, H., Wang, J., Jiang, W., Dong, B., Liu, G., Zuo, J., & Song, Q. (2017). Characterizing the generation and flows of construction and demolition waste in China. Construction and Building Materials, 136, 405-413 https://doi.org/10.1016/j.conbuildmat.2017.01.055.

[2] Mezhoud, S., & Houari, H. (2017). Valorisation des fraisât routiers et produits de démolition pour la fabrication de mélanges granulaires traites aux liants hydraulique. Algerian Journal of Environmental Science and Technology 3(3).

[3] Christen, H., van Zijl, G., & de Villiers, W. (2022). The Incorporation of Recycled Brick Aggregate in 3D Printed Concrete. Cleaner Materials. https://doi.org/10.1016/j.clema.2022.100090.

[4] Hou, Y., Ji, X., Zou, L., Liu, S., & Su, X. (2016). Performance of cement-stabilised crushed brick aggregates in asphalt pavement base and subbase applications. Road Materials and Pavement Design, 17, 120 - 135. https://doi.org/10.1080/14680629.2015.1064466.

[5] Poon, C.S., & Chan, D. (2006). Feasible use of recycled concrete aggregates and crushed clay brick as unbound road sub-base. Construction and Building Materials, 20, 578-585.https://doi.org/10.1016/j.conbuildmat.2005.01.045.

[6] Cavalline, T.L. (2012). Recycled brick masonry aggregate concrete: Use of recycled aggregates from demolished brick masonry construction in structural and pavement grade portland cement concrete.

[7] Dang, J., Zhao, J., Pang, S.D., & Zhao, S.B. (2020). Durability and microstructural properties of concrete with recycled brick as fine aggregates. Construction and Building Materials, 262, 120032.https://doi.org/10.1016/j.conbuildmat.2020.120032.

[8] Atyia, M.M., Mahdy, M.G., & Elrahman, M.A. (2021). Production and properties of lightweight concrete incorporating recycled waste crushed clay bricks. Construction and Building Materials, 304, 124655.

[9] Tavakoli, D., Fakharian, P., de Brito, J. (2022). Mechanical properties of roller-compacted concrete pavement containing recycled brick aggregates and silica fume. Road Materials and Pavement Design 23(8), 1793-1814. https://doi.org/10.1080/14680629.2021.1924236.

[10] Dang, J., Xiao,J., Duan, Z. (2022). Effect of pore structure and morphological characteristics of recycled fine aggregates from clay bricks on mechanical properties of concrete. Construction and Building Materials 358, 129455. https://doi.org/10.1016/j.conbuildmat.2022.129455.

[11] Helmy, S.H., Tahwia, A.M., Mahdy, M.G., & Elrahman, M.A. (2023). Development and characterization of sustainable concrete incorporating a high volume of industrial waste materials. Construction and Building Materials.

[12] Sharma, A., Shrivastava, N. (2022). Geotechnical assessment and large scale direct shear testing on recycled brick aggregates. Materials Today: Proceedings 65, 815-823. https://doi.org/10.1016/j.matpr.2022.03.318.

[13] Wu, J.,Guo, Y.,Shen, A., Dai, Xi., Li, Q., and Ren, G., and Liang, Tianyu (2023), Research on the Performance of Cement Stabilized Recycled Brick Concrete Aggregate Mixtures Made from Construction and Demolition Waste Based on Graded Replacement Plans. Available at SSRN: https://ssrn.com/abstract=4387411 or http://dx.doi.org/10.2139/ssrn.4387411

[14] AFNOR: NF EN 14227-1. Mélanges traités aux liants hydrauliques-Partie 1: Mélanges granulaires traités au ciment, (2005).

[15] Soil, A.C.D.-o. and Rock, Standard Test Methods for Laboratory Compaction Characteristics of Soil Using Modified Effort (56,000 Ft-Lbf/Ft3 (2,700 KN-M/M3)) 12009: ASTM international.

[16] EN, T., 196-1 (equivalence EN 196-1): Methods of Testing Cement—Part 1: Determination of Strength. Turkish Standards Institution, Ankara, TURKEY, 2002. 24.

[17] NF, P., P 18-459, Béton-Essai pour béton durci-Essai de porosité et de masse volumique. Mars, 2010.

[18] ASTM., Standard test method for density, absorption, and voids in hardened concrete. C642-13, West Conshohocken, PA. 2013.

[19] EN ,993-15, Test methods for dense shaped refractory products Part 15: Determination of thermal conductivity by the hot (parallel) wire method. 2006.

[20] ASTM, Standard test method for determining potential resistance to degradation of pervious concrete by impact and abrasion, 2013, ASTM C1747/C1747M.

[21] Kasinikota, P., Tripura, D.D. (2021). Evaluation of compressed stabilized earth block properties using crushed brick waste. Construction and Building Materials 280, 122520. https://doi.org/10.1016/j.conbuildmat.2021.122520.

[22] Sharma, A., Shrivastava, N., Lohar, J. (2023). Assessment of Geotechnical and Geoenvironmental Behaviour of Recycled Concrete Aggregates, Recycled Brick Aggregates and Their Blends. Cleaner Materials 7, 100171. https://doi.org/10.1016/j.clema.2023.100171.

[23] Debieb, F., Kenai, S. (2008). The use of coarse and fine crushed bricks as aggregate in concrete. Construction and building materials 22(5), 886-893. https://doi.org/10.1016/j.conbuildmat.2006.12.013.

[24] Halsted, G.E., D.R. Luhr, and W.S. Adaska, Guide to cement-treated base (CTB)2006.

[25] Bwayo, E., Obwoya, S.K. (2014). Thermal Conductivity of insulation brick developed from sawdust and selected Uganda clays. International journal of research in Engineering and Technology 3(9), 282-285.

[26] Dang, J. Zhao, J. (2019). Influence of waste clay bricks as fine aggregate on the mechanical and microstructural properties of concrete. Construction and Building Materials 228, 116757. https://doi.org/10.1016/j.conbuildmat.2019.116757.

DOI: 10.2478/sspjce-2023-0009

On the Assessment of Actual Compressive Strength of Concrete in Reinforced Columns: Influence of Core Diameter and Slenderness Ratio

Adel Benidir[1], Said Debbakh[1*], Siham Chaibeddra[1]

[1] National Center of Integrated Studies and Research on Building Engineering (CNERIB), El Mokrani New city, 16097, Souidania, Algiers, Algeria

*e-mail: debbakh.cnerib@gmail.com

Abstract

This paper studies the influence of core diameters and slenderness ratio on the assessment of the actual compressive strength of concrete on reinforced-concrete elements. The experiment consists of the preparation of three reinforced concrete columns and the extraction of cores to carry out both destructive (core diameter of 64 mm, 79 mm, and 103 mm) and non-destructive tests. The non-destructive test deals with the propagation of elastic and compressive waves by deriving the ultrasound pulse velocities. The results show that the assessment of the compressive strength of concrete depends strongly on the diameter of cores and the extraction zones. Furthermore, the derivation of the actual compressive strength by referring to the compressive strengths of the cores with a diameter of 64 mm shows a stringent appearance of a size effect. More interestingly, valuable details about the correlation between the concrete compressive strength assessment based on destructive and non-destructive tests are also presented.

Keywords: hardened concrete, compressive strength, ultrasound pulse velocity, core diameter, slenderness ratio

1 Introduction

The large integration of concrete in the civil engineering field has been strongly consolidated by its incisive qualities such as load-carrying capacity, sustainability, and cost. Despite the heterogeneity of the concrete, structures made as a combination of that material and reinforced elements are theorized and certified as a valuable solution to resist quasi-static and dynamic loadings [1 - 3]. However, with the impetus of improving the resiliency of cities, the monitoring of the degradation of reinforced concrete (RC) structures received much interest. Thus, structures made of concrete ceased to be consigned as maintenance-free [4]. Throughout the various indications about the degradation, the strength requirement and the seismic performance of the RC structures, the assessment of the compressive strengths of in-situ concrete is mainly advocated [5, 6]. Three main techniques are used to assess the compressive strength of concrete in-situ. These techniques are based on destructive, semi-destructive and non-destructive methods. The most common destructive method to evaluate the compressive strength of concrete is drilling and crushing cores [7]. One of the advantages of that method is direct access to representative specimens of concrete. Furthermore, crushing cores with a universal testing machine (UTM) provides rapid indications about the quasi-static concrete compressive strengths. However, the non-exhaustive limitation of that time-consuming method is that it breaches the integrity of the structures. Additionally, the strength controlling procedure depends on the estimation of in-place concrete strength variation volume and its accessibility. The semi-destructive methods were developed to compensate for some of the destructive method limitations. The most popular physical and in-field method is the pulling-out testing (CAPO test) [8, 9]. The test consists of the measurement of the pulling-out strength of an insert previously cast into fresh concrete or installed in hardened concrete. Strength relationships between the pulling-out strengths and the compressive strength results could be derived. On one hand, this method limits the damage inflicted upon the structures. Furthermore, the method could be applied to a large surface compared to the potential prospecting area covered by the destructive methods. On the other hand, the influence of parameters such as bearing ring dimensions or depth embedment is considered as important. The non-destructive tests represent methods and techniques that do not undermine the structural safety and integrity of the structure in any way. To this end, transducers and/or sensors are generally used to collect information from the concrete. Subsequently, models are developed to derive an estimation of the concrete compressive strength. For instance, an estimation of the compressive strength of the concrete by using ultrasonic pulse velocity (UPV) measurement has been developed and adopted [10].

Among the presented methods of the assessment of the compressive strength of hardened concrete in-situ, the destructive method is deemed to be the most reliable [11, 12]. However, the application of a direct conversion between the compressive strengths of cores and standard dimension specimens made of concrete should rely on core diameters higher than 100 mm and a slenderness ratio (SR) of 1 or 2 [13]. The slenderness ratio is the quotient (ratio) between the height and the diameter (width) of the core. Otherwise, the estimation of the actual compressive strength of concrete is obtained after the introduction of coefficients, called strength correction factors [14, 15]. These strength correction factors are principally associated with the core diameter, the SR, the presence of reinforcement steel in cores, moisture and damage due to drilling [16]. Further parameters such as, aggregate sizes, core conditioning, number of cores, drilling locations contribute to complete a well-founded method for the concrete strength evaluation upon existing RC structures [17 - 19]. In addition to the latter's, hand mixing of concrete and pouring operation (compaction of concrete, etc.) could further complicate reaching a reliable estimation of the actual strength of concrete. In fact, in many countries, the urgent need to rehouse people or the uncontrolled willingness of the population to access the dwellings makes prosper the appearance of illegal constructions built without referring to building national recommendations. Consequently, casting vertical element with highly variable concrete strength using long and uncontrolled drop chute or with old fashion hand methods raises the risk to build structural element with dispersed concrete strengths [20].

This paper outlines the influence of core diameter and SR on the assessment of the actual compressive strength of concrete on vertical reinforced structural elements (columns). Both non-destructive and destructive tests are performed. The non-destructive test consists of the measurement of the UPV through the concrete in columns and drilled cores. The destructive test refers to extracting and crushing specimens with three different diameters 64, 79 and 103 mm and SR of 1 and 2. The results show that the concrete in columns is affected by a severe strength variation as old fashion hand methods are used. A concrete downgrading has been confirmed by the analysis of core strengths with the largest diameter. The use of low core diameter and sample size pinpoints the importance of the scale effect on interpreting the strengths along the columns. More interestingly, a zone effect has been identified with non-destructive and destructive test methods.

2 Materials and Methods

2.1 RC Elements

An ordinary C25/30 class concrete with a standard consistency has been prepared (hand-mixed concrete) for the experiment. The constitutive elements of the concrete mixture and the compressive strength after 28 days of curing according to [21] and [22] are listed in Table 1. The mean compressive strength of lab-cured molded specimens with a cylindrical shape of 150 mm in diameter and 300 mm in length is 25.37 MPa. The fresh concrete is used to fill three full-scale reinforced columns (labeled C1, C2 and C3) with old fashioned hand method (Figure 1). This method is still extensively used in the majority of regions in the country (Algeria). The dimensions of the columns are 300 cm in high (as a maximum height), and dimension of cross-section is 40 cm x 40 cm. The diameter of the longitudinal reinforcing steel bar was 12 mm and the distance between the extremities of each bar was 15 cm. Equidistant stirrups with a diameter of 8 mm provided the transverse reinforcement bar. Each stirrup was placed every 15 cm. Three zones labelled 1, 2 and 3 are delimited to perform both non-destructive and destructive tests on concrete. To control the concrete qualities on site and to assess the influence of curing conditions, four moulded standard-dimension cylindrical specimens (150 mm × 300 mm) are prepared for each poured column. After demoulding, the specimens were left outside and placed near the filled column to be exposed to the same curing conditions. These specimens are called field-cured specimens (FCS).

Table 1: Mixture proportions of the ordinary concrete (C25/30) and its lab-cured compressive strength

Constituents	Units	Proportions
Cement	kg/m^3	350
Natural Sand from rivers	kg/m^3	464
Natural sand from dunes	kg/m^3	271
Aggregates	kg/m^3	1058
Water	kg/m^3	210
Maximum aggregate size	mm	20
Consistency class		S2 (slump range between 50 to 90 mm)
Mean compressive strength, cylindrical specimen (D = 150 mm, L = 300 mm)	MPa	25.37

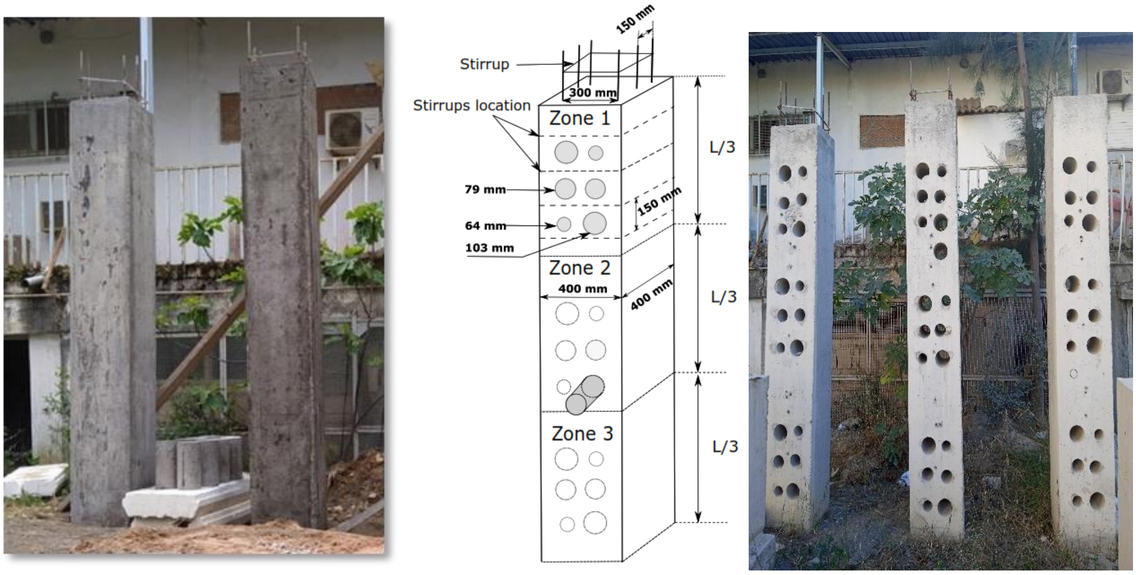

(a) (b) (c)

Figure 1: Reinforced columns (a) Columns after formwok removal (b) Drilling operation plan and delimitation of zones (c) Columns after drilling operation

2.2 Non-Destructive Testing

The measurement of the UPV has been used to perform non-destructive tests according to a standardized procedure [23]. The tests are carried out over the three delimited zones and on standard dimension specimens. The measurement spots on the columns have been pre-selected to be ulteriorly used to drill and extract cores. A portable pundit LAB ultrasonic pulse transmitter is used to generate longitudinal waves (Figure 2). The transmitter is connected to a transducer to emit waves with a nominal frequency of 54 kHz. The waves traveling along the specimens are captured after traversing the concrete by a second transducer (receiver). Direct transmissions are performed, and the wave velocities are automatically derived.

Figure 2: Ultrasound pulse velocity measurement (direct transmission performed on field-cured specimens)

2.3 Destructive Testing (DT)

The crushing tests were performed with a Universal Testing Machine (UTM) with a capacity of 2000 kN (Figure 3a). The applied loading rate in compression is 0.6 MPa/min, following standard recommendations [22]. The drilled cores are cut to study the unexposed volume of concrete in columns. From each extremity of a drilled core, a part of the concrete has been removed (Figure 3b). Before proceeding to the destructive test, the UPV is measured.

(a)

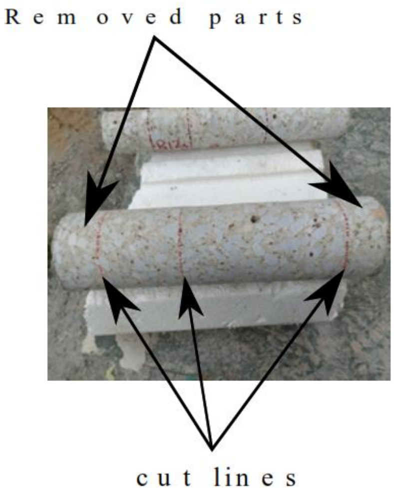

(b)

Figure 3: Destructive test machine and sample preparation: (a) Universal Testing machine (b) Drilled core with a diameter of 103 mm

3 Results and Discussions

3.1 Influence of Core Diameter

Figure 4 shows the evolution of compressive strengths of cores with a SR of 2 as a function of core diameters. The compressive strengths of field-cured specimens with standard dimensions (150 mm in diameter, 300 mm in length) are also mentioned in that figure. The results from whole columns are presented. The columns and the core diameters are color-unified. At the first glance, the results of crushing specimens with a diameter of 150 mm and a length of 300 mm show important differences between the mean compressive strength of lab-cured specimens (given in Table 1) and field-cured specimens (FCS). The mean compressive strengths of the FCS referring to columns, 1, 2 and 3 are 17.69 MPa, 18.49 MPa and 18.41 MPa, respectively. Thus, a difference in the compressive strength up to 7.68 MPa has been observed between strengths of the lab-cured specimens and FCS.

From that figure, and independently from the core diameter, a large discrepancy on the compressive strengths of cores is observed. A marked discrepancy has been identified for a core diameter of 64 mm. For that diameter, the compressive strengths of cores range from 12.85 MPa to 27.91 MPa. For specimens with diameters of 79 mm and 103 mm, the compressive strengths of cores range from 8.33 MPa to 19.12 MPa and from 16.11 MPa to 25.67 MPa, respectively. According to [13] and [25], the compressive strength of cores with diameters ranging from 100 mm to 150 mm and with a SR of 2 are equivalent to the compressive strengths of specimens with a diameter of 150 mm and a length of 300 mm. The application of that direct conversion concerns concretes prepared and conserved under the same conditions. By referring to the data plotted in Figure 4, the compressive strengths of cores with a diameter of 103 mm could be deemed as reliable and representative results. In fact, the strengths of these cores from each column are in majority higher than strengths of the field-cured specimens (83 % (5/6) for column 1, 83 % (5/6) for column 2 and 100 % (6/6) for column 3). This result could be considered as an indication that even though the columns were built with old-fashioned method, the direct conversion for strength assessment of concrete without using strength correction factor is reliable. However, the consistency of that direct conversion has been highlighted by analysing the strength of field cured specimens and large core diameter (103 mm).

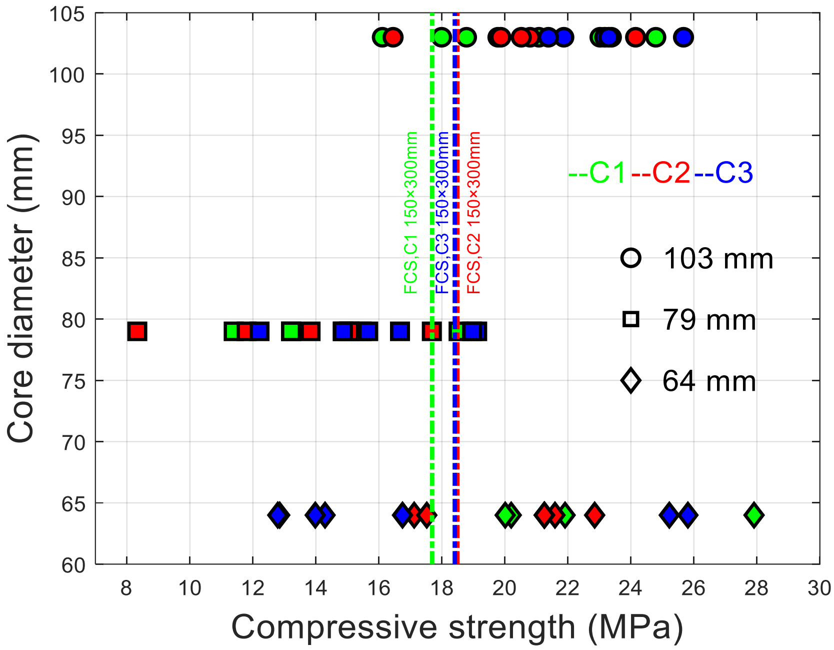

Figure 4: Compressive strengths of cores as function of core diameters

In practice, to estimate the class resistance of an in-place concrete, the estimated characteristic strength derived from core strengths ($f_{ck,core}$) should be compared with the onsite characteristic strength given in standards and code provisions [13, 24, 25]. For instance, according to [24] and [25], the onsite characteristic strengths of C20/25 and C25/30 concrete classes are 17 MPa and 21 MPa, respectively (see appendix). As the number of the cores for one diameter is six in each column, the estimated characteristic strengths of cores, $f_{ck,core}$, are calculated according to approach B cited in [24] and [25]. Thus, $f_{ck,core}$ is given as:

$$f_{ck,core} = minimum \begin{cases} f_{m(n),core} - k_n \\ f_{lowest,core} + 4 \end{cases} \tag{1}$$

where, $f_{m(n),core}$ is the mean strength of cores, n is the number of samples, called also the sample size ($n = 6$), k_n is a coefficient depending on n ($k_{n=6} = 7$) and $f_{lowest,core}$ is the lowest compressive strength value of the cores. It is important to mention that the Grubbs test has been applied to detect outliers. The results of the calculation associated with core diameters of 103 mm, 79 mm and 64 mm and the standard deviation (std) of the core compressive strengths are given in Tables 2, 3 and 4 respectively.

Table 2: Estimated characteristic strength, $\boldsymbol{f_{ck,core(D)}}$, for each column, core diameter D = 103 mm, SR = 2

Parameters (SR = 2)	**Column 1**	**Column 2**	**Column 3**
$f_{m(n),core\ (D=103mm)}$ (MPa)	20.29	20.26	23.13
Std	3.27	2.46	1.50
$f_{ck,core\ (D=103mm)}$ (MPa)	13.29	13.26	16.13

Table 3: Estimated characteristic strength, $\boldsymbol{f_{ck,core\ (D)}}$, for each column, core diameter D = 79 mm, SR = 2

Parameters (SR = 2)	**Column 1**	**Column 2**	**Column 3**
$f_{m(n),core\ (D=79mm)}$(MPa)	14.47	13.59	16.25
Std	2.47	3.21	2.62
$f_{ck,core(D=79mm)}$(MPa)	7.47	6.59	9.25

Table 4: Estimated characteristic strength, $f_{ck,core\ (D)}$, for each column, core diameter D = 64 mm, SR = 2

Parameters (SR = 2)	**Column 1**	**Column 2**	**Column 3**
$f_{m(n),core\ (D=64mm)}$ (MPa)	20.69	20.27	18.14
Std	4.82	2.36	5.86
$f_{ck,core(D=64mm)}$ (MPa)	13.69	13.27	11.14

From Table 2, the estimated characteristic strengths derived from the core strengths with a diameter of 103 mm and for columns 1, 2 and 3 are 13.29 MPa, 13.26 MPa and 16.13 MPa, respectively. The difference between the limit of a valid classification of a C25/30 concrete class and the results of the estimated characteristic strengths is up to 7.74 MPa. Accordingly, a concrete downgrading should be applied over each column. In consequence, and according to standard provision [13, 24, 25], the concrete compressive strengths associated with columns 1, 2 and 3 should be ranked as C12/15, C12/15, and C16/20 class concrete, respectively. Thus, despite a valid concrete formulation of the concrete in the laboratory (targeted class of C25/30), the experiment illustrates the influence of parameters such as, curing conditions, drilling operation, pouring and preparation method in lowering the characteristic strengths of cores of in-place concrete.

By referring to Tables 3 and 4, the analysis of the mean and the characteristic compressive strengths of cores with diameters of D = 79 mm and D = 64 mm shows that cores with a diameter of D = 64 mm provide much more resistance compared to cores with a diameter of D = 79 mm. This result has been observed over the three columns. Furthermore, the calculation of the characteristic strengths of cores also shows scattering results as the core diameter is reduced. This observation could be deduced by analyzing the evolution of the standard deviation values. More interestingly, the evolution of the characteristic compressive strength of cores as the diameter is reduced could be considered as a stringent indication about the appearance of a size effect. The size effect refers to the appearance of unexpected core strengths as the scale variation of cores is applied. For instance, the occurrence of that effect could be detected when the evolution of the compressive strengths of cores is not monotonic as the core diameter is progressively reduced for a constant SR [26]. In this perspective, half number of cores (50 %) with a diameter of 64 mm from 18 specimens provide compressive strengths higher than the on-site characteristic strengths of C25/30 class concrete (21 MPa). In comparison with the compressive strengths of cores with a diameter of 79 mm, the resistances of these specimens never exceed that value. The derivation of the actual strength and the class of the concrete by using core diameters less than 100 mm should be performed by introducing strength correction factors. This part will not be covered in this paper. The analysis of the characteristic compressive strength of cores as the core diameter is varied and the size sample (number of cores) is low shows clearly that, the approach B given in [24, 25] and expressed by (1) could be considered as severe. In fact, the calculation shows that the derived characteristic strengths are totally dependent on the coefficient k which implies a large deviation from the mean compressive strength of cores. Finally, to ascertain the appearance of a size effect, the influence of the drilling operation should be examined thoroughly as the drilling operations were performed at different locations along the vertical element. This parameter could probably have the influence on scattering the DT results. Thus, the influence of drilling locations will be discussed in the following section.

3.2 Influence of Drilling Location

Figure 5 shows the distribution of the core compressive strengths as a function of the drilling zones. The mean compressive strength and standard deviation (std) are given in Table 5. It could be observed that the zone least affected by the scatter of the compressive strength is the medium zone (zone 2). This observation is confirmed by the statistics. For instance, the value of the standard deviation of the core compressive strength with a diameter of 103 mm and drilled from the medium zone (zone 2) is 1.65. Comparatively, the values of the standard deviation derived from zone 1 (upper zone) and zone 3 (lower zone) are 2.83 and 3.02, respectively. Furthermore, this trend is confirmed and more marked as the core diameter is equal to 79 mm. For this diameter, the limitation of the lateral variation of the compressive strength of concrete has been achieved by selecting symmetrical emplacements for drilling (see Figure 1b). Additionally, the second important observation is the appearance of a zone effect, independently from the core diameter. It is worth noting that the mean compressive strength of the cores drilled from zone 1 (upper zone) is less than the mean compressive strength of the cores extracted from zone 2 and 3. This observation is confirmed whatever the core diameter. This phenomenon has been previously identified by authors and could be in relationship with critical factors in determining core strength such as method of compaction and the workability of concrete [12, 19]. More interestingly, the third important point to highlight is that the new representation of the mean compressive strength of cores as function of the drilling zone confirms the appearance of a size effect as a core diameter of 64 mm is used. The difference between the mean compressive strength of cores with diameters of 64 mm and 79 mm is quasi-constant and higher than 4 MPa. However, to confirm the consistency of these conclusions, the analysis of the compressive strength of cores with a SR of one might be performed. The next section will also treat the importance of the SR in the identification of a likely critical and/or recommended zone for drilling.

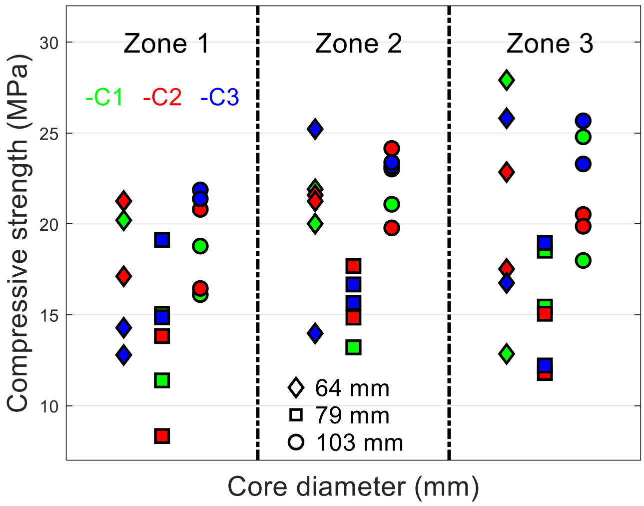

Figure 5: Distribution of the compressive strengths of cores as function of drilling zones, SR = 2

Table 5: Mean compressive strength of cores as function of drilling zones, SR = 2

	***D* = 103 mm**		***D* = 79 mm**		***D* = 64 mm**	
	$f_{m(n),core}$	Std	$f_{m(n),core}$	Std	$f_{m(n),core}$	Std
Zone 1 (upper)	19.45	2.83	13.76	3.65	17.82	3.60
Zone 2 (medium)	22.43	1.65	15.21	1.82	20.66	3.70
Zone 3 (lower)	22.02	3.02	15.34	3.02	20.61	5.83

3.3 Influence of the Slenderness Ratio

Tables 6, 7 and 8 show the calculation of the characteristic strengths of cores from the three columns with diameters of 103, 79 and 64 mm, respectively for a SR of 1. The straightforward way to assess the compressive strength of the in-place concrete is to deal with the characteristic strength of cores with a diameter of 103 mm. Thence, the estimated characteristic strength derived from DT applied on cores with that diameter are 13.95 MPa, 13.40 MPa, and 13.35 MPa for column 1, 2 and 3, respectively (see Table 6). To derive the concrete grade in columns, the obtained characteristic strengths should be compared with onsite characteristic strengths of molded cubic specimens with a lateral dimension of 150 mm. Thus, the strength of the in-place concrete in the three columns should be ranked according to [13, 25] provisions as a C12/15 (see appendix). In consequence, the DT results from cores with a diameter of 103 mm and with a SR of 1 and 2 (see part 3.1) confirm the severe downgrading of concrete by following the approach B in [24] and [25]. It is important to point out that this ascertainment has evolved as one drilling operation served to extract cores with a SR of 1 and 2. Furthermore, for a targeted concrete class of C25/30, the conventional assumption that the characteristic strengths of cores with a SR of 1 is higher than the characteristic strength of cores with a SR of 2 has not be confirmed.

For small diameter, the analysis of the characteristic strengths of cores over the three columns and for the cores with diameters of 64 and 79 mm confirms once more the appearance of a size effect as a core diameter of 64 is used. In fact, the characteristic strengths of cores with a diameter of 64 mm are higher than those of cores with a diameter of 79 mm. The maximum difference in the strength assessment has been detected in column 1 and is up to 54 %. This concrete strength variation could be originated from various parameters such as the influence of drilling zone. To confirm the presence of a zone effect as observed for cores with a SR of 2, Figure 6 shows the distribution of the compressive strengths of cores as function of the drilling zone for cores with a SR of 1. The mean compressive strengths and the strength standard deviations of cores are given in Table 9. From that table and in accordance with the conclusion made for a SR of 2, the upper zone contributes to lowering the characteristic strength of concrete whatever the core diameter. In fact, the mean compressive strength of cores drilled from the upper zones are generally less than the mean compressive strength of cores in each column. For instance, the mean compressive strength of cores with a diameter of 103 mm are all higher than the mean compressive strength of cores in zone 1 (19.25 MPa). According to the data analysis made over the DT results of cores with a SR of 1 and 2 and extracted from columns, the selection and the use of drilling zone located in the top zone to assess the compressive strength of the element could not be a representative way to conduct a reliable estimation. However, in this study, the use of specimens with a SR of 1 could be a valuable way to confirm or infirm the appearance of a size effect.

Table 6 : Mean and characteristic compressive strength of cores, SR = 1, *D* = 103 mm

Parameters (SR = 1)	**Column 1**	**Column 2**	**Column 3**
$f_{m(n),core}$ (MPa)	20.96	20.40	20.35
Std	2.03	1.94	1.88
$f_{ck,core\ (D=103mm)}$ (MPa)	13.95	13.40	13.35

Table 7 : Mean and characteristic compressive strength of cores, SR = 1, *D* = 79 mm

Parameters (SR = 1)	**Column 1**	**Column 2**	**Column 3**
$f_{m(n),core}$ (MPa)	14.04	15.53	18.02
Std	1.33	2.51	2.15
$f_{ck,core\ (D=79mm)}$ (MPa)	7.04	8.53	11.02

Table 8 : Mean and characteristic compressive strength of cores, SR = 1, *D* = 64 mm

Parameters (SR = 1)	**Column 1**	**Column 2**	**Column 3**
$f_{m(n),core}$ (MPa)	17.82	17.71	20.06
Std	2.58	2.31	2.33
$f_{ck,core\ (D=64mm)}$ (MPa)	10.82	10.71	13.06

Table 9 : Mean compressive strength of cores as function of drilling zone (SR=1)

(SR =1)	***D* = 103 mm**		***D* = 79 mm**		***D* = 64 mm**	
	$\boldsymbol{f_{m(n),core}}$	**Std**	$\boldsymbol{f_{m(n),core}}$	**Std**	$\boldsymbol{f_{m(n),core}}$	**Std**
Zone 1 (upper)	19.25	1.48	14.28	2.14	17.61	1.58
Zone 2 (medium)	20.99	2.07	15.73	2.24	18.21	3.37
Zone 3 (lower)	21.45	1.41	17.59	2.48	19.78	2.08

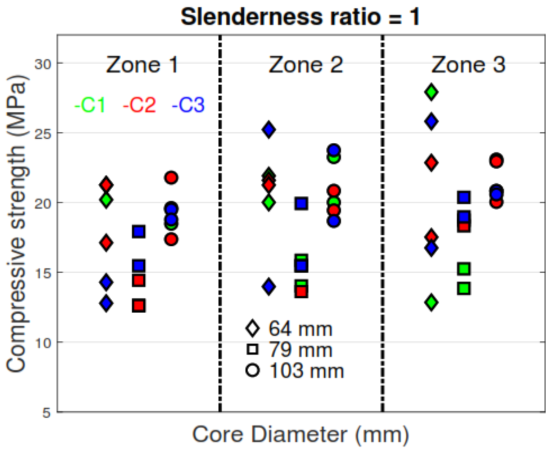

Figure 6: Distribution of the compressive strengths of cores as function of drilling zones, SR = 1

3.4 Ultrasonic Pulse Velocity (UPV) Testing

The UPV measurements are performed on columns (at core picking markers) using a longitudinal compression wave generated by a piezoelectric transmitter at a nominal frequency of 54 kHz and collected by a piezoelectric receiver (plane transducer). The European standard recommends to use grease to ensure perfect acoustic coupling between the column surface and the faces of the transducers [23]. The UPV measurements were made on all three areas (top, middle and bottom of each reinforced columns, as shown in Figure 1) at different curing ages of 7, 14, 21 and 28 days. The locations were chosen carefully, to avoid reinforcement bars, and to operate after that a valid core extraction from each measurement point.
Figure 7a shows the evolution of the UPV as function of curing age carried out on column 2 and on the location of picking marker corresponding to a pre-selected area to extract a core with a diameter of 103 mm. Figure 7b shows the evolution (characteristic trend) of the UPV measurements as function of curing age represented by drilling zones. In Figure 7b, each point on the curves represents an average of 18 UPV measurements collected from the three columns. From both figures, the ultrasonic pulse velocities increase with the curing time increase. The difference between the velocities of the ultrasonic waves at a curing age of 7 days and 28 days is almost constant, and it seems to be completely independent from the extraction zones. More interestingly, a stringent appearance of a zone effect has been observed. In fact, the ultrasound pulse velocities increase gradually from the top to the bottom of the reinforced column. This phenomenon can be explained by compactness of the concrete matrix at the bottom of reinforced columns due to the effect of gravity during the filling of the reinforced column using old fashioned hand method and the segregation of coarse aggregate that favor the increase of the ultrasound pulse velocity propagation [27, 28]. To analyze the difference between the UPV measurements performed on columns and cores, Figure 8a shows both measurements from the emplacement on columns and through the cores with a diameter of 103 mm and a SR of 2. It could be observed that the ultrasonic pulse velocity on RC columns before drilling are significantly lower than those on the cores. This result is in accordance with the conclusions of the European standard [23]. For completeness, Figure 8b represents the mean compressive strengths of cores as function of the mean UPV (clusters) through the different drilling emplacements and cores. The graphical representation of the points in Figure 8a has been

reduced to just six clusters in Figure 8b. The latter figure shows clearly that the UPV clusters on columns are concentrated in a narrow-banded range. Practically, it indicates that the elastic properties of the concrete along the columns are quite constant, and no significant impedance variation could be detected. However, after the extraction of the cores, the UPV clusters are confined in wide banded range. In addition, the clusters derived from the UPV measurements on cores with a diameter of 64 mm are higher than the clusters corresponding to other diameters. This observation is a clear indication about the reliability of the nondestructive testing on cores by using ultrasound to predict the appearance of a size effect.

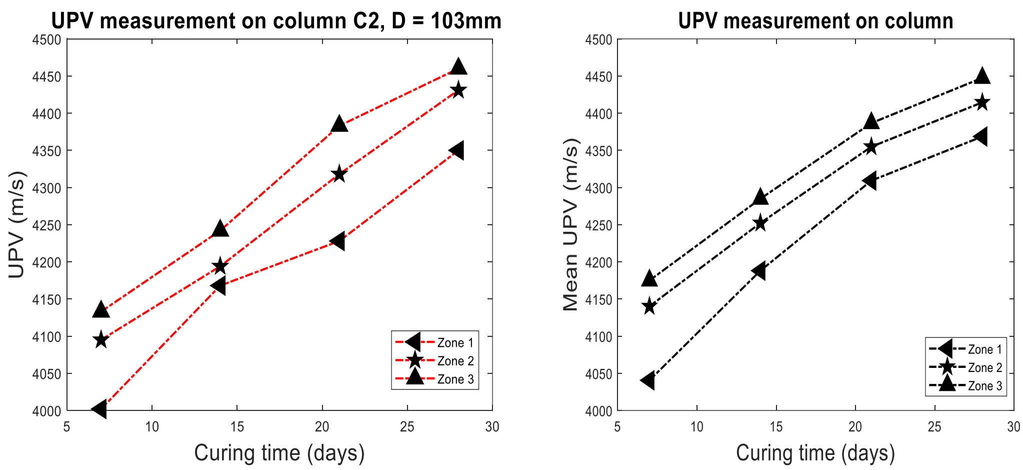

(a) (b)

Figure 7: UPV measurement as function of curing time (a) UPV measurement on column 2 (b) a characteristic evolution of UPV as function of drilling zones

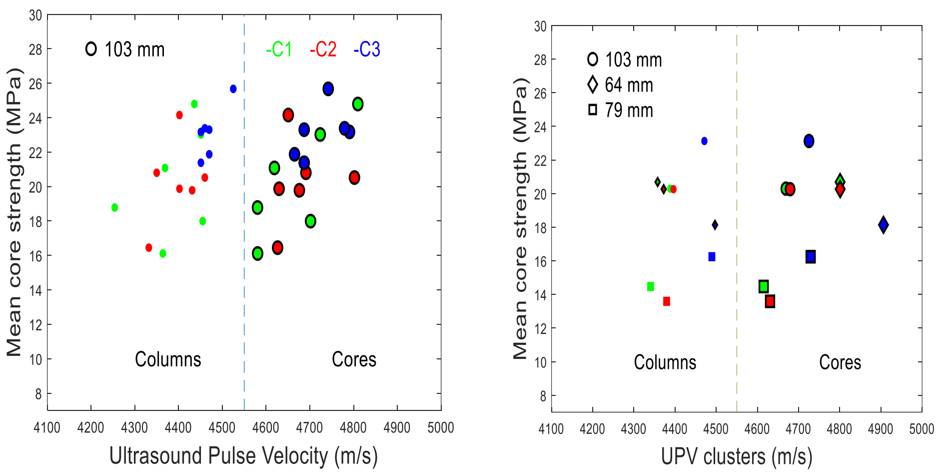

(a) (b)

Figure 8: Mean core strength vs UPV measurement (a) on markers and cores with D = 103 mm (b) UPV clusters for the three diameters

4 Conclusion

This paper highlights the influence of core diameter and slenderness ratio on the assessment of the actual compressive strength of hardened concrete. Full-scale columns were prepared and subjected to infield destructive and non-destructive methods to evaluate strength variation of concrete. The non-destructive test relies on the measurement of the ultrasound pulse velocity over the columns and cores. The destructive method consists of drilling and crushing cores with different diameters. The drilling operation was conducted in three zones and three core diameters were used (103 mm, 79 mm, 64 mm). The results are discussed, and the main conclusions are the following:

- Severe concrete downgrading according to the procedure described on approach B in [24, 25] has been observed as an old-fashioned method is used in placing concrete.
- The appearance of a size effect as a core diameter of 64 mm has been detected. This observation has been made even with respecting the ratio between the core diameter and the maximum aggregate size higher than 3.
- Using a double UPV measurements with a nominal transducer frequency of 54 kHz on columns and cores is a reliable method to confirm the presence of a size effect.
- The appearance of zone effect on columns has been pinpointed as old-fashioned method is adopted. The highlighted zone effect contributes to lowering the characteristic strength of cores.
- The characteristic strengths of cores with a slenderness ratio of 1 are not necessarily higher than the characteristic strengths of cores with a slenderness ratio of 2 as prescribed by standards. This conclusion has been made as a severe concrete downgrading is observed.

Appendix

Table A1 shows the minimum characteristic in situ concrete compressive strength for different concrete classes as reported in [13, 24, 25].

Concrete class	**Minimum characteristic in situ concrete compressive strength (MPa)**	
	Cylinder	Cube
C8/10	7	9
C12/15	10	13
C16/20	14	17
C20/25	17	21
C25/30	21	26

References

[1] Kumpyak, O.G., Galyautdinov, Z.R., & Kokorin, D.N. (2016). Strength of concrete structures under dynamic loading., vol. 070006, no. 2016, doi: 10.1063/1.4937876.

[2] Fedorova, N.V., Medyankin, M., & Fedorov, S.S. (2021). Strength of heavy concrete during static-dynamic deformation. IOP Conference Series: Materials Science and Engineering, 1030. doi: 10.1088/1757-899X/1030/1/012046.

[3] Mailyan, L.R., Beskopylny, A.N., Meskhi, B., Shilov, A.V., Stel'makh, S.A., Shcherban', E.M., Smolyanichenko, A.S., & El'shaeva, D. (2021). Improving the Structural Characteristics of Heavy Concrete by Combined Disperse Reinforcement. Applied Sciences.

[4] Swamy, R. (2008). Sustainable Concrete for the 21st Century Concept of Strength through Durability. R Narayan Swamy University of Sheffield, England," *Japan Soc. Civ. Eng. Concr. Comm. Newsl.*, 2008, [Online]. Available: http://eprints.whiterose.ac.uk/4617/.

[5] Pucinotti, R., & Tripodo, M. (2009). The Fiumarella bridge: concrete characterisation and deterioration assessment by nondestructive testing. International Journal of Microstructure and Materials Properties, 4, 128-139., doi: 10.1504/IJMMP.2009.028438.

[6] Stefano, M.D., Tanganelli, M., & Viti, S. (2013). On the variability of concrete strength as a source of irregularity in elevation for existing RC buildings: a case study. Bulletin of Earthquake Engineering, 11, 1711-1726. doi: 10.1007/s10518-013-9463-2.

[7] Bartlett FM and MacGregor JG. Effect of core diameter on concrete core strengths. ACI Materials Journal. 1994, 91(4), pp 339-348.

[8] ASTM 900-06, "Standard test method for pullout strenght of hardened concrete," *Am. Soc. Test. Mater.*, no. July 1999, pp. 1–10, 2013.

[9] Bickley, J. A. (1981). Pullout Testing of Concrete. *Concr. Constr. - World Concr.*, vol. 26, no. 7.

[10] Breysse, D. *et al.*, (2019). Recommendation of RILEM TC249-ISC on non destructive in situ strength assessment of concrete. *Mater. Struct. Constr.*, vol. 52, no. 4, pp. 1–21, doi: 10.1617/s11527-019-1369-2.

[11] Yan, J., Liu, K., Zou, C., Mo, Y., & Ou, J. (2020). Comparison of Evaluation Tests for Compressive Strength of Structural Concrete. *Period. Polytech. Civ. Eng.*, vol. 64, no. 2, pp. 387–395, 2020, doi: 10.3311/PPci.12545.

[12] Qasrawi, H. (2019). Effect of the position of core on the strength of concrete of columns in existing structures, Journal of Building Engineering, vol. 25, 100812, 2019, https://doi.org/10.1016/j.jobe.2019.100812

[13] NF EN 13791 Standard, "Assessment of in-situ compressive strength in structures and precast concrete components," August, 2019.

[14] Khoury, S.S., Aliabdo, A.A., & Ghazy, A. (2014). Reliability of core test – Critical assessment and proposed new approach. alexandria engineering journal, 53, 169-184., doi: 10.1016/j.aej.2013.12.005.

[15] Masi, A. & Vona, M. (2009). Estimation of the in-situ concrete strength: provisions of the european and italian seismic codes and possible improvements, *RELUIS - Eurocode 8 Perspect. from Ital. Standpoint Work.*, no. May 2014, pp. 67–77, 2009.

[16] ACI 214.4R-10, "Guide for Obtaining Cores and Interpreting Compressive Strength Results" American Concrete Institute 38800 Country Club Drive Farmington Hills, MI 48331 U.S.A. 2010.

[17] Carroll, A.C., Grubbs, A.R., Schindler, A.K., & Barnes, R.W. (2016). Effect of core geometry and size on concrete compressive strength. (Research Report No. 1 for ALDOT Project 930-828)," no. 1, pp. 1–136.

[18] Suprenant, B. A. (1995). Core Strength Variation of in-Place Concrete. The Aberdeen Group; Boston, MA, USA.

[19] Bartlett, F.M., & Macgregor, J.G. (1999). Variation of In-Place Concrete Strength in Structures. ACI Materials Journal. vol. 96, Issue 2, pp 261-270, 1999.

[20] de Stefano, M., Tanganelli, M., & Viti, S. (2013). Effect of the variability in plan of concrete mechanical properties on the seismic response of existing RC framed structures. Bulletin of Earthquake Engineering, 11, 1049-1060. doi: 10.1007/s10518-012-9412-5.

[21] NF EN 12390-2 Standard, "Testing hardened concrete-Part 2 : making and curing specimens for strength tests," June, 2019.

[22] NF EN 12390-3, "Testing hardened concrete - Part 3 : compressive strength for test specimens," June, 2019.

[23] NF EN 12504-4 Standard, "Testing concrete in structures- Part 4 : Determination of ultrasonic velocity" July, 2021.

[24] NA 17004, norme algérienne" Evaluation de la résistance à la compression sur site des structures et les éléments préfabriqués en béton," 2008.

[25] NF EN 13791 Standard, "Assessment of in-situ compressive strength in structures and precast concrete components," September, 2007.

[26] Benidir, A. (2018).Aggregate size and lateral dimension effects on core compressive strength of concrete, *Proc. IRF2018 6th Int. Conf. Integrity-Reliability-Failure*, no. July, pp. 479–486, 2018.

[27] Kou, S., Poon, C.S., & Wan, H. (2012). Properties of concrete prepared with low-grade recycled aggregates. Construction and Building Materials, 36, 881-889.,doi: 10.1016/j.conbuildmat.2012.06.060.

[28] Mohammed, T.U., & Rahman, N. (2016). Effect of types of aggregate and sand-to-aggregate volume ratio on UPV in concrete. Construction and Building Materials, 125, 832-841. doi: 10.1016/j.conbuildmat.2016.08.102.

DOI: 10.2478/sspjce-2023-0010

Impact of Passive Design Strategies on Environment, Cooling and Lighting Energy Demand. A Weighted Least Squares-Based Approach

Soufiane Boukarta [1*]

[1] Institute of Architecture and Urban Planning, IAU, Blida 1 University
*e-mail: boukarta.soufiane@univ-blida.dz

Abstract

The energy transition requires optimal knowledge of the thermal behaviour of different passive strategies. This paper explores the impact of 28 variables representing 4 shading devices, 5 external wall compositions (U_w), 3 window types (U_w), 4 window-to-wall ratios (WWR), 4 types of climates represented by 4 cities, and 8 orientations. Applying the Latin hypercube sampling method, a campaign of 300 dynamic thermal simulations is performed to assess the impact of the variables selected using the weighted generalised linear regression method for the energy demand for air conditioning, the energy demand for lighting, and the environmental impact expressed in kg of CO_2. The model of energy demand for cooling (R^2 = 0.951) shows that the weather data is the variable that most explains energy demand, followed by the glazing ratio, the thermal characteristics of external walls, and shading devices. The model explaining the energy demand for lighting (R^2 = 0.945) shows that the WWR and shading devices, the weather data, and the orientation, influence the energy demand for lighting. Finally, the model explaining the embodied carbon footprint (kg of CO_2) (R^2 = 0.989) shows that external walls and window type are the main influencing factors. Finally, the best combination for balancing the cooling-lighting-embodied carbon balance equation is discussed.

Keywords: passive design strategies, cooling and lighting energy demand, Latin hypercube sampling, simulation, weighted linear regression modelling

1 Introduction

Climate change has become a phenomenon that is being experienced more than predicted, and its accentuation is corroborated by the unbridled consumption of fossil fuels, which is releasing considerable quantities of greenhouse gases (GHG), destabilising the atmospheric balance and causing temperature spikes in some places and natural disasters in others, at rates that are difficult to prevent and on a massive scale. Cities are primarily responsible for this imbalance, and their activities are responsible for releasing almost three-quarters of energy demand, as well as greenhouse gases [1]. The most important consumption sectors are mobility, industry, agriculture, and construction, specifically, the residential sector, which alone consumes more than 50% of the world's final energy [2] and in Algeria 46% according to the latest figures from the [3].

To combat this phenomenon, the countries of the world, led by the developed countries, which are responsible for more than 70% of greenhouse gases, meet annually at what are known as COPs, conferences of parties, to try to find solutions and adapt to the dynamics of climate change. The main guidelines include stabilising the temperature at 1.5°C above the preindustrial level, and according to COP 21, from 2020 onwards, each signatory country to the COP21 protocol will be required to draw up a report on the actions taken to reduce greenhouse gases [4]. To encourage developing countries to join the fight against climate change, partnerships are planned to help them in terms of technology transfer and financial arrangements. Overall, two major strategies are clear for combating climate change: the gradual introduction of renewable energies RE and energy efficiency EE in consumer sectors. In Algeria, the government is aiming for a 30% introduction of RE by 2030 and energy efficiency in the four consumption sectors. Energy efficiency aims to rethink architectural design in order to reduce the energy demand of buildings. The introduction of the National Energy Management Plan (NEMP) in 2007 [5] led to the construction of 600 high-energy performance (HEP) homes. Several other actions are planned in the various NEMPs, all aimed at improving energy efficiency by improving the thermal insulation of buildings. To help architects and engineers apply the thermal regulations, CNERIB has set up a platform including the Regulatory Technical Document (DTR) on the *RETA.dz* website and CTBAT through APRUE.

In 2016, the APRUE published a guide for the introduction of energy efficiency in the building industry, with a proposal for specifications to help project owners set up a system for assessing projects from the point of view of energy efficiency [6]. For the time being, these guidelines remain proposals that could potentially lead to initiatives, but which remain more or less applicable in the day-to-day practice of architects because of their non-binding and non-mandatory scope, and also because the methods proposed are not in line with the modus operandi of architects, who rely on drawings to develop their projects. In response to the latter concern, this paper focuses on the issue of introducing energy efficiency into architectural practice. It proposes a methodology for multi-performance exploration of the impact of passive design strategies on energy demand and the environment.

2 Literature Review

The review of the scientific literature on energy efficiency clearly shows that it is possible to approach the issue from four possible angles, which in reality are intertwined in a single context, but for reasons of scientific simplification they can be organised as follows [7]:

- The building scale is the largest category in terms of the amount of research carried out. Bioclimatic tools list a number of strategies for improving a building's energy efficiency, depending on the specific climatic context. There are winter strategies and summer strategies. Strategies include the choice of building materials for the envelope, orientation, glazing ratio and type, shading devices, ventilation, and solar heating. The impact of building characteristics can affect energy demand by up to 200% [8].
- The urban scale is a relatively new entry point and studies have been appearing since the end of the last century and the beginning of the 21st century [8]. The urban scale has an impact on the variation in climatic conditions, creating more microclimatic conditions. This variation distorts sizing studies for heating and air conditioning

equipment [9]. Urban scale can be controlled by a number of urban form control parameters, such as built density, vegetation density, building height, prospect, etc. [10].

- The third scale relates to the performance of heating, cooling, and lighting systems [11].
- The fourth input is the occupant [12], who can vary the energy demand from 50 to 200% [13].

In this paper, we will focus on the building scale considering some control parameters. The other scales are considered fixed without variation in order to assess more accurately the impact of the chosen control parameters.

Energy efficiency assessment methods can be grouped into two main categories:

- The historicist approach, or the approach based on actual energy consumption data obtained from existing buildings. This approach has the merit of reducing the gap between the energy obtained from modelling and that obtained from actual consumption, but it does not allow the impact of new technologies to be assessed, as they do not exist in the existing built environment.
- The Engineering approach, which relies on calculation algorithms to assess the thermal behaviour of buildings. This approach is considered to be robust, but some studies have shown that simulations can lead to differences in assessment that can be as much as double [13]. This discrepancy is often caused by a misidentification of the activities of the occupant of the building in question. In order to reduce the size of this discrepancy, a significant evaluation is carried out in terms of parameter variation according to a representative sampling, which would make it possible to incorporate a wide range of possibilities and ipso facto reduce the gap between the simulated and the real energy demand [14, 15, 16]. Some authors prefer to proceed with calibration on an existing case by trying to parameterise the dynamic thermal simulations until calibration of the results and reducing the difference between the simulated and real energy demand to below 10% as a margin of error [17]. In the present study, we choose the dynamic thermal simulation approach while isolating the role of the occupant and varying the energy efficiency control parameters at the building scale by considering a representative sampling of possible combinations.

Among the sampling methods that exist in the scientific literature, we can cite:

- Monte-Carlo sampling, which is based on pseudo-random sequences and whose use is recommended for problems whose space does not exceed 100,000 combinations.
- Sobol and Halton sampling, which are so-called quasi-Monte-Carlo methods based on the use of sequences with low discrepancy [18]. The use of these methods provides a better representation of the space of possible combinations, see Figure 1 below.

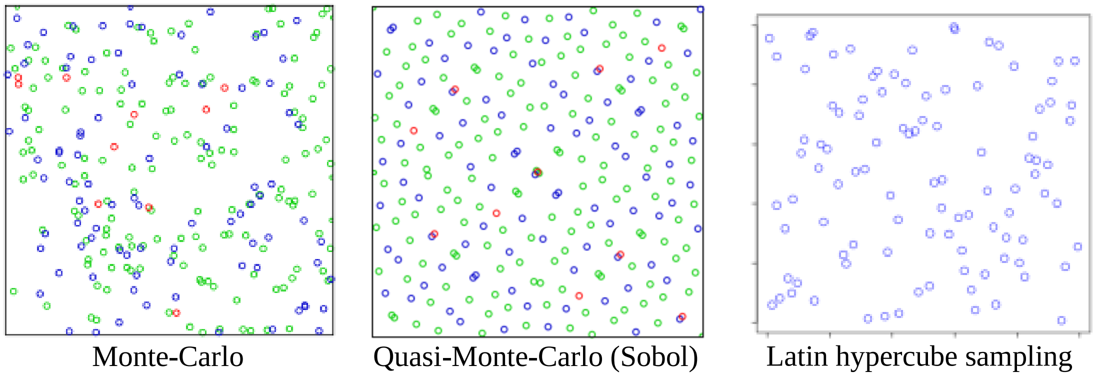

Figure 1: Differences between sampling methods [18]

- Latin Hypercube Sampling (LHS) is a very efficient multi-dimensional sampling method. As a general rule, a sample size of 10 times the number of design variables will be sufficient for the combinations to be modelled accurately, whereas other sampling methods require a minimum of 15 times the number of variables.

The difference between the LHS and Monte Carlo methods lies in the fact that the Monte Carlo method involves generating samples for one variable using a simple random sampling method, while the second method, Latin Hypercube, generates random samples that occur in equal probability intervals with a normal distribution for each range. In this paper, we have chosen the dynamic thermal simulation approach applied to a representative sample of possible combinations by applying the Latin hypercube sampling method in order to reduce the number of samples and gain accuracy.

3 Method

The method chosen to respond to the problem raised is to follow the following points, see Figure 2 below.

- The choice of climatic zones: Algeria is a large country with 4 climatic zones, and we have chosen a representative town for each climatic zone: Algiers for the humid climate, Médéa for the subhumid climate, Sidi-Bel-Abbès for the semi-arid climate and Adrar for the arid climate.

- The choice of control parameters: the choice mainly concerned the control parameters that architects tend to use without really having a quantitative estimate of the energy scope of what they choose as a parameter. We chose 5 control parameters: (a) construction materials for the external walls. We opted for the conventional choice, i.e., a standard double-skinned wall and a double-skinned wall with polystyrene insulation. Then we added materials that are often found locally, limestone, which is abundant in northern regions, and materials obtained from the earth that have been widely used in the south, namely mud-brick and terracotta. The thermal characteristics of each wall composition are presented in Table 1.

- The rate and type of glazing: the choice fell on a variation in terms of thermal performance of the windows, from single glazing to double glazing without and with rare gas. For the glazing ratio, the choice was made for a variation ranging from 10 to 70% of the external wall surface.

- Shading device: two types of solar protection were chosen. The 0.5 m louvers and the awning for 1 and 2 meters deep and a combination of the two types at 1m deep, see Figure 3.
- Finally, the orientation is considered according to a step of 45° which would give 8 orientations.

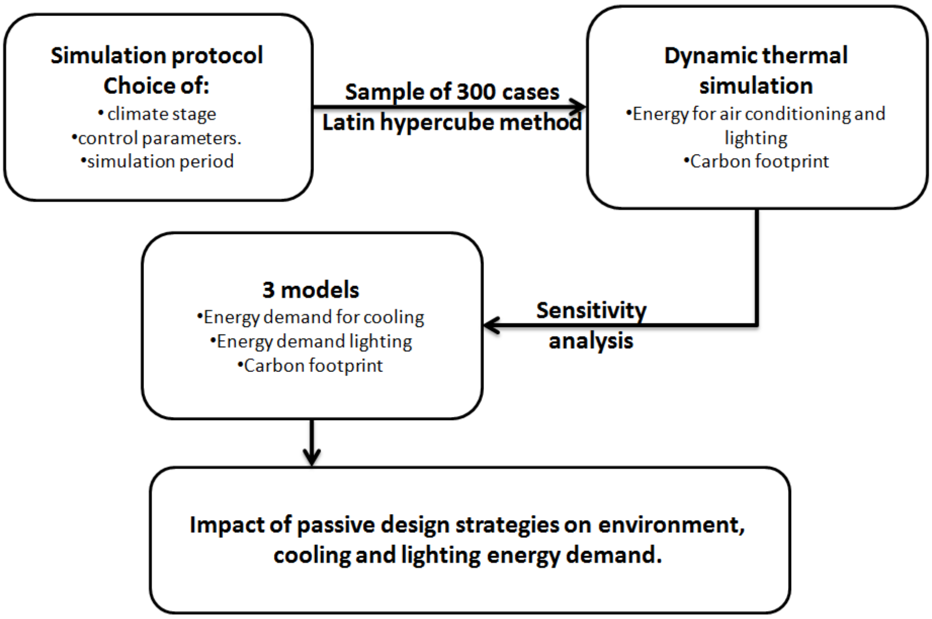

Figure 2: The adopted method

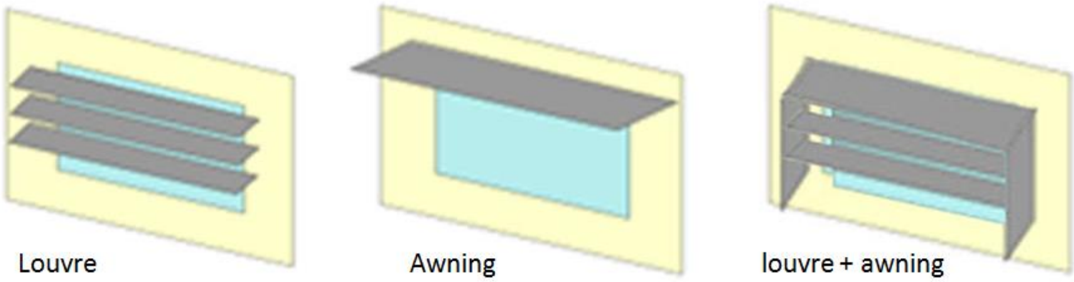

Figure 3: Solar protection considered for the study

This parametric variation is applied to a DOI, Design of Experiment, representing a single residential space (bedroom or living room) measuring 6 x 8 m, see Figure 4 below. One DOI was chosen instead of an entire dwelling in order to be able to correctly assess the impact of the chosen parametric variation on the thermal behaviour of the space in terms of energy demand for air conditioning, natural lighting (with a threshold of 150 Lux) and carbon embodied in the materials (ICE database, Inventory of Carbon and Energy, https://circularecology.com/). We chose embodied carbon instead of a full life cycle analysis to avoid the fact that the carbon cost of transporting materials remains fictitious and difficult to assess in our case.

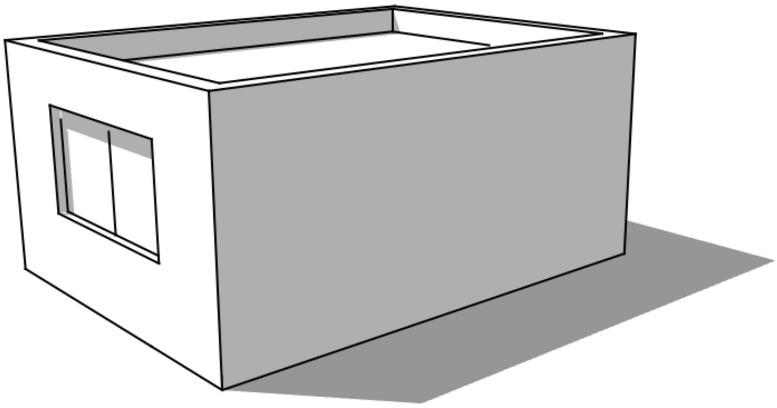

Figure 4: The study design

The simulation campaign is limited to 300 possible combination cases obtained using the Latin Hypercube approach. We introduced 6 explanatory variables and a campaign of 60 simulations would have been sufficient to assess the impact of the various control parameters. We have chosen to extend the sample so that each climate is represented by a minimum of 75 Dynamic Thermal simulations. This paper is therefore mainly concerned with assessing the thermal behaviour of the control parameters chosen for the first two weeks of July, as this is the hottest period according to the meteorological data representing the 15-year climatic variation. The simulations are run under Energy Plus, which is widely used by the scientific community [17]. Based on the methodology described above, three models will be presented in the next section, allowing us to assess the multi-performance of the chosen parameters.

4 Results and Discussion

The sample of 300 possible combinations obtained by the Latin Hypercube method gave us a sample whose descriptive statistics are presented in the Table 1 below.

Table 1 : Descriptive statistics for the sample

Variables	N	Min	Max	Avr	Std dev
City (Médéa, Alger, Sidibelabes, Adrar)	300	1	4	2.50	1.120
Orientation (steps of 45°)	300	0.00	315.00	157.5000	102.68836
Shading device (0.5 m louvers, 1 m awning, 2 m awning, 1 m awning + louvers)	300	1	4	2.50	1.120
U_w (Simple, double with air, double with gas)	300	1	3	2.00	0.818
U_{wall} (Limestone, Double-skinned wall, Double-skinned wall with insulation, mud brick, terracotta)	300	1	5	3.00	1.417
Window to Wall Ratio WWR (10%, 30%, 50%, 70%)	300	10	70	40.00	22.398

The results of the simulations carried out are described in the Table 2 below.

Table 2 : descriptive statistics for the simulation results

Variables	N	Average	Std dev	Minimum	Maximum
Embodied CO_2	300	12863.4282	6488.58188	4803.39	24318.42
Cooling energy demand	300	88.0688	125.63193	0.00	449.47
Lighting energy demand	300	3.4941	1.71647	2.17	9.84

4.1 Sensitivity Analysis

There are several methods of sensitivity analysis. For the present study, we have chosen the generalised linear regression method, as it allows an assessment at two levels:

- Assessment of the importance of each parameter in relation to the other variables, based on the *F* statistics.
- This method also allows us to assess the importance of all the variations per parameter in the three categories of analysis chosen, namely energy demand for air conditioning, energy demand for lighting below the threshold of 150 Lux and the importance of the CO_2 embodied.

The collinearity test is satisfied if all the variables have a VIF of less than 3 and a tolerance well above 0.2, see Table 3 below. The heteroskedasticity test is satisfied by applying the weighted linear regression method, and linearity and normality are also verified.

Table 3: Collinearity test

Variables	Colinearity statistics	
	Tolerance	**VIF**
Shading device	0.975	1.025
U_{wall}	0.991	1.009
U_w	0.989	1.011
Orientation	0.983	1.017
WWR (%)	0.984	1.017
City	0.982	1.018

4.1.1 Modelling Energy Demand for Cooling

The results of the modelling of energy demand for air conditioning gave us an explanatory model with 95.1% accuracy. The details of the model are presented in Table 4 below and the comparison in terms of effect on energy demand is developed from F statistics and the estimated marginal mean of each parameter, see Figure 5 below.

Table 4 : summary of the weighted generalized linear model for energy demand for cooling

	Sum of squares type III	Degree of freedom	Mean square	*F*	Signification (significant within a 0.05 interval)
Corrected model	5836.448*	22	265.293	244.301	0.000
Constant	2139.305	1	2139.305	1970.023	0.000
Shading device	170.866	3	56.955	52.448	0.000

Orientation	54.562	7	7.795	7.178	0.000
U_{wall}	106.857	4	26.714	24.600	0.000
U_w	19.285	2	9.643	8.880	0.000
WWR	206.089	3	68.696	63.260	0.000
City	2529.152	3	843.051	776.340	0.000
Error	300.802	277	1.086		
Total	1613263.622	300			
Corrected total	6137.250	299			

Weighted least squares regression - Weighted by weight_cooling
* $R2 = .951$ (Adjusted $R2= .947$)

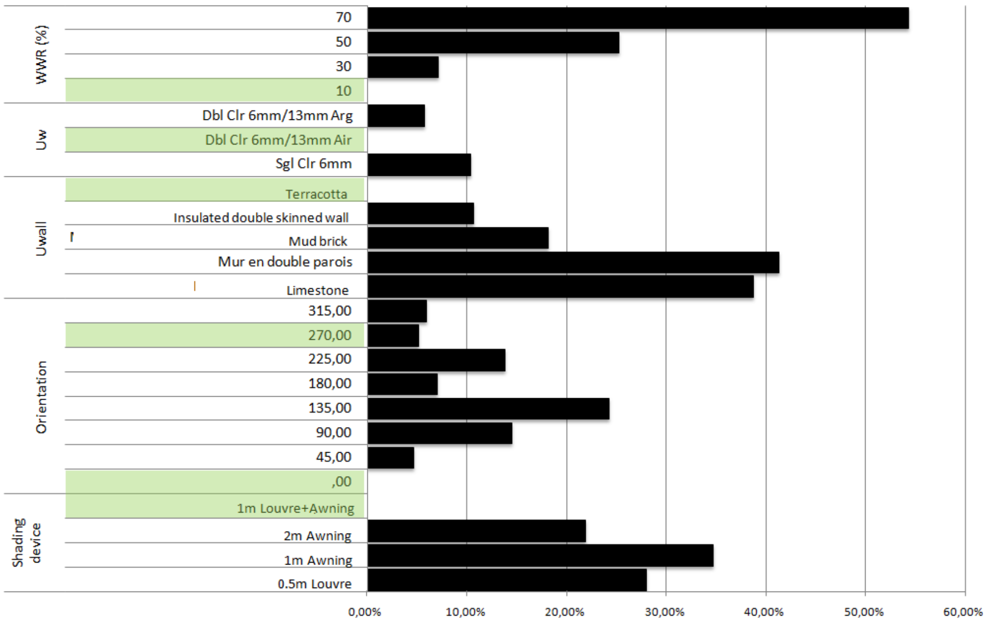

Figure 1. Importance of each in relation to the references (shown in green)

Based on the values of *F* statistics and the estimated marginal average for each variable, it was possible to estimate the percentage importance of each variable in relation to the reference value representing the lowest energy demand per variable, which is shown in green in Figure 5 above. This shows the 6 most effective control parameters for reducing energy demand for air conditioning. Three major parameters stand out on the graph: the climatic stage, the glazing ratio, and the external walls:

- The climatic stage is the first element to have an impact on energy demand. The humid climate appears to be the mildest, with virtually no energy demand for air conditioning. The Adrar climate, on the other hand, which is an arid climate, requires a higher energy demand than the other climates.
- The WWR comes in second place and increases energy demand by up to 54% (the case of 70% WWR) compared with the reference case of 10%.

- In 3rd position is the role of shading devices. The combination of louvres and awning is the best configuration for the overheating season as it reduces solar gains. A solar protection system consisting of an awning 1 m deep would require up to 35% more energy than a combined solar protection system consisting of an awning and louvers 1 m deep. It should be noted that 0.5 m deep louvers are more effective than a 1 m deep awning but are almost 7% less effective than a 2 m deep awning.
- The building material chosen for the external envelope is another important factor. Terracotta is the building material that responds best to the 4 climatic conditions. However, if we look at the details, it becomes clear that each material performs better in the climatic zone to which it belongs: limestone in the north (humid climate), and both bricks, mud, and terracotta perform better in the south (arid climate zone). In the conventional configuration, double-skinned walls have virtually the same thermal transmittance as limestone in the north, and as terracotta if insulation (polystyrene) is added for the arid climate. The main difference is in the embodied CO_2, limestone, terracotta, and mud brick have a very low embodied CO_2 compared with double-skinned walls with and without insulation.
- In fifth place is the type of glazing, and double glazing with air is the best configuration, reducing energy demand for air-conditioning by up to 5 and 10% compared with single glazing and double glazing with argon. This difference can be explained by the thermos effect that seems to form in the case of double glazing with argon, which increases the overheating situation.
- Finally, orientation comes in sixth place, and north orientation is the most favourable for reducing energy demand for air-conditioning, and the difference between north and south-east orientation (135°) can be as much as 25%.

4.1.2 Modelling Energy Demand for Lighting

Modelling energy demand for lighting using weighted least squares regression gave us a model with 94.5% accuracy. The results of the modelling are presented in Table 5 below.

Table 5: Summary of the model for lighting energy demand

Source	**Sum of squares type III**	**Degree of freedom**	**Mean square**	***F***	**Significance** (significant within a 0.05 interval)
Corrected model	7846.256*	27	290.602	173.713	0.000
Constant	4473.368	1	4473.368	2674.043	0.000
Shading device	138.858	3	46.286	27.668	0,000
Orientation	65.205	7	9.315	5.568	0.000
U_w	1.294	2	0.647	0.387	0.680**
WWR	225.780	3	75.260	44.988	0.000
City	126.445	3	42.148	25.195	0.000
Shad device WWR	133.514	9	14.835	8.868	0.000
Error	455.025	272	1.673		
Total	1239897.129	300			
Corrected total	8301.281	299			

Weighted least squares regression - Weighted by weight_lighting
* R2 = .945 (Adjusted R2 = .940)

** not significant

The importance of each control parameter is shown in the graph below (Figure 6).

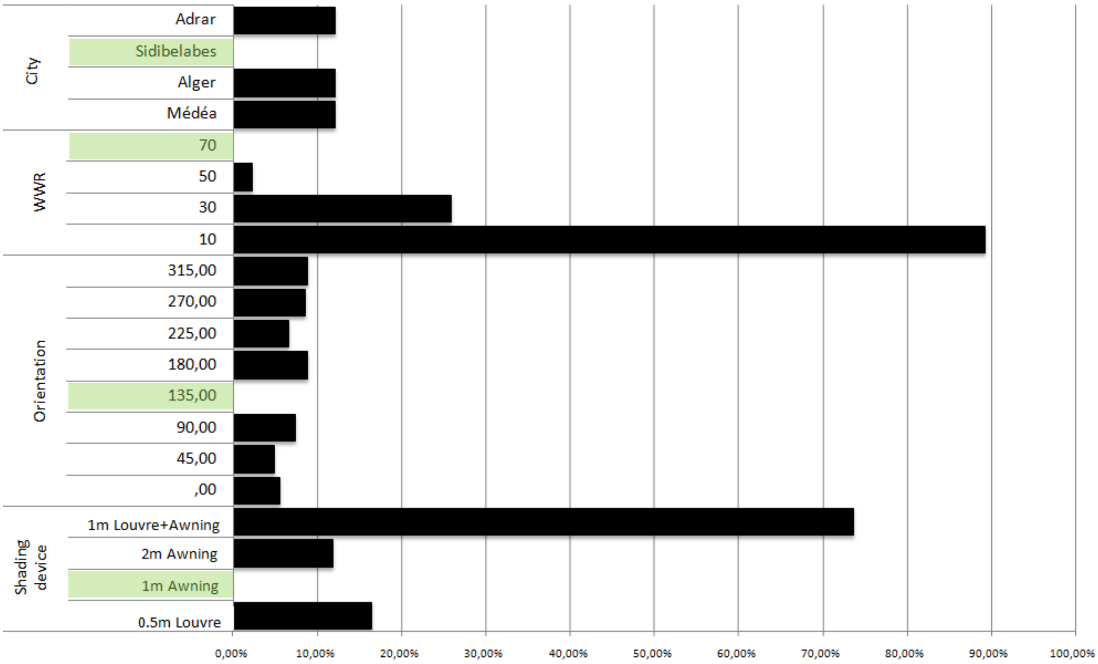

Figure 2 : Importance of lighting control parameters (150 Lux threshold) compared with references (shown in green)

The parametric variation applied shows us that all the variations occur within a consumption range limited to 9 kWh over the two weeks of simulation, which is marginal compared with the energy demand required for air conditioning, especially for cities in southern Algeria.

The WWR is the primary factor impacting lighting and generating or reducing the greatest energy demand to ensure lighting is at the 150 Lux threshold. A glazing ratio of 10% is the most unfavorable situation for natural lighting, and the energy demand is 89% higher than for a glazing ratio of 70%.

In second place comes shading devices, where the best provision for natural lighting is obtained with a 1m awning. The most unfavorable case is the combination of awning and louver, which generates an energy demand 73% higher than that generated by the 1m awning.

In third place comes the combination of shading device and WWR, the effect of which is shown in Figure 7 below. Two observations can be made from the graph: the amount of variation according to the type of shading device and the amount of energy generated. The device generating the least variation is the awning at a depth of 1m, the effect of which does not exceed 16% for a glazing ratio of 10%. However, the most unfavorable case is that of the combination of awning and louver at a depth of 1m, and this scenario has the greatest variation, from 6% (WWR 50%) to over 220% (WWR 10%).

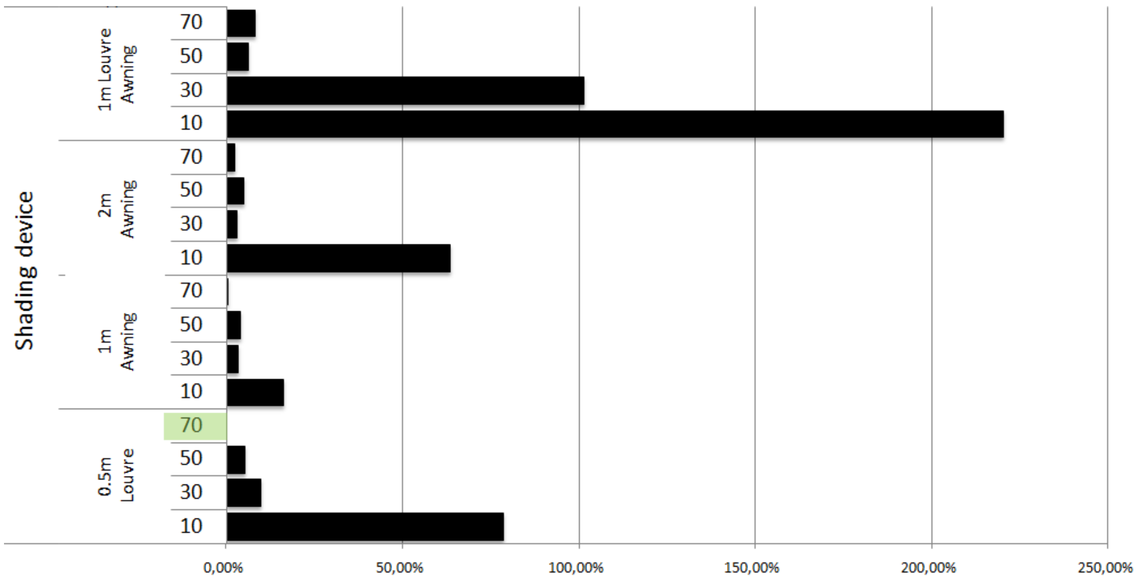

Figure 3. Effect of interaction, shading device, and WWR. (Reference case shown in green)

The impact of climatic conditions has an impact on energy demand for lighting and the effect varies slightly between the 4 cities (0.4 kWh variation) which represents 12% between the town of Sidibelabes and the other cities. In fifth place comes orientation. The most favourable orientation for reducing energy demand for lighting is 135°, i.e., south-east. Other orientations generate between 4% (45°) and almost 9% (180°) more lighting energy than the 135° orientation. The impact of the type of glazing was found to have no statistically significant impact, as the three types of glazing had almost identical transmittance factors.

4.1.3 Modelling the Embodied CO_2

For the embodied CO2, we only considered the part incorporated in the building materials for external walls, windows, and shading devices. The results of the modelling are clear, with external walls coming out top, followed by windows, while shading devices do not have a statistically significant impact, as shown in Table 6 below.

Table 6. Summary of the embodied carbon model

Source	**Sum of squares type III**	**Degree of freedom**	**Mean square**	***F***	**Significance** (significant within a 0.05 interval)
Corrected modem	232782.173*	9	25864.686	18065.979	0.000
Constant	951090.937	1	951090.937	664318.486	0.000
Shading device	7.715	3	2.572	1.796	0.148**
U_w	50.486	2	25.243	17.632	0.000
U_{wall}	232516.452	4	58129.113	40602.053	0.000
Error	415.187	290	1.432		
Total	1303397.976	300			

Corrected total	233197.360	299

Weighted least squares regression - Weighted by weight_CO_2
* $R2 = .998$ (R2 adjusted = .998)

** not significant

Looking at the details, it emerges that locally available materials are the ones with the lowest embodied carbon footprint. Limestone is the material with the lowest embodied carbon footprint (average of 5076 kg eqCO_2), followed by mud bricks (average of 7164.641 kg eqCO_2). The conventional double-skinned wall comes third (average of 14163.35 kg eqCO_2). In last place comes the double-skinned wall with insulation. Although its thermal resistance is very close to that of the terracotta, its carbon footprint is almost double (14465.433 kg eqCO_2), see Figure 8 below.

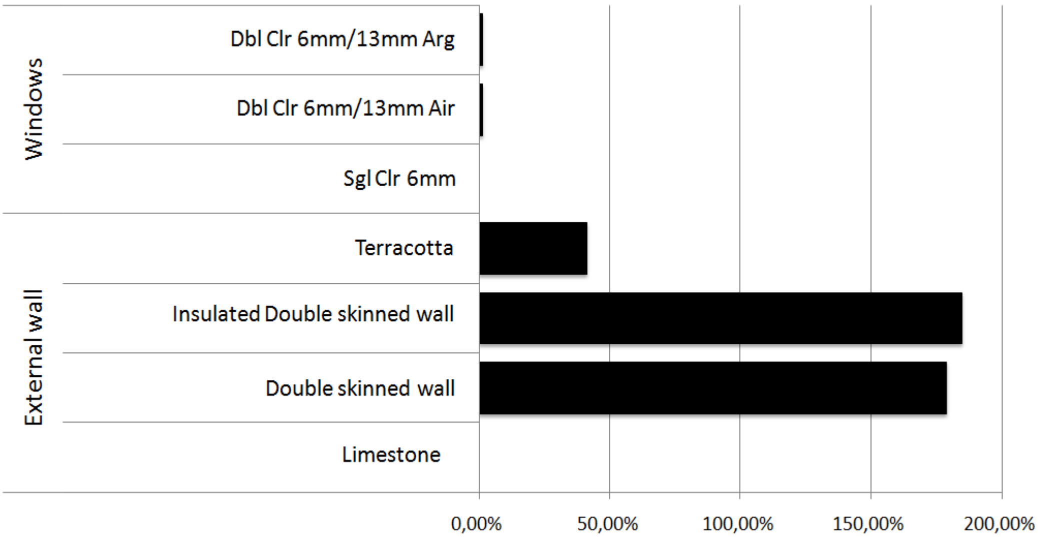

Figure 4. Comparison of the carbon-incorporated balance of different exterior wall compositions and windows

On the other hand, the choice of windows has little impact on the variation in the incorporated carbon footprint. The difference between single-glazing and double-glazing with air and gas is 1% to 1.26%.

5 Conclusion

What provision should be chosen for the lighting-cooling energy and carbon balance?

From the results obtained and presented above, it is clear that if we tend to choose the best configuration while seeking to reduce the energy demand for air conditioning and lighting and the carbon footprint for the 6 control parameters chosen, we will sometimes run into contradictions.

- For shading devices, the control parameters that reduce the energy demand for air conditioning are themselves the most unfavorable for lighting and increase the energy demand for lighting. But if we look at the variation intervals, it is clear that air conditioning requires more energy than lighting. So, the choice will clearly be for the awning + louver combination for shading devices.

- As regards the choice of materials, it is also clear that locally available materials offer the best performance in terms of both air conditioning and embodied carbon cost. For the northern regions, the stone is the best material, and for the south, raw and fired clay bricks are the most favorable, as both offer the best thermal performance for the climatic conditions, while reducing the embodied carbon footprint.
- The choice of glazing that reduces energy demand for air conditioning is double glazing + air, even though it slightly reduces solar access and increases energy demand for lighting. The embodied carbon of glazing does not significantly affect the overall balance.
- Orientation plays a similar role to the glazing ratio in the energy demand equation for air conditioning. North orientation is the best orientation, but it is not the best orientation for the winter season, so all orientations can be favorable as long as the most appropriate shading device is considered.
- The most favorable glazing ratio for cooling-lighting-carbon balance is 10%, even though it increases the energy demand for lighting. It is also possible to provide a higher glazing rate, if necessary, but it would be necessary to provide a shading device that could reduce solar access and reduce overheating time as well as the energy required for air conditioning. For cities in the south (such as Adrar), characterized by an arid climate, an introverted courtyard design is a very interesting solution, as it works on solar regulation and wind circulation.

Figure 5 shows the distribution of cases in different cities according to their energy demand for air conditioning and lighting. Our results clearly show that it is possible to make a connection in terms of summer design between humid and sub-humid climates, whereas it would be inadvisable to do so with a semi-arid (Sidibelabbes) or arid (Adrar) climate. In a humid and sub-humid climate, with good architectural design, it is possible to achieve zero or nearly zero energy buildings. However, in a hot climate, whether arid or semi-arid, it would be preferable to use other techniques and technologies to reduce the impact of climatic conditions on energy demand for air conditioning. Our future research will therefore focus on this southern region in order to test solutions and assess their energy and environmental costs.

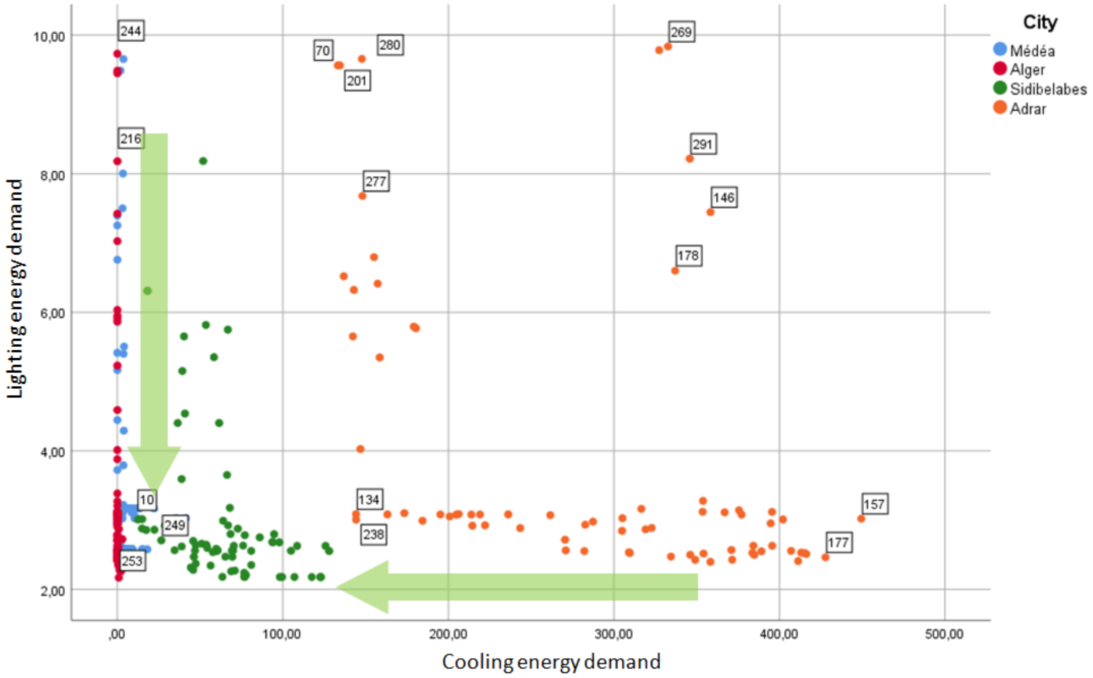

Figure 6. The distribution of cases according to their energy demand for air conditioning and lighting

Abbreviations

U_w: Thermal transmittance
WWR: Window to wall ratio
GHG: greenhouse gases
COP: Conference of parties
RE: Renewable energy
EE: Energy efficiency
HEP: high energy performance
NEMP: National Energy Management Plan
APRUE: National agency for the promotion and rationalization of energy use
RETA: National online thermal calculation software
CTBAT: National online thermal calculation software
DTR: Regulatory technical document
ICE: Inventory of Carbon and Energy
VIF: Variance Inflation Factor

References

[1] Rogers, R. G., & Gumuchdjian, P. (2008). Des Villes durables pour une petite planète. Moniteur.

[2] Fathi, S., et al. (2020). Machine learning applications in urban building energy performance forecasting: A systematic review. *Renewable and Sustainable Energy Reviews*, *133*, 110287.

[3] APRUE. (2021). L'Agence Nationale pour la Promotion et la Rationalisation de l'Utilisation de l'Énergie, La situation énergétique nationale, Chiffre 2019, édition 2019.

[4] Guillemot, H. (2020). 2 degrés, 1.5 degrés, neutralité carbone… Petite histoire des objectifs climatiques à long terme.

[5] Sénit, C. A. (2008). L'efficacité énergétique dans le secteur résidentiel: une analyse des politiques des pays du Sud et de l'Est de la Méditerranée. IIddri, Idées pour le débat, 14.

[6] APRUE & GIZ. (2016). Guide pour une construction Eco-énergétique en Algérie.

[7] Boukarta, S. (2021). Potentiel d'économie d'énergie d'un bâtiment résidentiel. In Confort, Habitat en milieu sensible et Ville Résiliente CHSVR, 13-14 octobre, Université de Guelma.

[8] Salat, S. (2011). Les villes et les formesurbaines: sur l'urbanisme durable. France.

[9] Bozzonnet, E. (2005). Impact des microclimats urbains sur la demande énergétique des bâtiments-Cas de la rue canyon. Diss. Université de la Rochelle.

[10] Wong, N.H., et al. (2011). Evaluation of the impact of the surrounding urban morphology on building energy consumption. *Solar energy*, *85*(1). pp. 57-71.

[11] Dascalaki, E. G., Droutsa, K., Gaglia, A. G., Kontoyiannidis, S., & Balaras, C. A. (2010). Data collection and analysis of the building stock and its energy performance—An example for Hellenic buildings. *Energy and Buildings*, *42*(8), 1231-1237.

[12] Boukarta, S., & Berezowska-Azzag, E. (2018). Energy demand of occupant's spatial modification in residential buildings. Case study of Médéa, Algeria. *Selected Scientific Papers-Journal of Civil Engineering*, *13*(1), pp. 15-28.

[13] Dall'O', G., Galante, A., & Torri, M., (2012). A methodology for the energy performance classification of residential building stock on an urban scale. *Energy and Buildings*, *48* (2012) 211–219.

[14] Boukarta, S. (2021). Exploring the impact of balconies on cooling energy demand in an arid climate zone. *Selected Scientific Papers-Journal of Civil Engineerin*g, *16*(2), 25-35.

[15] Boukarta, S. (2021). Predicting energy demand of residential buildings: A linear regression-based approach for a small sample size. *Selected Scientific Papers-Journal of Civil Engineering*, *16*(2), 67-85.

[16] Amiri, S.S., Mottahedi, M., & Asadi, S. (2015). Using multiple regression analysis to develop energy consumption indicators for commercial buildings in the US. *Energy and Buildings*, *109*, 209-216.

[17] Semahi, S., Zemmouri, N., Singh, M.K., et al. (2019). Comparative bioclimatic approach for comfort and passive heating and cooling strategies in Algeria. *Building and Environment*, *161*, p. 106271.

[18] Kaoula, D., & Bouchair, A. (2019). The pinpointing of the most prominent parameters on the energy performance for optimal passive strategies in ecological buildings based on bioclimatic, sensitivity and uncertainty analyses. *International Journal of Ambient Energy*, 1-28.

DOI: 10.2478/sspjce-2023-0011

Harmonic Response of CFRP Tensegrity System in a Suspen-dome

IfeOlorun Olofin[1,2*], Ronggui Liu [2]

[1]Federal University Oye-Ekiti, Nigeria
Faculty of Engineering, Department of Civil Engineering
[2]Jiangsu University, China
School of Civil Engineering and Mechanics
*e-mail: epher2002@yahoo.com

Abstract

Wind-induced excitation causes structure to vibrate which leads to instability. This paper focuses on the performance of CFRP tensegrity system in a suspen-dome subjected to wind load by assuming such load as harmonic. A comparison is made with the traditional steel tensegrity system, in order to justify the integrity of CFRP cable application in a suspen-dome system. A finite element software, namely ANSYS, was implemented for the simulation by analyzing a physical model of 4 m span and 0.4 m height. Results show that CFRP tensegrity system has similar performance as steel tensegrity system and can be used as a substitute for steel.

Keywords: suspen dome, tensegrity system, CFRP cable, steel cable, harmonic load

1 Introduction

Researchers have been critical about the dynamic behavior of structural systems in order to achieve stability and safety [1-4]. Wind loading is usually dominant in structural loading on roofs of large buildings. It is paramount to fully understand the behavior pattern of the structure in respect to dynamic effect such as wind load. This kind of load increases the amplitude of the structures' vibration along the wind direction.

Wind is a random and dynamic phenomenon that occurs in space and time in structural systems. The importance of dynamic resonant response to wind for large span roofs is dependent on the natural frequency of vibration which is in turn dependent on the mass, stiffness properties and the damping [5]. However, the use of stiffening cables often increases the stiffness of a system sufficiently to reduce resonant contribution to a minimal proportion [6]. A structural system such as a suspen-dome [7] must have sufficient strength and adequate stiffness to resist wind-induced forces. The response of the geometrical structure under wind loading is crucial. Therefore, the need to understand such performance is required. The structural performance of wind load can be realistic by assuming such loads as harmonic [8]. Sustained cyclic load produces harmonic response in a structure. When natural frequency of a structure coincides with the forcing excitation frequency, resonance occur causing maximum displacement. The harmonic regime is a representative of many excitation cases encountered in engineering practice, such as vibration induced by imbalance, and torsional vibration in engines [9].

From history, damage to structures by severe winds has been a fact of life and solution to resist wind forces is required. With the upcoming development in the utilization of CFRP cable in space spatial structures [10-14], it is salient to understand the behavior pattern of such structure induced by wind.

In this paper, harmonic response technique was adopted on ANSYS software for a suspen-dome prototype constructed with CFRP as the tensegrity system and comparison was made with steel tensegrity system based on natural frequency and maximum displacement, in order to justify the implementation of CFRP cables in a suspen-dome.

2 Literature review

In this section, a brief explanation of wind loads on large roofs, harmonic response and theory of harmonics are presented in some detail.

2.1 Wind flow over large span roofs

Wind is the terminology used to describe air in motion and it is usually applied to the natural horizontal motion of the atmosphere. A constant flow of wind can suddenly gust to a rush of air. This sudden variation in wind speed plays an important part in determining a structure’s oscillation. The flow of wind is not steady and fluctuates in a random fashion. Because of this, wind loads imposed on buildings are studied statistically [5]. Wind load effect on a large roof has some significant difference in comparison with its effect on smaller roof; the resonant effects, although not dominant can be significant. Upward and downward external pressures are also significant. Domed structures are sensitive to wind load distribution hence the possibility of critical unbalanced pressure distribution must be considered [6]. When considering dynamic response of a structure to wind, distinguishing between the resonant response or near the natural frequency of the structure is necessary. The fluctuating responses at frequencies below the first or lowest frequency are usually great contributors [6]. However, because of the huge fluctuating components in wind loading on large roofs, the statistical correlation between pressure separated by a sizable distance is nanoscopic.

2.2 Harmonic Assessment

The response of the single degree of freedom systems to harmonic excitation is a consequential subject matter in structural dynamics. Apart from the fact that excitations are encountered in engineering system, for example force caused by unstable revolving machinery, the reaction of structures is understood based on harmonic excitation. This provides an insight to what degree the system will respond to any other type of force [13]. Forced harmonic vibration theory has a functional implementation in earthquake engineering because of its structural dynamics.

2.2.1 Theorem

Within a structural system any sustained cyclic load will produce harmonic response[15-16] as illustrated in Figure 1.

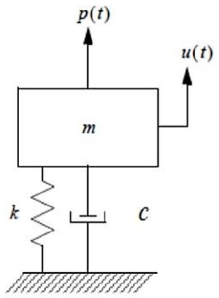

Figure 1: A system subjected to harmonic excitation [16]

A harmonic force is represented as [15]:

$$P(t) = P_0 \, sin \, \omega \, (t) \tag{1}$$

where P_o is the amplitude, ω is the exciting frequency and t is the period of excitation.

The governing differential equation for forced harmonics vibration for damped system is given as [17]:

$$M\ddot{U} + C\dot{U} + KU = P_0 \, sin \, \omega \, (t) \tag{2}$$

Solving the Equation (2) for initial condition, $U = U(0) and \, \dot{U} = \dot{U}(0)$ and the complimentary solution is the free vibration response given as:

$$U_c = e^{-\xi\omega_n t}(A \, cos \, \omega_D \, t + B \, sin \, \omega_D \, t) \tag{3}$$

$$A = U_0, B = \frac{\dot{U}_0}{\omega_n} - \left(\frac{\left(\frac{P_0}{k}\right)\left(\frac{\omega}{\omega_n}\right)}{\left(1 - \left(\frac{\omega}{\omega_n}\right)^2\right)} \right) \tag{4}$$

where

$$\omega_D = \omega_n \sqrt{1 - 2\xi,} \tag{5}$$

The solution for Equation (3) is given as:

$$U_P(t) = C \, sin \, \omega \, t + D \, cos \, \omega \, t \tag{6}$$

where

$$C = \left(\frac{P_0}{k}\right)\left[\frac{(1-\xi^2)}{(1-\xi^2)+2\xi(r)^2}\right] \tag{7}$$

$$D = \frac{-P_0}{k}\left[\frac{2\xi r}{(1-\xi^2)^2+(2\xi r)^2}\right] \tag{8}$$

The total response is given as:

$$U_t = e^{-\xi \omega_n t}(A\cos\omega_D\, t + B\sin\omega_D\, t) + C\sin\omega\, t + D\cos\omega\, t \tag{9}$$

3 Model Verification

A small-scaled suspen-dome was designed according to Chinese specification [18-20] with a span of 4 meters and a rise of 0.4 meters, as shown in Figure 2. The tensegrity system is made of the struts, radial and hoop cables. The tension members were constructed with CFRP.

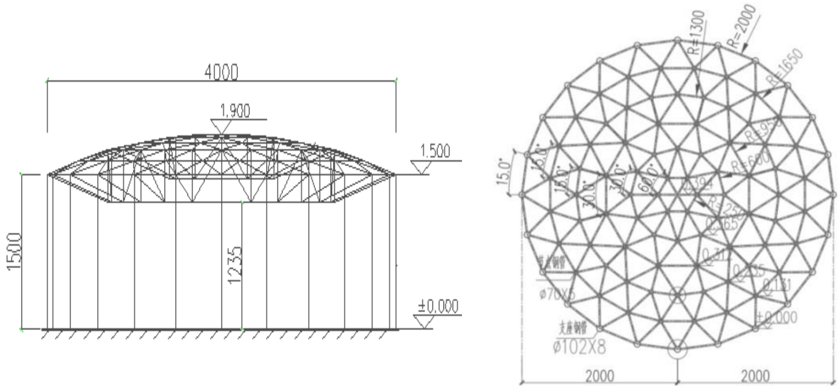

Figure 2: Model and reticulated single layer plan

Figure 3: Construction and deflection dial indicator layout

With the successful construction of the prototype as illustrated in Figure 3, experimental static performance was compared with numerical analysis via ANSYS software to validate the application of CFRP cables as a tensegrity system in a suspen-dome. Contrast between experimental and numerical findings for CFRP and steel cables was established. Figure 4(a) illustrates the maximum stresses generated on the single reticulated layer at high imposed load.

Similarly, Figure 4(b) shows the maximum displacement at specified nodes obtained for analysis.

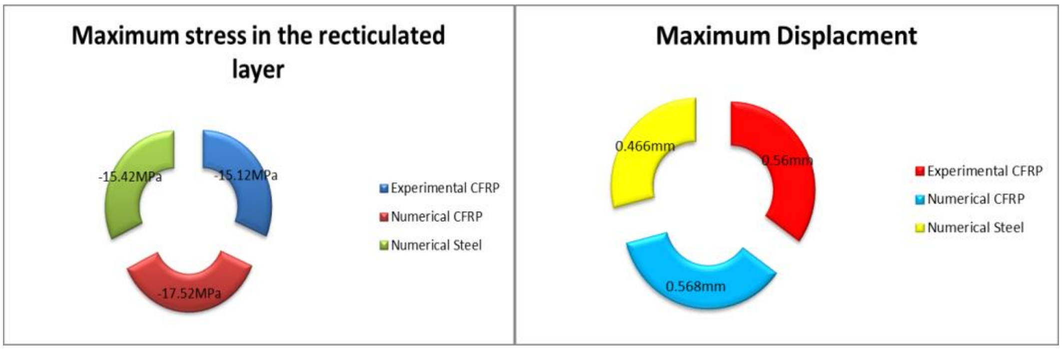

(a) (b)

Figure 4: Contrast of maximum values for stress and displacement

In addition, forces generated internally within the cables had similar values. It can be concluded that the digital analysis using ANSYS achieved a similar trend with the experimental findings with an excellent accuracy [21]. With positive findings obtained for the static investigation, it is paramount to further investigate the integrity of the structure, especially in dynamics which is a common practice. Although dynamic analysis is computationally extensive, complex and expensive compared with static analysis, numerical simulations are essential to observe the structure's performance before experimentation on the structure, in order to establish guidelines.

4 Numerical Technique

This section explains in detail the Finite Element Analysis (FEA), material properties utilized, and loading conditions.

4.1 Finite Element Method

With the vast development of software, the calculation of the behavior of suspen-dome application can be realistic and economical. The ability of CFRP structure to withstand critical loading can be evaluated by computational method. The two materials (steel and CFRP cables) are subjected to finite element analysis. Basic assumptions for the structure include cables are elastic and the tensegrity members are pin-jointed. The complexity of the suspen-dome structure allows results for three-dimensional FEM (Finite Element Method) analysis to be more comprehensive and reliable than results of empirical formula. The analysis was conducted with ANSYS 10 finite element software package [22]. The algorithm for the analysis is illustrated in Figure 5.

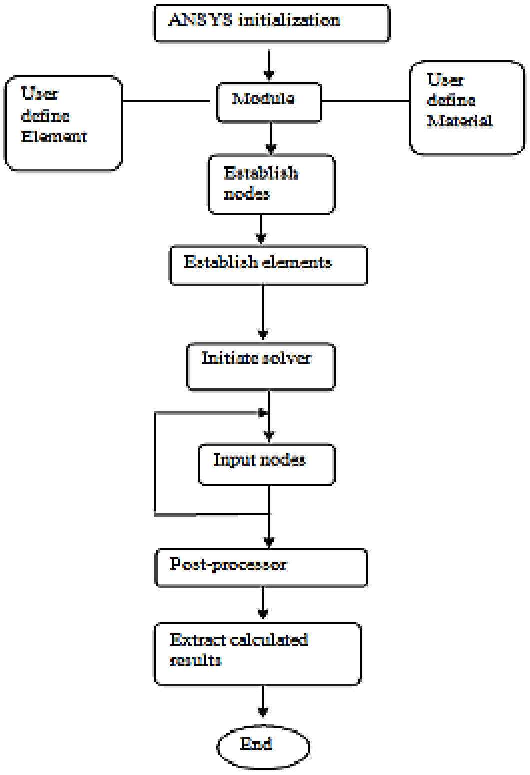

Figure 5: Simulation Algorithm

4.2 Model and Mesh

The finite element digital model is illustrated in Figure 6. Fixed boundary condition was assigned at the edge of the model. Beam 188 was incorporated for the single reticulated layer while link 10 was incorporated for the cable system. A mesh of 1mm x 1mm was utilized. CFRP cable was modeled as an anisotropic linear-elastic material and an isotropic elastic-plastic material was assumed for the mechanical behavior of steel cables.

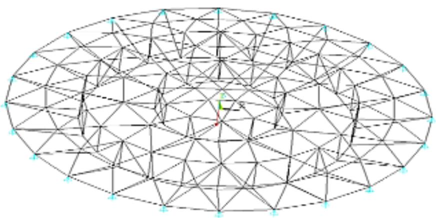

Figure 6: Finite element model

4.3 Material Properties

The mechanical properties of the materials used for the simulation are shown in Table 1.

Table 1: Material properties for the suspen-dome members

Member	Elastic Modulus (MPa)	Density (kg/m^3)
Steel Tensegrity System	$1.8x10^5$	78.5
CFRP Tensegrity system	$1.6x10^5$	16.0
Single reticulated layer	$2.05x10^5$	78.5

Material properties used in the analysis are subjected to certain loads which have an impact on the structural behavior of the suspen-dome system.

4.3.1 Dimensions

The dimension for the tension members is illustrated in Table 2.

Table 2: Illustrates the dimensions of the tension members

Cable	ϕ Radial (mm)	ϕ Hoop (mm)
Steel	8	10
CFRP [21]	5	7.9

The length for the hoop cable was 2.6 m and radial cable was 44 mm.

4.4 Loading

Modal analysis is the most fundamental of all types of dynamic analysis; it allows a given design to avoid resonant vibration and gives the engineer an idea of how the design will respond to dynamic load. The wind load coefficient was computed based on the codal provisions from the relevant standard GB50009-2012 [18]. The wind load on the structure was assumed to be sinusoidal and applied at nodes. All loads are assumed to have similar frequency and the maximum amplitude is identified by the static load intensity. Damping of 5% is considered for the models through the dynamic analysis.

5 Results and Discussion

Mode superposition method was employed for the analysis of harmonic response. The system frequency response domain is often utilized for experimental identification for a dynamic system. Prior to the method, modal analysis was carried out as a pre-requisite by using reduced method for mode extraction. Secondly, the system was assumed to be excited through external loads, namely loads that had time variation. An assumption made was that forces applied for a time period were enough for transients to vanish [13], so that the only response is a forced motion.

5.1 Modal Analysis

The structure's natural frequencies were obtained because when the structure excites at one of these frequencies, and the resonance occurs, this prevents the structure from fulfilling its desired function. Hence, resonance should be avoided because vibration generates dynamic stress and strain which causes fatigue and failure of a structure [23].
Modal analysis was computed and the natural frequencies and modal periods evaluated. Six mode values were extracted as illustrated in Figures 7 and 8.

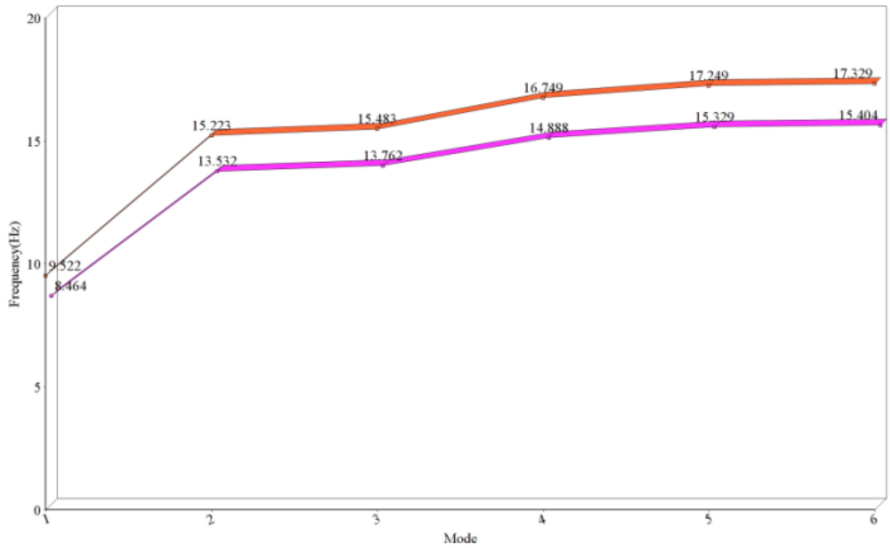

Figure 7: Natural frequency response (red = steel, purple = CFRP)

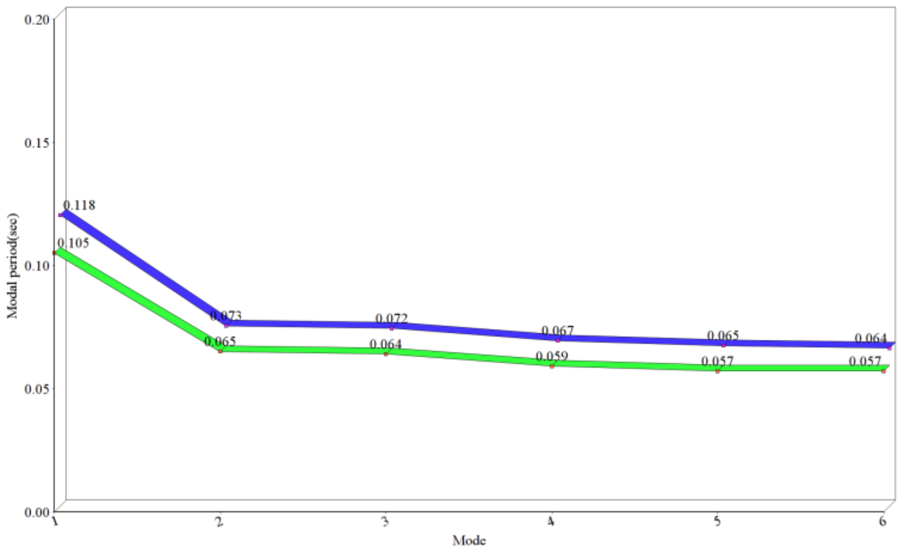

Figure 8: Modal period response (green = steel, blue = CFRP)

The displacement of the whole structure with steel tendons was 0.021 mm and that of CFRP was 0.029 mm at first modal period. The value for CFRP was 0.118 sec which is not a high value indicating that the whole structure is stiff enough. From the first six modes, it can be observed that the integrity of the roof with CFRP cables is very good and has similar behavior as that of steel cables. Similarly, Figures 9 and 10 illustrate the sixth mode for the structural system; both CFRP (Carbon Fiber Reinforced Polymer) and steel had similar structural shape.

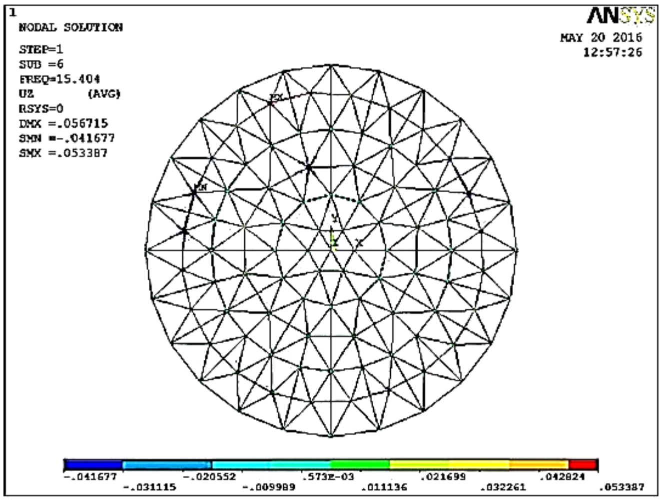

Figure 9: Sixth mode for CFRP

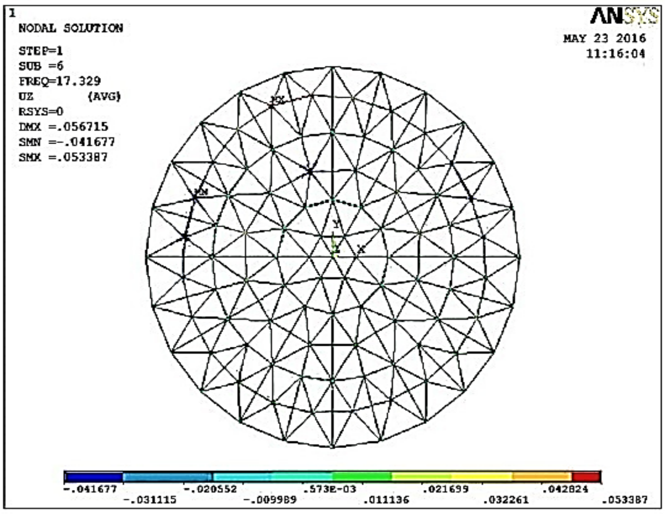

Figure 10: Sixth mode for steel

Frequencies obtained from the analysis were relatively low. The fundamental frequency of CFRP tensegrity system from the modal analysis was approximately 15.404 Hz, as shown in Figure 9, which is sufficiently similar to steel (Figure 10) with frequency of 17.329 Hz. The difference was 12% compared to steel, which still falls into the acceptable criteria within design. This satisfies the assertion of Cheng and Lau [24] which states that the modal frequencies and order don’t affect the motion of the cable. Substituting steel cable with CFRP has a stiffening effect on the structure.

5.2 Harmonic Response

The harmonic response was performed using mode superposition method on ANSYS. The response was obtained from the modal analysis in previous section and by considering the center node of the structural system to draw out conclusive findings for design process. The wind load on the structure was assumed to be sinusoidal and applied at nodes. All loads are assumed to have similar frequency and the maximum amplitude is identified by the static load intensity. The first mode and lowest frequency value was used in performing the harmonic response analysis from the modal solution because it is associated with wind and wave forces [6]. Due to the symmetrical nature of the structure any node or element can be represented by one of the typical nodes or elements. However, the node at the mid-section of the structure was considered because the effect is concentrated at the central part of the single reticulated layer. Figures 11-16 illustrate the typical response curves for the center node of the structure for both CFRP cables and steel cables at *x*, *y*, and *z* axis.

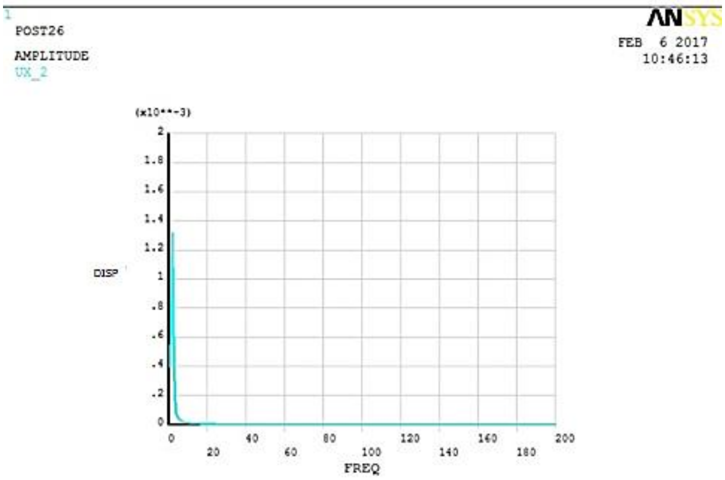

Figure 11: Typical response curve for the centre node (steel) *x*-axis

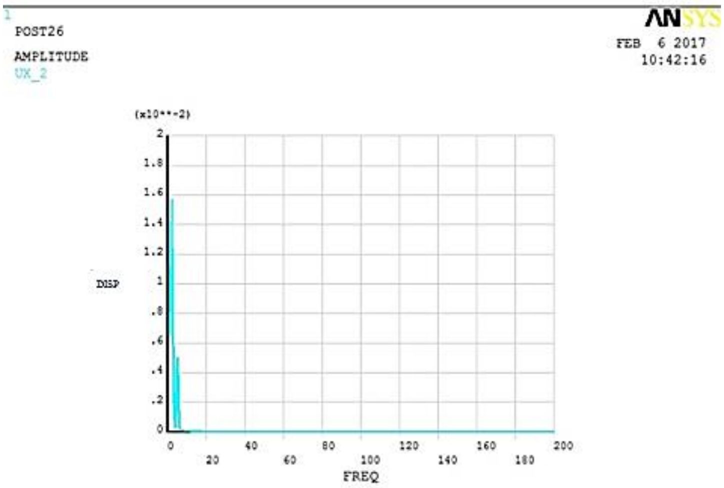

Figure 12: Typical response curve for the centre node (CFRP) *x*-axis

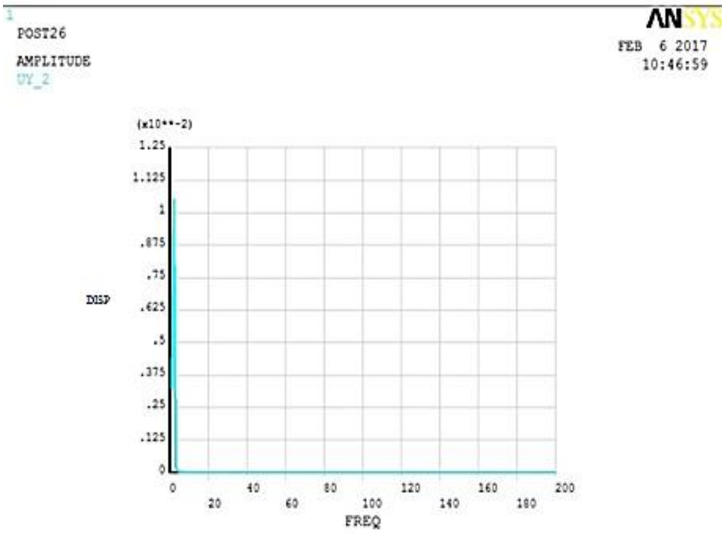

Figure 13: Typical response curve for the centre node (steel) *y*-axis

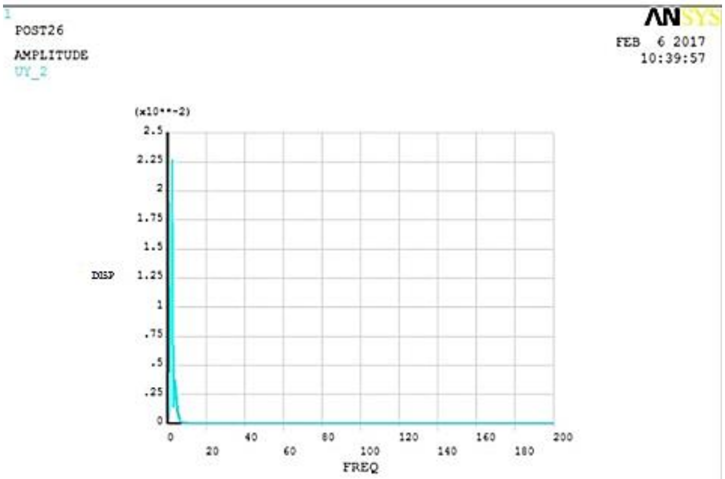

Figure 14: Typical response curve for the centre node (CFRP) *y*-axis

It can be observed that the peak frequency occurred at 0.2 Hz. At the *x*-axis, the maximum displacement was 0.016 mm for CFRP and 0.0135 mm for steel, at the *y*-axis, the maximum displacement was 0.0115 mm for steel and 0.0225 mm for CFRP, and at the *z*-axis, the maximum displacement for CFRP was 0.0128 mm and that of steel was 0.0087 mm. When one cable is at resonance, the other is at a different frequency which acts to dampen the resonance vibration, hence the total vibration amplitude is kept small for both steel and CFRP, thanks to the nature of tensegrity systems. It was also observed that all amplitudes reduced as natural frequencies increased. Internal forces in the cables and bars are not significant under vertical frequency for both materials.

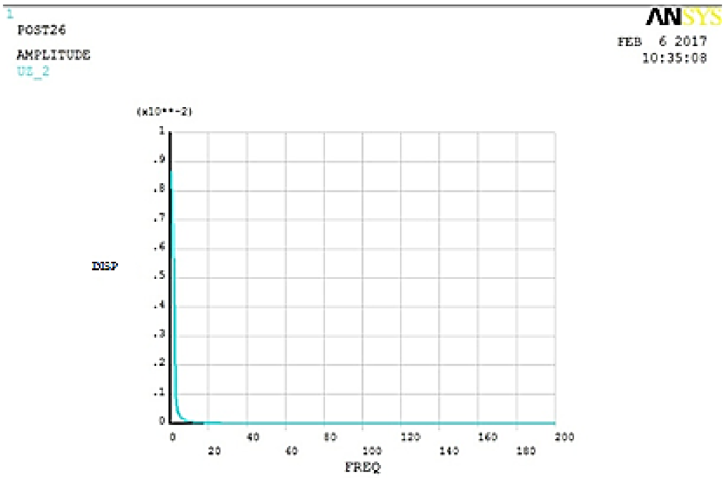

Figure 15: Typical response curve for the centre node (steel) *z*-axis

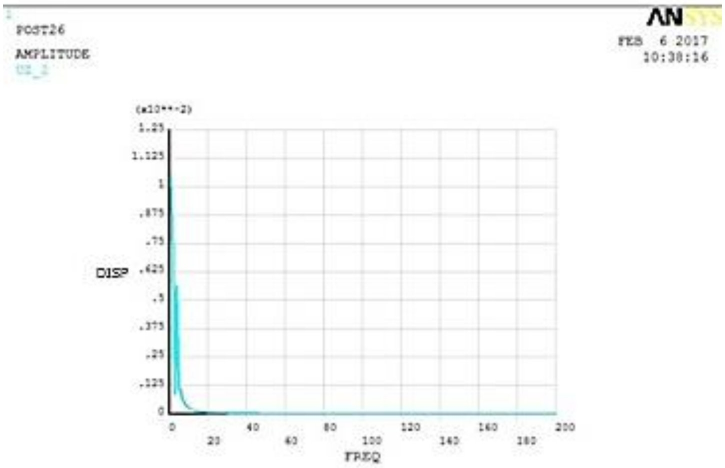

Figure 16: Typical response curve for the cenre node (CFRP) *z*-axis

6 Conclusion

Numerical analysis of the tensegrity system model was proposed to predict the dynamic mechanical response of the suspen-dome. From the simulated results, the following conclusions are drawn:

- CFRP is highly stable and has a good damping behavior.
- The vibration of CFRP cable is similar to that of steel, validating its exceptional mechanical properties of high stiffness-to-weight ratio and less curvature under gravity load. Such behavior resists vibration.

From a technical point of view, the harmonic response was assumed as wind induced response, the behavioral pattern of the suspen-dome with CFRP tensegrity system correlated well with that of steel system irrespective of the natural frequency difference. This is a realization that CFRP cables can resist wind forces and the novel material is suitable for designing of suspen-domes.

References

[1] Rezaiee, P.M., Aftabi, S.A., Hozhabrossadati, M. (2017). Free vibration analysis of a six degree of freedom mass spring system suitable for dynamic vibration absorbing of space frame. *International Journal of Engineering, Transaction B: Applications*. 30(1),pp. 30-39.

[2] Kerman, H., Behnamfar, F., Morsali, V. (2016). Seismic design of steel structures based on ductility and incremental nonlinear dynamic analysis. *International Journal of Engineering, Transaction B: Applications*. 29(1), pp. 23-30.

[3] Shahmardani, M., Mirzapour, J.,Tariverdilo, S. (2014). Dynamic response of submerged vertical cylinder with lumped mass under seismic excitation. *International Journal of Engineering, Transaction B: Applications.* 27(10),pp. 1547-1556.

[4] Jalili, R., Heydari, M.M., Fereydouni, A. (2013). Proposed relationship to design the waffle floor under harmonic vertical load. *International Journal of Engineering, Transaction B: Applications*. 26(10), pp. 1111-1118.

[5] Bungale, S.T. (2005). *Wind and earthquake reisistant buildings: Structural analysis and desgin*. Marcel Dekker, New York.

[6] John, D.H.(2003). *Wind loading of structure*. Spon press,London.

[7] Olofin, I., Liu, R. (2017). Suspen-dome System: A Fascinating space Structure. *The Open Journal of Civil Engineering*. 11, pp. 131-142.

[8] Salman, S.B., Mamta, M., Mohankumar, H. (2014). Harmonic response analysis of multi-storey building. *International Journal of Current Engineering and Technology*. l4(4), pp. 2387-2391.

[9] Micheal, G.,Daniel, R. (2015). *Mechanical vibrations: Theory and application to structural dynamic*. Wiley.

[10] Yue, L., Bernd, Z., Schlaich, M. (2016). Advantages of using CFRP cables in orthogonally loaded cable structures”. *AIMS Material Science*. 3(3), pp. 862-880.

[11] Olofin I, Liu R. (2016). Numerical modal analysis of a suspen-dome with CFRP tensegrity system. ASME *Journals: Series Modelling, Measurement and Control Series A*. 89(1),pp. 13-24.

[12] Olofin, I., Liu, R. (2017). Structural Optimization of Beijing Gymnasium Suspen-dome with CFRP (CFRP) cable. *Scientific Herald of the Voronezh State University of Architecture and Civil Engineering*. 36(4), pp. 106-115.

[13] Olofin, I., Liu, R. (2017). Transient behavior of CFRP tensegrity system in a Suspen- dome. *Civil Engineering Journal.* 3(8), pp. 547-555.

[14] Olofin, I., Liu, R. (2018). Analysis of thermal effect on CFRP cable. *Modelling, Measurement and Control B.* 87(2), pp. 97-100.

[15] Bingen, Y.(2004). *Stress, Strain and Structural dynamics*. Elseiver, Oxford.

[16] ThandavaMurthy, T.S. (2005). *Analysis of structures, Strength and Behaviour*. Oxford University Press.

[17] Anil, K.C.(2004). *Dynamics of structures, Theory and application to Earthquake Engineering*. Prentice-Hall of India, New Delhi.

[18] GB50009-2012. *Load code for the design of building structures*. Chinese planning press, Beijing (In Chinese).

[19] GB50017-2003. *Code for design of steel structures*. Chinese planning press, Beijing (In Chinese).

[20] GBJGJ7-2012. *Technical specification for space frame structure*. Chinese planning press, Beijing (In Chinese).

[21] Olofin, I., Liu, R. (2020). Research on the Static Behaviour of a Suspen Dome with CFRP (CFRP) Tensegrity System. *Iranian Journal of Science and Technology, Transactions of Civil Engineering*. 45, pp. 1-19. 10.1007/s40996-020-00488-5.

[22] ANSYS. (2008). *Release 10.0 Documentation for Ansys*, USA.

[23] Beards, C.F. (1984). *Structural Vibration Analysis: Modeling, Analysis and Damping of*

Vibrating Structure. John Wiley and Sons, USA.
[24] Cheng, S., Lau D. (2006). Impact of using CFRP cables on the dynamic behavior of cable stayed bridges . *IABSE Symposium Report*. 92, pp. 19-26.

DOI: 10.2478/sspjce-2023-0012

Mono-objective Optimization of Retaining Wall Using Genetic Algorithm

Ghania Boukhatem[1*], Moussaoui Moufida[1], Goudjil Kamel[2] and Rehab Bekkouche Souhila[3]

[1]LMGE Laboratory, Department of Civil Engineering, Faculty of Technology, Badji Mokhtar-Annaba University, Annaba, Algeria
[2] Laboratory infraRES, Department of Civil Engineering, University of Souk Ahras
[3] Laboratory LMGHU, Department of Civil Engineering, 20 August 1955 University of Skikda
e-mail: gboukhatem3@yahoo.fr

Abstract

This paper examines the importance of geotechnical optimization techniques for soil engineering applications, with a particular emphasis on evaluating geotechnical structures. Due to its prevalence in civil engineering, the complex interplay of geotechnical, structural, and financial considerations necessitates a trial and error approach. The study focuses on design elements, geometric dimensions, and volume considerations in order to highlight the economic viability of reinforced concrete retaining walls. Three code files are created using MATLAB to analyze their impact on active and passive thrusts and, as a result, the structure's volume. The slope angle, backfill overload, and friction angle are varied. The results demonstrate the effectiveness of using evolutionary algorithms to precisely optimize a single goal and demonstrate that this approach can enhance the design of retaining walls in reinforced concrete. This method demonstrates the ability to improve design procedures in this crucial area, which makes it an invaluable resource for structural engineering researchers and civil engineers.

Keywords: geotechnical engineering, genetic algorithm, retaining wall, optimal design, mono-objective optimization

1 Introduction

Structures known as retaining walls are frequently employed in civil engineering projects. These kinds of structures are frequently utilized to stabilize and maintain unstable land masses on their naturally occurring slopes. Due to the frequent occurrence of these soil slopes during the construction of highways, bridges, railroads, and other projects, the minimal cost design of reinforced concrete retaining walls is a crucial task in design optimization for the civil engineering industry. Multiple studies have examined the best design for retaining walls. Saribas and Erbatur, presented a detailed study on the optimal design of reinforced concrete cantilevered retaining walls using the cost and weight of the walls as objective functions, they controlled the overturning breaks, slip breaks, resistance, shear and moment capacities of the foot slab, the heel slab, and the foot of the wall as constraints [1]. Ceranique and Fryer proposed an optimization algorithm based on simulated annealing to calculate the minimum design cost of reinforced concrete retaining walls [2]. Sivakumar and Munwar, presented a new approach to reliability for the optimization of the design of retaining walls [3]. Ahmadi Nedushan and Varaee, have proposed an optimization algorithm based on particle swarms. They claim that this method requires fewer function evaluations, while leading to better results in the optimization of the support structure [4]. Deep, Singh, Kansal and Mohan applied the real coded genetic algorithm (RCGA) to test a large number of different walls sections and select the gravity retaining wall design with the lowest construction cost [5]. Khajehzadeh, Taha, El-Shafie and Eslami, the objective function was considered as the design of the total cost of the retaining walls, in addition, geotechnical and structural constraints were used for the optimization procedure of the retaining wall, [6]. Ghazavi et al., to arrive at an optimal design of the concrete retaining wall used the ant colony optimization algorithm (ACO), which is a technique based on the indirect communication of a colony of simple agents, called artificial ants, mediated by artificial phenomena, serve as distributed digital information, which the ants use to build probabilistically solutions to the problem to be solved [7]. Sheikholeslami et a.l, according to ACI318-05, the hybrid Firefly (FA) algorithm with an upper bound strategy is used to minimize the concrete wall cost [8]. Rowshanzamir and Aghayarzadeh, their study concerns the retaining walls of the layers reinforced by geogrids with different oblique angles as well as an inclined face in order to obtain optimized design alternatives [9]. Another study by Sheikholeslami et al., concrete retaining walls combined the two algorithms, Firefly and Ceiling strategies, demonstrating the superior performance of the hybrid approach compared to other approaches [10]. Jellali and Frikha, discussed deterministic and stochastic nonlinear constrained optimization methods, by applying a partial swarm optimization (PSO) algorithm which required the transformation of the problem into an equivalent unconstrained problem in order to determine the critical stability factor [11]. In the study by Gandomi et al., three evolutionary metaheuristic optimization algorithms (evolutionary strategy (ES), differential evolution (DE) and optimization algorithm based on biogeography (BBO)), are applied to the optimal design of reinforced concrete retaining walls using two objective functions the cost and the weight of the structure [12]. Chen, Asteris, Jahed Armaghani, Gordan, Pham, designed intelligent models, considering parameters such as wall thickness, stone density, wall height, soil density and the internal friction angle of the soil which were examined under different dynamic conditions and assigned as inputs to predict the safety factor (SF) of retaining walls [13]. BagheriSereshki and Derakhshani, studied the optimization of mechanically stabilized earthen walls with the algorithm of the Salpswarm and the gray wolf optimizer, and the classical algorithm of particle swarm optimization, to this end the results reveal that the modification of the internal friction angle of the reinforced soil has a fairly identical effect on the optimal costs of walls of different heights, in addition, it is shown that by increasing the height of the wall, the effects of variations in the unit weight of the reinforced soil and the angle of the slope of the embankment on the optimal cost are increased [14]. Mergos and Mantoglou, studied the flower pollination algorithm (FPA) applied for the first time, to the optimal design of reinforced concrete (RC) cantilevered retaining walls, where it was concluded that the optimal costs increase rapidly and non-linearly with the height of the wall, on the other hand, they increase almost linearly but rather regularly with the surcharge [15]. Kalemci, Ikizler, Dede, Angın, in their article the retaining wall was formulated as an optimization problem based on the ACI code 318-05 and Rankine's theory for the lateral pressure of the earth, the geotechnical constraints were determined as the safety factor against overturning, bending, the rupture of the load-bearing capacity and the structural stresses were determined as the moment and shear capacities of the wall elements to evaluate the effectiveness of the GWO algorithm compared to similar studies [16]. Kaveh, Hamedani, Bakhshpoori, concrete retaining walls were optimized for optimal design using eleven population-based metaheuristic algorithms; all algorithms used quickly converged to high-quality optimal designs [17]. Chen et al., indicated that the multiparametric optimization approach has also been applied in the field of geotechnics, in the design of backfill piles with basal reinforcement [18]. Pradeep et al., examine the in-depth reliability of cantilever sheet pile walls buried in a coherent soil and backfilled with a coherent soil. Through the use of various optimization strategies, namely the artificial bee colony, the optimization of the ant colony, the ant-lion colony, the imperialist competitive algorithm, the mixed complex evolution and the optimization based on teaching and learning, the artificial neural network (ANN) widely used to predict the embedding depth of a cantilever sheet pile wall; according to the experimental results, hybrid models (ANN) and optimization based on teaching and learning (ANN-TLO) are more efficient in predicting the reliability of cantilever sheet pile walls [19]. Boumezrane carried on, optimization according to different deterministic and stochastic optimization schemes by a selection on a mathematical basis, of the objects best suited with respect to defined criteria, by choosing values or input functions within a certain range of parameters. It can be mono-objective (a single function) or multi-objective (several objective functions), sometimes even contradictory (Pareto optimization) [20]. Even though the weight and the cost of the task do not have opposing goals, the cost of the work increases as its weight increases. The retaining wall optimization problem has been approached as a multi-objective optimization problem employing the functions (cost, weight, and safety factor) that need to be minimized in each of the aforementioned studies. In this study, we choose to optimize a retaining wall using a genetic algorithm, one of the single-objective artificial intelligence techniques. Important design variables, such as geometric variables that describe the thickness of the veil and sole as well as the lengths of the foot and heel, are included in the formulation of the problem. The main goal of this work is to use the genetic algorithm to find the best design for a cantilever type retaining wall. MATLAB software was used to create a code consisting of three files (objective function file, constraints file, and main file).

2 Application of the Genetic Algorithm

It has been demonstrated that most of the techniques used are based on metaheuristic methods, but the Genetic Algorithm GA and the Particle Swarm Optimization PSO (optimization by surface modification) have been widely used compared to other methods and appear to effectively treat the non-linearities encountered in many geotechnical problems [20]. Therefore, the application of the genetic algorithm is highly recommended (Table 1).

Table 1: Occurrence of different optimization methods [20]

Methods	**Foundations**	**Slope Stability**	**Soil Properties and Investigation**	**Total geotechnical optimization methods**
GeneticAlgorithm GA	5	4	3	12
ParticleSwarmOpt PSO	3	7	1	11

Artificial Neural Networks ANN	3	2		5
Surface AlteringOptimization SAO		4		4
Differential Evolution DE	1	2	1	4
Artificial Bee Colony ABC	2	1	1	4
Non LinearProgramming NLP	1	3		4
ANFIS and Fussy sets	1		3	4
DiscreteLayoutOptimization DLO	4			4
EvolutionaryAlgorithm EA	3			3
Harmony Search HS		3		3
Reliabilitymethods	1	1	1	3
BBO Boo-geo Based Algorithm	2			2
Monte Carlo Optimization MCO	1	1		2
Ant Colony AC	1			1
Multiple Regressions MR		1		1
GrasshopperOpt. Algorithm CAA		1		1
MultiverseOpt. Algorithm MVO		1		1
GravitationalSearchAlgorithm GSA		1		1
Smooth Part. Hydrodynamics SPH		1		1
Improved Arith Optimizer IAO	1			1
Interior Point Method IPM		1		1
MARS M.variate Adap. RegrSplines		1		1
TopologyOptimization	1			1
RSM Res. Surface Methodology		1		1
Least Squares Method		1		1
Geostatistics			1	1
Adaptive Metamodels			1	1
Inverse Analysis			1	1
Other	8	4	3	15
Total optimization methods used	38	41	16	95

In geotechnical engineering, retaining walls are used to secure embankments that are not stable in the long term against lateral loads from the ground. The design of the retaining wall is divided into two phases: Geotechnical design and structural design, which are evaluated using selected wall dimensions. Varga et al pointed out that if the initially selected dimension does not satisfy the stability constraints, a new dimension is selected and reassessed until the stability constraints are satisfied. Even if the conditions are met, it is not certain that the determined wall dimensions will result in the most economical wall design [21]. In the geotechnical design phase, the wall must withstand the different modes of rupture by calculating the safety factors sliding, overturning and bearing capacity. As regards the structural design phase, the wall must be checked for breakage due to shearing and at the moment at the junction of the veil with the sole and the junction of the veil with the heel and the skate. The design procedure used in this work to verify the two design phases is based on Rankine's theory. Figure 1 shows the different geometric variables and the forces taken into consideration in this study. Geometric constraints are made of boundary constraints and linear constraints of equalities and inequalities defined to produce practical designs. Based on Rankine's theory and the geometry of the example studied in this work, several constraint formulas have been used, the latter direct the algorithm to search for solutions (in our example from *X1* to *X*6) within a certain interval fixed by the lower and upper limits of each part of the work.

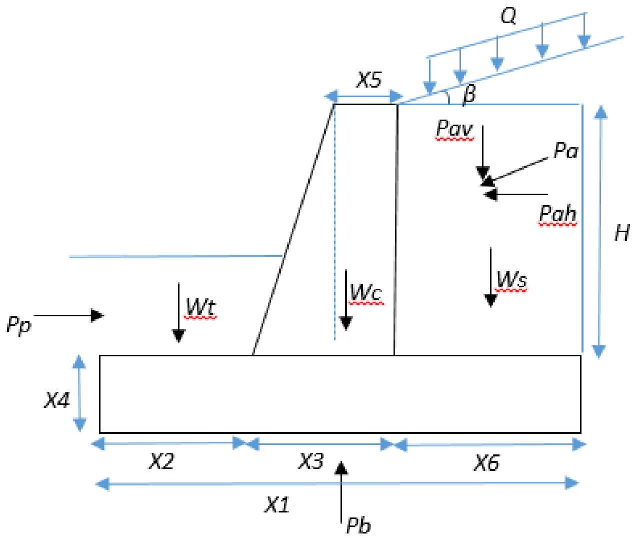

Figure 1: The retaining wall's design parameters

where

Ws: the backfill's weight pressing against the wall's heel;

Wt: the floor's weight on the wall's foot;

Wc: the total weight of the reinforced concrete wall's individual sections;

Q: is an overload;

Pb: the reaction of the soil;

Pa and *Pp*: are the resulting forces from the lateral pressures, both active and passive;

Equations 1 and 2 are used to calculate the active and passive earth pressure coefficients based on Rankine's theory.

$$K_a = \cos\beta \frac{\cos\beta - \sqrt{\cos^2\beta - \cos^2\theta}}{\cos\beta + \sqrt{\cos\beta^2 - \cos\theta^2}} \quad (1)$$

$$K_p = tan^2\left(45 + \frac{\theta}{2}\right) \quad (2)$$

where

θ: The backfill's internal friction angle

β: The embankment's angle

To build a retaining wall, three geotechnical rupture modes are taken into account. These requirements are as follows:
Equation 3 provides the safety factor with relation to overturning.

$$F_{S0} = \frac{\sum \mathrm{M}_R}{\sum \mathrm{M}_0} \tag{3}$$

$\sum M_0$: total of the unstable moments
$\sum M_R$: sum of the resistant moments
Safety factor with respect to sliding is given by the Equation 4.

$$F_{SS} = \frac{\sum \mathrm{F}_R}{\sum \mathrm{F}_D} \tag{4}$$

$\sum F_D$: total of the horizontal forces that are unstable
$\sum F_R$: total of the horizontally resisting forces

$$\sum F_R = \sum(\mathrm{W}_{wall}) \tan\left(\frac{2\emptyset_{base}}{3}\right) + \frac{2BCbase}{3} + P_p \tag{5}$$

$$\sum F_D = \mathrm{P}_a cos\beta \tag{6}$$

P_p: the stop
P_a: the push
$\sum W_{wall}$: total weight of the wall
$\emptyset_{base}$: friction angle of the foundation soil
B: total width of the sole
C: cohesion of the sole and foundation soil interface
Safety factor with respect to the lift of the ground is given by the Equation 7.

$$F_{SB} = \frac{q_u}{q_{max}} \tag{7}$$

q_{max}: maximum pressure produced as a result of the forces acting on the retaining wall, as shown by Equation 8.
q_u: ultimate bearing capacity of the foundation soil

$$q_{min_{max}} = \frac{\sum V}{B}\left(1 \mp \frac{6e}{B}\right) \tag{8}$$

B: the width of the base
$\sum V$: maximum pressure generated by the forces acting on the retaining wall given by Equation 8.
e: the resulting force system's eccentricity, which is stated as follows:

$$e = \frac{\mathrm{B}}{2} - \frac{\sum M_R - \sum M_0}{\sum V} \tag{9}$$

3 Using a Genetic Algorithm to Optimize a Cantilever Wall

3.1 Formulation of an Optimization Problem Mathematically

The majority of the time, optimization issues aim to minimize an objective function *f(x)* while taking needs or restrictions into account. It might be non-linear or linear. A formulation for an optimization issue is as follows:

$$\begin{aligned} &hj\,(x) \leq 0 \qquad j = 1, 2, \ldots, m \\ &gi\,(x) \leq 0 \qquad i = 1, 2, \ldots, p \\ &Lk \leq Xk \leq Yk \quad k = 1, 2, \ldots, n \end{aligned} \tag{10}$$

h (x): are equality constraints
g (x): are inequality constraints
L, Y: are constraints to the limits

In the following we describe the objective function *f(x)* and the constraints used in this work, in order to achieve an optimal design using meta-heuristic techniques, since our problem is a mono-objective optimization problem, a single objective function which is the volume of the work has been used in this work. According to (Fig. 1), the volume of the wall can be given by Equation 11.

$$f(x) = XI \text{ x } X4 + (X3 + X5) \text{x } H/2 \tag{11}$$

According to Algerian earthquake laws (RPA 99), designing safe and stable retaining walls necessitates fulfilling a number of requirements pertaining to the stability, capacity, and geometry of the wall. According to the technical engineer's document, Equations 11, 12, and (13) describe the stability of a retaining wall as follows:

$$F_{SO} \geq F_{SO\ design} \tag{12}$$
$$F_{SS} \geq F_{SS\ design} \tag{13}$$
$$F_{SB} \geq F_{SB\ design} \tag{14}$$

$F_{S0design}$: safety concern with regard to overturning equal to 1.5.
$F_{SSdesign}$: safety factor with regard to sliding equal to 1.5.
$F_{SBdesign}$: safety factor with regard to the bearing capacity equal to 3.
Based on Rankine's theory and the geometry of the case explored in this work, various constraint formulae have been employed for the geometric constraints, which are made up of limit constraints and linear constraints of equalities and inequalities defined to build practical designs. The latter tell the algorithm to look for answers (in our example, from *X1* to *X6*) inside a predetermined window determined by the lower and upper bounds of each component of the work. In Figure 1, it is shown how much the variables *X1* through *X6* might vary.

$$X1 = X2 + X3 + X6 \tag{15}$$
$$X3 > X5 \tag{16}$$
$$X6 > X2 \tag{17}$$

$$X6 > X3 \tag{18}$$

Linear constraints are shown by the equations above. Three of the constraints are linear inequality constraints, while the first is a constraint on linear equality. The steps taken in this section are described in the form of an algorithm in Figure 2.
The three files (the main file, the constraints file, and the objective function file) that make up the process used in this study were created using the MATLAB programming language. This is depicted in Figure 2.

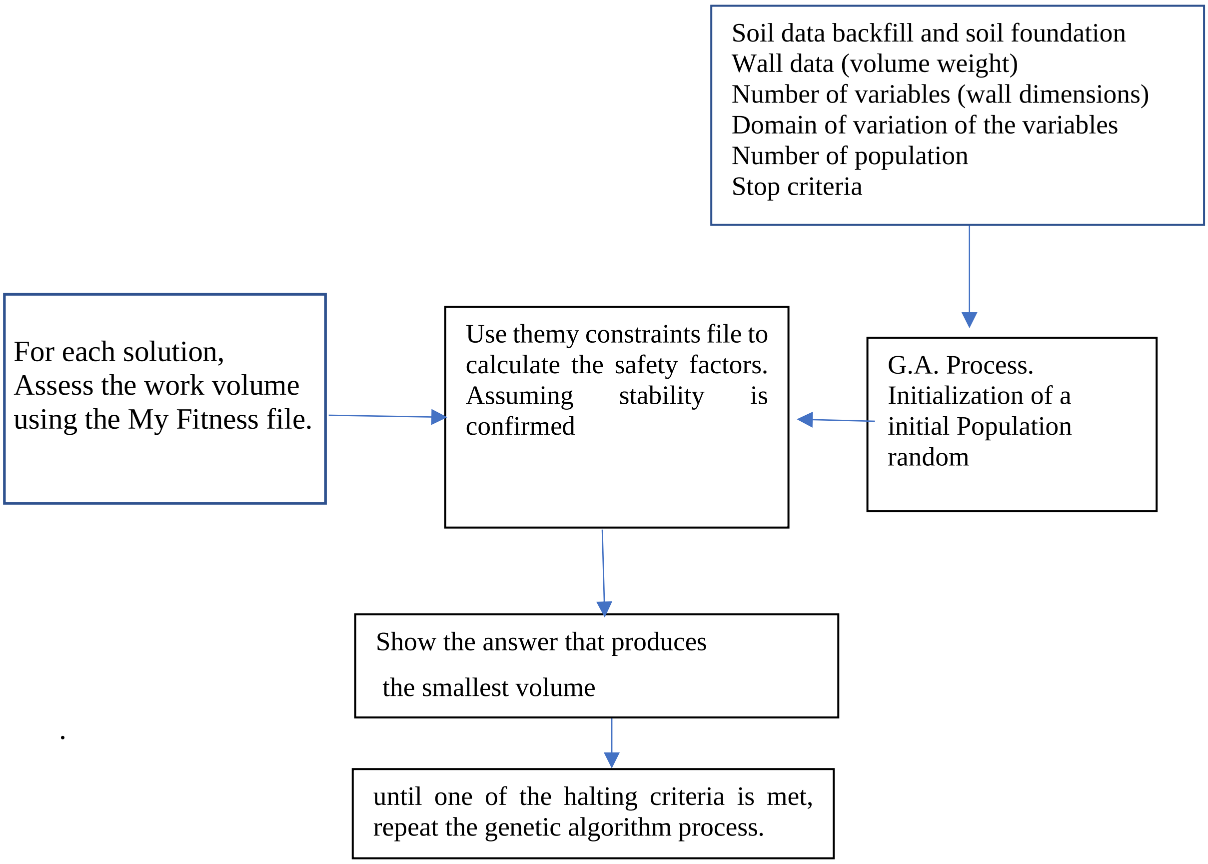

Figure 2: Application of the genetic algorithm in optimization flowchart

4 Validating the Model

Our findings show that there are three key differences among all metaheuristics, regardless of their objective type: The parameters used in our study to illustrate the genetic algorithm's efficacy and performance in solving restricted mono-objective optimization problems are displayed in Figure 3. These parameters encompass the fitness attributing method, the diversity maintenance technique, and the elite conservation strategy.

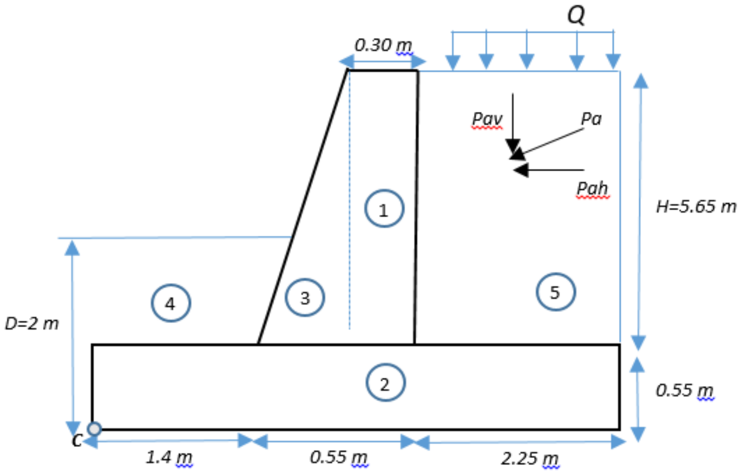

Figure 3: The validation retaining wall's dimensions.

The latter has a length of (130 m) and a height of (5.65 m) retaining a horizontal embankment with an overload Q =10.2 kN/m^2. The characteristics of the structure as well as of the soil are given in Table 2.

Table 2: Floor and retaining wall characteristics

Floor and retaining wall characteristics	**Value**
Tensile Strength (10^3kN/m^2)	2.1
Resistance of concrete to Compression (10^3kN/m^2)	25
Steel yield strength (10^3kN/m^2)	400
Veil height (m)	5.65
Volume weight of the backfill (kN/m^3)	18
Volume weight of the foundation soil (kN/m^3)	18.8
Internal friction angle of the embankment (°)	30
Cohesion of the embankment (kN/m^2)	0
Internal friction angle of the foundation floor (°)	15
Foundation soil cohesion (kN/m^2)	27.7
Installation of the structure (m)	2
Slope angle (°)	0

Table 3: The retaining wall's ideal construction

The design of the wall with GA	Unit	The values
X1	m	3.0881
X2	m	1.1010
X3	m	0.2928
X4	m	0.4713
X5	m	0.2033
X6	m	1.6940
fval (wall volume)	m^3	2.8566

Table 3 shows that the wall's design has a volume of 4.71 m^3, whereas the optimization method used in the study yielded a volume of 2.85 m^3. This shows a 1.86 m^3 difference in linear meters. Nevertheless, there is insufficient context or information in the search results to determine the importance or ramifications of this difference.

5 Parametric Study

We chose to conduct a parametric study in order to examine the sensitivity of the model created in this investigation. The values that the fixed parameters in this parametric study took are displayed in Table 4.

Table 4: Parameter values that were fixed during the parametric study

	distribution Laod over (kN/m^2)	Unit Weight (kN/m^3)	Bearing Capacity (kN/m^2)	Embedding Df (m)	Friction angle (°)	Cohesion (kN/m^2)	Angle of slope (°)
Retaining Wall		23.58		1.5	/	/	
Embankment	0	20			34°	0	10°
Soil Foundation		20	574.07		40°	40	

The margin of the values of the various parameters used is given in Table 5.

Table 5: Different parameter values are taken into account in a parametric investigation

Load (kN/m^2)	The embankment's angle of friction (°)	Angle of slope (°)
20	29°	0°
30	30°	5°
40	34°	15°
	38°	25°
	42°	30°

5.1 The Influence of the Slope Angle α

As seen in Figure 4, the values in Table 6 show that an increase in the embankment's angle causes the structure's volume to increase. Instead of decreasing the slope's angle as is usually the case with the horizontal component, the rise in the height h was the reason for the increase in the active thrust. The fill angle affects the structure's stability, which results in the volume of the structure expanding. There is insufficient context or information in the search results to determine the significance or ramifications of this discovery. To guarantee that embankments are secure and stable, the findings do, however, imply that the stability of the structure should be taken into account during the design process [22].

Table 6: The influence of the slope angle *α*

α (°)	*Fval* (m^3)	*X1*	*X2*	*X3*	*X4*	*X5*	*X6*
0°	2.23	2.5092	0.6133	0.3393	0.4068	0.2120	1.5561
5°	2.26	2.3939	0.6680	0.3996	0.3780	0.2041	1.3273
15°	2.43	2.5835	0.6087	0.4491	0.3750	0.2011	1.5252
25°	2.69	2.3610	0.4328	0.6002	0.3757	0.2030	1.3277
30	2.71	3.3325	1.1511	0.4445	0.3751	0.2056	1.7349

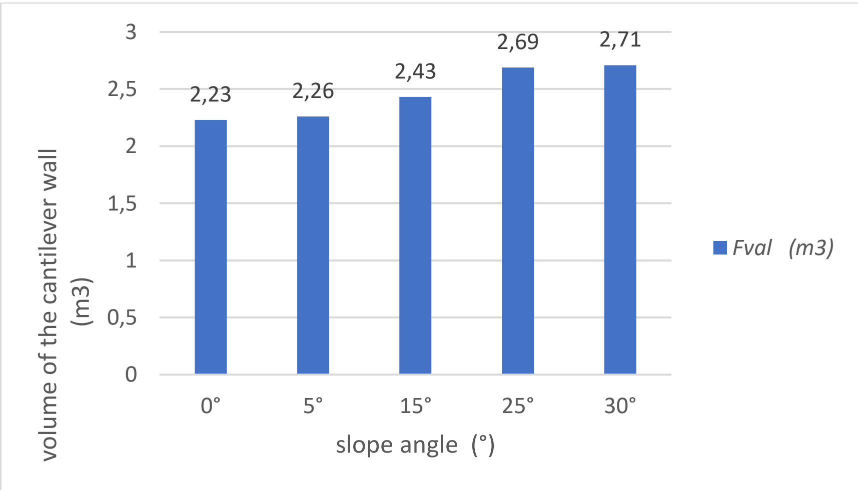

Figure 4: The Influence of the slope angle

5.2 The Influence of the Backfill Friction Angle

Table 7 lists the sizes of the different parts that make up the retaining wall. Keyhan [23] suggests that it makes sense for the cantilever wall's volume to decrease as the friction angle rises. As shown in Figure 5, the increase in the angle of friction causes a drop in the earth's active thrust coefficient, which reduces the active thrust. The search results contain more resources on the design and analysis of cantilever retaining walls, such as optimization evaluations, case studies, and design guidelines.

Table 7: The influence of the backfill friction angle

Ø1	***Fval* (m^3)**	***X1***	***X2***	***X3***	***X4***	***X5***	***X6***
29°	2.88	2.6306	0.4250	0.6391	0.376	0.2023	1.5661
30°	2.78	2.6692	0.5618	0.5881	0.3780	0.2033	1.5191
34°	2.26	2.5450	0.5835	0.3741	0.3793	0.2055	1.5876
38°	2.06	2.4239	0.7135	0.2923	0.3773	0.2172	1.4180
42°	1.76	1.8996	0.5863	0.2622	0.3781	0.2035	1.0502

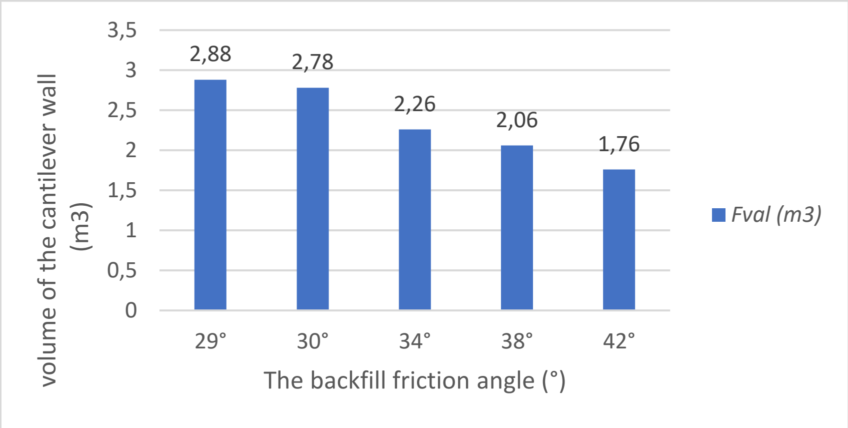

Figure 5: The Influence of the backfill friction angle

5.3 The influence of *Q* overload

Table 8: The influence of *Q* overload

***Q* (kN/m^2)**	***Fval* (m^3)**	***X1***	***X2***	***X3***	***X4***	***X5***	***X6***
20	1.98	2.5125	0.2432	0.6182	0.3863	0.2058	1.4694
30	2.14	2.7261	0.8189	0.2928	0.3775	0.2011	1.6142
40	3.08	2.7701	0.5123	0.7063	0.3751	0.2018	1.5516

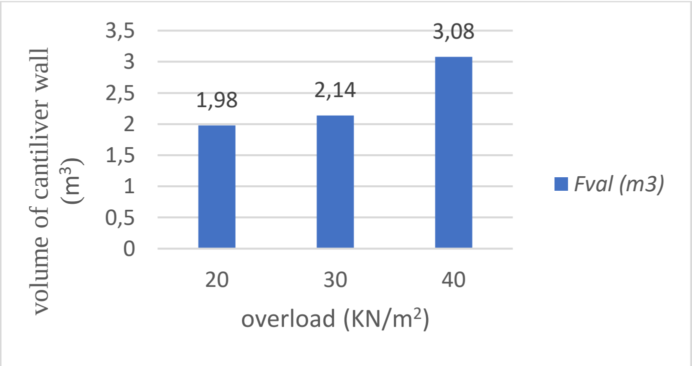

Figure 6: The Influence of the overload

Based on the values in Table 8, it is evident that an increase in overload causes an increase in the cantilever wall's volume, as shown in Figure 6. This is because an increase in overload leads to an increase in active thrust, as indicated by Huang's search results [24]. Therefore, it is required to increase the structure's dimensions in order to increase the stabilizing forces in response and resist this thrust, which is a destabilizing force.

6 Conclusion

The Genetic Algorithm (GA), a highly effective metaheuristic optimization algorithm modeled after the process of natural selection, is used in this work. This algorithm shows to be a reliable tool for solving optimization issues, especially when it comes to finding the best design for retaining walls made of reinforced concrete. A genetic algorithm with constraints is used to accomplish this goal, evaluating both passive and active pressure using the Rankine theory of earth pressure. The genetic algorithm places restrictions on the design structure, such as the need to provide a safety factor against overturning, sliding, and bearing capacity.

The suggested model was created by mono-objective optimization using a genetic algorithm, varying the load from 20 to 40 kPa, base soil friction angle from 29 to 42, and backfill slope from 0 to 30. A comparative study with retaining walls built in Skikda city, Algeria, used a traditional method. The parametric study's findings demonstrate that raising the load and slope angle causes the structure's volume to increase. On the other hand, the cantilevered wall's volume decreases as the friction angle increases. The suggested model, however, is an effective and ideal design procedure for cantilever retaining walls, according to the results obtained. These algorithms exhibit effective performance in meeting both structural and geotechnical stability requirements at the same time. GA has been used to design retaining walls with success and has shown to be a reliable optimization method.

Références

[1] Saribash, A., & Erbatur, F. (1996). Optimization and Sensitivity of Retaining Structures. Journal of Geotechnical Engineering, ASCE, Vol. 122, No.8, pp. 649-656.

[2] Ceranic, B., & Fryer, C. (2001). An Application of Simulated Annealing to Optimum Design of Reinforced Concrete Retaining Structures. Journal of Computers and Structures, Vol. 79, pp. 1569-1581.

[3] Sivakumar Babu, G.L., &Munwar, Basha B. (2008). Optimum Design of Cantilever Retaining Walls Using Target Reliability Approach. International Journal of Geomechanics, ASCE, Vol. 8, No. 4, pp. 240-252.

[4] Ahmadi Nedushan, B., &Varaee, H. (2009). Optimal Design of Reinforced Concrete Retaining Walls Using a Swarm Intelligence Technique. The first International Conference on Soft Computing Technology in Civil, Structural and Environmental Engineering, UK

[5] Deep, K.; Singh, K.P.; Kansal, M.; Mohan, C. (2009). A real coded genetic algorithm for solving integer and mixed integer optimization problems. Appl. Math. Comput. 212, 505–518.

[6] Khajehzadeh, M., Taha, M.R.; El-Shafie, A.; Eslami, M. (2010). Economic design of retaining wall using particle swarm optimization with passive congregation. Aust. J. Basic Appl. Sci. 4, 5500–5507.

[7] Ghazavi, M., & Bonab, S. B. (2011). Optimization of reinforced concrete retaining walls using ant colony method. Geotechnical Safety and Risk. ISGSR 2011, 297-306.

[8] Sheikholeslami, R., Khalili, B.G., Zahrai,S.(2014). Optimumcostdesignof reinforced concrete retaining walls using hybrid firefly algorithm. Int. J. Eng. Technol. 6(6), 465.

[9] Rowshanzamir, M.A., Aghayarzadeh, M. (2015). Comprehensive study of geogrid-reinforced soil retaining walls with tilted faceandreinforcements. Aust. J. Civ. Eng. 13, 48–63.

[10] Sheikholeslami, R., Khalili, B.G.; Sadollah, A.; Kim, J. (2016). Optimization of reinforced concrete retaining walls via hybrid firefly algorithm with upper bound strategy. KSCE J. Civil Eng. 20(6), 2428–2438.

[11] Jellali, B., Frikha, W. (2017). Constrained Particle Swarm Optimization Algorithm Applied to Slope Stability. Int. J. Geomech.17,06017022.

[12] Gandomi, A.H., Kashani, A.R., Roke, D.A. et al. (2017). Optimization of retaining wall design using evolutionary algorithms. Struct Multidisc Optim 55, 809–825. https://doi.org/10.1007/s00158-016-1521-3

[13] Chen, H., Asteris, P.G., Jahed Armaghani, D., Gordan, B., Pham, B.T. (2019). Assessing Dynamic Conditions of the Retaining Wall: Developing Two Hybrid Intelligent Models. Appl. Sci. 9, 1042. https://doi.org/10.3390/app9061042

[14] Bagheri Sereshki, A., Derakhshani, A. (2019). Optimizing the Mechanical Stabilization of Earth Walls with Metal Strips: Applications of Swarm Algorithms. Arab J Sci Eng 44, 4653–4666. https://doi.org/10.1007/s13369-018-3492-8

[15] Mergos, P.E., Mantoglou, F. (2020). Optimum design of reinforced concrete retaining walls with the flower pollination algorithm. Struct Multidisc Optim 61, 575–585. https://doi.org/10.1007/s00158-019-02380-x

[16] Elif Nur Kalemci, Sabriye Banu İkizler, Tayfun Dede, Zekai Angın. (2020). Design of reinforced concrete cantilever retaining wall using grey wolf optimization algorithm, Structures, Volume 23, Pages 245-253, ISSN 2352-0124, https://doi.org/10.1016/j.istruc.2019.09.013.

[17] Kaveh, A., Hamedani, K.B., Bakhshpoori, T. (2020). Optimal Design of Reinforced Concrete Cantilever Retaining Walls UtilizingElevenMeta-Heuristic Algorithms: A Comparative Study. Period. Polytech. Civ. Eng. 64, 156–168.

[18] Chen, C., Mao, F., Zhang, G., Huang, J., Zornberg, J., Liang, X., Chen, J. (2021). Settlement-Based Cost Optimization of Geogrid-Reinforced Pile-Supported Foundation. Geosynth. Int. 1–39, online ahead of print.

[19] Pradeep, T., GuhaRay, A., Bardhan, A. et al. (2022). Reliability and Prediction of Embedment Depth of Sheet pile Walls Using Hybrid ANN with Optimization Techniques. Arab J Sci Eng 47, 12853–12871. https://doi.org/10.1007/s13369-022-06607-w

[20] Boumezerane, D. (2022). Recent Tendencies in the Use of Optimization Techniques in Geotechnics: A Review. Geotechnics, 2, 114-132. https://doi.org/10.3390/geotechnics2010005

[21] Varga, R., Žlender, B., Jelušič, P. (2021). Multiparametric Analysis of a Gravity RetainingWall. Appl. Sci. 11, 6233. https://doi.org/10.3390/app11136233.

[22] Yingchaloenkitkhajorn, Kongkit. (2019). Analysis of embankment slope stability: the comparison of finite element limit analysis with limit equilibrium methods. MATEC Web of Conferences.,270., https://doi.org/10.1051/matecconf/201927002004

[23] Keyhan, S.O., Cheshmi, B., Jahangirinia, A., Bayat, M., Yousefi, P. (2021). Mandibular Angle Augmentation. In: Keyhan, S.O., Fattahi, T., Bagheri, S.C., Bohluli, B., Amirzade-Iranaq, M.H. (eds) Integrated Procedures in Facial Cosmetic Surgery. Springer, Cham. https://doi.org/10.1007/978-3-030-46993-1_14

[24] Huang, Z.; Zhang, D.; Zhang, D. (2021). Application of ANN in Predicting the Cantilever Wall Deflection in Undrained Clay. Appl. Sci., 11, 9760. https://doi.org/10.3390/app11209760

DOI: 10.2478/sspjce-2023-0013

Experimental Study of the Physico-Chemical Stabilization of a Loess by Sodium Silicate: Case of Southern Algeria

Ouassila Bahloul[1*], Fatima Zohra Tebbi[2], Laid Lekouara[3,4]

[1]LGC-ROI. Civil Laboratory-Risks and Structures Interactions. Faculty of Technology University of Mostepha Ben Boulaid, Batna 2, Algeria
[2]LRNAT Laboratory, Earth Sciences and Universe Institute. University of Mostepha Ben Boulaid, Batna 2, Algeria
[3]Faculty of Science and Technology, University of Abbés Laghrour Khenchela, Algeria
[4]Material and Hydrology Laboratory, University of Sidi Bel Abbes, Faculty of Technology, Algeria.
*e-mail: o.bahloul@univ-batna2.dz

Abstract

This study focuses on collapsible soil from hyper-arid regions in the south of Algeria (Zeribet El Oued, Biskra). A physical characterization of the studied soil was performed which revealed that the soil samples are loess. After this, an experimental study was done on the influence of the sodium silicate solution (Na_2SiO_3) at different doses on the collapse potential (CP) and the microstructure of the material. The microstructure investigation was made through a scanning electron microscope (SEM) observation.The main results of this study show that the treatment of collapsible soil with sodium silicate has led to a significant reduction of the collapse potential, exceeding 87%. An effective treatment is obtained with a sodium silicate solution at the optimal dose of 0.8 $mol.L^{-1}$. The SEM observations have revealed micro-structural transformations which are correlated to changes to geotechnical behavior.

Keywords: open structure, collapsible soil, chemical treatment, microstructure.

1 Introduction

Loess soils cover a large part of the world's land, including China, Russia, the USA, New Zealand, and other mid-latitude countries having large loess distribution areas [1-3]; Algeria too has a large loess area. Loess has poor engineering properties such as strong water sensitivity and severe collapsibility because of the inherent metastable structure [4]. Important structural disorders, caused by collapsible soils due to water, were observed in many parts of the world, especially in arid and semi-arid regions. The risk of collapse of a loess is related to several conditions such as significant porosity related to an open structure, and the binding elements that are strong enough to stabilize the contacts inter-granular and relatively weak to disappear or be weakened when water is introduced [5] and a high void ratio and an unstable arrangement of the soil particles [6]. Loess soils are the result of an accumulation of wind-blown soil particles mainly silty, clay and sand heterogeneously distributed [7]. In fact, collapsible soils are unsaturated soils that may undergo inter-granular rearrangement with a significant reduction in

their volume after having been flooded. Loess is a complex mineral with clay minerals like quartz, feldspar, and illite. Its large pores, weak cementation, and high salt content cause poor engineering characteristics, including compressibility, collapsibility, and wetting strength reduction [8]. The world's common foundation treatment methods include dynamic consolidation, replacement cushion, compaction pile, impact compaction, pre-soaked treatment, and chemical stabilization. Traditional compaction reduces loess' collapsibility, but wetting-drying and freezing-thawing cycles can affect compacted foundations, causing secondary or multiple collapse. Physical stabilization methods cannot eliminate collapsibility, leading to research on chemical stabilization methods [9]. Chemical methods involve adding stabilizing agents to soil, reacting with minerals or water, and cementing particles to make the structure denser. These methods offer rapid speed, easy construction, and stable performance. Traditional stabilizing agents like lime and cement are commonly used in engineering practice to improve loess mechanical properties [10]. Many studies performed experimental studies to illustrate that the mechanical resistance of collapsible soils can be improved by different stabilizing agents [11-14]. Recent studies concentrated on the influence of various parameters such compaction energy, initial water content and stress level, and saline solutions at different concentrations (ammonium sulfates $(NH_4)_2SO_4$, potassium chloride KCl, and sodium chloride NaCl) [15, 16]. Those studies were performed at a microstructural level to better understand the effect of salts on the treatment of collapsible soils. The results of those studies showed a favorable effect of salts on the structure of collapsible soils with a significant reduction in collapse potential [12, 17]. Gu, Lv [8] studied the effect of sodium silicate on the geotechnical parameters and microstructure of a loess. The results confirmed the effectiveness of this treatment. Siddiqua and Bigdeli [18] studied the stabilization of a collapsible soil using magnesium chloride ($MgCl_2$). The results showed that 7% $MgCl_2$ over 28 days of hardening had the best effect on stabilizing the soil collapse.
This study is a contribution to the application of chemical stabilization technique of a soil from the region of Zeribet El Oued, district of Biskra in southern Algeria, by addition of sodium silicate solution (Na_2SiO_3) at different concentrations and its effect on the collapse potential of the loess. Also, XRD and Scanning Electron Microscopy (SEM) were studied for soil samples and the treated material.

2 Methods and Materials

The soil in this study is loess from the region of Zeribet El Oued, district of Biskra in Algeria. In summer, the climate of this region is hyper-arid, dry, and warm but cold and wet in winter Figure 1. Part of the material was excavated by mechanical excavator at about 1.50 m below ground surface.
To characterize the physical and geotechnical parameters of the loess soil, the tests were conducted according to the standards NF P94-050 [19]. The Atterberg limits, as NF P94-051 [20] standard, were applied on soil fractions below 400 µm, which were extracted from untreated soils. The consistency limits were measured on soil- sodium silicate mixtures. Similarly, based on NF P94-048 [21] the percentage of calcium carbonate (% $CaCO_3$) was estimated by Calcimeter. Shear tests were carried out on treated and untreated samples, using direct shear apparatus according to NF P94-071-1 [22]. The soil pH was measured on the soil extract 1/2.5, using a pH meter.

The different soil properties are presented in Table 1. The fractions of sand, silt, and clay are 9%, 80%, and 11%, respectively. This material has a fraction of 12% of calcium carbonate. According to the classification of Casagrande, the material is classified as CL or low plasticity clay. The sieve analysis of the subject material is presented in Figure 2. Table 1 shows comparative index properties for Libyan, French and Algerian loess. All plasticity values for the studied soil are close to the values of different loess soil of the different regions.

Gibbs and Holland [23] classified the loess material into three types: sandy loess, silty loess and clayey loess, as shown in Figure 3. The soil sample of Zeribet El Oued has a liquid limit, LL of 31% and a plasticity index, PI of 12, so our soil sample is a silty loess. In order to assess the collapse potential, researchers used experimental and empirical approaches based on characteristics specific to such soils. Based on dry density, the studied soil is classified as moderately susceptible to settlement due to its medium density [24].

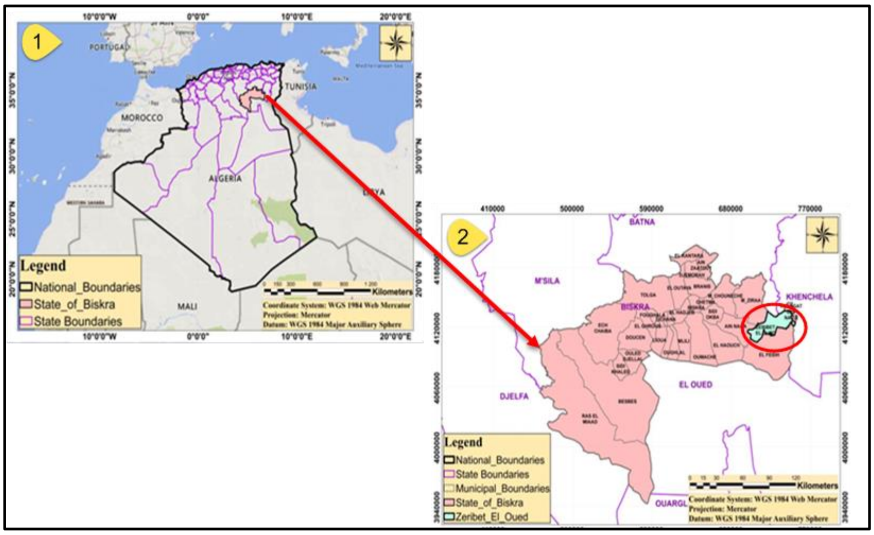

Figure 1: Location of the national and state boundaries (1) and Location of the ground site (2)

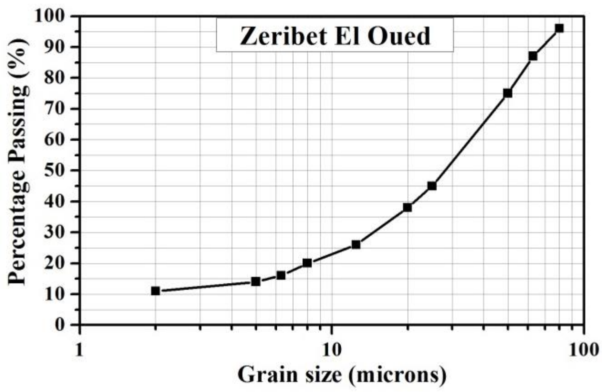

Figure 2: Sieve analysis of the subject material (Zeribet El Oued)

Figure 4a shows an open structure that is poorly cemented between the different elements of the loess, with the appearance of pores with different shape and opening with loose areas.

The X-ray dispersive energy microanalysis (EDAX) of untreated soil allows to observe the presence of the feldspar group (Potassium Aluminium Silicate $K(Si_3Al)O_8$), and (Calcium magnesium Carbonate ($CaMg(CO_3)_2$), this type of analysis was reported by [3], (Figure 4b).

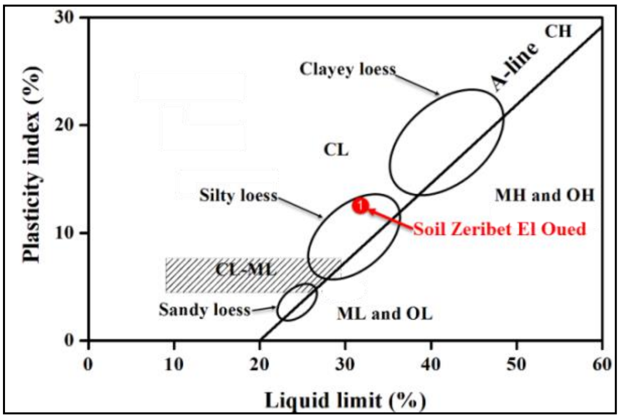

Figure 3: Plasticity properties of Zeribet El Oued Soil as compared with loess types defined by [23]

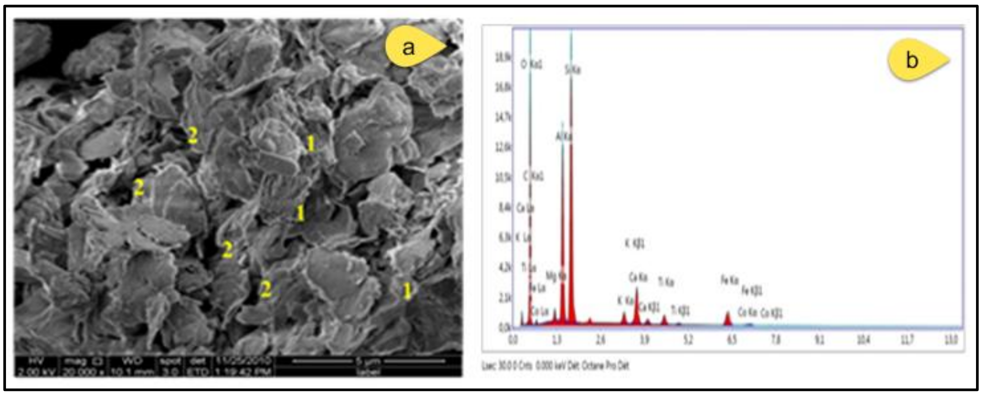

Figure 4: (a) SEM Observation of a loessic soil (Aggregations of grains of silt (1), (2) pores); (b) X-ray dispersive energy microanalysis (EDAX) of untreated soil

Table 1: Index properties of Libyan, Algerian, French and Loess of present study [3, 25, 28]

Soil parameters	**Method or standards**	**[25]**	**[25]**	**[3]**	**[3]**	**[1]**	**Zeribet ElOued Loess Algeria**
Natural water content, *w* (%)	NF P94-050 [19]	6.0	3.0	5.0	6.0	14.0	**13.8**
Void ratio, *e*	/	0.87	0.84	0.89	0.91	0.84	**0.88**
Natural dry unit, γ_d kN/m^3)	NF P94-050 [19]	13.6	14.0	14.2	14.3	14.5	**14.2**
Specific gravity,Gs	/	2.66	2.68	2.68	2.73	2.67	**2.67**
< 2 µm fraction of clay (%)	NF P94-056 [26], NF P94-057 [27]	11	13	9	12	16	**11**

Liquid limit, LL (%)		27	31	30	33	28	**31**
Plastic limit, PL (%)	NF P94-051	19	20	23	22	19	**19**
Plasticity index, PI (%)	[20]	8	11	7	11	9	**12**
$CaCO_3$ content, (%)	NF P94-048 [21]	/	/	/	/	6	**12**

2.1 Methods

Jennings [29], proposed an experimental approach to the collapse potential of soils based on the oedometer tests. That approach was followed by a theoretical study formulated by [30]. The oedometer approach is based on the concept of a single point oedometer test according to ASTM standard on an as is soil sample at its natural moisture content. Then the sample is flooded after a specific vertical stress is applied, As illustrated in Figure 5 from [31], a direct estimation of the collapse potential is obtained from the deformation the soil sample.

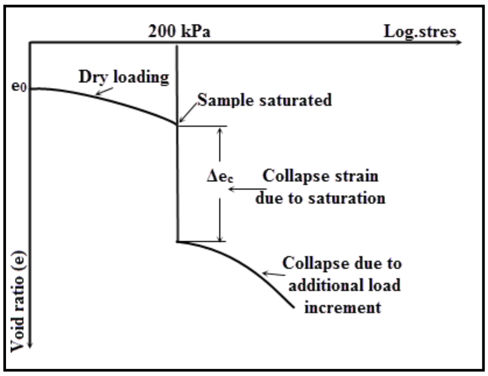

Figure 5: Simple Oedometer Curve [31]

The test program was conducted on undisturbed soil sample with different flooding liquids such as distilled water, saline solution of the sodium silicate (Na_2SiO_3) at different doses (0.2, 0.4, 0.6, 0.8 and 1.0 mol.L^{-1}). For this purpose, two collapse potentials, before and after treatment, will be determined by the following formula:

$$CP = \left(\frac{\Delta e_c}{1+e_0}\right) 100\% \tag{1}$$

with: $\Delta e_c = e_1$ (200 kPa) - e_2 (200 kPa, flooded).
e_0: initial void ratio.

The most used concept to estimate the consequence of collapsible soils to supported structures was proposed by [31] and is based on the degree of the collapse potential resulting after the introduction of water to a soil sample under a specific stress of 200 kPa and that correlation is presented in Table 2.

Table 1: Identification of collapse associated structural problems [31]

Collapse potential (CP)	**Severity of problem**
0%-1%	No problem
1%-5%	Moderate problem

5%-10%	Trouble
10%-20%	Severe trouble
>20%	Very severe trouble

3 Results and Discussion

3.1 The Effect of Silicate Sodium Treatment on pH

To explain the results of the tests of compressibility and change of the- microstructure, it has proved very important to analyze the physico-chemical change and particularly the pH level of the solution after addition of sodium silicate (Na_2SiO_3) with a density of 1.38 g/cm^3 at different concentration (0.2, 0.4, 0.6, 0.8, and 1 mol.L^{-1}).
Figure 6 shows that the pH increases with the concentration of silicate of sodium until 0.8 mol.L^{-1}, beyond that; there is a very small change in that parameter. This result can be explained by the pH of the pure solution of the sodium silicate, which is 12.

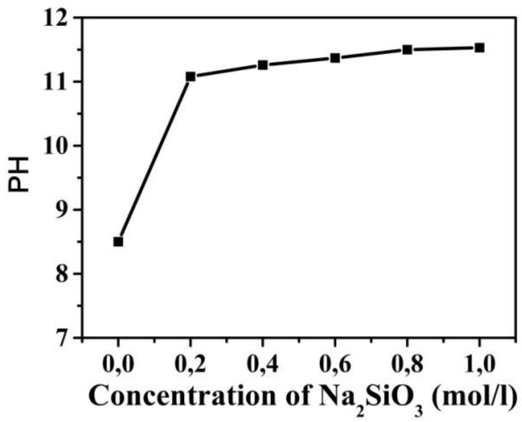

Figure 6: Effect of Sodium Silicate (Na_2SiO_3) on PH

3.2 The Effect of Sodium Silicate Treatment on Atterberg Limits

Regarding the influence of the used solution on other geotechnical properties of the studied soil, Figure 7 clearly shows that the liquid limit decreases when the concentration of the stabilizer (Na_2SiO_3) increases. For measurements of 0.8 and 1 mol.L^{-1}, it is noted that the liquid limit values obtained are close and consisted of 26.7 and 25.3%, respectively. However, the plasticity limit increased slightly, leading to a remarkable effect on the reduction in the plasticity index regardless of the percentage of the stabilizer.

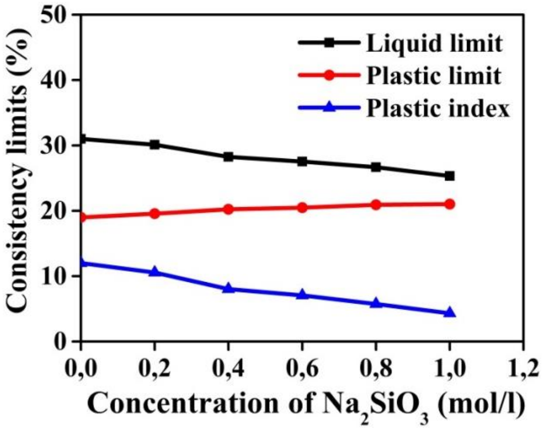

Figure 7: Atterberg Limits Measured on Untreated and Sodium Silicate Treated Soil

3.3 Collapse Tests

Figure 8a shows the change in the collapse potential based on the concentration (0.2, 0.4, 0.6, 0.8 and 1.0 mol.L^{-1}) of the sodium silicate solution (Na_2SiO_3), for loess. The collapse potential of the untreated sample is 6.42%. Based on the classification of [31], the untreated soil may lead to trouble. We also notice that the soil sample has an important collapse potential because it has a percentage of 12% of $CaCO_3$, which is a cementing agent that dissolves once water is introduced, creating an unstable soil structure, due to a flocculation of the material with high porosity. However, there is a significant reduction in the collapse potential for soils treated with the sodium silicate solution (Na_2SiO_3) when the concentration increases This can be explained by the cementing effect of the sodium silicate solution (Na_2SiO_3), which forms layers that lead to new formations by covering the particles, creating a smooth surface. As sodium silicate is injected, it fills voids, forming independent structural aggregates. The stiff skeleton and silicate gel have different physicomechanical properties, with the stiff skeleton having elasticity and absorbing stresses, while the gel component has viscous properties. these results corroborate those of Beketov and Seleznev [32]. The review of the curve of Figure 8b highlights the considerable influence of the sodium silicate solution (Na_2SiO_3) on the collapse potential. The treated soils with 0.8 and 1 mol.L^{-1} develop the same collapse potential of about 0.78%. The stabilization of the values of the collapse potential beyond 0.8 mol.L^{-1}, can be explained by the lack of variation of the alteration of the material due to the low variation of pH at concentrations of the sodium silicate at 0.8 and 1.0 mol.L^{-1}. Thus, the dose of 0.8 mol.L^{-1} of the sodium silicate solution can be considered as an optimal concentration because an additional amount would not improve further the properties of the collapse.

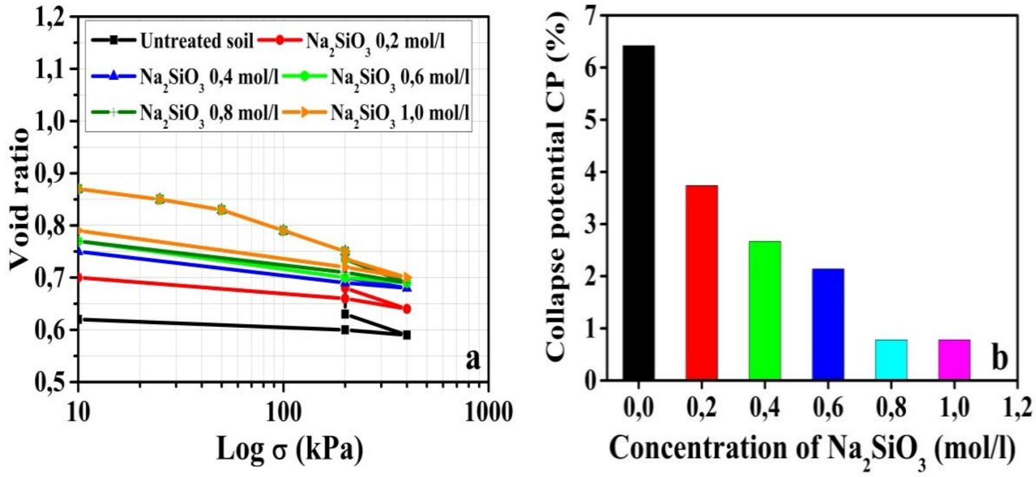

Figure 8: a- Effect of sodium silicate (Na_2SiO_3) on oedometric tests, b- Effect of sodium silicate (Na_2SiO_3) on the collapse potential

3.4 Effect of Sodium Silicate on Cohesion and Friction Angle from Shear Test

The results in Figure 9 show that cohesion C and friction angle φ increase when the percentage of concentration of the treatment increases. Sodium silicate treatment has led to an increased resistance to shear of the treated soil, resulting in an improved soil carrying capacity. The treatment of the soil by sodium silicate has highlighted its stabilizing role on the geotechnical behavior of the loess.

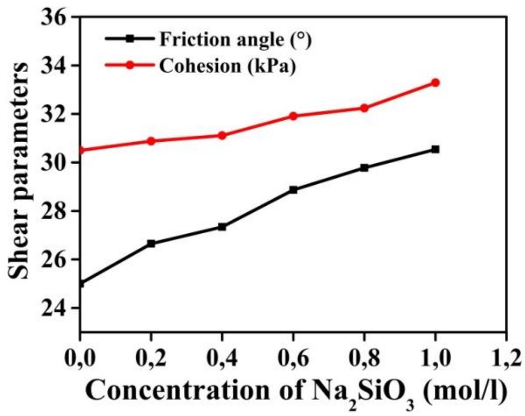

Figure 9: Effect of the addition of sodium silicate (Na_2SiO_3) on the shear parameters of soil

3.5 Effect of Sodium Silicate on the Microstructure

To better appreciate the change and reduction of the collapse potential by addition of sodium silicate solution (Na_2SiO_3) to loess soils, soils, there has been an analysis of the changes of the microstructure from the scanning electron microscope (SEM) observation. That analysis was performed to compare treated and untreated samples.

Figure 4 shows that reference loess soil has a high concentration of fine silt and clay with a high porosity between aggregates of relatively large size. After flooding, the collapse occurs creating loose areas and an unstable structure. This structure was already observed in the loess in France [6, 33]. The samples treated with the sodium silicate solution (Na_2SiO_3) have a relatively stable microstructure and low sensitivity to collapse compared to untreated samples. Figure 10 a, b and c, show disappearance of the aggregation because of the presence of sodium silicate salt which is very alkaline. The material appears smooth, cemented without porosity. The sodium silicate strengths the micro-structural body with a dense and compact material. It is the result of the chemical effect of silicate (alteration and dissolution) on the material. In addition to strengthening the existing bonds in loess, silicate injection creates new, stronger, and more water-resistant bonds as a result of the adsorption of silicic acid on the solid phase of calcium hydroxide. The original structure of the material disappears because of the destructive effect on the siliceous components of the sodium silicate due to its strong alkalinity on silicates components (clay and quartz) and release of silica and alumina leading of a formation of a precipitate consisting of an amorphous material or gel without any micro-structural organization filling the voids around aggregates. The EDAX analysis for soil treated with 0.8 and 1 mol.L^{-1} of sodium silicate on Figure 10d indicates the presence of higher concentration of silicon (Si), aluminum (Al) and sodium (Na), as well as zones of low concentration in in potassium (K), magnesium (Mg) and trace of iron (Fe).

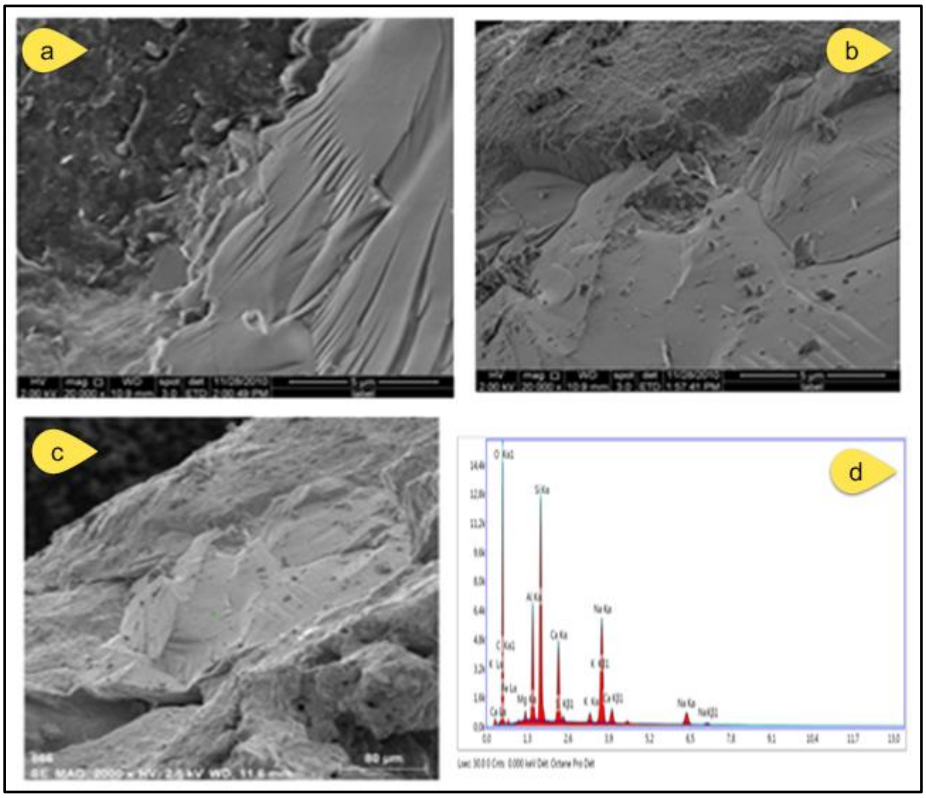

Figure 10: Observation SEM of Soil Treated by Na_2SiO_3, X-ray Dispersive Energy Microanalysis (EDAX) of Soil Treated with 1.0 mol.$L^{-1}$of Na_2SiO_3

4. Conclusion

This study is part of the chemical stabilization of a collapsible soil. The results obtained in this study have led to the following conclusions:

The liquid limit and the plasticity limit have gone slight increases with the added percentage of sodium silicate. Therefore, the plasticity index PI has gone an important reduction with the treatment. In addition, the treatment has increased the mechanical characteristics such as cohesion C and friction angle φ, leading in an improved soil carrying capacity.

It is clearly demonstrated that the treatment of collapsible soil with the addition of the sodium silicate solution (Na_2SiO_3) at doses ranging from 0.2 to 1.0 $mol.L^{-1}$, greatly improves the parameters of compressibility and decreasing the collapse potential over 87%. These improvements are caused by a strong alteration of the loess soil causing structural changes. It appears that for the concentration 0.8 $mol.L^{-1}$of the sodium silicate, the collapse potential remains relatively constant, which could be explained by the maximum amount of alteration of the material obtained by this dose. The analysis by the scanning electron microscope of the untreated loess soil indicates a loose structure; however, the treated soil by sodium silicate has highlighted its stabilizing role on the geotechnical behavior of the loess.The dominant mechanism and its effect on the reduction of collapse potential is chemical in nature by an alteration and dissolution of silicates components of the loess soil with consequences on the reduction of the porosity and of a consolidated microstructure. Based on this study, the dose of 0.8 $mol.L^{-1}$ of Na_2SiO_3 is the optimal value for treatment of collapsible soil. The mechanism of loess reinforcement by sodium silicate is reinforcement of the bond strength of cement in microstructure and formation of new strengthened material. This treatment technique is applied by injecting a chemical solution.

References

[1] Delage P., Y.-J. Cui & P. Antoine. (2008).Geotechnical problems related with loess deposits in Northern France.

[2] Meier C., C. Boley & Y. Zou. (2008).Collapse and deformation behaviour of alluvial loess soils from Afghanistan. in Geotechnics of Soft Soils: Focus on Ground Improvement: Proceedings of the 2nd International Workshop held in Glasgow, Scotland, 3-5 September 2008. CRC Press.

[3] Nouaouria M.S., M. Guenfoud & B. Lafifi. (2008). Engineering properties of loess in Algeria. Engineering Geology. 99 (1-2): p. 85-90. 10.1016/j.enggeo.2008.01.013.

[4] Houston S.L., W.N. Houston & D.J. Spadola. (1988). Prediction of field collapse of soils due to wetting. Journal of Geotechnical Engineering. 114 (1): p. 40-58.

[5] Barden L., A. McGown & K. Collins. (1973). The collapse mechanism in partly saturated soil. Engineering Geology. 7 (1): p. 49-60. https://doi.org/10.1016/0013-7952(73)90006-9.

[6] Cui Y.-J., J.-M. Terpereau, D. Marcial, P. Delage, P. Antoine, G. Marchadier & W.-M. Ye. (2004). A geological and geotechnical characterisation of the loess of Northern France. in Advances in geotechnical engineering: The Skempton conference: Proceedings of a three day conference on advances in geotechnical engineering, organised by the Institution of Civil Engineers and held at the Royal Geographical Society, London, UK, on 29–31 March 2004. Thomas Telford Publishing.

[7] Pécsi M. (1990). Loess is not just the accumulation of dust. Quaternary International. 7: p. 1-21.

[8] Gu L., Q. Lv, S. Wang, J. Xiang, L. Guo & J. Jiang. (2021). Effect of sodium silicate on the properties of loess stabilized with alkali-activated fly ash-based. Construction and Building Materials. 280: p. 122515. https://doi.org/10.1016/j.conbuildmat.2021.122515.

[9] Li G.-y., X. Hou, Y.-h. Mu, W. Ma, F. Wang, Y. Zhou & Y.-c. Mao. (2019). Engineering properties of loess stabilized by a type of eco-material, calcium lignosulfonate. Arabian Journal of Geosciences. 12 (22): p. 700. 10.1007/s12517-019-4876-0.

[10] Yifei H., P. Li & W. D. (2021). Review of chemical stabilizing agents for improving the physical and mechanical properties of loess. Bulletin of Engineering Geology and the Environment. 80. 10.1007/s10064-021-02486-x.

[11] Bell F. and I.d. Bruyn. (1997). Sensitive, expansive, dispersive and collapsive soils. Bulletin of the International Association of Engineering Geology, (56): p. 19-38.

[12] Bahloul O., K. Abbeche & A. Bahloul. (2016). Study of the microstructure of collapsible soil treated with the potassium chloride. Journal of Applied Engineering Science & Technology, (1): p. 39-42%V 2.

[13] Ziani H., K. Abbèche, I. Messaoudene & L.J. Andrade Pais. (2019) .Treatment of Collapsible Soils by Additions of Granulated Slag and Natural Pozzolan. KSCE Journal of Civil Engineering. 23 (3): p. 1028-1042. 10.1007/s12205-019-0051-0.

[14] Bellil S., K. Abbeche & O. Bahloul. (2018). Treatment of a collapsible soil using a bentonite–cement mixture. Studia Geotechnica et Mechanica. 40 (4): p. 233-243. doi:10.2478/sgem-2018-0042.

[15] Abbeche K., O. Bahloul, T. Ayadat & A. Bahloul. (2010). Treatment of collapsible soils by salts using the double consolidation method, in Experimental and Applied Modeling of Unsaturated Soils2010. p. 69-78.

[16] Abbeche K., O. Bahloul & A. Bahloul. (2016).Study of the influence of the saline solution NaCl on the potential collapse of soil. E3S Web Conf. 9: p. 07001.

[17] Bahloul O., K. Abbeche, A. Bahloul & A. Halitim. (2018). EFFECT OF SODIUM CHLORIDE ON THE WETTING INDUCED COLLAPSE STRAIN OF SOILS. Malaysian Journal of Civil Engineering. 26 (2). 10.11113/mjce.v26.15881.

[18] Siddiqua S. and A. Bigdeli. (2022). Utilization of MgCl2 solution to control collapse potential of soil. Transportation Geotechnics. 33: p. 100731. https://doi.org/10.1016/j.trgeo.2022.100731.

[19] NF P94-050, Determination of moisture content. Oven drying method, 1995, AFNOR: Paris France.

[20] NF P94-051, Determination of Atterberg's limits. Liquid limit test using Casagrande apparatus. Plastic limit test on rolled thread., 1993, AFNOR: Paris, France.

[21] NF P94-048, Determination of the carbonate content - Calcimeter method, 1996, AFNOR: Paris France.

[22] NF P94-071-1, Direct shear test with shearbox apparatus - Part 1 : Direct shear, 1994, AFNOR: Paris France.

[23] Gibbs H.J. and W. Holland, Petrographic and engineering properties of loess1960: Technical Information Branch, Denver Federal Center.

[24] Holt W. (1961).Settlement of soil foundation due to saturation. in Proc. of the 5th Int. Conf. on SMFE.

[25] Assallay A.M., C.D.F. Rogers & I.J. Smalley. (1996). Engineering properties of loess in Libya. Journal of Arid Environments. 32 (4): p. 373-386. https://doi.org/10.1006/jare.1996.0031.

[26] NF P94-056, Granulometric analysis - Dry sieving method after washing, 1996, AFNOR: Paris France.

[27] NF P94-057, Granulometric analysis - Hydrometer method, 1992, AFNOR: Paris France.

[28] Muñoz-Castelblanco J., J.-M. Pereira, P. Delage & Y. Cui. (2012). The Influence of Changes in Water Content on the Electrical Resistivity of a Natural Unsaturated Loess. Geotechnical Testing Journal. 35: p. 103587. 10.1520/gtj103587.

[29] Jennings J. (1957). The additional settlement of foundations due to a collapse of structure of sandy subsoils on wetting. in Proc. 4th Int. Conf. on SMFE.

[30] Alonso E.E., A. Gens & A. Josa. (1990). A constitutive model for partially saturated soils. Géotechnique. 40 (3): p. 405-430.

[31] Jennings J. and K. Knight. (1975). A guide to construction on or with materials exhibiting additional settlement due to “collapse” of grain structure: Sixth Regional Conference for Africa on Soil Mechanics and Foundation Engineering. Durban, South Africa: p. 99-104.

[32] Beketov A.K. and A.F. Seleznev. (1971). Nature of the deformation and failure of silicate-stabilized loess. Soil Mechanics and Foundation Engineering. 8 (6): p. 408-410. 10.1007/bf01705220.

[33] Delage P., Y.-J. Cui & P. Antoine. (2008). Geotechnical problems related with loess deposits in Northern France. arXiv preprint arXiv:0803.1435.

DOI: 10.2478/sspjce-2023-0014

Fatigue Life Prediction for Reinforced-Concrete Low Domes

Nacer Logzit [1,2*], Rabie Mezouar [1,4], Salah Daoud [1,3]

University Mohamed El Bachir El Ibrahimi of Bordj Bou Arreridj, Algeria
[1] Materials and Electronic Systems Laboratory, [2] Department of Civil Engineering, Faculty of Science and Technology, [3] Department of Mechanical Engineering, Faculty of Science and Technology
[4] Institue of Optics and Fine Mechanics, University of Ferhat Abbas Setif 1, 19000 Setif, Algeria
*e-mail: n_logzit@yahoo.fr

Abstract

The study of fatigue of thin reinforced-concrete shells presents a complex modelling approach. This work is devoted to the numerical evaluation of the fatigue life of reinforced-concrete domes, with the concrete class of *C25/30*. For the formulation of a fatigue criterion under a symmetrically alternating load, with a very high number of cycles (10^6), the approach begins with the study of mechanical behavior under monotonic loading, related to the fatigue response. The numerical correlation results of the studied cases, based on a conservative fatigue limit of concrete in compression, enables to estimate the service life of these structures, knowing only the response under monotonic loading. The correlation formula proposed in this article can therefore directly estimate the service life of reinforced concrete domes, based on the maximum stress resulting from monotonic loading.

Keywords: reinforced-concrete domes, long span, monotonic loading, mechanical behavior, fatigue

1 Introduction

Three-dimensional thin-walled reinforced-concrete structures are generally used in civil and industrial constructions. However, they have the common characteristic of being among the most delicate structures to study. Through these structures, the performance of materials and shapes is sought [1]. But for the civil engineer, in the field of shells and slender structures, an essential requirement arises: to know how to choose optimal stable and resistant shapes under different types of loading. This requirement is too often neglected, or left only to the architect, whereas, in this type of structure, the analysis is linked with construction and optimization.

The objective of this work is to propose an approach to deal with complex problems of calculation and simulation of fatigue of slender reinforced-concrete domes. We used the mathematical formulation of the fatigue problem of reinforced-concrete applied to domes, to finish with the modeling and the exploitation of the results of numerical simulation. This approach allowed us to introduce the notion of fatigue criteria, and to know the behavior of the structure first under monotonic loading, followed by the analysis under cyclic loads with a very large number of cycles (i.e., 10^6).

Through this approach, a model based on a probabilistic numerical correlation will be proposed in order to predict the service life of these structures under cyclic loading.

In the case of occasional cyclic loading, where the full design load is repeated, for a very large number of cycles (10^6), the concrete undergoes stress concentration, exhibits excessive cracking, and may eventually lead to failure after a sufficient number of load repetitions, even if the maximum stress is less than the static (monotonic) strength of a similar specimen. This is referred to as the fatigue limit, which is, in this article, defined as the highest stress magnitude for which failure is not observed after 10^6 load cycles.

The subject of fatigue of reinforced concrete is generally treated experimentally or analytically through the study of reduced elements (column, beam, node...) [2-6], the analysis of full-scale structures, are the subjects least addressed by the scientific community; the fatigue of large-span domes is rarely addressed under realistic conditions.

The service life of a reinforced concrete structure depends directly on the stress level, stress range, and number of loading cycles [4]. Several models have been proposed for the evaluation of the service life of reinforced concrete under cyclic loading, the commonly used models are those based on the stress level for service life estimation [7].

This paper is aimed to find a numerical correlation of the mechanical behavior of reinforced concrete domes, between the monotonic loading response and the fatigue response.

2 Approaches and Models of Analysis

To know and control the mechanical behavior in monotonic loading mode, and in a cyclic mode of reinforced concrete domes, the following approaches have been adopted:

- Analysis of material linearity of the materials (concrete and steel).
- Analysis of geometrical non-linearity of the structure.

Shrinkage and creep are not considered here, for more details on these phenomena, it is preferable to refer to the research work developed by Ehab et al. [8]. Regarding the fatigue analysis of the structure under cyclic loading, we have adopted the criteria of the critical plane as these criteria are more suitable for brittle materials. We used the following three fatigue criteria: Mataké criterion [9], Findley criterion [10], and Dang Van criterion [11]. For a detailed comparative study of the fatigue criteria, a reliability analysis is proposed by Bianzeube et al. [12]. Mataké's criterion [9], is based on experimental data from bi-axial torsion-bending tests performed on three different materials (including copper and steel). It describes the critical plane in which the amplitude of the shear stress is maximum, and that the normal to the criticized plane is determined by max (τ_a (φ_c, Θ_c)). The criterion is written as follows (Equation 1):

$$\tau_a + \mu . \sigma_{n\,max} < \lambda \qquad (1)$$

of which τ_a is the shear stress, μ and λ are the material parameters, determined by two fatigue tests:

a) Pure torsion:

$$\tau_a = \tau_{-1} \quad \text{and} \quad \sigma_{n\,max} = 0 \qquad \text{then:}$$

$$\lambda = \tau_{-1} \tag{2}$$

b) Symmetrical alternating traction:

$$\tau_a = \frac{\sigma_{-1}}{2} \quad \text{and} \quad \sigma_{n\,max} = \frac{\sigma_{-1}}{2} \quad \text{then:}$$

$$\mu = 2.\frac{\tau_{-1}}{\sigma_{-1}} - 1 \tag{3}$$

with:

$\boldsymbol{\varphi}$ and θ: are the angles that determine the position of the material plane normal.

τ_{-1} and σ_{-1}: are the endurance limit in symmetric alternating torsion, and endurance limit in symmetric alternating tension, respectively.

The area of validity is:

$$\frac{\boldsymbol{\tau}_{-1}}{\boldsymbol{\sigma}_{-1}} > \frac{1}{2} \tag{4}$$

Findley's criterion [3], uses a linear combination of shear stress τ_a and normal stress σ_n, it is given by the following formula (Equation 5):

$$\tau_a(\varphi_c, \theta_c) + k.\sigma_{n\,max}(\varphi_c, \theta_c) < f \tag{5}$$

with k: sensitivity coefficient of the normal stress, and f: limit factor. The values of these quantities are given as follows (Equation 6a and 6b):

$$k = \frac{2 - \frac{\sigma_{-1}}{\tau_{-1}}}{2.\sqrt{\frac{\sigma_{-1}}{\tau_{-1}} - 1}} \tag{6a}$$

$$f = \sqrt{\frac{\sigma_{-1}^2}{4.\left(\frac{\sigma_{-1}}{\tau_{-1}} - 1\right)}} \tag{6b}$$

Dang Van [11], developed a microscopic-macroscopic approach based on a change of scale, to calculate the stress in the grains of a material subjected to fatigue, in relation to the stress known at the macroscopic scale. Based on this concept, the author proposed his criterion (Equation 7):

$$max_n max_t\{\|\alpha.\rho(t)\|\} < \beta \tag{7}$$

where ρ(t) is the hydrostatic pressure.

$$\text{with } \beta = \tau_{-1} \text{ and}$$

$$\alpha = 3.\left[\frac{\tau_{-1}}{\sigma_{-1}} - \frac{1}{2}\right] \tag{8}$$

where α and β are two constants defined from the endurance limits τ_{-1} (alternate torsion) and σ_{-1} (alternate tension) of the material. The condition for using this criterion is shown in (Equation 9):

$$\boldsymbol{\alpha} > 0, \quad \text{and}$$

$$\frac{\boldsymbol{\tau}_{-1}}{\boldsymbol{\delta}_{-1}} > \frac{1}{2} \tag{9}$$

Fatigue is estimated through a coefficient of use noted *E*, when the endurance limit of reinforced concrete at 10^6 cycles is reached [13], we will have *E* = 1 for any multiaxial cycle under the assumption that the criterion accurately reflects the real fatigue behavior of the material. The interpretation of the fatigue function of a criterion, i.e., its practical use in fact, is as follows:

- if *E* < *1*, the criterion is non-conservative for the designer: it predicts stress levels at endurance greater than those obtained experimentally.
- if *E* > *1*, the criterion is safe for the designer. It is conservative with respect to the real behavior of the material in fatigue. The multiaxial cycle at endurance is perceived by the criterion as more severe than it is in reality.

A complete multiaxial fatigue study, applied on a different and innovative structural system, is presented in a recent work of Logzit and Kebiche [14]. Regarding the study under monotonic loading, and before subjecting the structure to cyclic loading, an optimization of the structural system is required, based on the verification of the strength and stability of the dome at the service limit state; the same optimization approach, applied on a different structural system is proposed in [15].

3 Parameters and Basic Data

The class of concrete used is *C25/30*, with a compressive strength measured on a *16/32* cm cylindrical specimen of *25 MPa*. The steel reinforcement is class *FeE400*, with a tensile strength of *400* MPa, longitudinal modulus of elasticity of *200* GPa, and an elastic elongation of 0.002%.

The design of the various dome objects for this work is based on the following principles :

- The span of the domes (diameter *D*) is variable between 10 and 100 m.
- Low-profile form, the deflection at the center (*f*) is close to (*f* /*D* = 0.10).
- The thickness of the domes is kept constant, it is optimized in monotonic loading by checking the stability and the resistance of the system.
- The circular peripheral edge of the dome is considered as an embedding.

- The reinforcement of the meridian bars is obtained by considering a minimum regulatory section according to [16]. For the influence of the reinforcement rate, three variable sections were chosen:

  - S1: HA 10, 30 cm spacing, i.e., a reinforcement rate of 0.00263.

  - S2: HA 12, 30 cm spacing, i.e., a reinforcement rate of 0.00377.

  - S3: HA 14, spacing 30 cm, that is to say, a rate of reinforcement of 0,00523.

- Based on the principle of uniaxial fatigue in the direction of the meridians, the effect of the reinforcement in hoops is neglected.

In addition to the load due to the self-weight of the dome: *G*, the load applied to the dome is of the uniformly distributed type, $P = 100$ kg / m², largely sufficient for non-accessible covers. For the cyclic loading signal, the *P*-load model was used, with symmetrical fluctuations, with constant amplitude (Figure 1).

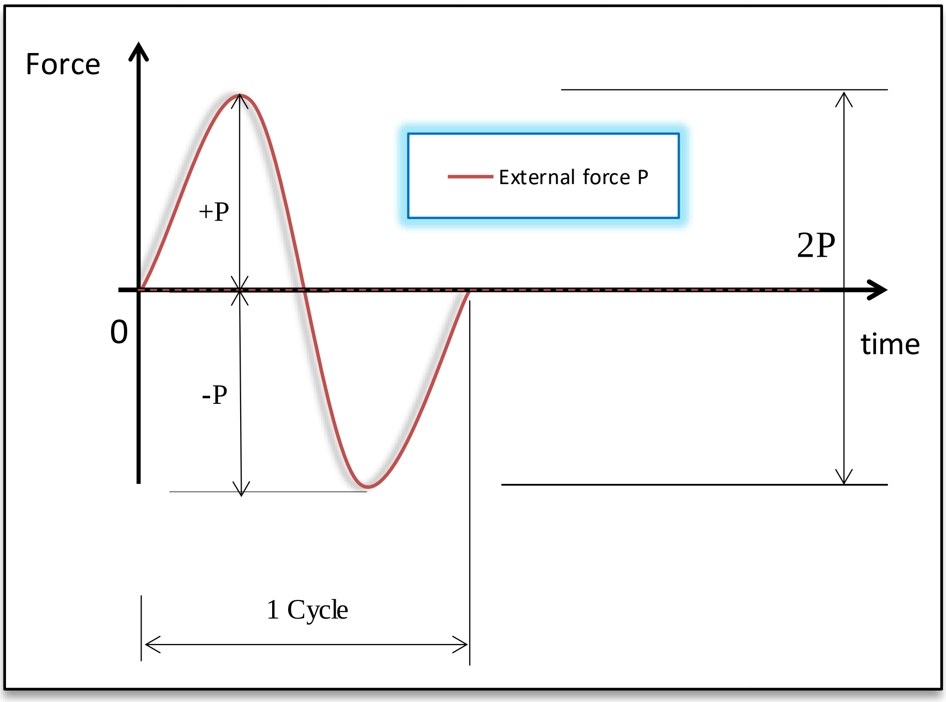

Figure 1: Cyclic loading signal

Concerning the parameters of the fatigue analysis, we considered a fatigue limit of the concrete at a very large number of cycles, close to 0.6 of the static limit of compression of the concrete. This limit is generally admitted by the codes of calculations and regulations, it results from the fatigue limits concerning the traction and the torsion as follows (Table 1).

Table 1: Fatigue limits of concrete

Material	**Fatigue tests**	**Endurance limits**	**Unit**	**Value**
	Symmetrical alternating traction: $R = -1$	σ_{-1}	MPa	1.50

Concrete class *C25/30*	Symmetrical alternating torsion: R = -1	τ_{-1}	MPa	1.00

Through these values, we can deduce the parameters (Coefficient of sensitivity of the normal stress k, and the limit factor f) of the different criteria, exploiting the formulas of each criterion (Table 2).

Table 2: Parameters of concrete fatigue criteria

Material	**criteria**	**Parameters**	**Unit**	**Value**
Concrete class *C25/30*	Dang Van	k	-	0.50
		f	MPa	1.00
	Mataké	k	-	0.33
		f	MPa	1.00
	Findley	k	-	0.35
		f	MPa	1.06

For the fatigue limits of the steel used, we took the experimental results reported in the literature (Table 3).

Table 3: Steel fatigue criteria parameters

Designation	**Solicitation/Criteria**	**Parameter**	**Unit**	**Value**
Experimental results in fatigue of reinforcing steel	Symmetrical alternating traction: R = -1	σ_{-1}	MPa	206.00
	Rotational symmetric bending: R = - 1	σ_0	MPa	337.00
	Symmetrical alternating torsion: R = -1	τ_{-1}	MPa	123.00
Steel fatigue parameters of reinforcing bars	Dang Van	k	-	0.291
		f	MPa	123.00
	Mataké	k	-	0.194
		f	MPa	123.00
	Findley	k	-	0.198
		f	MPa	125.40

4 Numerical Simulation of the Behavior

The simulation of the mechanical behavior under monotonic loading and cyclic loading was done using the Comsol Multiphysics software. In mechanical behavior under monotonic loading, we considered the structure of the dome (Figure 2), the dimensions of the shape are defined as shown in Table 4, the dome is subjected to a permanent load per m^2 noted *G* (dead weight), and a uniformly distributed operating load, noted *P*. For the design, the combination of load is fixed at the ultimate limit state: 1.35 *G* + 1.5 *P*. For optimization, the verification of the system at the limit state of service under the combination *G* + *P*, is necessary.

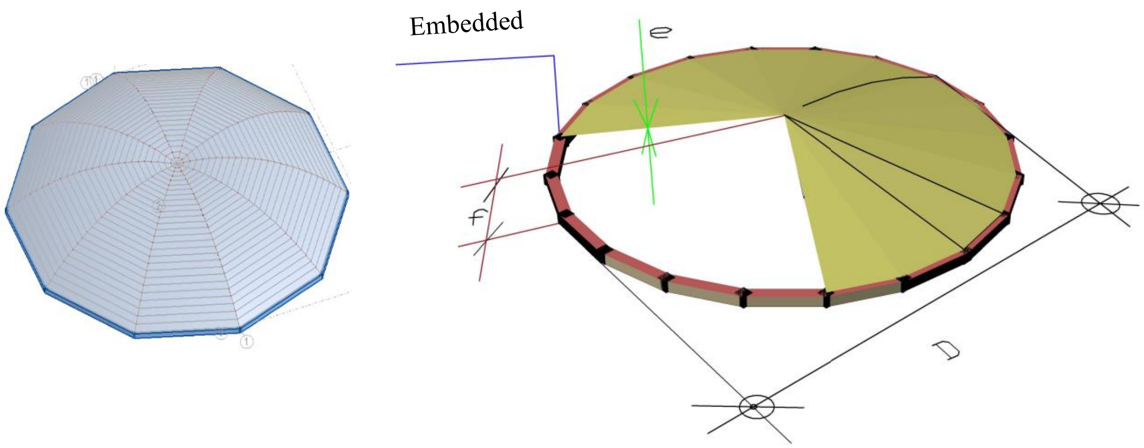

Figure 2: Design and shape dimensions of the dome

Table 4 shows the different dome shape dimensions, and the verification limits under monotonic loading, at the service limit state.

Figure 3 shows the mechanical behavior of the domes under the combination 1.35 *G* + 1.5 *P*, with *P* = 100 kg/m^2. A non-linear relationship is observed between the normal diaphragm force, calculated at the foot of the dome (at the level of the embedding), as a function of the diameter of the dome. From *D* = 60 m to *D* = 100 m, this force has increased by 263%, which implies a particular attention to the balance of this force concerning the slender domes.

Table 4: Dome design and system optimization

Case N°	***D* [m]**	***f* [mm]**	***e* [cm]**	**Maximum compressive stress under the combination *G* + *Q* [MPa]**	**Limit stress 12 [MPa]**	**Max. displacement in the center [mm]**
1	20	2000	8	0.413	0.900	
2	30	3000	10	0.568	0.750	
3	40	4000	13	0.695	0.731	
4	50	5000	19	0.786	0.854	

5	60	6000	25	0.890	0.937
6	70	7000	32	0.956	1.028
7	100	10000	55/70	1.232	1.237

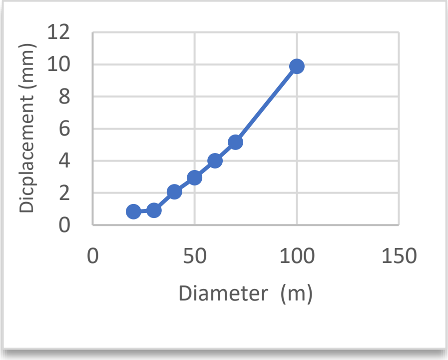

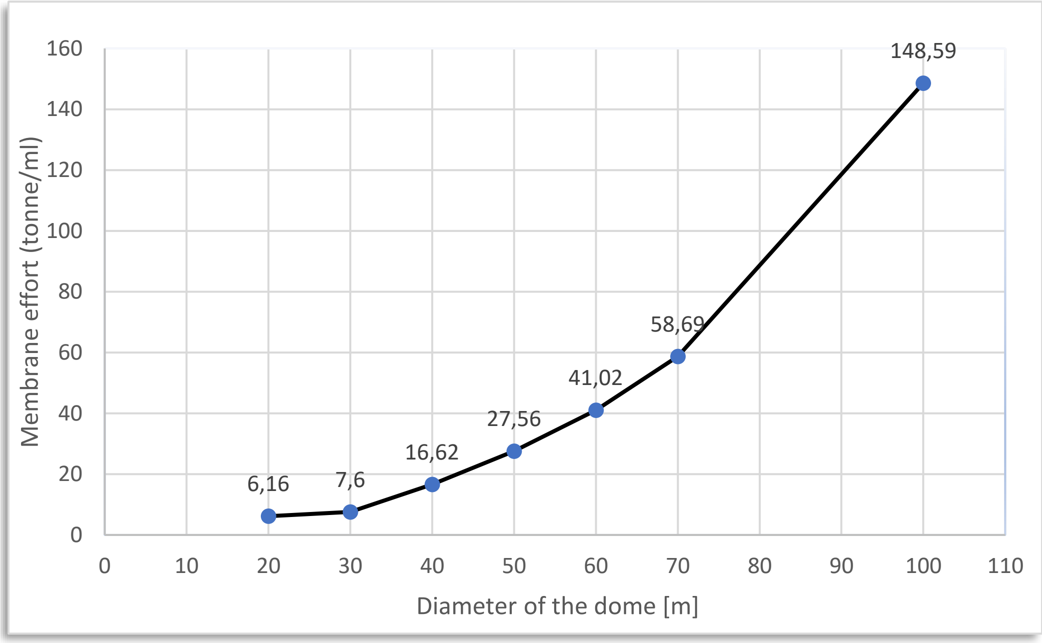

Figure 3: Normal membrane force as a function of dome diameter, a combination of 1.35 G + 1.5 P, with P = 100 kg/m^2

Regarding the behavior under an upwardly directed load (dome uplift), Figure 4 illustrates the stress concentration and displacement.

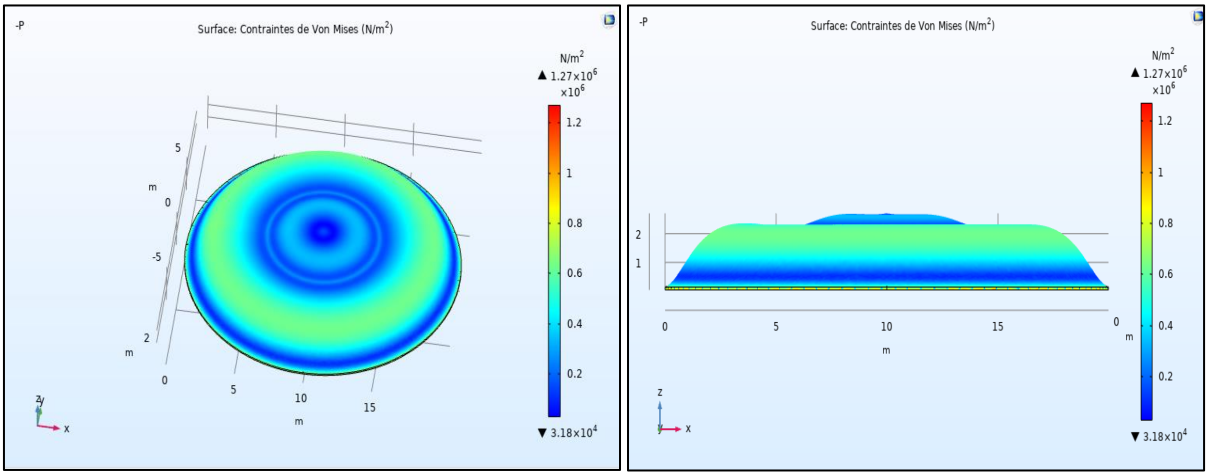

a) 3D view b) Side view

Figure 4: Behavior under monotonic loading. Dome of D = 20 m, P = 100 kg/m², Combination: -P

Through Figure 4, we can see under a monotonic load P (oriented upwards), a concentration of stresses at the junction of the dome with the peripheral edges. This concentration is also noticed in the center of the dome.

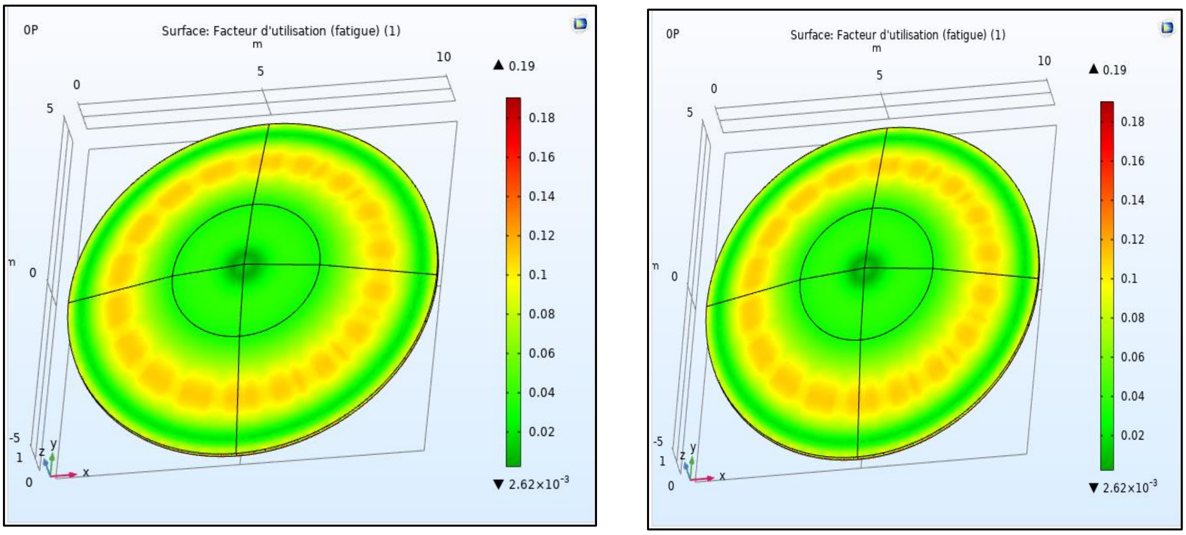

a) With reinforcement b) Without reinforcement

Figure 5: Fatigue risk map of a dome of D = 10 m, P = 100 kg/m^2 , Mataké criterion, with and without reinforcement

Figure 5 shows the distribution of the fatigue risk in the dome, the most sensitive areas are located near the transition zones, between the points with a high concentration of stresses and those with low stresses. Fatigue results in damage to the directly connected areas of the dome's peripheral edges. In the absence of the flexural behavior of the dome under fluctuating load P, the effect of the reinforcement is insignificant, which is why the fatigue behavior is similar without and with reinforcement. This last observation is justified by the pure compression behavior of the dome; the flexural behavior requiring a balance by the reinforcement, is not considered here.

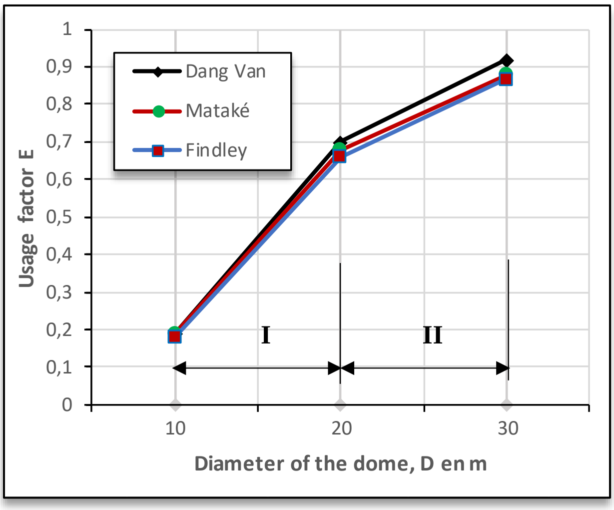

Figure 6: Fatigue risk of domes as a function of diameter *D*; *P* = 100 kg/m^2. The three criteria

Figure 6 shows the variation of the fatigue risk of the domes between the diameters *D* = 10 m and *D* = 30 m. The three criteria give similar results. It is clear, that the fatigue response becomes faster and faster for larger dome diameters. We can also observe a variation of the fatigue risk of 100% in interval I, while in interval II, a variation of 40%. The decrease of this variation with increasing dome diameter is justified by the flexibility of the dome. The dome, at slender spans, becomes more sensitive to loading, which causes relatively large displacements, the fluctuation of displacements due to repeated cyclic loading at very high numbers, excites fatigue at the most sensitive locations.

The approach of estimating the fatigue life of reinforced concrete domes is based on the notion of the fatigue limit of concrete, at a very high number of cycles (10^6), close to 0.60 of the compressive limit stress in static, this consideration leads us to propose a fatigue criterion for these structures in correlation with the behavior under monotonic loading.

5 Numerical Correlation

The fatigue response of the studied domes is related to the behavior in monotonic loading mode. In this section, we try to find the numerical correlation between these two behaviors, to propose the model of the fatigue response knowing only the response under monotonic loading. For this reason, and through the exploitation of the results of Table 4, the relationship between the maximum stress calculated at the foot of the dome under the combination *G* + *P*, to the diameter of the dome, is of the linear type, with a very good correlation (coefficient of determination R^2 close to 0.98), which leads us to propose the formula of the mechanical behavior under monotonic loading in the following way (Figure 7).

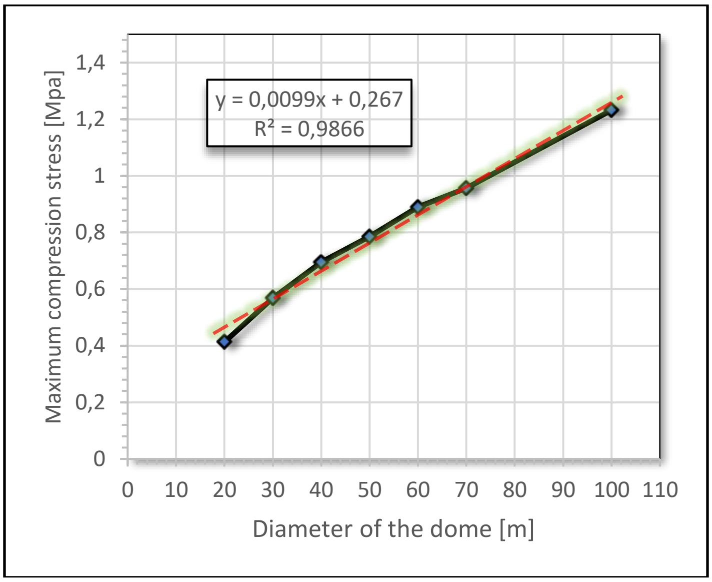

Figure 7: Maximum compressive stress as a function of the diameter of the dome, under the combination: $G + P$

We can therefore write (Equation 10):

$$\sigma_{max} = [0.009D] + (0.267) \tag{10}$$

with σ_{max}: Maximum compressive stress in MPa, at the foot of the dome under the combination $G + P$.

D: Diameter of the dome in m.

Adopting the average value of the usage factor E, deduced from the three fatigue criteria in Figure 6, and replacing the values of D, with the values corresponding to σ_{max}, we obtain the correlation shown in Figure 8.

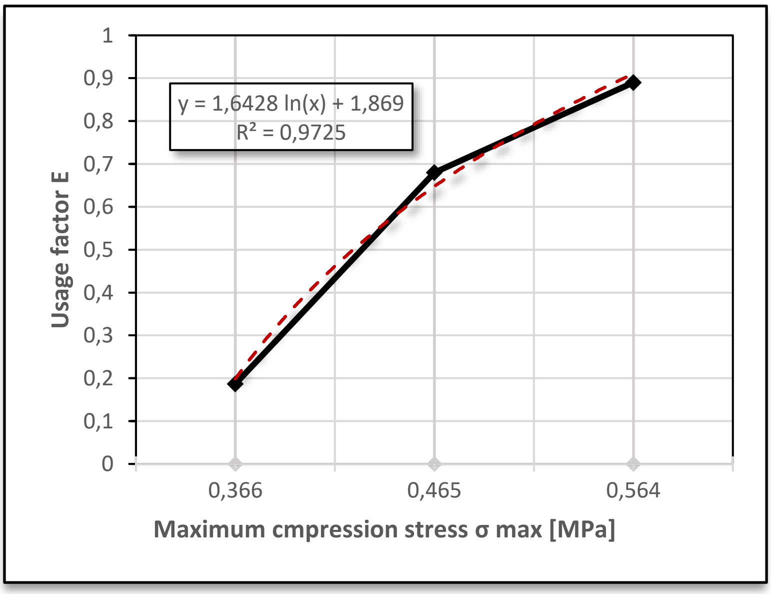

Figure 8: Correlation of fatigue response vs. of the maximum compressive stress σ_{max}

This correlation (Figure 8), with a trend curve in logarithmic form, and with a coefficient of determination R^2 close to 0.97, leads us to propose a fatigue criterion specific to reinforced concrete domes, this criterion can be written in the following form (Equation 11):

$$E = 1.6428\, ln(\sigma_{max}) + 1.869 \tag{11}$$

with :
E: Usage factor indicating the risk of fatigue, E = 1 implies a fatigue situation.
$\sigma_{\max}$: Maximum compressive stress of concrete at the foot of the dome, calculated under the $G + P$ combination under monotonic loading.
The advantage of this fatigue criterion is to predict the service life of reinforced concrete domes, knowing only the response under monotonic loading. It is valid for the following conditions:

- Reinforced concrete domes, the class of concrete is *C25/30*.
- Reinforcement type *FeE40*, with elastic limit in traction *400* MPa.
- Diameter of the domes D from 10 to 100 m.
- Fault in the center f is close to 0.10 D, corresponding to the lowered domes.
- Dome thickness: Checking the limit of compressive stress of concrete under monotonic loading ($G + P$), and the limit of displacement at center.
- Compressive fatigue limit of concrete: close to 0.6 of its limit in static.
- Fatigue under fluctuating load P at 10^6 cycles.

6 Conclusion

The work in this article was devoted to the study of the mechanical fatigue behavior of reinforced concrete domes. Through a numerical simulation of this behavior by studying several cases and based on the study of the response under monotonic loading and fatigue, followed by a correlation of the results, a numerical model for predicting the fatigue limit was aimed at. Existing fatigue criteria were exploited to predict this behavior.

In this study, the response under monotonic loading was coupled to the fatigue response. Numerical correlation made it possible to propose a fatigue criterion capable of predicting the service life of these complex structures without the need for a fatigue study. This criterion is of a conservative type, as it is based on a fatigue limit of concrete in compression ensuring sufficient safety in relation to dimensioning aspects and will therefore make a practical and rapid tool for a safety assessment of these structural systems.

The work discussed in this article offers researchers an interesting avenue to push towards a wider field of application in this area.

Acknowledgments

First of all, we would like to thank our team at the LMSE laboratory for their collaboration and supervision of this work. Our thanks also go to our students in the Civil Engineering Department, Mr NEMIR I. and Mr BOUDIAF NKE, for enriching the bibliographical research on this subject.

References

[1] Mohammed, M. R., (2018). Behavior of RPC hemispherical dome concentrically loaded. *The 1st National Conference on Civil and Architectural Engineering* 26-28.

[2] Chenxu, Z., Jinquan, Z. & Ruinian, J. (2020). Fatigue flexural performance of short-span reinforced concrete t-beams considering overloading effect. *The Baltic journal of road and bridge engineering*, *15*(2): 89–110. DOI: 10.7250/bjrbe.2020-15.474.

[3] Dineshkumar, R. & Ramkumar, S. (2019). Review paper on fatigue behavior of reinforced concrete beams. *Materials Today: Proceedings*, https://doi.org/10.1016/j.matpr.2019.05.353.

[4] Catalin, G., Pierre, L. & Jean, P. (2007). Response of CFRP-strengthened beams under fatigue with different load amplitudes. *Construction and Building Materials*, *21*(4), pp. 756-763.

[5] Suryanto, B. & Staniforth, G. (2019). Monitoring the Shear Fatigue Response of Reinforced Concrete Beams Subjected to Moving Loads using Digital Image Correlation. *Civil Engineering Dimension*, *21*(1), March 2019, 6 – 12. DOI: 10.9744/CED.21.1.6-12.

[6] Purnomo, J. Octaviani, V. Chiaulina, P. K. & Chandra, J. (2020). Evaluation of a Macro Lump Plasticity Model for Reinforced Concrete Beam-Column Joint under Cyclic Loading. *Civil Engineering Dimension*, *22*(2), September 2020, 82 – 93. DOI: 10.9744/CED.22.2.82-.

[7] Benard, I. (2017). Fatigue damage analysis of reinforced concrete structural elements. *Doctoral Thesis*, University of Toronto.

[8] Ehab, H. Mark, A. Bradford, R. & Ian, G. (2010). Nonlinear long-term behaviour of spherical shallow thin-walled concrete shells of revolution, *International Journal of Solids and Structures*, *47*, 204–215. https://doi.org/10.1016/j.ijsolstr.2009.09.027.

[9] Matake, T. (1980). An explanation on fatigue limit under combined stress. *Bulletin of the Japan Society of Mechanical Engineers.*

[10] Findley, MN. (1959). A theory for the effect of mean stress on fatigue of metals under combined torsion and axial load or bending. *Journal of Engineering for Industry*.

[11] Dang Van, K. (1993). Macro-Micro Approach in high-cycle Multiaxial Fatigue. *Advances in Multiaxial Fatigue. ASTM STP I191. D. L. McDowell and R. Ellis, EDS., American Society for Testing and Materials, Philadelphia.*

[12] Bianzeube, T., Nadjitonon, N., Djonglibet, W-D. & Jean-Louis, R. (2018). Multiaxial fatigue criteria based on an integral approach: justification of the superiority of this approach over the critical plane approach. *International Journal of Current Research*, *10* (1), pp. 63910-63917.

[13] Nadjitonon, N. (2010). Contribution to the modeling of fatigue damage. *Doctoral Thesis*, UNIVERSITY OF BLAISE PASCAL – CLERMONT II.

[14] Logzit, N. & Kebiche, K. (2021). Biaxial fatigue analysis model under non-proportional phase loading of tensegrity cable domes. *Engineering Structures*, *245*. 112791, ISSN 0141- 296, https://doi.org/10.1016/j.engstruct.2021.112791.

[15] Logzit, N. & Kebiche, K. (2020). Numerical Model for High Relative Capacity of Tensegrity Cable Domes. *Civil Engineering Dimension*, *22*(1). DOI: 10.9744/ CED.22.1.29-36.

[16] DTRF, (2021). *Cahier des clauses techniques générales applicables aux marchés publics de travaux de génie civil, Fascicule 74 : Construction des réservoirs en béton et réhabilitation des réservoirs en béton ou en maçonnerie*. Version 4.01.

DOI: 10.2478/sspjce-2023-0015

Steel-Concrete Composite Bridge Diagnostics and Reconstruction

Patricia Vanova*, Stefan Kusnir, Daniel Dubecky, Slavka Harabinova, Peter Orolin, Vincent Kvocak, Martin Lavko

Technical University of Kosice, Slovakia
Faculty of Civil Engineering, Institute of Structural Engineering and Transportation Structures
*e-mail: patricia.vanova@tuke.sk

Abstract

Many bridges in Slovakia are reaching their designed life span these days. Due to frequent errors during the construction of those bridges as well as bad maintenance, steel-concrete bridges are now in a critical state and urgent repairs of those structures are needed. In this article progressive methods of retrofitting existing concrete bridges are shown. In the presented method, the original pillars and original bridge deck will remain in their place, and on the existing deck new composite, steel-concrete bridge deck with encased steel members of progressive shape will be created. This method brings significant cost reduction for such retrofitting and enables the application of increased loads on the bridge.

Keywords: continuous shear connector, bridge repair, steel-concrete composite

1 Introduction

The technical condition of many bridges in Slovakia as well as meeting the requirements of their purpose are currently not satisfactory. Their maintenance, repair or reconstruction are limited by the limited financial sources for such purpose. For this reason, new innovative construction designs and techniques need to be considered in such processes that lower the construction time and cost.

This paper describes the steel-concrete pedestrian bridge diagnostics and reconstruction using such innovative solutions. In the new structure, continuous shear connectors will be used. There are no documented bridges with such design in Slovakia. Typically, the whole I-beam is used, such as in the Hodonín – Holič bridge [1]. To lower the cost, the existing structure will not be taken down, but rather serve as a formwork during the construction period.

Worldwide, bridges with encased steel continuous shear connectors are more widely used. In Germany, the so-called PRECObeam (Prefabricated enduring composite beams), containing clothoid-shaped continuous shear connectors, were introduced. The first such bridge was built in 2003. Several bridges based on this design were also built in Poland and France since 2009 [2]. Although typically used as short-span road bridges, in 2011 in Germany, a railway bridge was build using the VFT-Rail type of PRECObeam cross-section. In the VFT-Rail design, the clothoid-shaped shear connectors are placed from both top and bottom edge of the bridge [3].

2 Existing Bridge

The bridge in question (see Figure 1) is situated in the village of Čečejovce, in southeastern Slovakia. It is a steel-concrete pedestrian bridge composed of two steel rails laid longitudinally at the bottom surface of concrete deck (see Figure 2). The lower structure consists of outer supports and three internal supports. The central pillar is based on slab foundations. The interior supports, as well as the end supports, are probably based on slab foundations. The overall length of the bridge is 19.1 m, with the longest span of 5.9 m. There is no available documentation for the existing bridge. The year of construction of the bridge, or any additional reconstruction, is unknown.

Figure 1: Existing pedestrian bridge

Two pipelines are lying in parallel with the bridge deck, supported by a steel structure connected to the bridge (see Figure 2).

The existing bridge no longer meets the requirements of the investor (the village of Čečejovce), whose request was the small vehicles to be able to cross the bridge.

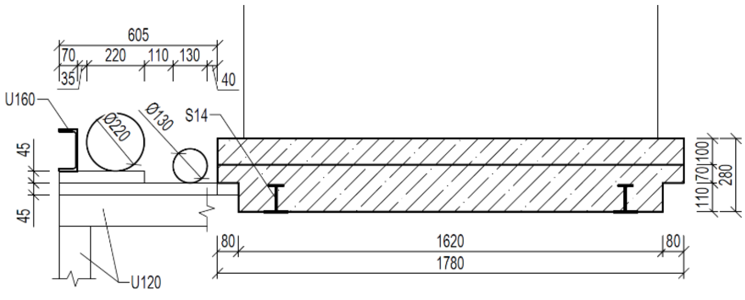

Figure 2: Cross-section of the existing bridge

3 Diagnostics

Based on the investor's requirements, a diagnosis of the existing bridge was carried out to identify its shortcomings and the potential for its expansion. It consisted of taking measurements of actual dimension of the bridges upper and lower structure, as well as of the evaluation of concrete strength and geological foundations for increased loading from vehicle line.

3.1 Assessment of Concrete

The analysis was performed on boreholes (see Figure 3a) from the middle pillar - borehole 1; bridge supports - borehole 2; and from the bridge deck - borehole 3. Based on the analysis, the following deficiencies of the existing structure were found [3]:

- Bore 1 had a total length of 190 mm. The concrete was porous - probably under-compacted.
- Bore 2 had a total length of 220 mm. Similar to the pillar and the end support, the concrete was porous.
- Bore 3 had a total length of 107 mm. It was created over a concrete-covered steel rail. The borehole was realized in order to determine the quality of the bridge deck concrete and to determine the height of the concreted steel rail.

The concrete sample specifications and concrete test results are shown in Table 1.

Table 1: Measured strength of concrete

Soil class	**Bore 1**	**Bore 2**	**Bore 3**
Height of bore (mm)	190	220	107
Weight (g)	1918.5	1846.9	1989.2
Diameter (mm)	104.80	104.50	104.30
Height of tested sample (mm)	105.00	105.20	103.10
Manner of violation	common	common	common
Reinforcement	without	without	2/6/21 and 27 mm from the bottom edge
Max grain size (mm)	30.0	32.0	23.0
Density (kg/m^3)	2118	2047	2258
Surface (mm^2)	8626	8577	8544
Force (kN)	108.6	96.7	257.2
Compressive strength in cube (MPa)	12.6	11.3	30.1

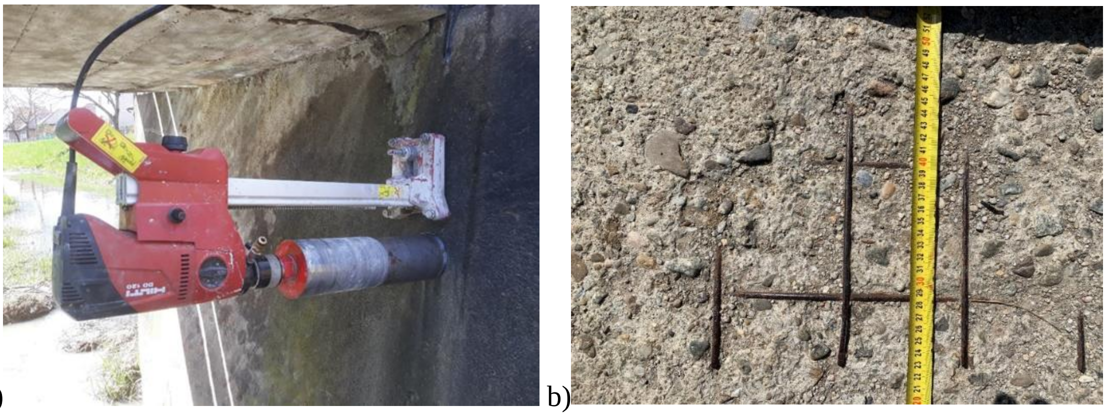

a) b)

Figure 3: a) Sampling from the middle pillar, b) reinforcement at the upper surface above the pillar

Based on the optical assessment of the bridge, other violations of the structure threatening its stability were found, namely insufficient coverage of the reinforcement and its corrosion, mechanical damage to the concrete, corrosion, and degradation of the concrete at the place of anchoring of the railing, and others (see Figure 3b).

3.2 Engineering-Geological Ratios

The village of Čečejovce is situated in the Košice Basin 22 km southwest of Košice at an altitude of 205 m. Due to the fact that no geological survey was carried out in this location, the information was obtained from available sources from the State Geological Institute of Dionýz Štúr, Map server - Geological map of the territory (see Figure 4) [5].

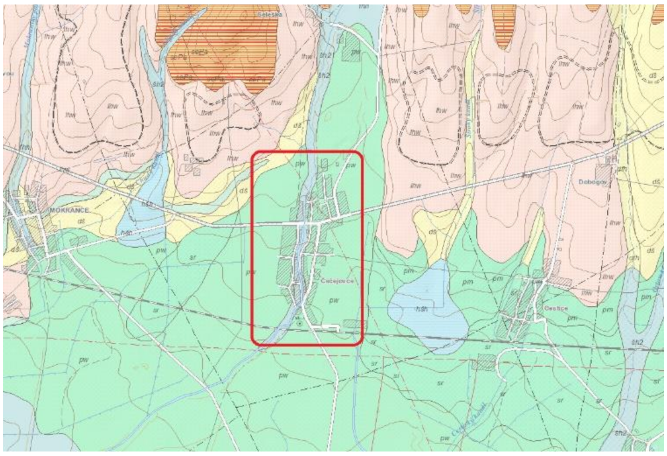

Figure 4: Geological map of the territory of the village of Čečejovce

From the point of view of the regional geomorphological division of the territory of Slovakia, the area of interest and its surroundings belong to the southern part of the Košice basin. Sediments of the Quaternary, Neogene substratum participate in the geological structure of the territory [4].

The Quaternary is represented in the surroundings by sediments, which are made up of sandy to clayey gravels. "These are sediments rising directly to the surface in floodplains, or only floodplain sections of streams. They are mostly found in the immediate vicinity of recent streams, mainly in the alluvial parts of meanders, as well as in parts of the artificially removed surface of alluvial clays and fine sandy clays of the flood facies." [5]

"Due to the influence of the laterally moving flow, during its simultaneous slight deepening, the gravels of the bot-tom accumulation were washed away and subsequently deposited. The resedimented material mostly comes from the upper gravel horizon of the bottom accumulation of the relevant stream, while the current state of the sur-face of the bottom accumulation, compared to its original surface, always represents an erosion reduction of ap-prox. 0.5 - 4 m. A characteristic feature of resedimented sandy gravels is their often alternating, but not very pronounced sorting of the positions of fine sands and gravels compared to bottom accumulation gravels. The thickness of the layers of resedimented gravel ranges from 0-2 (3) m." [5]

On the basis of this information, alternating positions of sandy silts (F3) and sandy to clayey gravels (G2 to G4) can be considered as a possible base soil in the given location under the existing load-bearing elements of the footbridge.

A detailed engineering-geological profile was not implemented in the given location, therefore, for the purpose of assessing the bearing capacity of the foundation soil, it is possible to consider only indicative values of the bearing capacity (see Table 2). For the design and assessment of sheet foundation structures in accordance with EC-7, in design situations where computational models are not available, limit states may be avoided by the use of prescribed measures. These include conventional and generally conservative design rules [6][7][8].

Table 2: Estimated bearing capacity of the soil at the construction site

Soil class	**Soil symbol**	**The name of the soil**	**Bearing capacity of the soil R_p (kPa)**
F3	MS,p	Sandy silt	275
G2	GP	Poorly grained gravel	650 (for b=1m)
G4	GM	Silty gravel	300 (for b=1m)

The proposal by adopting the prescribed measures can be used on the basis of comparable experience, i.e., documented or otherwise clearly established information relating to the foundation soil considered in the proposal (the values listed in Table 2 are according to STN 73 1001 from 1987) [6].

3.3 Results of Diagnostics

By diagnosing the footbridge in the village of Čečejovce, the dimensions of the existing footbridge were deter-mined, on the basis of which the drawing documentation was processed. Samples were taken from the bridge deck and the substructure, from which the concrete strengths of the outer supports and the intermediate pillar were determined. From the available documents on engineering-geological conditions, it follows that the foundation soil could be sandy silt or clay gravel. From the assumed values of the bearing capacity of the foundation soil and the dimensions of the foundations, the bearing capacity of the foundations under the central pillar was determined to be 1343 kN; and the bearing capacity of the foundations under the outer supports to be 472 kN.

The expected load from the new bridge construction with one lane for road traffic and emergency vehicles is:

- End support N_{Ed} = 385 kN < 472 kN
- Middle pillar N_{Ed} = 636 kN < 1343 kN

Where N_{Ed} is the design value of the compressive normal force.

Based on these analyses, it can be concluded that the existing footbridge support structures are suitable for a new bridge with one lane for passenger traffic and pedestrians.

4 New Bridge

In order to lower the cost of construction, the deck of the new bridge was designed to be on top of the existing structure, which can serve as the concrete formwork during the construction process.

4.1 Design

During the inspection of the bridge, two pipelines were found laying on the supports of the bridge parallel to the bridge. As part of the design of the new supporting structure, it is not necessary to relocate these lines. The new supporting structure avoids them (see Figure 5).

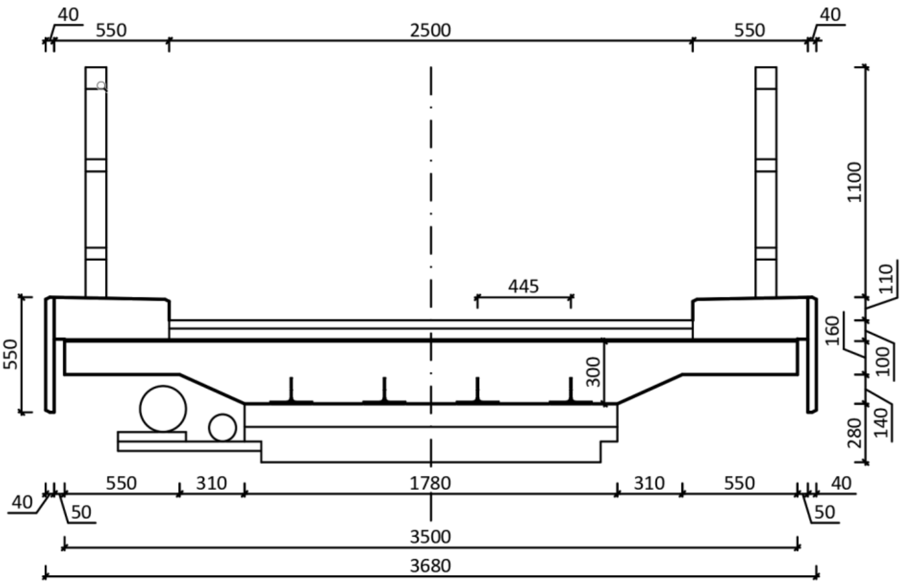

Figure 5: New cross-section

The supporting structure of the bridge is formed by four steel-concrete composite beams (see Figure 6a) created by longitudinally cutting the HE200A steel beam, creating puzzle dowels (see Figure 6b), with upper concrete consoles of dimensions 0.55 m x 0.16 m with a run-up length of

0.31 m on both sides of the cross-section of the bridge. The axial distance of the beams is 0.445 m. In the longitudinal direction, the cross-section is almost constant, the height of the middle part must be adjusted on the spot to compensate for the unevenness of the existing structure and create the proposed longitudinal slope of 0.5%. The height should not exceed 300 mm in any place, and its possible increase should be reflected in the increase of the cover layer of the bottom reinforcement. The load-bearing elements were created from rolled steel profiles of steel with strength S355, load-bearing concrete reinforcement marked B500 and concrete class C30/37 [8][9][10][11].

The specific shape of shear connectors used in the new bridge design is based on previous research of continuous shear connectors at Technical University of Košice [12][13][14]. In-between each of the dowels the concrete stud is formed, which provides high longitudinal shear resistance. The puzzle shape of the connector allows easier placement of the reinforcement cage into the con-vex parts of the puzzle cut and therefore simplifies and shortens the construction.

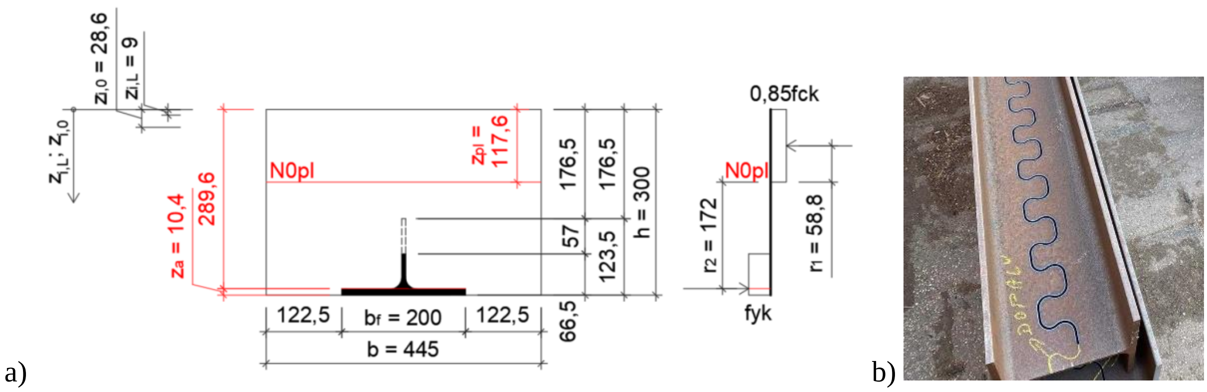

Figure 6: a) Characteristics of one composite beam, b) the H-beams with puzzle shaped cut, before separations (measurements in mm)

The railing of the bridge is designed as steel. The railing is anchored to the monolithic reinforced concrete ledge 0.2m from the outer edge. The cornice is anchored to the supporting structure by means of bow ties as stated in VL 4 (Sample sheets 4 of the Slovak Road Administration). The cornices are designed monolithically with a cornice prefab made of polymer concrete with a width of 40 mm and a visual height of 0.55 m.

The drainage of the new bridge structure is designed based on the existing condition. The bridge is designed with a longitudinal slope of 0.5% towards Kostolna Street. At the end, it is necessary to create a drainage channel and ensure the drainage of rainwater.

4.2 Construction

During the construction process it will be necessary to fully support the deck of the existing structure, which will serve as a formwork. After the construction will be finished, the original steel-concrete deck will only support its own weight. To prevent any unwanted connection between the existing deck and the new deck, it is necessary to create a hydro isolation layer in between the two decks. Also, it is necessary to leave a sufficient expansion joint filled with flexible material at the ends of the bridge to allow volume changes of the bridge.

Before the opening of the bridge, traffic signs limiting the maximum weight of the vehicle (3.5 tons) will be placed at its entrance.

5 Conclusion

This paper presented the diagnostics and reconstruction of a pedestrian bridge in the Slovak village of Čečejovce. Based on the results of diagnostics, the new bridge deck was designed. It included a continuous shear connector with puzzle dowel connection. This type of shear connector is not traditionally used in Slovak steel-concrete composite bridges.

Also, the new innovative solution for bridge structures that no longer meet the requirements for their use or are in bad technical condition was described. The solution brings advantages such as lower financial expenses as well as quicker, easier and more environmentally friendly construction process.

Unfortunately, after the problems with the construction company, in 2023 the investor decided to change not only the company, but also the design of the new bridge. The new road bridge, built in December of 2023, has an steel orthogonal deck. This type of solution is very common in Slovakia, and uses a large amount of steel, which typically increases the price of the bridge.

Acknowledgments

The paper has been supported by The projects: VEGA 1/0172/20 “Stress and deformation analysis of load-bearing components made out of steel, glass and compo-site materials“ of the Scientific Grant Agency of the Ministry of Education, science, research and sport of the Slovak Republic and the Slovak Academy of Sciences and by the project Slovak Research and Development Agency under the contract No. APVV-15-0486 “Analysis of Shear Connection Influence in Bridges with Encased Beams”.

References

[1] Bujňák, J., Odrobiňák, J., Kvočák, V. & Kožlejová, V. (2018). *Spriahnuté oceľobetónové konštrukcie*, first edn, Žilinská univerita v Žiline.

[2] Berthellemy, J., Zanon, R., Seidl, G., & Lorenc, W. (2014). *An innovative solution for small span bridges.* Toronto: Innovative steel bridges.

[3] Seidl, G., Hoyer, O., Zanon, R., Popa, N., Lorenc, W., Rowiński, S., Kożuch, M., Franssen, J.-M., Fohn, T., Quinchia, J. P., Carrasco, C. H., Farhang, A. & Nüsse, G. (2012). *Prefabricated Enduring Composite Beams based on innovative Shear Transmisson*.

[4] STN EN 206-1 – Betón. Časť 1: Špecifikácia, vlastnosti, výroba a zhoda.

[5] Geologická mapa SR M 1:50 000, Available online: https://www.geology.sk/geoinfoportal/mapovy-portal/geologicke-mapy/

[6] STN 73 1001 – Geotechnické konštrukcie. Zakladanie stavieb.

[7] STN 73 0037 – Zemný tlak na stavebné konštrukcie.

[8] STN EN 1997 – Navrhovanie geotechnických konštrukcií.

[9] STN EN 1990 – Zásady navrhovania konštrukcií.

[10] STN EN 1991 – Zaťaženie konštrukcií.

[11] STN EN 1992 – Navrhovanie betónových konštrukcií.

[12] STN EN 1994 – Navrhovanie spriahnutých oceľobetónových konštrukcií.

[13] Kvočák, V., Kožlejová, V., Dubecký, D., Kanishchev, R., & Vaňová, P. (2019). *Experimental and Software Analysis of Composite Action in Steel-Concrete Composite Bridges with Continuous Shear Connectors*. Berlin: Ce/Papers, Ernst & Sohn, 3(3–4), 307–312. doi:10.1002/cepa.1163.

[14] Vanova, P., Kvocak, V., Kozlejova, V., Dubecky, D., & Kanishchev, R. (2021). *FEM Analysis of Bridges with Encased Continuous Shear Connectors*. Berlin: Ce/Papers, Ernst & Sohn, 4(2–4), 731–735. doi:10.1002/cepa.1355.

[15] Kvočák, V., Dubecký, D., & Vaňová, P., (2021). *Prefabricated Composite Beams Based on Innovative Shear Connection*. Computational Engineering and Physical Modeling., Iran: Semnan Pouyan Press 4(2), pp. 20-26, doi:10.22115/CEPM.2021.233573.1109.

DOI: 10.2478/sspjce-2023-0016

Hydraulic and Water Quality Simulation in a Drinking Water Supply Network: A Case Study of the Ain Regada Network

Mazouz Kherouf [1*] and Fatoumata Goita [1]

[1] Engineering and Hydraulics Laboratory, Faculty of Science and Technology, 8 May 1945 University, Guelma, Algeria
*e-mail: kherouf.mazouz@univ-guelma.dz

Abstract

To ensure the quantitative and qualitative safety of the drinking water supply to urban and rural areas, drinking water supply network managers are always concerned to improve the quality of the service provided to consumers and the continuity and quality of the water distributed. They are also concerned to ensure better management of all water supply systems. The development of computer software has made network modelling an essential part of the design and management of water supply systems. In this context, this study focuses on the operation of the Ain Regada water supply network. The simulation of the operation of the network in its current state is carried out using Epanet software.

Keywords: hydraulic simulation, Epanet, water quality, Ain Regada, drinking water supply network

1 Introduction

A high-quality water supply and distribution network is one that is reliable and ensures a continuous supply of drinking water at appropriate speeds and pressures. In terms of drinking water, the community's essential mission is to guarantee satisfactory service to all users with the following four objectives:

- Quality: It must not harm the consumer's health and must comply with health regulations.
- Quantity: Users should have a sufficient quantity of water to meet their needs, with a continuous effort to control consumption and combat waste.
- Continuity of service: The distribution service must be ensured 24 hours a day.
- Pressure: The pressure, neither too high nor too low, must guarantee user comfort [1].

The exploration of hydraulic systems and the quality of water supply networks represents a crucial and interdisciplinary field at the intersection of engineering, environmental science, and public health. Researchers and experts have delved into diverse facets of this domain, investigating not only the hydraulic dynamics of water supply systems but also the preservation and management of water quality. Foundational contributions by early scholars such as Davis and DeWalle [2] laid the groundwork for analysing water quality in distribution networks. These seminal studies focused on unravelling the physical and hydraulic factors influencing water movement within networks, addressing issues encompassing flow rates, pressure fluctuations, and the potential for contamination.

Technological advancements and sophisticated modelling techniques have significantly bolstered our capacity to scrutinize and administer water supply networks. Researchers like Zhang et al. [3] have delved into the integration of real-time monitoring systems, smart sensors, and advanced computer models to promptly assess variations in water quality and facilitate proactive interventions.

The nexus between hydraulic studies and water quality considerations has gained increasing significance within the context of environmental sustainability. Scholars like Wang et al. [4] underscore integrated approaches to water quality management, harmonizing inventive treatment techniques with effective monitoring strategies within water supply networks.

Water distribution networks face vulnerability from various sources of accidental and deliberate contaminations, as highlighted by the US EPA [5]. Piazza et al. [6] contributes to this discourse by investigating accidental contamination and deliberate toxic agent injection into water sources. Their research emphasizes the imperative for widespread monitoring sensor deployment. Supported by the NSGA-II genetic algorithm coupled with a new diffusive–dispersive hydraulic simulator, their analysis concludes that the incorrect positioning of water quality sensors can result in inefficient monitoring networks. Additionally, the intensity of changes in water quality parameters varies depending on the duration of water loss and pressure in the distribution system, as described by Fontanazza et al. [7].

As the demand for water resources surges and environmental pressures heighten, the imperative for comprehensive studies on hydraulic systems and water quality becomes increasingly apparent.

This study focuses on the modelling and simulation of the drinking water supply network in the municipality of Ain Regada. Our work involves simulating the existing drinking water supply network in Ain Regada from a hydraulic perspective to obtain results on parameters (speeds and pressures). Additionally, we aim to conduct a water quality study to assess water degradation over time.

2 Case Study

The municipality of Ain Regada is located at the western end of the Guelma province, approximately 50 km from the provincial capital (Figure 1). It is traversed by the national road RN20, coming from the Constantine province and leading towards Guelma.

It is bordered by the following municipalities:

- North: Bordj Sabat
- South: Tamlouka
- East: Oued Zenati
- West: Constantine province.

Figure 1: Global view of Ain Regada

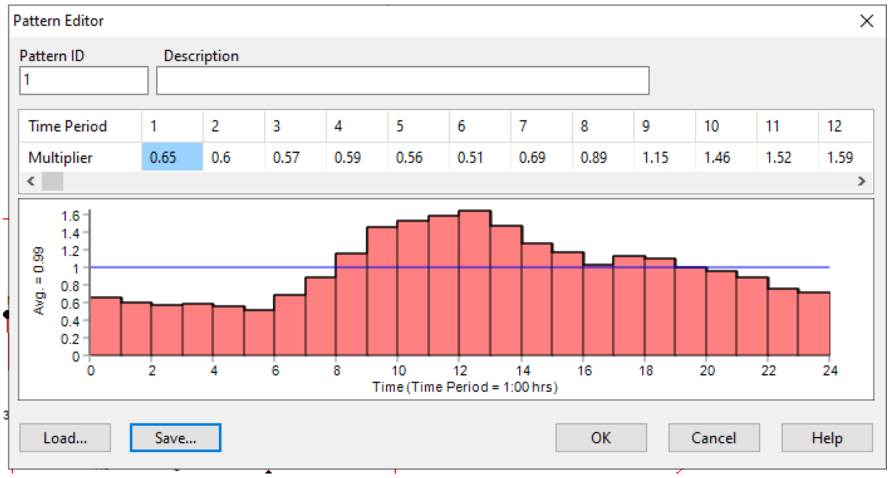

Figure 2: Hourly modulation curve

The Ain Regada city network is a branched network. It consists of 15 nodes, including a supply node (a reservoir) with a reservoir elevation of 831.09 m. The following table (Table 1) shows the characteristics of the various nodes and pipes.

Table 1: Characteristics of nodes and pipes

Node ID	**Elevation (m)**	**Link ID (pipe)**	**Label**	**Length (m)**	**Diameter (mm)**	**Rougness (mm)**
Tank	831.09	Link 1	Tank-N1	2	176.2	0.01
Junc N1	831,09	Link 2	N1-N2	30.5	176.2	0.01
Junc N2	827,81	Link 3	N2-N3	284.93	110.2	0.01
Junc N3	816,20	Link 4	N3-N4	165	79.2	0.01
Junc N4	810,03	Link 5	N2-N5	110.23	176.2	0.01
Junc N5	821,71	Link 6	N5-N6	33.21	110.2	0.01
Junc N6	819,16	Link 7	N5-N7	113.22	110.2	0.01
Junc N7	818,10	Link 8	N7-N8	175.17	79.2	0.01
Junc N8	813,56	Link 9	N6-N9	84.38	55.4	0.01
Junc N9	816,94	Link 0	N7-N10	69.04	79.2	0.01
Junc N10	816,29	Link 11	N10-N11	40.89	44	0.01

Junc N11	815,77	Link 2	N6-N12	40.57	96.8	0.01
Junc N12	818,86	Link 13	N12-N13	102	55.4	0.01
Junc N13	816.471	Link 14	N12-N14	115.3	55.4	0.01
Junc N14	815.76	Link 15	N1-N15	196.32	79.2	0.01
Junc N15	825.1					

2.1 Daily Demand Curve

To make our study more realistic, we added a modulation curve to simulate the off-peak and peak hours of the day (Figure 2). These periods correspond respectively to the period of low water consumption and the period of high-water consumption. This is because demand varies throughout the day, and consumption is generally higher in the morning and evening than at night or in the middle of the day. This is why we have assigned multiplication coefficients to be applied hour by hour to the demand nodes. The standard daily demand curve for small towns developed by AWWA [8] was used for simulation in this study. The curve shows how the rate of water consumption changes over the course of the day (24 hours) and provides the highest demand factors as multipliers that can be applied to the average base demand at any given time. The same approach has been adopted in other studies [9].

2.2 Hydraulic Simulation Model

Different computer models are now available and utilized in the water industry to forecast and assess the hydraulic performance of water distribution networks. Hydraulic analysis determines pressure head, flow rate, velocity, and head loss in each element of the system. Epanet is one of the most frequently used models [10]; it has been widely employed in research and industry and forms the basis for several commercial modelling software, including Picollo, Porteau, and Watercad [10].

The Epanet software was developed by the United States Environmental Protection Agency and can be used to simulate steady-state conditions and extended-period simulations of hydraulic behaviour and water quality in water supply networks [5]. Epanet tracks water flow in each pipe, head at each node, and water elevation in each reservoir. It can also be employed to simulate the concentration of a chemical species, water age, and source tracing throughout the entire network during a simulation period.

2.3 Water Quality Simulation Model

The water quality simulator of Epanet employs a Lagrangian approximation to track at defined intervals, what occurs in discrete water portions as they flow through pipes and mix at demand nodes [6].

2.4 Tank Mixing

One can assume that the water in tanks and reservoirs is completely mixed. Reservoirs that are periodically filled and emptied can be considered fully mixed if the incoming momentum is sufficient. If we assume perfect mixing, the water present in the reservoir is a homogeneous mixture of the initially present water and the incoming water quantity. At the same time, the internal concentration may change due to reactions in the reservoir. These phenomena are expressed by the following equation:

$$\frac{\partial V_S C_S}{\partial t} = \sum_{i \in I_s} Q_i C_{i/x=L_i} - \sum_{j \in O_s} Q_j C_S + r(C_S) \tag{1}$$

where:

V_s: the volume of a substance in the tank at time t

C_s: the concentration of the substance in the reservoir

I_s: all the arcs supplying water

O_s: all the arcs that evacuate water

2.5 Convective Transport in Pipes

A dissolved substance travels through a pipe at the same average speed as the fluid carrying it. During transport, it undergoes a reaction (formation or decomposition) with a certain reaction speed [7].
Usually, longitudinal dispersion is not an important transport mechanism. This means that the different elementary volumes of water in a pipe are not mixed.

2.6 Mixing at Pipe Junctions

At junctions that receive water from several pipes, mixing is considered to be instantaneous and perfect [8]. The concentration of a substance in the water leaving the junction is the weighted average of the flows entering the junction. For the node we can write:

$$C_{i/x=0} = \frac{\sum_{j \in I_k} Q_j C_{j/x=L} + Q_{k,ext} C_{k,ext}}{\sum_{j \in I_k} Q_j + Q_{k,ext}} \tag{2}$$

where:

i: is an arc whose flow leaves node k

I_k: the set of arcs whose flow is directed towards k

L_j: the length of arc j

Q_j: the flow (volume/time) through arc j

$Q_{k,ext}$: the external flow entering the network at node k

$C_{k,ext}$: the concentration of the flow from the outside entering the network at node k

$C_{i/x=0}$: the concentration at the start of arc i

$C_{i/x=L}$: the concentration at the end of this arc

2.7 Reactions at the Walls

The rate of a reaction occurring at or near the surface of a pipe can be considered to be dependent on the concentration in the body of water using an expression of the form [9]:

$$\mathrm{R} = \left(\frac{A}{V}\right) K\mathrm{w}C\mathrm{n} \tag{3}$$

where:

*K*w: is a reaction coefficient at the walls

*C*n: concentration of reactant of order n

(*A*/*V*): is the ratio of the internal surface area of the pipe to the internal volume (equal to divided by the diameter of the pipe). This last term modifies the units of mass reacting per units of surface into units of mass per units of volume.

(*Note:* A positive value should be used for growth reactions, a negative value for decomposition reactions).

The value of *K*w is generally between -5 and 0 feet/day and inversely proportional to the diameter of the pipe:

-1 foot/day for pipes with diameters of 1000 and 1200;

-3 feet/day for pipes with a diameter of 600 mm;

-5 feet/day for pipes with a diameter of less than 600 mm.

For our study we note:

Chlorine has a decomposition of order one, so the value of *K*w is negative *K*w = -5 ft/day = -1.524 m/day (pipes with a diameter of less than 600 mm) [8].

The WHO (World Health Organization) standard for drinking water stipulates that 2 to 3mg/l of chlorine should be added to water to achieve satisfactory disinfection and residual concentration. The maximum amount of chlorine that can be used is 5mg/l. For more effective disinfection, the residual amount of free chlorine should exceed 0.5 mg/l at a pH value of 8 or less [10].

3 Results and Discussions Heading

The modulation curve (Figure 2) constructed will be applied to all demand nodes. After entering all the appropriate data for the nodes and sections, the next step is to validate the hydraulic model. The simulation was successful, as shown in Figure 3 and Figure 4. According to Figure 3, the pressures and speeds obtained after simulation are acceptable. As can be seen from Figure 4, the chlorine content of the network varies between 0.25 and 1 mg/l. Most of the network ends have acceptable chlorine levels (between 0.75 and 1 mg/l), with the exception of the reservoir downstream. We can therefore conclude that there is no risk of deterioration in water quality in the Ain Regada network at 4 o'clock.

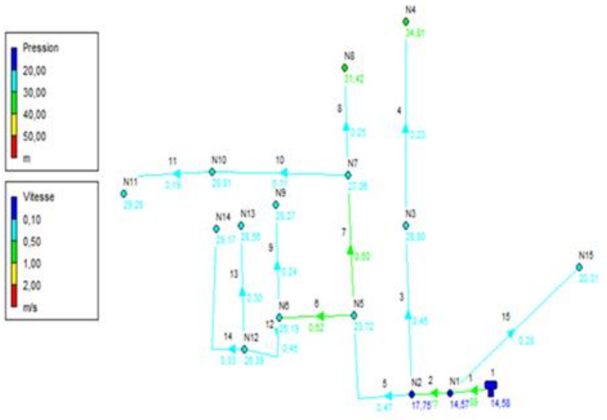

Figure 3: System diagram after simulation

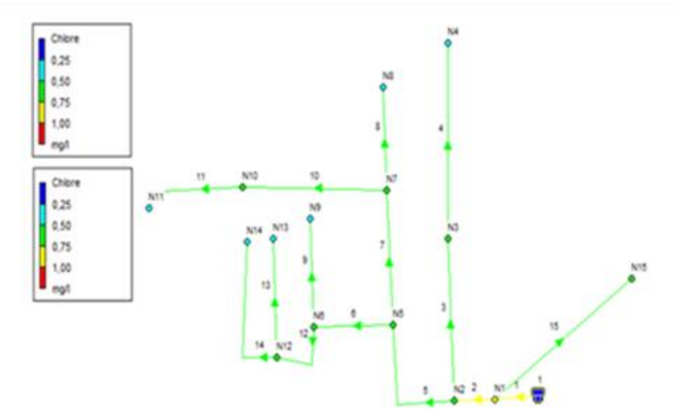

Figure 4: Schematic of system quality status after simulation

3.1 Status of Network Arcs

The status of the network arcs is summarized in the following table (Table 2).

Table 2: Status of network arcs and nodes at 12:00 (noon)

ID Nœud	Demad (l/s)	Head(m)	Pressure(m)	Chlorine (mg/l)
Junc N1	4.64	844.16	13.07	0.55
Junc N2	8.71	843.51	15.69	0.49
Junc N3	9.2	839.55	23.34	0.42
Junc N4	3.38	838.5	28.46	0.35
Junc N5	5.25	842.55	20.84	0.45
Junc N6	3.23	841.94	22.78	0.38
Junc N7	7.31	840.64	22.54	0.38
Junc N8	3.58	839.41	25.85	0.32
Junc N9	1.72	841.04	24.1	0.29
Junc N10	2.25	840.27	23.98	0.32
Junc N11	0.84	839.91	24.14	0.23

Junc N12	5.26	841.28	22.41	0.32
Junc N13	2.08	839.75	23.28	0.23
Junk N14	2.36	839.12	23.36	0.23
Junk N15	4.02	842.45	17.35	0.45
Tank 1	-63.83	844.21	13.12	0.61

After chlorine injection, we note that the state of the arcs (referenced in Table 3) presents no risk of deterioration in terms of network quality, particularly as the minimum recommended chlorine level, set at 0.1 mg/l, is respected.

Table 3: Status of arcs with chlorine injection at 4 o'clock

Link ID	**Coefficient of mass**	**Wall coefficient**	**Unit Headloss**	**Reaction Velocity**	**Chlorine**
Link 1	-1	-1.524	3.91	20.76	0.85
Link 2	-1	-1.524	2.97	18.29	0.78
Link 3	-1	-1.524	1.99	21.35	0.68
Link 4	-1	-1.524	0.94	17.61	0.53
Link 5	-1	-1.524	1.23	14.31	0.72
Link 6	-1	-1.524	2.62	22.29	0.67
Link 7	-1	-1.524	2.41	21.91	0.67
Link 8	-1	-1.524	1.04	18.78	0.55
Link 9	-1	-1.524	1.59	28.72	0.59
Link 0	-1	-1.524	0.8	18.79	0.59
Link 11	-1	-1.524	1.36	29.04	0.53
Link 2	-1	-1.524	2.34	21.35	0.59
Link 13	-1	-1.524	2.22	27.56	0.51
Link 14	-1	-1.524	2.77	29.12	0.51
Link 15	-1	-1.524	1.28	25.81	0.72

As can be seen from (Figure 4), the chlorine content of the network varies between 0.25 and 1 mg/l. Most of the network ends have acceptable chlorine levels (between 0.75 and 1 mg/l), with the exception of the reservoir downstream. We can therefore conclude that there is no risk of deterioration in water quality in the Ain Regada network at 4 o'clock.

4 Conclusion

This work involved hydraulic and water quality modelling using software, and our choice was based on the Epanet model. The objective of this model, which simulates the hydraulic behavior of pressurized network systems, is to enhance the understanding of water flow in the distribution system. Data and values of the physical components (pipes, reservoirs, nodes, etc.) and non-physical components (modulation curves) of the water distribution system in the municipality of Ain Regada were used to create the Epanet model for this distribution system. The simulation of the model was successfully executed, allowing us to assess the hydraulic parameters throughout the network and gain a better understanding of our system's operation.

According to the results obtained from simulating the operation of the water supply network in the Ain Regada area using the Epanet simulation software, it is observed that the study area experiences acceptable pressures at all points (nodes) in the region (pressure below 34m).

Regarding velocities, more than 60% of the pipes have velocities ranging from 0.1 to 0.5 m/s, and less than 40% of the pipes have velocities ranging from 0.5 to 1.6 m/s.

It should be noted that low velocities promote deposits in the distribution pipes. Concerning water quality through chlorination, values between 0.23 - 0.85 mg/l were found for peak demand and 0.31 - 0.85 mg/l for fire demand. It is noteworthy that the chlorine concentration remains at least equal to 0.1 mg/l.

This project was carried out in several stages. The modelling begins with the creation of a digital database that is as representative as possible of reality and is complemented by data collection, which is a crucial step for the validity of the model. The modelling conducted using Epanet allows us to characterize the current state of the drinking water distribution network and facilitates the planning of interventions that can be carried out at any point in the network.

Looking ahead, we recommend the use of another modelling software to compare the obtained results. Calibration of this model can provide valuable insights into the model and the results of this modelling.

Acknowledgments

The authors very much appreciate the support by the university 8 May 1945 Guelma, Algeria and Ministry of Higher Education and Scientific Research.

References

[1] Abekhiti, F. Z. & Harid, L. (2018). Modélisation d'un réseau d'AEP par deux logiciels avec élaboration d'un SIG, Mémoire de master 2, Université 8 Mai45 Guelma.

[2] Davis, J. C., & Dewalle, F. B. (1967). Design and Control of Water Quality in Water Distribution Systems, Journal of the Sanitary Engineering Division, 93(3), 69-100

[3] Zhang, X., Zhang, Y., & Yu, X. (2015). Smart water quality monitoring and managing system: Application and validation,Procedia Environmental Sciences, 26, 2-7

[4] Wang, Q., Lei, Z. & Meng, F. (2020). An integrated approach for water quality management in water distribution systems, Journal of Hydroinformatics, 22(5), 1174-1190

[5] US EPA., (2023). Response protocol toolbox, Planning for and responding to drinking water contamination threats and incidents, 17p, Online version, 2003, http://www.epa.gov/safewater/watersecurity/pubs/guide_response_overview.pdf. Accessed January 28, 2023.

[6] Piazza 0.S., Blokkere, J. M. G., Freni V., Puleo, M., & SAMBITO (2020). Impact of diffusion and dispersion of contaminants in water distribution networks modelling, and monitoring

[7] Fontanazza, CM., Notaro, V., Puleo, V., Nicolosi, P. & Freni, G. (2015). Contaminant intrusion through leaks in water distribution system: Experimental analysis,Procedia Eng., 119 426 – 33,2015, https://doi.org/10.1016/j.proeng,2015.08.90.

[8] AWWA.: Manual M32 - distribution network analysis for water utilities, Denver, colo., awwa, 1989.

[9] H.I, M. & Abozeid, G. (2011). Dynamic simulation of pressure head and chlorine concentration in the city of Asyut water supply network in abnormal operating conditions, Arab. J. Sci. Eng., vol. 36, no. 2, 2011, pp. 173-184.

[10] Clark, R.M., Hakim. S., & Ostfeld A. (2011). Handbook of water and wastewater systems protection, New York, springer

[11] Rossman, L.A. (2000). Computer models/ Epanet, L.W. Mays, Ed., Water Distribution Systems Handbook. McGraw-Hill, New York,pp. 12.1-12.23.

[12] Banerjea, R. (1950). The use of potassium permanganate in the disinfection of water, ind. Med. Gaz, 85, 214- 219.

[13] Bacha, M., Achour, S. & Guergazi, S. (2004). Chloration des bases puriques et pyrimidiques dans les eaux minéralisées, Colloque international « terre et eau » Université Badji Mokhtar Annaba. Département de géologie, 2004.

[14] APHA. (1992). Standard Methods for The Examinations of Water and Wastewater, 18th Ed, Washington D.C, American Public Health Association.

[15] Betty, M ., Jy, S. & Wu. (1985). Removal of Organic Precursors by Permanganate Oxidation and Alum Coagulation, Water Res,19 (3), 309- 314.

[16] Christman, R.F., Johnson, J. D., Norwood, D.L, Liao, W.T., Hass, J.R, et al. (1981). Chlorination of aquatic humic substances. Us environmental protection agency, municipal environmental research, laboratory, Cincinnati, Ohio, (epa- 600/s2-81-016)

DOI: 10.2478/sspjce-2023-0017

Plastic Waste Sheets Effects on Reclaimed Asphalt Pavement Performances

Adel Boulemaizet [1*], Khaled Boudjellal [1], Karima Messaoudi [1], Souhila Rehab Bekkouche [1]

[1] LMGHU Laboratory, Civil engineering Department, 20 Août 1955 University, Skikda, Algeria
*e-mail**:** boulemaizetadel@gmail.com

Abstract

This paper aims to examine physical and mechanical performances of a Reclaimed asphalt pavement (RAP) material reinforced with 5 to 15 mm size sheets of plastic waste. The three types of plastic used in the study are: low density polyethylene (LDPE), high density polyethylene (HDPE) and polyethylene terephthalate (PET) with 1%, 1.5%, and 2% dosage by weight of aggregates.
Obtained Duriez test results testify to a 9% to 30% improvement in moisture resistance for all types of plastic compared to virgin mixture while for LDPE waste plastic type workability test attests an acceptable compaction condition for RAP material with less than 1.5% of waste plastic.
Nevertheless, it has been noticed an increase in void index and compaction difficulties starting from 1.5% dosage, resistance to rutting has also improved with the addition of waste plastic, an improvement in fatigue strength was also observed particularly at 2% dosage.

Keywords: pavement, aged bitumen, RAP material, plastic waste, plastic recycling, rutting, fatigue

1 Introduction

Rutting and cracking of roads and highways surface layer built with asphalt concrete could be signs of pavement aging, however they might also be pathologies related to fatigue, manufacturing, or design defects such as poorly adapted mixture design or even inadequate material quality. The increase in road traffic, particularly heavy trucks, accelerates pavements deterioration, mainly the wearing course. Road rehabilitation requires the manufacture of new materials based on increasingly scarce, expensive, and polluting raw materials. Old materials Recycling is an excellent alternative to save energy reduce costs and protect the environment. For the past few decades, the reuse of materials from old pavements milling has become a widely used technique throughout the world, and research is leaning towards both mobilizing the maximum amount of recycled materials and optimizing their performance.
Several studies have evaluated the air pollution by CO_2 gas emission following the production of asphalt mixes, thus a ton of hot mix asphalt emits 48 kg of CO_2 [1], according to national

and European Asphalt Pavement Association [2] in an environmental impact study, this emission can reach 50 kg/t.

As a result, the introduction of recycled asphalt aggregates can dramatically reduce greenhouse gases and reduce the energy required to manufacture and process the raw materials, it is indicated that increasing RAP materials in the mix to just 25% will reduce greenhouse gases by 10% over the overall life cycle by eliminating the fuel consumption required to manufacture and process virgin asphalt raw materials [3]. However, other studies have shown that the use of RAP at 30% and 70% reduces CO_2 emissions by 20% and 35% respectively [4-5].

Technical advantages have also been reported in numerous studies and research, for example, the long-term performance of asphalt concrete (AC) pavements was examined using virgin asphalt mixtures and were compared to those containing only 30% RAP, it was found that the latter performed better than virgin mixtures in terms of rutting and roughness [6], However the addition of aged binders to bituminous mixtures especially at high rates has generally changed the relatively soft binder which is common at both high and low temperatures, by one grade [7].

For this purpose, the introduction of additives of certain types and at certain dosages, could be one of the best remedies to overcome the inadequacies and shortcomings in the use of RAP products at high rates. The quality of binder has a close impact on that of mixes, indeed, to act on the properties of recycled materials, particularly bituminous concretes, in order to rectify certain performances, the understanding of bitumen ageing phenomenon and its new characteristics would be essential.

Multiple searches aimed at improving the quality of aged bitumen by lowering its rigidity and restoring its adhesive capacity. Studies have shown that the incorporation of additives called regenerators or rejuvenators in bitumen matrix, as the example of certain oils, substantially improves the quality of bitumen.
Polymer-based modification of aged bitumen has also shown its effectiveness in correcting mixtures characteristics [8], bitumen modification is mainly done by the so-called wet method where polymer particles are introduced into the binder, on the other hand the so-called dry method consists in incorporating these plastic additives into the mixture during mixing [9-10].
A literature review on the effects of widely used recycled plastics (LDPE, HDPE, PET, PP) on virgin asphalt mixes performances, which may also concern aged bitumen, has been carried out by [11], it was illustrated that polymers and plastics offered a better Marshall stability, thus in general, the addition of plastic waste increases fatigue cracking resistance, nevertheless this resistance occurs essentially from the dosage of 4.5% by weight of bitumen. This improvement is due to the fact that the addition of polymer increases the tensile strength and elastic response in the binder, properties that are strictly related to G^* and δ in the DSR (Dynamic Shear Rheometer) tests [12].

In a recent study, it was confirmed that waste plastics used in bituminous mixes, have no negative impact on the environment (leachability) and / or worker safety (harmful fumes) [13]. several research works found that heating of waste in the range of 109 to 180 C in controlled conditions are not emitting toxic gases, emission will start if we heat beyond 270° C [14].
However, in the literature, only little research has been carried out on the use of polymers derived from recycling (plastic waste) in RAP material, although the majority of the work focused on the use of polymer granules of a few millimeters (1 to 4 mm) to modify bitumen by wet method [15]. In our study we will use instead leaves of about 5 to 15 mm in size from the

shredded plastic waste using dry process; this means we are not looking for modifying bitumen but examining plastic sheets effects on RAP material.
The current research doesn't consist in modifying aged bitumen, nevertheless it consists in exploring physical and mechanical performances of a RAP material reinforced with sheets (in sheet shape) of three types of plastic waste (LDPE, HDPE, PET) with different dosages 0%, 1%, 1.5%, 2% by weight of aggregates, the mixture at 0% is considered each time as a control sample. We have tested moisture resistance for mixtures with all types of plastic and then we chose a RAP material with LDPE to undergo a series of tests to characterize it in relation to specifications of virgin bituminous materials.

The choice of polymer types was made based on their high availability as waste generated from everyday plastic objects [16, 17]. Polymer dosages and their ranges were set taking into consideration dosages used in literature [14-19], however an extension of plastic amount incorporated in the mixtures was adopted after several attempts and experiences to better understand material behavior beyond dosages usually practiced in previous Polymer Modified Bitumen (PMB) researches.

2 Materials and Methods

2.1 Origin of Materials

RAP material used in this research comes from the mechanical milling of asphalt concrete layer during the rehabilitation of National Road N° 27 in the region of Mila (Algeria). The removed wearing course was laid in 2009 and has since undergone local degradation such as rutting and cracking. Archive documents of Roads and Bridges Services permitted the identification of the material mixing design and characteristics of different components as well as the control results related to material implementation.
Plastic waste comes from the industry that recovers various household or industrial objects and articles in the same region. Waste is collected and sorted by type of polymer, then washed with hot water and household detergents, and crushed to different particle sizes. The LDPE products come from soft plastic objects, packaging, bags etc. HDPE products come from rigid piping and packaging, PET plastic comes mainly from soda and mineral water bottles.

2.2 Material Characterization

2.2.1 RAP Material

RAP material was about 10 years old at the time of sampling on site; archive documents reveal a 35/50 grade bitumen with 5.25% binder content, while the aggregates came from a limestone rock. Some characterization tests of the material were carried out, namely:

- Binder content by the distillation column extraction

The results obtained for three samples tested are presented in Table 1.

Table 1: Binder content of RAP material

	Standard	Sample 1	Sample 2	Sample 3	Average
Binder content %	NF EN 12697-4	5.19	5.11	5.16	5.15

- Recovered RAP material aggregate gradation

After extracting bitumen from aggregates, and in accordance with the method of NF EN 12697-2 standard, the recovered material (gravel and sand) will be subjected to a sieve analysis by placing it in relation to a BBSG 0/14 type spindle, as shown in Figure 1, we notice a content of fine elements close to the upper limit due to the milling process that increases their amount by breaking up the aggregates and decreasing their size.

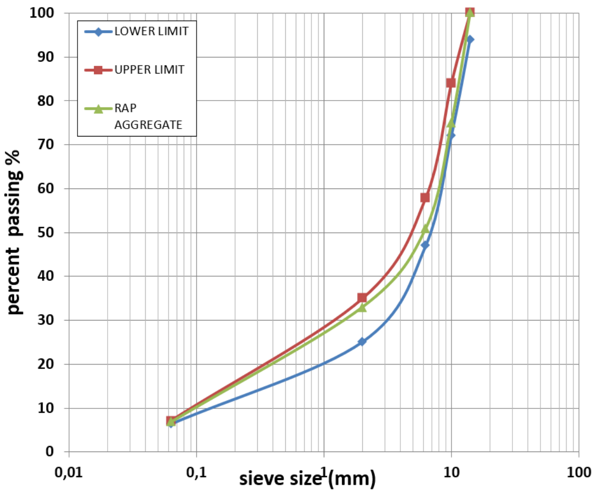

Figure 1: Recovered RAP material aggregate gradation

- Aggregates and sand characterization

Aggregates and sand characterization tests were carried out in accordance with the corresponding standards, density NF EN 1097-6, Los Angeles abrasion test NF EN 1097-2, Micro Deval abrasion test NF EN 1097-1, results obtained are given in Table 2.

Table 2: Characteristics of aggregates and sand of RAP material

	Standard	Value
Density (g/cm^3)	NF EN 1097-6	2.63
LA %	NF EN 1097-2	26
MDE %	NF EN 1097-1	18

2.2.2 Plastic Waste

Plastic sheets have a maximum dimension of about 15 mm, and a thickness of between 1 and 2 mm. They have been washed with household detergent and dried before being put in separate boxes with marking according to polymer type (Figure 2).

Some characteristics were given by the supplier (particle gradation curve, density), others were determined in our research (softening & melting temperature); Table 3 gives some physical characteristics of waste according to plastic type, while Figure 3 shows particle gradation curve of each polymer.

Table 3: Polymer additives characteristics (plastic sheets)

	Standard	**LDPE**	**HDPE**	**PET**
Density (g/cm^3)	NF EN ISO 3838	0.926	0.979	1.188
Softening temperature ° C	EN ISO 2507	121	134	155
Fusion point ° C	NF EN ISO 3146	185	204	226

Figure 2: Washing and drying of plastic waste

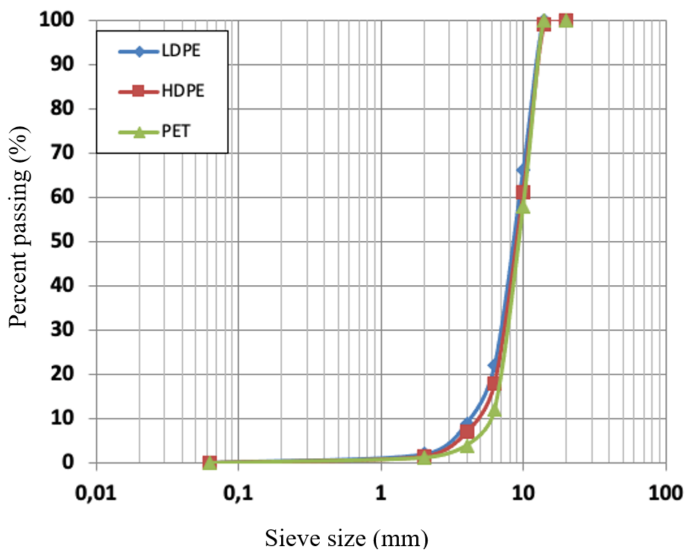

Figure 3: Plastic particle gradation curve of each polymer

2.3 Sample Preparation

RAP material has not undergone any treatment or addition of bitumen; the binder content has been maintained the same. It is heated in a tray at a temperature of 180° C for about 2 hours, while plastic waste is placed in a tray and heated separately in an oven at a temperature of 110° C for 2 hours.

For each type of polymer (LDPE, HDPE, PET), the desired mixture consists of RAP material and plastic waste in different percentages, namely: 0%, 1%, 1.5%, 2% by weight of aggregates.

In a mixer preheated to 180° C, bituminous material is poured into the mixer and rotated at a speed of 200 rpm. Plastic sheets are gradually introduced in order to have a homogeneous mixture; the whole is left to rotate for 2 to 5 minutes depending on mixture quantity.

2.4 Methodology and Test Program

Laboratory tests carried out were conducted in accordance with European standards including sample preparation, procedure, presentation and interpretation of results, standards adopted for each test are given as follows; moisture resistance “Duriez” (NF EN 12697-12 + NF P 98-251-1), SGC test (Superpave Gyratory Compactor) NF EN 12697-31 or PCG in French standards, rutting test NF EN 12697-22 *FWTT* (French Wheel Tracking Test), fatigue resistance NF EN 12697-24. The following tables (Table 4-7) give specifications on the results for each test:

Table 4: Allowable values of Duriez test results

Mixture type (Bitumen grade 35/50)	**Standard**	**r/R**
BBSG*	NF EN 12697-12	0.70
BBME*		0.80

*BBSG (semi-granular bituminous concrete), BBME (high modulus mixes)

Table 5: Specification of void index values in accordance with the recommendations of LCPC (Central Laboratory of Bridges and Roads – Paris - France) [20]

Gyrations Nbr	**Standard**	**void index V (Specifications)**
09	NF EN 12697-31	≥ 11 %
80		≤ 08 %
120		≥ 04 %
200		≥ 02 %

Table 6: Permissible rut depth values

Mixture type (Bitumen grade 35/50)	**Standard**	**Mixture class**	**Number of cycles**	**Depth (mm)**
	NF EN 12697-22	1	30 000	≤ 10% (P_{10})
BBSG/BBME		2	30 000	≤ 7.5% ($P_{7,5}$)
		3	30 000	≤ 5% (P_5)

Table 7: Fatigue resistance permissible values [21]

Mixture type	**Standard**	**Class**	**Specification in fatigue ε_6 10° C 25 Hz in µdef**
BBSG	NF EN 12697-24	1 to 3	≥ 100 (ε_{6-100})
BBME		1	≥ 100 (ε_{6-100})
BBME		2 and 3	≥ 100 (ε_{6-100})

3 Results and Discussion

3.1 Moisture Resistance (Sensitivity) Test (Duriez)

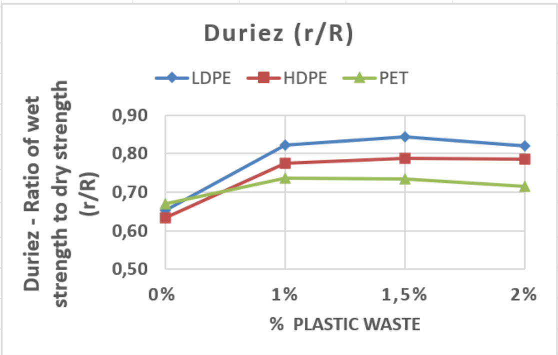

Figure 4: r/R variation as a function of plastic waste type and dosage

Figure 4 illustrates the r/R variation as a function of plastic waste type and dosage, it should be noted that for LDPE & HDPE r/R ratio increases with the dosage of 1% and 1.5% then begins to decrease slightly for LDPE but it stabilizes for the HDPE in the range of 1.5% up to 2% dosage, however r/R ratio increases with 1% of PET and then mixture maintains a plato in the range of 1% up to 1.5% dosage and then starts to decrease, LDPE seems to be less sensitive to moisture with a 30% increase in r/R value at dosage of 1.5% (r/R=0.82), HDPE increased this value by 21% at a dosage of 1.5% and 2% (r/R=0.79) while PET caused only a slight increase of about 9% at a dosage of 1% and 1.5% (r/R =0,72).

A study of Marshall stability in PMB found an improvement in Marshall Quotient with 7.5% PET [14], on the other hand it was indicated a 50% improvement with 4% HDPE all by weight of bitumen [22], these dosage values used to modify bitumen seem to be lower than the dosage we have used (1 to 2% by weight of aggregate equals approx. 20 to 40 % by weight of bitumen). Increase in moisture resistance in RAP material with 1 and 1.5 % dosage is due to the increased adhesiveness in mix that was lost during bitumen aging [23], indeed plastic adheres to aggregates when it softens at the mix preparation temperature (180° C), the closer softening and melting temperatures of plastic are to those of bitumen (Table 3), the greater adhesion increases between mix components, furthermore plastic combines in part with binder [20] which strengthens their bonds. For the PET and due to its high softening temperature relative to LDPE and HDPE, it adheres less strongly to aggregates, nevertheless the decrease in moisture resistance starting from 1.5% of plastic dosage is due to the increase in void index which permits to water to infiltrate and weaken the material bonds, though compressive resistance doesn't really decrease after 1.5% dosage.

3.2 Compactivity and Workability Test (Superpave Gyratory Compactor)

Six specimens for each type and dosage of plastic (0%, 1%, 1.5%, 2%) were prepared (72 specimens in total), value retained corresponds to the average of the six results found. Figure 5 shows void index regression curves in relation to gyration number for each LDPE plastic waste dosage.

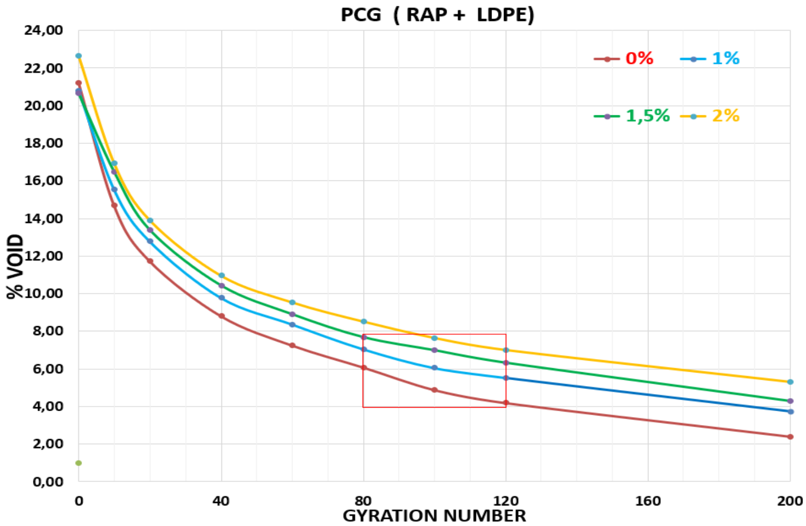

Figure 5: Void index regression curves in relation to gyration number for each LDPE plastic waste dosage

The graph clearly shows that void index increases proportionally with addition of sheets, thus at 80 gyrations and for a dosage varying from 0% (RAP alone) to 2% of plastic, void index increases from 6.1% to 8.8% for LDPE.
At the end of test cycle (200 rotations), for the same variation in dosage (0 to 2%), void index increases from 2.4% to 5.3% for LDPE blend.
In terms of specifications (Table 5), void index values of specimens with 1% and 1.5% of dosage are in conformity, mixture with 2% of LDPE plastic is out of tolerance.
The increase in void index with plastic waste addition is explained by the presence of plastic particles, the plastic sheets were heated to only 110 degrees so as not to stick to each other and then rotate with the bituminous mixture for 2 to 5 minutes which does not allow them to melt sufficiently and fill the voids during compaction especially since these particles were not taken into account during the mixture design [24], this fact is not generally observed in PMB researches according to the literature when void index doesn't increase this way because of fine plastic aggregates used which combine with bitumen and fill void [20].

3.3 Rutting Test (FWTT)

Figure 6 shows the rut depth curves of each mix in relation to cycle number of test wheel.

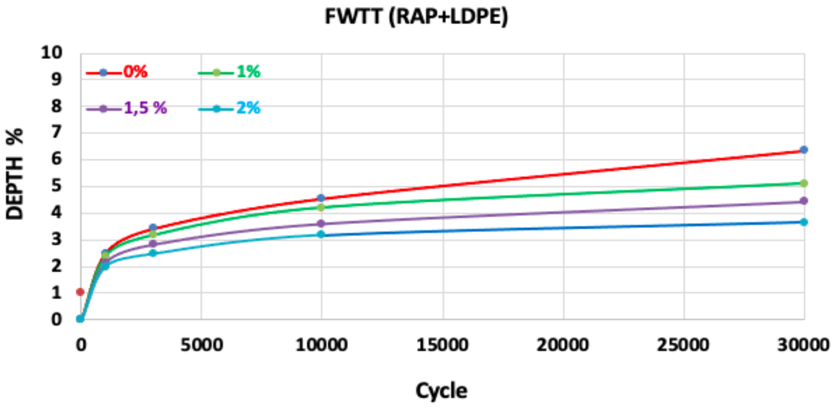

Figure 6: Rut depth curves RAP+LDPE

Curves of rutting test above show that addition of LDPE plastic sheets proportionally increases RAP material resistance to permanent deformation in a substantial way. Indeed, for a plastic dosage varying from 0% (RAP alone) to 2%, rut depth for the RAP with LDPE goes from 6,4 mm to 3.7 mm, these results are in line with those found by [18] with the use of 4% LDPE by weight of bitumen.

Result of plastic waste addition is visible on RAP mixture in this test due to the increase in material stiffness [25-26]. Indeed, this was possible according to compressive strength values in Duriez test (r/R), which gives an indication of material behavior with respect to strain stresses. It is confirmed that values obtained for 30 000 cycles could correspond to 3rd class BBSG /BBME according to Table 6 [20], starting from 1.5% of dosage.

3.4 Fatigue Test

For deformation levels ranging from 87 to µ126 def. Figure 7 shows fatigue curves (Wöhler curves) for LDPE plastic in a semi-logarithmic graph.

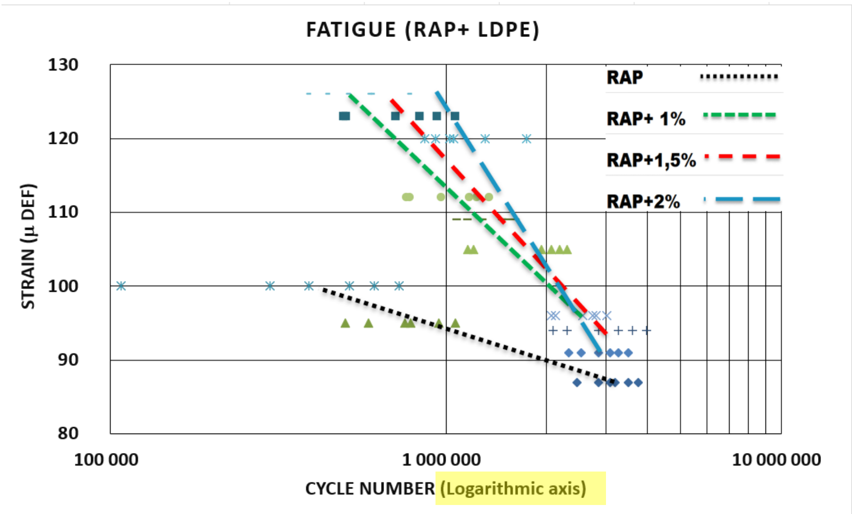

Figure 7: Fatigue curve RAP + LDPE

The general trend of curves shows a clear improvement in fatigue resistance while increasing plastic dosage, however RAP mixture with 2% LDPE plastic sheets added have better fatigue resistance with ε_6 values above 120μdef (specification value ≥ 100 μdef).
Results obtained are due to the increase in tensile strength and enhancement of elastic property in binder due to addition of plastic [12] besides they are due to reinforcement of granular structure of mixture by plastic that adheres to aggregates to form solid bonds and provides a bridging effect in the mixture [27]. Results of the same trend have been found by [28] who showed that addition of more than 10% PET by weight of bitumen, improves fatigue resistance of bituminous mixtures even though they worked on PMB with PET plastic than LDPE and with smaller size particles.

4 Conclusion

According to obtained results from various characterization tests carried out on RAP material reinforced with plastic waste sheets, we note in overall a clear improvement in mechanical performances at precise dosages and for certain types of polymers while the physical characteristics, precisely the void index, will become poor for high plastic dosages, nevertheless very few are similar researches using plastic sheets (5 to 15mm), most of studies are rather directed towards bitumen modification (wet method) with grains of inferior size (1 to 4 mm).
Indeed, addition of LDPE waste to RAP material improved its moisture sensitivity by increasing its compressive strength of 30% at a dosage of 1.5% while HDPE caused a 21% improvement at a dosage of 1.5% and 9% at a dosage of 1% for PET.
The workability test reveals that the addition of plastic waste sheets increases void index values for any type of polymer. It was found that PET comes first followed by HDPE and then LDPE in terms of increasing voids in material. Void index values at 1% dosage for all three types of plastics are within specification, at 1.5% dosage, blend values are acceptable except for material with PET. In addition, mixtures with 2% of all types of plastic are out of tolerance, this means that workability starts to be confused at 1.5% and up of plastic dosage where compaction becomes difficult.
In resistance to permanent deformation test, it is concluded that addition of plastic waste to RAP material leads to results in favor of excellent rutting resistance, mixes submitted for study correspond well to 3^{rd} class BBSG /BBME [20], starting from dosage of 1.5% plastic waste for all types used.
Fatigue resistance of RAP material with different plastic types and dosages was tested, results found express clear improvement in fatigue resistance while increasing plastic dosage particularly with LDPE and HDPE.
Plastic additives used in sheets shape have a key role in creating bonds or bridges between aggregates, thus consolidating the material structure to better withstand different stresses. As a result, the current research was able to highlight physical and mechanical performances of 100% RAP material with recycling plastics in sheets shape, LDPE and HDPE in particular, at a dosage of 1 and 1.5% beyond which workability becomes failing.

It is recommended to study a possible combination of plastic with bitumen addition in order to adjust void index which is considered pivotal in bituminous mixtures quality.

Acknowledgement

This research received no external funding.

References

[1] Hammond, G.P., Jones, C.I. (2008). Embodied energy and carbon in construction materials. *Proc. Inst. Civ. Eng. Energy* 2, 87e98.

[2] The Asphalt Paving Industry – A Global Perspective (3rd ed.) (2011). Retrieved from: https://www.yumpu.com/en/document/read/11782428/the-asphalt-paving-industry-a-global-perspective-eapa

[3] National Asphalt Paving Association (NAPA) (2009). Black and Green: Sustainable Asphalt, Now and Tomorrow. Special Report Number 200, National Asphalt Paving Association, Lanham.

[4] Zaumanis, M., Mallick, R. B., & Frank, R. (2014). 100% recycled hot mix asphalt: A review and analysis. Resources, Conservation and Recycling, 92, 230-245.

[5] Lopez, E., Willem, M., & Mabille, C. (2015). Recycled and regenerated bituminous concrete with high milling content. Revue générale des routes et de l'aménagement (RGRA), (928), 22-27. http://www.hotmix.org/images/stories/sustainability_report_2009.pdf

[6] Wang Y. (2016).120, 335–348 The effects of using reclaimed asphalt pavements (RAP) on the long-term performance of asphalt concrete overlays/ Construction and Building Materials

[7] Xiao, F., Su, N., Yao, S., Amirkhanian, S.N., & Wang, J. (2019). Performance grades, environmental and economic investigations of reclaimed asphalt pavement materials. Journal of Cleaner Production. https://doi.org/10.1016/j.jclepro.2018.11.126

[8] Ayad Subhy 156 (2017) 28–45 Advanced analytical techniques in fatigue and rutting related characterizations of modified bitumen: Literature review /Construction and Building Materials.

[9] Sharp, K, Ralston, K, Bogumil, K, Asadi, H & Latter, L (2017), Review of future pavement technologies, WARRIP project no. 2016-006, Main Roads Western Australia, June.

[10] Gurü, M., Çubuk, M., Arslan, D., Farzanian, S., & Bilici I. (2014). An approach to the usage of polyethylene terephthalate (PET) waste as roadway pavement material, Journal of Hazardous Materials, vol. 279, pp. 302-10. DOI: 10.1016/j.jhazmat.2014.07.018

[11] Rahman, M.T., Mohajerani, A., Giustozzi, F. (2020). Recycling of waste materials for asphalt concrete and bitumen: a review. Materials 13 (7), 1495. https://doi.org/10.3390/ ma13071495.

[12] Leng, Z., Sreeram, A., Padhan, R.K., & Tan, Z. (2018). Value-added application of waste PET based additives in bituminous mixtures containing high percentage of reclaimed asphalt pavement (RAP). Journal of Cleaner Production. https://doi.org/10.1016/j.jclepro.2018.06.119

[13] White, G. (2019). Evaluating recycled waste plastic modification and extension of bituminous binder for asphalt', Proceedings 18th Annual International Conference on Pavement Engineering, Asphalt Technology and Infrastructure, Liverpool, United Kingdom.

[14] Ponnada, S., &Vamsi Krishna, K. (2020). Experimental investigation on modification of rheological parameters of bitumen by using waste plastic bottles. Materials Today: Proceedings. doi: 10.1016/j.matpr.2020.03.243

[15] Chin, C., Damen, P. (2019). AP-T351-19 Viability of Using Recycled Plastics in Asphalt and Sprayed Sealing Applications. 2019 52.

[16] Advancing Sustainable Materials Management: (2016 and 2017) Tables and Figures EPA, Assessing Trends in Material Generation, Recycling, Composting, Combustion with Energy Recovery and Landfilling in the United States November 2019.

[17] Vargas, C. A., & El Hanandeh, A. (2020). Systematic literature review, meta-analysis and artificial neural network modelling of plastic waste addition to bitumen. Journal of Cleaner Production, 124369. doi: 10.1016/j.jclepro.2020.124369

[18] Imran M. Khan et al. 145 (2016) 1557 – 1564 Asphalt Design using Recycled Plastic and Crumb-rubber Waste for Sustainable Pavement Construction Procedia Engineering

[19] Jassim, H., & Mahmood, O. T., & Ahmed, S. (2014). Optimum Use of Plastic Waste to Enhance the Marshall Properties and Moisture Resistance of Hot Mix Asphalt. 7. 18-25. Volume 7 Number 1.

[20] Delorme J.L., C. La Roche, L. Wendling. (2007). LPC Manual for the formulation of asphalt mixes], Groupe de travail RST, Formulation des enrobés, Paris, Laboratoire des Ponts et Chaussées.

[21] Technique et méthode des laboratoires des ponts et chaussées: Catalogue des dégradations de surface des chaussées, (V 1998) – Méthode d'essai N° 52 Laboratoire central des ponts et chaussée (Paris)

[22] Hınıslıoglu, S. (2004). Use of waste high density polyethylene as bitumen modifier in asphalt concrete mix. Materials Letters, 58(3-4), 267–271. doi:10.1016/s0167-577x (03)00458-0

[23] Hadi Goli, Manouchehr Latifi / 247 (2020) 118526 Evaluation of the effect of moisture on behaviour of warm mix asphalt (WMA) mixtures containing recycled asphalt pavement (RAP) Construction and Building Materials

[24] González A., J. Norambuena-Contreras, L. Storey, E. Schlangen / 159 (2018) 164–174 Effect of RAP and fibers addition on asphalt mixtures with self-healing properties gained by microwave radiation heating. Construction and Building Materials

[25] Attaelmanan, M., Feng, C.P., Al, A.-H. (2011). Laboratory evaluation of HMA with high density polyethylene as a modifier. Constr. Build. Mater 5, 2764e2770.

[26] Lastra-González, P., Calzada-Pérez, M. A., Castro-Fresno, D., Vega-Zamanillo, Á., & Indacoechea-Vega, I. (2016). Comparative analysis of the performance of asphalt concretes modified by dry way with polymeric waste. Construction and Building Materials, 112, 1133–1140. doi: 10.1016/j.conbuildmat.2016.02.156

[27] Slebi-Acevedo, C. J., Lastra-González, P., Pascual-Muñoz, P., & Castro-Fresno, D. (2019). Mechanical performance of fibers in hot mix asphalt: A review. Construction and Building Materials, 200, 756 –769. doi: 10.1016/j.conbuildmat. 2018.12.

[28] Modarres, A., & Hamedi, H. (2014). Effect of waste plastic bottles on the stiffness and fatigue properties of modified asphalt mixes. Materials & Design, 61, 8–15.doi: 10.1016/j.matdes.2014.04.046

DOI: 10.2478/sspjce-2023-0018

Reuse of Wastewater and Hydrogeneration: Sustainable Land Division Project

Jorge Cardoso-Gonçalves [1*], Samuel Gonçalves [2]

[1]Ph.D. degree in Civil Engineering, Engineering Consultant
[2]Master degree in Architecture, Summary Architecture
*e-mail: jjtc.goncalves@gmail.com

Abstract

The present case study - Sustainable Cerrado Subdivision Project in Arouca (Portugal) - proposes the implementation of a design solution that promotes 'sustainable neighborhoods', expanding the concept of 'sustainable homes'. This type of project results from the application of established construction methodologies and innovative solutions, aiming to meet society's needs with the least possible mobilization of resources (natural, energy, and financial), considering water and energy efficiency as central elements. More specifically, the goal is to reduce the inflows into public wastewater and stormwater drainage systems by changing the consumption habits of the population and collecting rainwater in impermeable areas, as well as treating greywater for non-potable reuse. In water supply systems, there is potential for energy production through microturbines that can harness the energy required for pressure control - hydrogeneration.

Keywords: hydrogeneration, reuse, sustainability, circularity, innovation

1 Introduction

1.1 Initial Considerations

The design of resilient buildings and infrastructures, given the established context and the challenges that arise, requires the application of methods and constructive techniques consolidated by the scientific community, together with the study, development, and application of innovative solutions, which make it possible to respond to the needs of the society with the least mobilization of resources (natural, energy, financial).

The Sustainable Subdivision of Cerrado is a public project that aims to respond to the shortage of supply that is currently felt in the housing market in the municipality of Arouca – a problem that extends to a large part of the Portuguese territory. This project aims to be a reference in terms of environmental sustainability, considering water and energy efficiency as a central element, namely through the implementation of a Rainwater and Greywater Harvesting System (SAAPC) and a Hydrogeneration System (energy production with microturbine associated with the water supply system) [1, 2].

Concerning hydrogeneration, it is intended to use a high-level water supply pipeline for the installation of this system and, simultaneously, make it visible, allowing any inhabitant or passer-by to realize in real time, through an interactive panel, the amount of energy that is being produced, its destination and the economic savings associated with it.

In this project, the solutions for efficient performance of houses (e.g., thermal insulation, cross ventilation, promotion of natural lighting) have relevance. However, the solutions associated with the two systems presented here will have an unquestionably higher ecological impact. On the one hand, because they work on the scale of the territory and not on the scale of housing or, in other words, more than promoting the principle of 'sustainable houses', they promote 'sustainable neighborhoods'. On the other hand, because these systems are not dependent on the individual management of each resident, which facilitates the maintenance and constant monitoring of the overall solution by the municipality [1].

The proposal for this circular management system for building hydraulic installations, applied to the present case study, aims to develop a resilient solution (economically viable, environmentally sustainable, technologically innovative). The decrease in the tributaries flowing to the public wastewater and rainwater drainage systems, the decrease in the drinking water consumption, and the production of 'clean energy' are referred to as contributions of this project to global sustainability [1].

2 Framework

2.1 Sustainable Use of Water

The need for efficient use of water is referred to as an environmental imperative, which involves raising citizens' awareness of resource scarcity and rationalizing consumption, replacing equipment and other alternatives [3]. The sustainability of water resources is intrinsically related to the use of drinking water. The decrease in drinking water consumption is a need to guarantee the quality and quantity of this resource for future generations. Rainwater harvesting and greywater reuse systems are referred to as a strategy for reducing drinking water consumption [4].

Compliance with the design of efficient use of the water resource, reducing the consumption of drinking water, is related to the change in the consumption habits of the populations, with the installation of efficient equipment and with alternatives to drinking water supply (e.g., use of rainwater, reuse of greywater). The potential advantages of these strategies are identified by [4] as follows: reduction of charges for drinking water consumption; reduction of the cost of drinking water and wastewater treatment infrastructures; future reduction of the capacity and costs of installing and maintaining water supply and wastewater drainage infrastructures.

2.2 Framework – Rainwater and Greywater Harvesting System

The harvesting of rainwater is one solution to increase water efficiency in buildings, being residential, commercial, or industrial [5]. Rainwater harvesting systems are characterized by water removal from waterproofed areas (e.g., roofs, terraces), through filtration and discharge into a reservoir, from which the water can be used in the various building equipment [6].

Advantages of this type of system are the high variety of rainwater harvesting systems, easy application and adaptability, saving water from the public water supply system, and relative speed of investment amortization [7].

Reusing greywater can reduce the consumption of drinking water and the overload of public wastewater drainage systems (collection and treatment infrastructures). However, there are some challenges with the implementation of this practice: acceptance by the population, cost, security, and reliability of the system; necessary information to validate and support the solutions to be implemented [8].

The quantity and quality of greywater produced in single-family homes reveals that they should not be seen as waste and can be used for non-potable purposes. The use of these waters in situ (e.g., floor washing, flushing) should be deemed, considering that the use of high-quality water is avoided for purposes where the water is not required to be drinkable [9]. Apart from the variations associated with the standard of living of the inhabitants and the water efficiencies of the different equipment of the buildings, domestic consumption is estimated at 100 L/inhab/day and the production of greywater at about 70L/inhab/day. It refers to the potential for reuse of approximately 48 L/inhab/day. For example, toilet bowls cleaning represents a value between 25 to 35 L/inhab/day of the referred reuse potential [10].

2.3 Framework - Hydrogeneration System

Water supply systems are referred to as hydraulic infrastructures that have a potential for energy production. Energy production systems associated with water supply (hydrogeneration) may serve the public electricity grid or self-consumption [11].

The production of electricity in water supply systems could be an interesting path towards innovation. In system locations where energy needs to be dissipated to control service pressures, turbomachinery can be installed to recover the energy that would be dissipated with traditional solutions (e.g., pressure reducing valves) [8]. In pipeline systems, which ensure the supply of high-level water, it is highlighted that a significant part of the components of the electricity generation system already exists, requiring only its adaptation, without compromising its initial function [12].

3 Case Study

3.1 Sustainable Plot of Cerrado Project

The intervention site is located south of the center of the village of Arouca. The property has a total area of about 37 000 m^2 and is currently occupied, essentially, by mountains and agricultural areas. The landscape has a very sharp altitude variation, from a height of 410.50 in the west to 430.00 in the east. The ecologically responsible attitude, deepened here in terms of the use of rainwater and greywater and the hydrogeneration system, is also reflected in other aspects of the project, namely:

- the modelling of the landscape (respecting the existing topographic conditions and reducing the movements of land and the sealing of the soil to the minimum necessary.

- promotion of smooth forms of locomotion, in particular, by including a bike path.
- phasing of the intervention (3 phases), that is, the subdivision operation progresses as the plots are sold and occupied, avoiding the anticipation of the intervention and, consequently, the excessive use of resources associated with this work.

Figure 1 shows the Sustainable Plot of Cerrado Project.

Figure 1: Cerrado Subdivision Project (source: Project of Summary architecture)

The project includes the implantation of 25 plots (corresponding to the 25 houses, with 4 typological variations, from T1 to T3) with different settings, with a design that follows the agricultural and cadastral composition existing on that location, instead of geometric guidelines. Accordingly, the proposed limits for the plots correspond, in many cases, to irrigation lines, changes in elevation levels, and the boundaries of old agricultural tracks. The proposal takes advantage of the existing road infrastructures (which face the land), in addition to proposing a new infrastructure, which crosses the subdivision in the east-west direction [1]. This new strip will allow to create and consolidate a new housing nucleus, being inserted in an interior area of the land. The more intimate character of this new road may help to differentiate it in terms of uses, since it is limited by relatively low walls, loads of vegetation, and single-family houses. This new road and pedestrian infrastructure are expected to have a more welcoming character, essential to the well-being of the inhabitants. A new north-south section is also planned, linking the existing infrastructure at the southern limit of the land to the proposed infrastructure. This section will serve exclusively pedestrians and cyclists, proposing an integrated bike path [1].

The general implementation of this subdivision, proposed for a place considered "urban" under the master plan (PDM) of Arouca, presents a clear concern with the provision of green areas for the enjoyment of the inhabitants, going far beyond the regulatory requirements. About 50% of private spaces are assigned to unpaved areas (without any legal obligation at this level) and we have about 6000m^2 of green, unpaved areas for collective use, whereas in regulatory terms only

700m^2 would be required (Ordinance No. 216-B/2008 of March 3, Table I) [1]. This is intended to promote the implementation of small vegetable gardens, promoting organic farming practices. It also seeks to improve the living conditions and the climatic behavior of the area (which ultimately translates into the greater energy efficiency of housing), protecting the area from the "heat island effect " that affects many urban areas [13].

While contributing to the well-being of the inhabitants and sets up an ecologically responsible approach, this proposal also requires a significant amount of water for the irrigation of all these green areas, hence the focus given to water management issues in this subdivision.

3.2 Rainwater and Greywater Harvesting System

The SAAPC, conceptually addressed in this report, intends to set up a strategy to reduce the consumption of drinking water in Cerrado Subdivision, through the use and treatment (e.g., phytoremediation filter) of rainwater, collected in waterproofed areas and grey wastewater, produced in the building [1]. The proposed solution makes it possible to contribute to the environmental sustainability of the project by reducing inflows to the public rainwater and wastewater drainage systems, as well as the reduction of drinking water consumption.

The use of rainwater and the reuse of grey water requires the appropriate treatment of the water according to the purpose for which it is intended. It is recommended that rainwater utilization systems (SAAP) and building greywater reuse systems (SPRAC) be used on sites that have enough physical space for all the necessary equipment, with adequate non-potable water consumption for the use of the utilized and regenerated water. Utilization of the reclaimed and regenerated water, and which have properly trained operation and maintenance teams [13].

Supplying building systems with rainwater and greywater for uses that do not require drinking water may be relevant from a standpoint of water preservation. The treatment of rainwater and grey wastewater can be carried out by mechanical means or through natural processes (e.g., biological treatment through phytoremediation filters).

Regarding the operation of the SAAPC, the process of using rainwater and greywater should include the following main steps: collection of rainwater and greywater; conduction of collected water to the treatment system; rainwater and greywater treatment through phytoremediation; distribution of treated water to non-potable water consumption points. Figure 2 schematically represents the circularity of the proposed system [1].

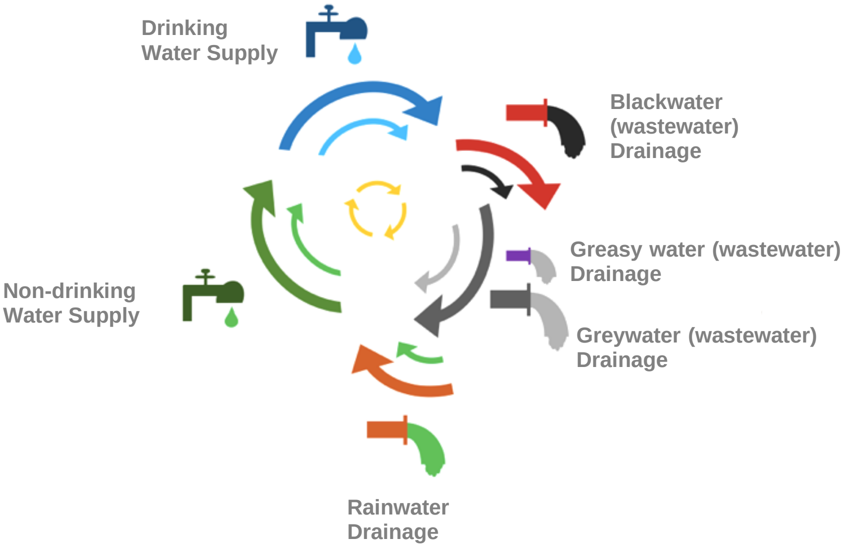

Figure 2: Schematic representation of the circularity of the SAAPC

The building rainwater drainage system collects the precipitated water in waterproofed areas, leading them to the phytoremediation filter. This system must have a connection to the public rainwater drainage infrastructure, which will come into operation whenever the filter treatment or storage capacity of the treated non-potable water reservoir is exceeded.

The building greasy water drainage system, if necessary, will consist of wastewater collection elements with corresponding characteristics (e.g., sinks), which will lead to a grease separation system. Subsequently, these waters will be led to the greywater drainage system.

The building greywater drainage system collects the wastewater drained by equipment that produces effluents with these characteristics (e.g., washbasins, bidets), as well as the effluent from the grease separation system. Greywater is driven into a septic tank, where pretreatment takes place. Subsequently, the effluent from the septic tank enters the phytoremediation filter. This system must have a connection to the public rainwater drainage infrastructure, which will come into operation whenever the filter treatment or storage capacity of the treated non-potable water reservoir is exceeded. The connection will be made by connecting to the building collector that drains the effluent from the blackwater drainage system.

The building blackwater drainage system collects the wastewater drained by equipment that produces effluents with these characteristics (e.g., toilet bowls), draining directly into the public wastewater drainage infrastructure [1].

The phytoremediation filter receives effluents from the building rainwater and greywater drainage systems, starting the process of cleaning rainwater and greywater, through the action of selected plant species, physical (e.g., sedimentation), chemical (e.g., ultraviolet radiation, precipitation), and biological (e.g., microbiological decomposition, assimilation by plants) processes.

The non-potable water distribution system will be supplied, through a pressurization system, from the regenerated water reservoir. Devices for the use of non-potable water [1] (which, in addition to the external water points used in the irrigation system, may also include toilet bowls, washing machines, and taps for cleaning) must be properly identified with appropriate signage clarifying that this is non-potable water. In the case of defective functioning, interruption, or deactivation of the SAAPC, the system will be able to work by collecting raw water, with storage in the buried reservoir, and subsequent pressurization to the non-potable water distribution system. The autonomous collection promotes, nevertheless, efficient use of water, by reducing the consumption of drinking water in devices that do not require it [1].

The drinking water distribution system is fed by the public water supply infrastructure and supplies water to devices that require higher quality (drinking) water (e.g., washbasins, bathtubs/showers, kitchen equipment). There is the possibility of feeding the non-potable water distribution system from this network, emphasizing the obligation to guarantee that the systems are not connected, with the flow only being able to occur from the drinking water system to the non-drinking water system, not the other way round [1].

Given the relationship between water and energy, reducing water consumption in the construction cycle is also reflected in significant energy efficiency, given the inherent reduction in energy consumption needed to heat domestic hot water and pressurize water. These energy savings are also reflected in public systems, reducing the volumes to be abstracted and the flows of water and wastewater to be pumped and treated [8].

The conceptual development of this system for the use and reuse of wastewater, as well as the valorization of available raw water sources, promotes the optimization of drinking water consumption, directing it to the strictly necessary uses. The choice of equipment with lower water consumption is also one of the points to be considered in the development of the execution project.

3.3 Hydrogeneration System

The proper functioning of the supply systems is associated with different factors, related to the design of the system, the state of preservation of the systems, their operation, among others. Pressure control is identified as one of the components of relevance, namely for the control of water losses. Pressure control is usually carried out using pressure reducing valves, which induce a loss of energy in the flow, controlling the pressure. The conceptual proposal of the hydrogeneration system points towards the use of runoff energy, which is necessary to dissipate to control the pressure in the public water supply, to produce electricity. The use of this energy will be possible through microturbines, to be installed in the water supply pipes.

The electric energy produced in the water supply systems, depending on the production regime, the associated power, and the total energy produced, may be used for different purposes, namely self-consumption, or supply to the national electricity grid. In the case of the Hydrogeneration Project of the Cerrado Subdivision, it is suggested to analyze the possibility of using the energy from the runoff associated with the high-level supply pipeline to the municipality of Arouca, under the responsibility of Águas do Douro e Paiva, S. A. (AdDP), whose layout partly develops on the road next to the subdivision [1].

The implementation of a hydrogeneration system could be achieved by installing a 'by-pass' to this pipeline of the Arouca Water Supply System, causing the flow to pass through a turbine, which would introduce a pressure drop in the flow, compatible with the appropriate operating pressures of this pipeline, converting the dissipated energy into electrical energy, according to the schematic representation of Figure 3 [1].

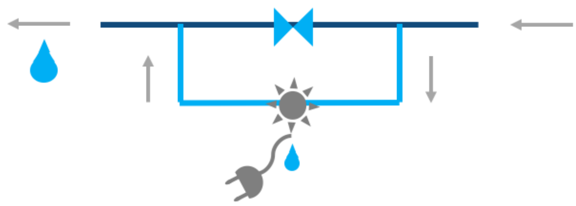

Figure 3: Schematic representation of the hydrogeneration system

It should be stressed that the proposed solution must be linked with the managing entity (ME) of the pipeline (AdDP) to ensure that the installation of the hydrogeneration system benefits the operation of the infrastructure, namely in the pressures control. The system under analysis may supply some equipment that the ME deems to be relevant (e.g., flow meter). It's worth mentioning that this system does not imply any consumption of water, but only a change in the water path.

The production of energy associated with water supply will also have a pedagogical point of view, proposing this innovative solution to be associated with a visual and promotional character through an information panel accessible to the public. With this tool, it would be possible to consult the energy produced at any time, the energy produced in previous periods, the energy used for different purposes, and also the water reused by the SAAPC, what can be an incentive for the public to enforce these types of systems.

According to the flow data provided by the ME of the pipeline and with the support of a specialized company (INSITU-Consultores), a pre-dimensioning of the energy production equipment to be installed was carried out. Taking into account the available flow and pressure regimes and the operating conditions to be ensured in the pipeline, it is estimated an annual production of electricity of around 30 MWh, with an investment of less than €25,000, and a payback period that should be between 6 and 7 years [1].

4 Final Remarks

4.1 Discussion

The basic options of the Sustainable Plot of Cerrado Project within the architectural scope can have a direct influence on the water management solutions to be implemented. In this case study, choosing a dispersed layout of the building, promoting green spaces and large areas of permeable soil, motivated the search for solutions for the use and reuse of greywater and rainwater. The symbiosis between architecture and environmental sustainability may benefit the preservation of resources, the adequate occupation of the territory, and the quality of life [1].

The implementation of the hydrogeneration system constitutes a careful use of the resources available on site. The fact that this subdivision is served by a road, which would inevitably be intervened, where a pipeline of the Arouca water supply system is installed, motivated the design of the hydrogeneration system, in a perspective of circularity and compensation – if the work to be carried out will necessarily involve the consumption of energy (in its construction and its use), every effort must be made to counterbalance this consumption with new forms of production. Hydrogeneration arises here not as an alternative means of energy production, but rather complementing others (such as energy production from solar radiation), taking advantage of a specific pre-existence of the area to be intervened.

The use of rainwater and greywater for uses that do not require drinking water is a contribution of the Cerrado Subdivision to the sustainable use of water. The preservation of this resource can be fostered by reducing the consumption of drinking water, reducing the volume of wastewater discharged into the public wastewater drainage infrastructure, and damping the flood flows tributaries to the rainwater drainage infrastructure [1].

5 Conclusion and Future Development

The development of innovative, economically viable, and potentially replicable solutions is an important contribution to the design of sustainable buildings that promote efficient use of resources. The educational character of this project (dissemination of environmentally interesting solutions), as well as the potential scientific and academic interest of proposed solutions (hydrogeneration, phytoremediation, use of rainwater and greywater), are factors that can make the Cerrado Subdivision an example of crafts conciliation.

As a note for future developments, reference is made to the investigation of hydrogeneration systems and built SAAPC, systematizing their main characteristics, benefits, and weaknesses. The adaptation of stabilized solutions and developing innovative solutions is also highlighted as an important development to be carried out. Within the scope of the execution project of the Sustainable Plot of Cerrado, the characteristics of the various components of the system should be specified.

According to the estimates, about half of the water used for domestic purposes may be non-potable (regenerated or autonomous collection), which shows the potential of the thorough study of the implementation of the SAAPC. In the case of the energy produced by the hydrogeneration system, it can be directed to the equipment of the subdivision, reducing the energy supplied by the public grid. It is therefore suggested the study of consumption (water and electricity) to be detailed in the case of the subdivision, according to the construction typologies and the expected occupation, to estimate the environmental and economic benefits of this project, in global terms and also for the future residents of the subdivision (e.g., reduction of drinking water consumption in each plot and common spaces; reduction of the electricity bill for lighting).

References

[1] Cardoso-Gonçalves, J. & Gonçalves, S. (2020). Reutilização de Águas Residuais e Hidrogeração. Projeto de Loteamento Sustentável, In XI Congresso Ibérico de Gestão e Planeamento da Água da Fundación Nueva Cultura del Agua.

[2] Silva-Afonso, A. & Pimentel-Rodrigues, C. (2017). Manual de Eficiência Hídrica em Edifícios. ANQIP.

[3] Rossa, S.R.L.G.S. (2006). Contribuições para um Uso mais Eficiente da Água no Ciclo Urbano. Poupança de água e reutilização de águas cinzentas. Dissertação de Mestrado, Faculdade de Engenharia da Universidade do Porto.

[4] Santos, D., Moreira, M. & Almeida, A.B., (2011). Avaliação do risco da degradação da qualidade da água em sistemas públicos de abastecimento. 6o Congresso Luso-Moçambicano de Engenharia.

[5] Sacadura, F.O.M.O. (2011). Analysis of rainwater harvesting systems in buildings. Master's Dissertation in Civil Engineering, Faculdade de Ciências e Tecnologia, Universidade Nova de Lisboa.

[6] Sousa, F.A.B. (2017). Energy Production in Water Distribution Systems – Decentralised Production. Master's Dissertation, Faculdade de Engenharia da Universidade do Porto.

[7] Verdade, J.H.O. (2008). Rainwater Harvesting and Reuse of Grey Water. Master's Dissertation, Faculdade de Engenharia da Universidade do Porto.

[8] Soares, F.M.R.C.G. (2012). Contribution to the Assessment of the Possibility of Reusing Greywater. Master's Dissertation in Environmental Engineering, Faculdade de Ciências e Tecnologia, Universidade Nova de Lisboa.

[9] Coutinho, A.C.R.A.M. (2009). Water reuse. Use of greywater in situ. Ph.D. Thesis in Engineering Sciences – Civil Engineering, Universidade de Trás-os-Montes e Alto Douro.

[10] Valente-Neves, M. & Silva-Afonso, A. (2010). Technical Specifications for the Use of Rainwater and Grey Water in Buildings. 5th Hydraulics, Water Resources, and Environment Conferences, FEUP, ISBN 978-989-95557-4-7.

[11] Samora, I., Manso, P., Franca, M.J., Schleiss, A.J. & Ramos, H.M. (2016). Energy Recovery Using Micro-Hydropower Technology in Water Supply Systems: The Case Study of the City of Fribourg. Water 2016, 8, 344 (www.mdpi.com/journal/water).

[12] Piqueiro and Cardoso-Gonçalves (2018). Hydrogeneration. Decentralised energy production in the operation and control of water supply systems. 14th Water Congress, March 7, 8, and 9, 2018, Évora.

[13] Menezes, G.O., Gonçalves, A., Ribeiro A.C. & Feliciano, M. (2017). Analysis of the Urban Heat-Island Effect in the City of Bragança. 3rd Ibero-American Congress of Entrepreneurship, Energy, Environment and Technology, July 12 to 14, 2017, Bragança.

DOI: 10.2478/sspjce-2023-0019

Soil Erosion Estimation of Wadi Medjerda in Algeria Using the Revised Universal Soil Loss Equation (RUSLE) through GIS

Karima Allaoui [1*], Rachid Mansouri [1], Meriem Dorbani [1]

[1] University of 08 May 1945 Guelma, Algeria, Science and Technology Faculty, Department of Civil Engineering and Hydraulics
*e-mail: allaoui.karima@univ-guelma.dz

Abstract

Water erosion is a major problem in the semi-arid environments of Algeria. In this vein, the objective of this study is to use the Revised Universal Soil Loss Equation (RUSLE) on the watershed of Medjerda which is located at the extreme of the North-Eastern part of the Algerian territory. Based on the crossing of various factors in raster mode under ArcGIS allows the production of diverse thematic maps corresponding to multiple factors: erosivity of precipitations, erodibility of soils, topography, the vegetal cover and the anti-erosive practices. Moreover, the risks' map of water soil erosion was obtained depending on the combination of the previous thematic maps with four class risks has been made up indicating an average erosion value of 2.68 t/ha/year. However, this value is relatively reasonable in relation to the given rate by the interpretation of the bathymetric measures carried out in the Ain Dalia dam.

Keywords: watershed, Medjerda, Dam Ain Dalia, SIG, RUSLE, erosion

1 Introduction

Algeria is subjected to a noticeable process of agricultural and altered lands erosion and substantially eroded during periods of high rainfall intensities. As a result, this process leads to the evident increase in solid transport and its corollary the increasing siltation of dams. In the light of several research, the erosion of soil is proved as a serious threat to the environment in different parts of the globe and one of the most serious problems of land degradation [1] caused by the removal, transport, and soil particles deposition [2]. Several natural and anthropogenic factors lead to the increase in soil degradation that promote the initiation and the evolution of erosion processes. The already mentioned factors are divided into two categories; those of a relatively semi-static nature (morphology, erodibility, and infiltration, etc.) and others which vary timely such as vegetal cover, land use, the intensity of rainfall and agricultural practices [3, 4, 5].

However, the impact of the associated action of these factors is manifested by an increase in the amount of materials lost, deposited downstream in stream beds, reservoir dams, lakes and sedimentation areas [6]. Since the 1950s, the problem of solid transport and the extent of the phenomenon of siltation of dams have caught the interest of many researchers. Many explanatory models of solid transport on the basis of parameters such as GIS models are since widely used to derive the necessary variables to estimate soil erosion, determine soil conservation measures and allow analysis of huge data on arid and semi-arid views. Based on an objective, spatial and comparative attitudes, the evaluation, and quantification of erosion processes is an essential step in order to propose methods of rational management of natural resources (water, soil, vegetation) for reducing the adverse effects of erosion processes.

Our study reveals that several approaches have been used to diagnose and analyze the loss of land, among these the Universal Soil Loss Equation (USLE) [7], and the RUSLE 2 which is its ameliorated version [8]. The model of RUSLE has been widely used by hydrologists all over the globe to estimate the erosion of soils according to the GIS and remote sensing environments [9-14]. Thus, the present article takes into account the use of the RUSLE approach for discovering soil loss and highlighting zones that are exposed to the risk of water erosion in the watershed of Wadi Medjerda, which could contribute to the creation of a tool to support decision-making and intervention in the development of this region.

2 The Area of Study

Concerning the sub-watershed trans boundary of Medjerda (Figure 1), it is considered as one of the five sub-basins that make up the great basin of Medjerda-Mellegue, the latter is located at the extreme of the North -Eastern part of the Algerian territory with 1438 km^2 area and with 276.30 km perimeter. According to Hydrographics Basins Agency (ABH), the sub-basin of interest carries the code [12 01].

The area of study is situated in the territory of the Souk-Ahras state between the meridians 7°37'E and 8°25' and the North parallels 36°05' and 36°27'. However, it is bordered in the North by the basin of the Eastern coast of Constantine, in the East by Tunisia, in the West by the basin of Seybouse and in the South by the sub basins of Mellegue upstream [12 04] and Mellegue downstream [12 05].

In effect, the Medjerda Basin is drained by the Medjerda wadi and its tributaries supplying the Ain Dalia Dam, whose water is directed to supply drinking water to Souk-Ahras town and other towns. The study area is dominated by a semi-arid climate where the average annual rainfall is between 327 mm and 723 mm, with an average of 557 mm/year.

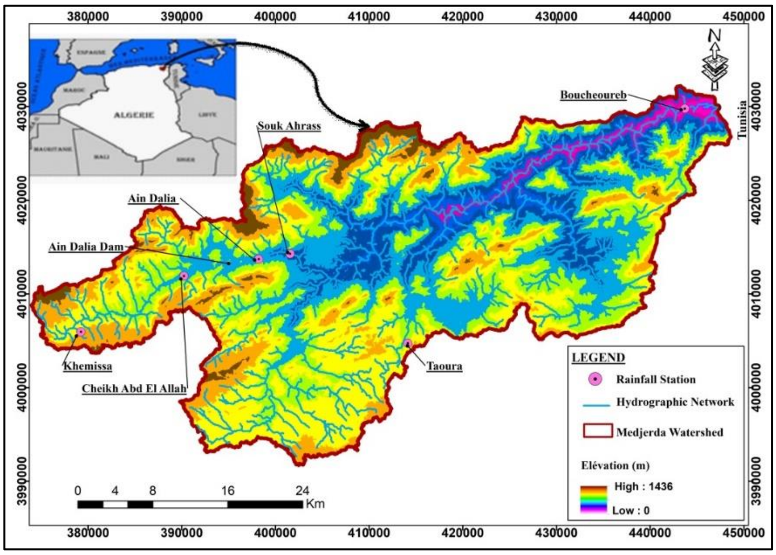

Figure 1: Geographic situation of the area of study

3 Methods

The examination of various parameters involved in erosive processes and their spatialization in thematic maps depends on the application of the RUSLE model. The use of GIS techniques for the evolution of every RUSLE factor leads to their superposition and processing. The main purpose for designing such a model is to estimate annual rates of erosion in agricultural areas for the long-term. According to [15], the equation is widely used for its simplicity and reliability in spite of the several flaws and limitations that it has. However, it also represents a standardized approach. The empirical basic equation of the RUSLE model is the Universal Soil Loss Equation which is given below:

$$A = R.K.Ls.C.P \tag{1}$$

where: A is the Average soil loss (annual); R is the erosion factor of precipitation; K is erosion factor of soil; Ls is topographic factor; C is exploitation factor of cover; P is Anti-erosive practices.

Each individual GIS file that is related to RUSLE has been built for each one and combined on a modulization process of ArcGis on cell by cell 10.4 (30 m resolution) in order to predict soil loss in a spatial approach [16]. All layers have been projected with UTM 32N using datum WGS 1984.

3.1 Model Factors

3.1.1 Erosion Factor of Rainfall (*R*)

The erosion factor of precipitation R is a climatic factor that reflects the effect of rainfall intensity on soil erosion. According to the equation proposed by 17, its calculation requires the determination of the total rainfall kinetic energy E_c (mm.h^{-1}) and the peak rainfall intensity in 30-minute consecutive (J.m^{-2}.mm^{-1}). The process of destroying the soil particles is triggered by the energy of the raindrops while the runoff ensures their transport [5]. [17] present the formula of the R erosivity like follows:

$$R = M.Ec\ .I30 \tag{2}$$

where: M is the coefficient that depends on the system of measurement units; E_c is the intensity of kinetic energy in 30 minutes (I30) of raindrops for each storm.

In the present study, it is impossible to use the prior formula because of the shortage of data on the intensity of precipitation. However, it is a general fact for most watersheds goes through in Algeria. Reliable data about the precipitations are recorded at daily, monthly, and annual scales. For such a reason we prefer to use an alternative equation based on monthly and annual precipitation (Equation 3). This formula has been used by many researchers [6, 18, 19, 20, 21]:

$$logR = 1.74log \sum_{i=1}^{12} \frac{pi^2}{p} + 1.29 \tag{3}$$

where: P_i is the monthly precipitation (mm); P is the annual precipitation (mm).
The R factor is calculated using monthly and annual rainfall data for a period of 29 to 48 years collected from 6 rainfall stations have been provided by (ANRH) the National Agency of Hydraulic Resources (see Table 3).
The values obtained for the R factor over the entire watershed were interpolated using the Ordinary Kriging method in the GIS.

3.1.2 Soil Erosion Factor (*K*)

For Kumar and Gupta [22], the K-factor of soil erosion is a risk parameter that affects erosion processes through soil contribution measurement. Soils differ in terms of erosion resistance, texture, structure, harshness and the content of organic matter and soil moisture. Soil resistance is weaker when the soil is less deep, and it is stronger when the soil is deeper. However, the saturation of surface soil leads to the movement of particles on the slope even at very low values as indicated by Ryan [23]. In the present study, the global soil map, which is labeled the Global Soil Harmonization Database, HWSD is employed to identify the K-factor [24].
This latter offers a wealth of information on the parameters of soil around the world by estimating the productivity of potential land helping that allows for determining land and water boundaries and improving the land degradation risks' assessment, in particular the erosion of soil (Figure 2). The HWSD is a bow matrix database of 30 seconds that has more than 16.000 different units of soils' cartography; it combines the existing regional and national updates of data about soils all over the world. The earth's territory is covered by raster database that comprise of 21600 rows, 43200 columns with 221 million grid cells that are related to harmonized data on the characteristics of the soil. The K-factor (Table 1) has been calculated by the following formulas that are proposed and used by [9, 25, 26].

$$K_{USLE} = f_{csand} \cdot f_{orgc} \cdot f_{hisand} \tag{4}$$

where: f_{csand} is a parameter that diminishes the K indicator in the soils containing of coarse sand; $f_{cl\text{-}si}$ offers weak soil erosibility factors for soils that have strong silty clayish ratios; f_{orgc} decreases *K* values in soils that have organic carbon; f_{hisand} reduces the values of *K* in highly sandy soils.

$$f_{csand} = \left(0.2 + 0.3exp\left[-0.256\, m_s\left(1 - \frac{m_{silt}}{100}\right)\right]\right) \tag{5}$$

$$f_{cl-si} = \left(\frac{m_{silt}}{m_c + m_{silt}}\right)^{0.3} \tag{6}$$

$$f_{orgc} = \left(1 - \frac{0.25orgc}{orgc + \exp[3.72 - 2.95orgc]}\right) \tag{7}$$

$$f_{hisand} = \left(1 - \frac{0.7(1 - \frac{m_S}{100})}{\left(1 - \frac{m_S}{100}\right) + exp[-5.51 + 22.9(1 - \frac{m_S}{100})]}\right) \tag{8}$$

where: m_s is the percent (%) of sand (particles 0.05-2.00 mm in diameter), m_{silt} is the percent (%) of silt (particles 0.002-0.05 mm in diameter), mc is the percent (%) of clay (particles < 0.002 mm in diameter) and org *C* represents organic carbon's percent (%) in the layer.

Table 1: Estimation of *K*-Factor in the watershed of Medjerda

Soil sample	**m_s (san topsoil) %**	**m_{silt} (silt topsoil) %**	**m_c (clay topsoil) %**	**Orgc (oraganic carbon) %**	**f_{csand}**	**f_{cl-si}**	**f_{orgc}**	**f_{hisand}**	**K_{USLE}**	***K***
Xk	40	37	23	0.56	0.357	0.865	0.983	1.00	0.3040	0.0395
Bk	38	41	21	0.63	0.369	0.883	0.978	1.00	0.3186	0.0414
Be	42	36	22	1.00	0.351	0.867	0.921	1.00	0.2799	0.0364
Cmc	31	50	19	2.01	0.402	0.908	0.763	1.00	0.2783	0.0362

Xk: Calcic Xerosols, Bk: Calcic Cambisols, Be: Eutric Cambisols, Cmc: Calcaric Cambisols

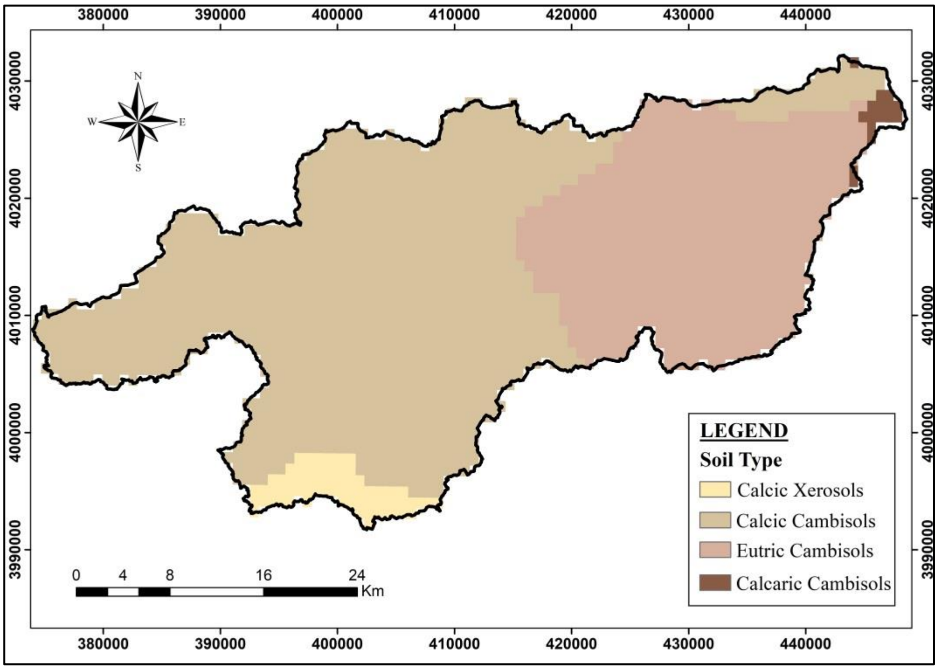

Figure 2: Study map of the types of soils within the watershed

3.1.3 Topographic Factor (*LS*)

The determination of the topographic factor *LS* in the study area is based on the use of the Digital Terrain Model and its derived maps.

On the basis of the Digital Elevation Model (DEM) of a resolution 30 m × 30 m (ASTER 2011) using Esri ArcMap 10.4, it is possible to obtain the map of the slope's degree (Figure 3), the direction and the cumulative length of the slope. The latter has a big influence since it offers its erosive energy to the water. This parameter is certainly the most important concerning erosion processes because of its gravitational action and its impact on detritic materials.

There are several ways for calculating the LS factor namely by using approximations in GIS from the flow accumulation map. Several steps, using the raster mode spatial analysis functions under GIS have been subsequently carried out.

- The first one is related to the establishment of a raster flow direction from each cell towards to its lower altitude neighbor.
- Determining the flow direction of the theoretical hydrographic network then makes it possible for calculating the length of the slope; at first for one cell and then for all cells.

The second phase deals with calculating the slopes in degrees for each cell. Depending on slopes, the value of the exponent m varies [17] as shown in Table 2.

Table 2: Meters variation as a slope function [17]

slope %	$S < 1$	$1 \leq S \leq 3$	$3 \leq S \leq 5$	$S \geq 5$
m	0.2	0.3	0.4	0.5

The last step is to cross the calculations of Li and S, the final result is then divided by 100. Finally, the LS factor is determined by the following formula:

$$LS = \left(Flow\ Accumulation\ .\frac{resolution}{22.13}\right)^m 0.065 + 0.045S + 0.0065S^2 \tag{9}$$

where the resolution is the cell size representing the grid (30 m) 22.13 is the standard cast field slope length; S is the slope.

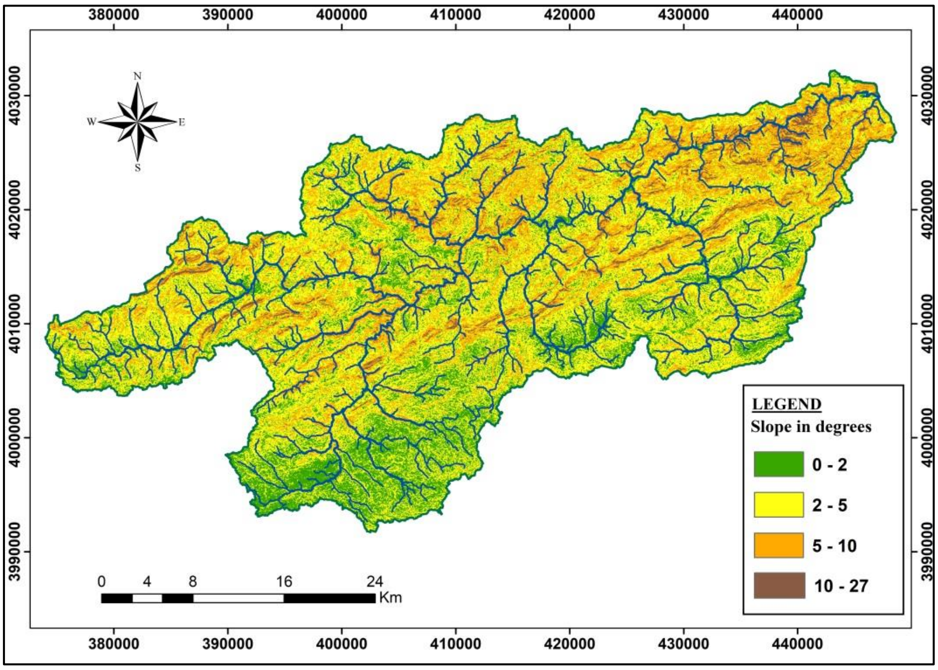

Figure 3: Slope map of the study area

3.1.4 Factor *C*

Kalman [21] advanced the view that vegetation plays a screen role that conditions the speed of surface runoff and reduces its erosion energy and intensity. For that reason, it is considered a pivotal factor in soil protection against erosion. In other words, this is the influence of the vegetal cover in the reduction of the erosion of soil [27].

The researchers have developed a lot of methods that estimate the factor *C* by using NDVI depending on the USGS website (http:// earth explorer.usgs.gov) for the evaluation of soil loss [28, 29]. In the above-shown study, the Normalized Difference Vegetation Index (NDVI) estimates the values of this parameter. The difference between the reflectance of the Red Band (R) and of the Near Infrared Band (NIB) of the electromagnetic spectrum is expressed by the mathematical formula (Equation 10). This indicator is linked to the vegetal nature and its own percentage. The land-use map was developed from a LandsatTM8 image taken on 27/3/2021 with a 30 m resolution, which was previously processed, using the index of vegetation normalized NDVI based on the colored compositions of the image bands (bands 4 and 5).

$$NDVI = \frac{\boldsymbol{NIB}-\mathbf{R}}{\boldsymbol{NIB}+\mathbf{R}} \tag{10}$$

where NIB: Near infrared band
A: Red band
The highest percentage of vegetal cover is reflected by the maximum value of NDVI. This means that zones that are void of vegetation (bare soil and water bodies) have a weak value of NDVI (Figure 4). [30] has used the following equation for calculating the C parameter:

$$C = 0.9167 - 1.1667\ (NDVI) \tag{11}$$

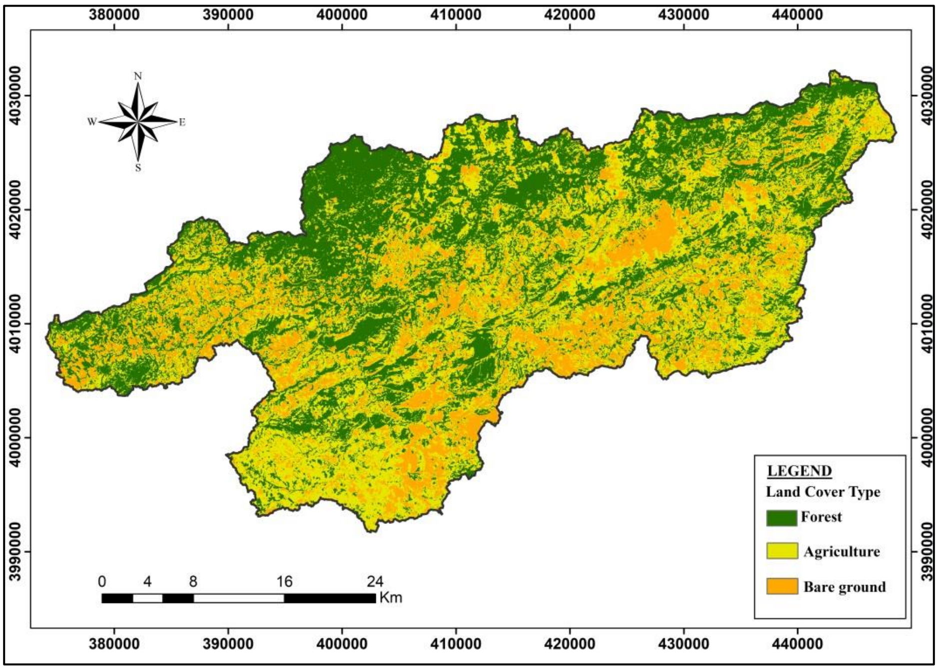

Figure 4: Map of vegetal cover type. (NDVI) data source

3.1.5 Factor of Anti-Erosive Practices *(P)*

The practices that are more efficient for soil conservation are cropping in curves, alternating bands or terraces, reafforestation berms, earthing and ridging that reduce the erosive effect of precipitation and runoff and hence reduce the quantity of the erosion of soil [31]. It varies from 1 for land on which none of the above practices are used to approximately 0.1 when in the case of low slope, partitioned timbering is practiced [32].
In the study area, anti-erosion schemes do not exist; cultivators never use anti-erosion cropping practices. Indeed, the crops are particularly cereal ones, and the plowings are rarely parallel to

the level of curves. In the absence of information on soil conservation practices, the *P* factor was assigned a value of 1.0 to the entire area of the watershed.

4 Results and Discussion

4.1 Factor *R*

By using the rainfall data of six rainfall stations, the factor *R* values for every station have been estimated. Subsequently, the values of factor *R* of the entire watershed have been interpolated using ordinary kriging interpolation in the GIS.
The spatial spreading of erosivity of rainfall in the Wadi Medjerda watershed shows that the values of factor *R* vary from 56 to 100 (MJ mm/ha/h/ year). These values of *R* that are above 56 (MJ mm/ha/h/ year) show that the entire watershed is exposed to a severe degree of climatic aggressiveness.
Based on precipitation characteristics, the values of factor *R* that are very low have been recorded in the North-East portion of the watershed and the ones that are very high have been recorded in the North-West and South-West portions. In accordance with Table 3 in excess of 70% of the area of study is exposed to heavy rainfall erosivity then it introduces the values of factor *R* that are superior to 56 (MJ mm/ha/h/ year) it is therefore concluded the basin's erosive power of precipitations is pivotal. The erosion intensity related to the amount and intensity of precipitations is increasing from the East of the watershed to the West with a slight decrease in the Western part of the region (Figure 5). The Wadi Medjerda watershed is prone to a high degree of climatic impact.

Table 3: Average annual precipitations and *R* - factor rates

Stations	**code**	**Data**		**Annual precipitation (mm)**	**Period (number of years)**	**Erosivity**
		X	**Y**			
Souk Ahrass	120101	967.25	342.25	564.9	1970-2018 (48 y)	80
Khemissa	120104	945.5	332.5	496.36	1970-2018 (48 y)	73
Taoura	120105	980.55	331.55	593.70	1972-2018 (46 y)	81
Cheikh AbdEllah	120113	956.55	339.25	640.5	1975-2018 (43 y)	90
Ain Dalia	120115	956.1	339.15	723.9	1989-2018 (29 y)	100
Boucheoureb	120116	1008.288	360.422	327.4	1999-2018 (19 y)	56

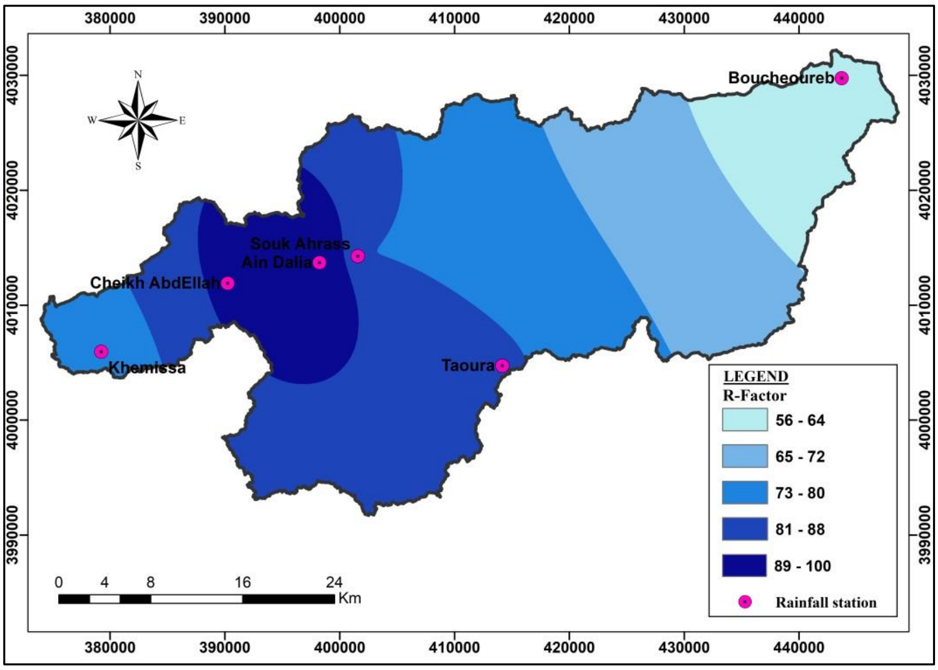

Figure 5: Map of the Rainfall Erosivity Factor *R*

4.2 Erodibility factor of Soil (*K*)

The watershed of Medjerda wadi includes four different soil types with different characteristics. The composite map of factor K has been generated to designate the spatial spreading of erosibility (Figure 6). The soil map has been reclassified with the assigned values of factor *K*. the values of factor *K* range from 0.0362 to 0.0414 t.ha.h/ha.MJ.mm. The highest values of factor K are related to soils highly vulnerable to erosion which are the Calcic Cambisols in this study; it is located in the greatest part of the North-West of the watershed.
The Soils of the area of study are considered as moderately sensitive to erosion with a moderate value of 0.0388 t.ha.h/ha.MJ.mm on the basis of [33] Resistance Classification related to Soils' Erosion which is based on the factor *K* (Table 4).

Table 4: Classification of Soil Resistance on Erosion by [33]

The Type of Soil	**Factor *K* (t.ha.h/ ha.MJ.mm)**
Very resisting soils to erosion	$K < 0.0132$
Soils fairly resistant to erosion	0.0132 – 0.0329
Soils moderately sensitive to erosion	0.0329– 0.0461
Soils fairly sensitive to erosion	0.0461 – 0.0593
Soils very sensitive to erosion	> 0.0593

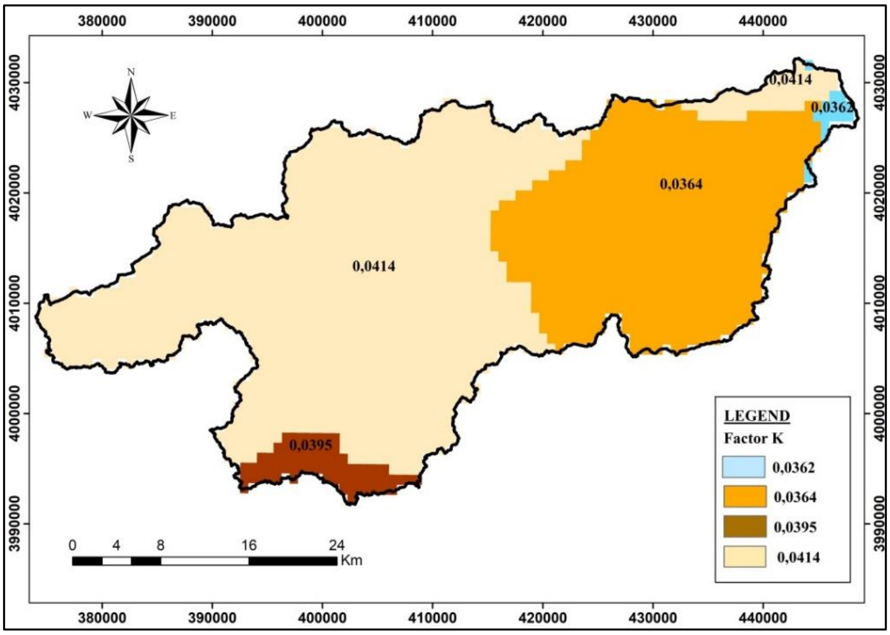

Figure 6: Spatial Distribution of soil Erosibility Factor *K* in (t.ha.h/ha.MJ.mm)

4.3 The Factor of Topography (*LS*)

Based on calculations, it is shown that the values *LS* range from 0 to 23.755 having 5.36 as an average (Figure 7). The obtained map has designated that the factor *LS* is directly related to the topography. The highest values take place primarily in mountainous areas of the high valley of the Wadi Medjerda watershed whereabouts the high and very high slopes prevail. This parameter presents a risk factor of erosion as a function of slope areas on the scale of the watershed. As the factor heightens, the watershed becomes more affected by erosion.

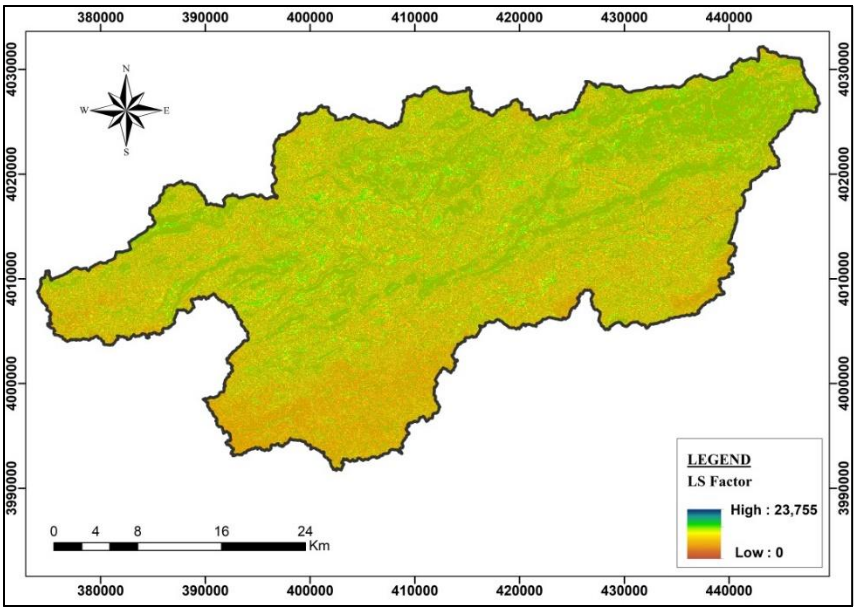

Figure 7: *LS* factor map of the study area

4.4 *C*-Factor

The surface cover of soil determines factor *C* through the vegetation and the height of plant strata a. In the database assigned to it, the values of factor *C* for each land use have been determined from the tables of [17, 34], it is between 0 and 1 for each type of vegetal cover in the area of study. Table 5 and Figure 8 show the vegetal cover distribution and the factor *C* values in the Wadi Medjerda watershed.

Areas with high vegetation are associated with the lowest values ($C < 0.24$) provide better soil protection and correspond to forest formations where human influence is low. The highest values ($C > 0.25$) correspond to soils with a higher susceptibility to erosion. These results have confirmed that bare grounds are more affected by erosion and soil loss while vegetative cover zones are highly resistant to this phenomenon.

Table 5: Distribution of the Factor *C* in the Wadi Medjerda Watershed

Type	***C*-Factor**
Water Plan	0
drill	0.24
Agriculture	0.45
Bare land	1

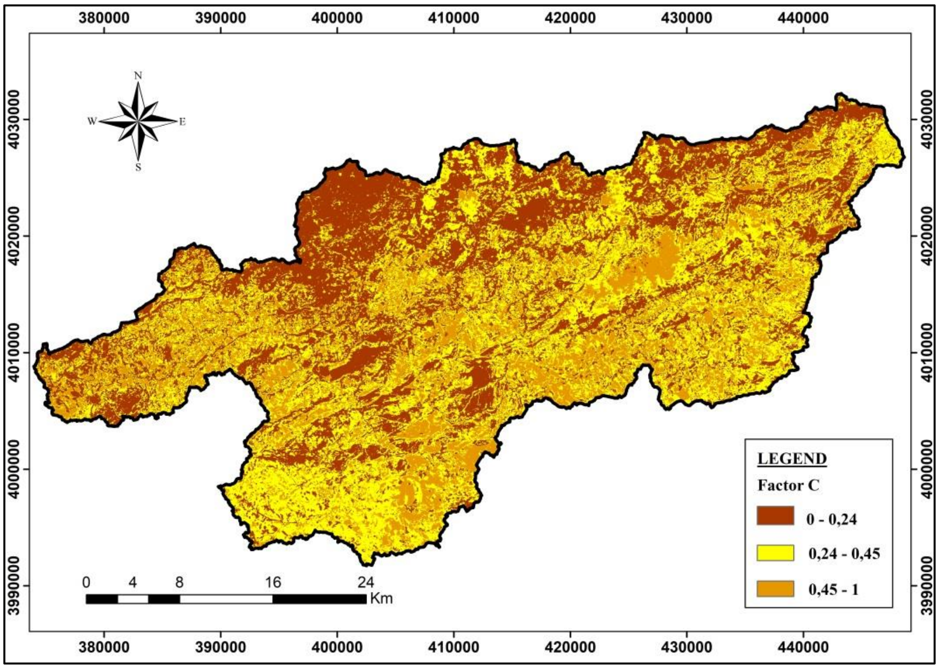

Figure 8: Spatial distribution of factor *C*

The Limitations of the study include the delay in adopting the bathymetry measures data the National Agency of Dams and Transfers (ANBT), as well as the monthly and annual rainfall data at the level of (ANRH) the National Agency of Hydraulic Resources, where the administrations were closed because of the Covid 19 (mid-March – mid-September 2020).

5 Estimated Potential Annual Soil Losses (*A*)

The goal of this article is to evaluate soil losses provoked by the erosive phenomenon and to delineate areas possibly delicate to the erosion of water in the Wadi Medjerda watershed by applying the RUSLE empirical model of soil erosion integrated in GIS to identify critical areas. The evaluation of soil losses due to water erosion obtained by the crossing of factors in raster mode under ArcGIS and the multiplication of layers introduced by the parameters and thematic maps of RUSLE, in particular, the climatic aggressiveness *R* (or erosion of precipitation), the erosibility of soils *K* and the mixed effect of the degree and the length of the *LS* slope, the vegetal *C* cover and the practices of anti-erosion *P*. The cartographic representation of these factors (thematic maps) and their crossing led to the evolution of a summary map highlighting four classes of soil vulnerability to water erosion, resulting from an average erosion rate of 2.68 (t/ha/year). This rate is relatively reasonable with the rate given by interpreting the bathymetric measurements made in the Ain Dalia dam.
The classification in Figure 9 shows that the weakest erosion category is associated with gently sloping of 2 degrees areas which dominates the entire southern part of the area of study.
It is chiefly composed of agricultural land. The low erosion category concerns surface whose soil loss is less than 4 (t/ha/year) representing 40.54% of the surface of the watershed. 31.95%

of the area of study is exposed to moderate erosion; it is a mountainous region with slopes greater than 8 degrees where forests are predominant and only subsistence agriculture is practiced by the rural population (Table 6). Severe erosion takes place in some parts of the watershed exclusively in soils of high erodibility and steep landforms are primarily located in the Northern part of the watershed.

Table 6: Distribution of Soil loss A Classes in Wadi Medjerda Watershed

Soil loss (t/ha/year)	**Area (ha)**	**Area (%)**
< 2	35920.97	24.98
2-4	58296.02	40.54
4-7	45945.96	31.95
7-16.7	3637.05	2.53

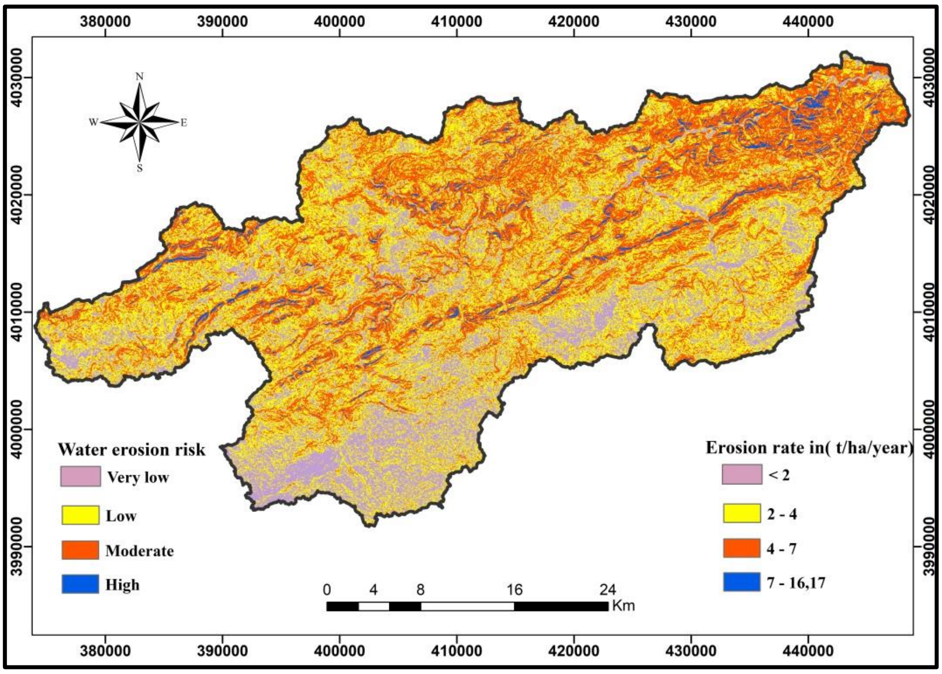

Figure 9: Map of erosion risk in the watershed Wadi of Medjerda

6 Validations

In this article, the obtained results through the RUSLE model application must be validated against actual sediment transport measurements. To this end, the Ain Dalia dam has been the subject of bathymetry measures by the National Agency of Dams and Transfers in different periods of time 2004 and 2019.

The results show that the siltation of the reservoir since the launching of the 1988 dam was 7.39 million cubic meters which corresponds to a loss of 9.012% of its initial capacity or an average annual volume of 238 387.10 m^3/year; this reduction in water storage capacity is due to soil

erosion. The following Table 7 summarizes the evolution of the loss of dam retention capacity. It is considered that the average rate of erosion reaches 2.48 t/ha/year when the density of settled sludge is 1.5. This value is relatively close to the value obtained by RUSLE, the difference between the two values is estimated at 7. 46%; this shows that the rates of soil erosion estimated by the model of RUSLE and by the bathymetric measurements are compatible to each other.
The map is an indispensable tool in the fight against erosion. It contributes to an overview of threatened areas and identifies areas requiring priority intervention with a view to sustainable land management.

Table 7: Evolution of the Loss of Capacity of the Ain Dalia Dam

	Launch Year 1988	**2004 Survey**	**2019 Survey**
Capacity (hm^3)	82.00	76.08	74.61
Loss compared to 1988 (hm^3)	-	5.92	7.39
Loss in %	-	7.22	9.012

7 Conclusion

On the light of this study, the methodology of water erosion characterization is applied through the use of a spatialization and quantification of the principal factors involved in the erosive process, the estimation and spatial distribution of the erosion of soil in the Medjerda wadi basin employing the Universal Soil Loss Equation (RUSLE) and GIS techniques estimating that the basin has had to cope with very low to high soil loss. It is worthy to note that the outcomes indicate that the rainfall erosivity R-factor of RUSLE was found to be 78 MJ mm/ha/hr/yr and the soil erodibility *K*-factor varied from 0.0362 to 0.0414 t.ha.h/ ha.MJ.mm. Slopes in the catchment varied between 0 degrees and 27degrees having LS factor values ranging from 0 to 23.755. The C factor was computed from NDVI (Normalized Difference Vegetative Index) values derived from Landsat-TM8 data. The P factor was assigned a value of 1.0 to the entire area of the watershed. The annual soil loss estimated in the watershed using RUSLE is 2,68 t/ha/yr. The map of soil loss has been classified into four risk classes on the basis of the quantity of soil loss: very weak (< 2 t /ha/y), weak (2–4 t /ha/y), moderate (4–7 t /ha/y), strong (7–16.17 t /ha/y). Hence, the average annual soil loss map will be helpful in identification of priority areas for implementation of soil conservation measures and effective checking of soil loss.

Reference

[1] Aiello, A., Adamo, M., & Canora, F. (2015). Remote sensing and GIS to assess soil erosion with RUSLE3D and USPED at river basin scale in southern Italy. Catena, 131, 174-185. DOI:10.1016/j.catena.2015.04.003

[2] Parveen, R., & Kumar, U. (2012). Integrated approach of universal soil loss equation (USLE) and Geographical Information System (GIS) for Soil Loss Risk Assessment in Upper South Koel Basin, Jharkhand. Journal of Geographic Information System, 4, 588-596

[3] Kheir, R. B., Cerdan, O., & Abdallah, C. (2006). Regional soil erosion risk mapping in Lebanon. Geomorphology, 82(3-4), 347-359.

[4] Vrieling, A. (2006). Satellite remote sensing for water erosion assessment: A review. Catena, 65(1), 2-18.

[5] Roose, EJ, Lelong, F. (1976) Les facteurs de l'érosion hydrique en Afrique Tropicale. Études sur petites parcelles expérimentales de sol. Revue de géographie physique et de géologie dynamique, 18(4), 365-74

[6] Sadiki, A., Bouhlassa, S., Auajjar, J., Faleh, A., & Macaire, J. J. (2004). Utilisation d'un SIG pour l'évaluation et la cartographie des risques d'érosion par l'Equation universelle des pertes en sol dans le Rif oriental (Maroc): cas du bassin versant de l'oued Boussouab. Bulletin de l'Institut Scientifique, Rabat, section Sciences de la Terre, 26(2004), 69-79.

[7] Wischmeier, W. H., & Smith, D. D. (1965). Predicting rainfall-erosion losses from cropland east of the Rocky Mountains: Guide for selection of practices for soil and water conservation (No. 282). Agricultural Research Service, US Department of Agriculture.

[8] Foster, G. R., Toy, T. E., & Renard, K. G. (2003, October). Comparison of the USLE, RUSLE1. 06c, and RUSLE2 for application to highly disturbed lands. In First interagency conference on research in watersheds (Vol. 27, No. 30, pp. 154-160). Washington, DC: US Department of Agriculture, Agricultural Research Service.

[9] Khanchoul, K., Balla, F., & Othmani, O. (2020). Assessment Of Soil Erosion by RUSLE Model Using GIS: A Case Study Of Chemorah Basin, Algeria. Malaysian Journal of Geosciences (MJG), 4(2), 70-78. DOI:10.26480/mjg.02.2020.59.67

[10] Duarte, L., Teodoro, A. C., Gonçalves, J. A., Soares, D., & Cunha, M. (2016). Assessing soil erosion risk using RUSLE through a GIS open source desktop and web application. Environmental monitoring and assessment, 188(6), 1-16. DOI:10.1007 /s10661-016-5349-5.

[11] Fernández, C., & Vega, J. A. (2016). Evaluation of RUSLE and PESERA models for predicting soil erosion losses in the first year after wildfire in NW Spain. Geoderma, 273, 64-72. DOI:10.1016/j.geoderma.2016.03.016

[12] Ouadjane, Y., Yacine, E. A. A., Benzougagh, B., Nassiri, L., & Ibijbijen, J. (2021). Evaluation Des Risques D'érosion Hydrique Et Cartographie Des Zones Vulnérables Par La Méthode RUSLE Couplée Aux SIG Et À La Télédétection Dans Le Bassin Versant d'Agoudal En Amont De La Vallée d'Imilchil (Haut Atlas Central, Maroc). European Scientific Journal, 17(21), 66-91.

[13] Michalopoulou, M., Depountis, N., Nikolakopoulos, K., & Boumpoulis, V. (2022). The significance of digital elevation models in the calculation of LS factor and soil erosion. Land, 11(9), 1592.

[14] Khemiri, K., & Jebari, S. (2021). Évaluation de l'érosion hydrique dans des bassins versants de la zone semi-aride tunisienne avec les modèles RUSLE et MUSLE couplés à un Système d'information géographique. Cahiers Agricultures, 30, 7.

[15] Desmet, P. J. J., & Govers, G. (1996). A GIS procedure for automatically calculating the USLE LS factor on topographically complex landscape units. Journal of soil and water conservation, 51(5), 427-433.

[16] Atoma, H., Suryabhagavan, K. V., & Balakrishnan, M. (2020). Soil erosion assessment using RUSLE model and GIS in Huluka watershed, Central Ethiopia. Sustainable Water Resources Management, 6(1), 1-17.

[17] Wischmeier, W. H., & Smith, D. D. (1978). Predicting rainfall erosion losses: a guide to conservation planning (No. 537). Department of Agriculture, Science and Education Administration.

[18] Bouhadeb, C. E., Menani, M. R., Bouguerra, H., & Derdous, O. (2018). Assessing soil loss using GIS GIS based RUSLE methodology. Case of the Bou Namoussa watershed – North-East of Algeria. Journal of Water and Land Development No. 36 p. 27–35. DOI: 10.2478/jwld-2018-0003

[19] Rango, A., & Arnoldus, H. M. J. (1987). Aménagement des bassins versants. Cahiers techniques de la FAO, 36.

[20] Arnoldus, H. M. J. (1977). Methodology used to determine the maximum potential average annual soil loss due to sheet and rill erosion in Morocco. FAO Soils Bulletins (FAO).

[21] Kalman, R. (1967). Le facteur climatique de l'érosion dans le bassin de Sebou. Projet Sebou, Rapp. inédit.

[22] Kumar, S., & Gupta, S. (2016). Geospatial approach in mapping soil erodibility using CartoDEM–A case study in hilly watershed of Lower Himalayan Range. Journal of Earth System Science, 125(7), 1463-1472.

[23] Ryan, J. (1982). Perspective on soil erosion and conservation. Publ. no. 69. Fac. Agric. and Food Sci., Am. Univ., Beirut, Lebanon.

[24] Fao, I., & Isric, I. (2012). Harmonized world soil database (version 1.2). FAO, Rome, Italy and IIASA, Laxenburg, Austria.

[25] Neitsch, S. L., Arnold, J. G., Kiniry, J. R., & Williams, J. R. (2011). Soil and water assessment tool theoretical documentation version 2009, Texas Water Resources Institute Technical Report No. 406. System, College Station. DOI:10.1016/j.scitotenv.2015.11.063

[26] Wawer, R., Nowocien, E., & Podolski, B. (2005). Eal and calculated kusle erobility factor for selected Polish soils. Polish Journal of Environmental Studies, 14(5), 655-658.

[27] Renard, K.G., Foster, G.R., Weesies, G.A et cal, coordinators. (1997) Predicting Soil Erosion by Water: A Guide to Conservation Planning with the Revised Universal Soil Loss Equation (RUSLE), US Government Printing Office, Washington, Agriculture handbook, No. 703, 404 pp.

[28] Lin, C. Y., Lin, W. T., & Chou, W. C. (2002). Soil erosion prediction and sediment yield estimation: the Taiwan experience. Soil and Tillage Research, 68(2), 143-152. DOI:10.1016/S0167 -1987(02)00114 -9

[29] Wang, G., Wente, S., Gertner, G. Z., & Anderson, A. (2002). Improvement in mapping vegetation cover factor for the universal soil loss equation by geostatistical methods with Landsat Thematic Mapper images. International Journal of Remote Sensing, 23(18), 3649-3667. DOI:10.1080/01431160110114538

[30] Gitas, I. Z., Douros, K., Minakou, C., Silleos, G. N., & Karydas, C. G. (2009). Multi-temporal soil erosion risk assessment in N. Chalkidiki using a modified USLE raster model. EARSel eproceedings, 8(1), 40-52.

[31] Payet, E., Dumas, P., & Pennober, G. (2012). Modélisation de l'érosion hydrique des sols sur un bassin versant du sud-ouest de Madagascar, le Fiherenana. VertigO: la revue électronique en sciences de l'environnement, 11(3). http://journals.openedition. org/vertigo/12591

[32] Roose, E. (1996). Land husbandry: components and strategy (Vol. 70). Rome: FAO

[33] Bollinne, A., & Rosseau, P. (1978). L'érodibilité des sols de Moyenne et Haute Belgique. Bull. Soc. Géogr. Liège, 14, 127-140.

[34] Cormary, Y., & Masson, J. (1964). Etude de conservation des eaux et du sol au Centre de Recherches du Génie Rural de Tunisie: application à un projet-type de la formule de perte de sols de Wischmeier. Cahiers ORSTOM. Série Pédologie, 2(3), 3-26.

DOI: 10.2478/sspjce-2023-0020

Digital-age Urbanism with Eddy3D for Grasshopper

Lenka Kabošová[1]

[1]Technical University of Kosice, Faculty of Arts, Watsonova 4, Košice, Slovakia
*e-mail: lenka.kabosova@tuke.sk

Abstract

The changing climate is a trigger for architects to reconsider the conventional design approach and possibly enrich it with novel approaches brought by the digital age. Sun analysis for urban planning with wind analysis too, proves inevitable for creating comfortable public spaces and built environment in general. When incorporating wind analysis into the process of architectural/urban design, several crucial pre-requisites determine the use of CFD (Computational Fluid Dynamics) simulations: (1) the demand from the client, (2) the time-space needed for the investigations, (3) the powerful enough hardware, and (4) software that enables a fast, user-friendly interface for parametric investigations. Among the benefits of investigating wind speed and flowlines in the digital environment is the possibility to compare design alternatives very quickly and with the same boundary conditions. Moreover, the popular algorithmic software Grasshopper currently enables wind investigation of the geometry directly in the modeling environment without the need to export the file to a standalone CFD software. This way, multiple design options can be investigated once the parametric geometry is prepared, and the digital wind tunnel is set.

Keywords: digital-age urbanism, Computational Fluid Dynamics, wind comfort, Eddy3D

1 Introduction

Even though climate change is currently a very relevant and highly discussed topic [1], the investigations of wind flow in urbanism are still seldom in practice, or they are applied to almost finished projects. Any change that would arise from the wind studies at this point would be costlier and more time-consuming compared to this task being done in the conceptual phase [2]. Indeed, the wind simulations per se require hours if not days of computations using computers with at least 16 GB of RAM and multiple processors for calculations. For exploring multiple design options within the conceptual design phase, parametric modeling is a fitting approach [3]. Complex real-world data (terrain morphology, heights of buildings, urban density, solar radiation, wind flow) can be considered and evaluated within the parametric model. Moreover, incorporated in the early design stage, this can contribute to forming a sustainable urban environment [4, 5].

To analyze every desired design option and its impact on the wind flow, a separate calculation must be performed for each option. For this, having the wind analysis integrated into the modeling environment is a plus.

1.1 Wind Analysis in Urbanism

In some cities (mainly Nordic), city authorities request comprehensive wind studies before a building permit can be granted [6]. In many other cities, however, mainly for the reason of the extra financial and time cost, this kind of assessment is not yet required. This may result in new urban developments that negatively impact pedestrians in public spaces [7]. The wind speed and flowlines in the built environment strongly depend on three main factors: urbanism, terrain morphology and roughness, and building shapes. As the wind analysis is oftentimes disjointed in several engines (modeling/simulation/post-process), this also contributes to consequently omitting the wind analysis from the design process. The parametric environment of Grasshopper integrates various environmental simulation plug-ins and thus enables a smooth project progression [8].

Still, a big challenge of the CFD simulations is time [9], which becomes especially noticeable in large-context urban analyses. In this paper, Eddy3D, a plug-in for Grasshopper utilizing the OpenFOAM platform, will be utilized for the wind analysis.

2 Methods

The setup of a digital model for wind analysis can be, generally, divided into three steps: Pre-processing, Simulation, and Post-processing. Through the case study located in Košice, Slovakia, the wind-based urban design is introduced.

2.1 Pre-Processing Utilizing Grasshopper

Pre-processing is the most crucial part of CFD simulations as if incorrectly set, it can cause the simulation to crash or diverge. The weather data is obtained as an *epw file, downloaded from the website *https://energyplus.net/weather* [10]. Alternatively, the *epw file can be extracted from *climate.onebuilding.org* or a new toolset in Ladybug for Grasshopper can be employed. The two alternatives will not be explained in this paper. For a general weather analysis, data from Lobelia Earth [11] is used, containing historical meteorological data available from the ECMWF archive. Figure 1 shows (a) the air temperature by month in a typical meteorological year, (b) the monthly average wind speed and maximum wind gusts, and (c) the warming trend since 1979. From the obtained *epw data, it is apparent that the northerly winds are prevailing in Košice with the strongest wind gusts from this direction. The average wind speed of 9.6 m/s will be used in the wind analyses (obtained from the Lobelia Earth data).

After preparing the data, the geometry for analysis is modeled in the 3D digital environment of Grasshopper for Rhino. It must be watertight and relatively simple to enable a fast wind analysis without errors. The OpenFOAM platform, running through the Linux virtual operating system, uses the Finite Volume Method (FVM) [12] for computation. The Eddy3D plug-in for Grasshopper launches OpenFOAM and controls the settings. The cell size for the whole virtual wind tunnel is specified as 20 meters, and the meshing becomes finer near the investigated geometry, where the cell size is refined to the level of 3, meaning the cell will have a 2.5 m side. Snapping and layering techniques are used to correctly capture the shape of the geometry [13].

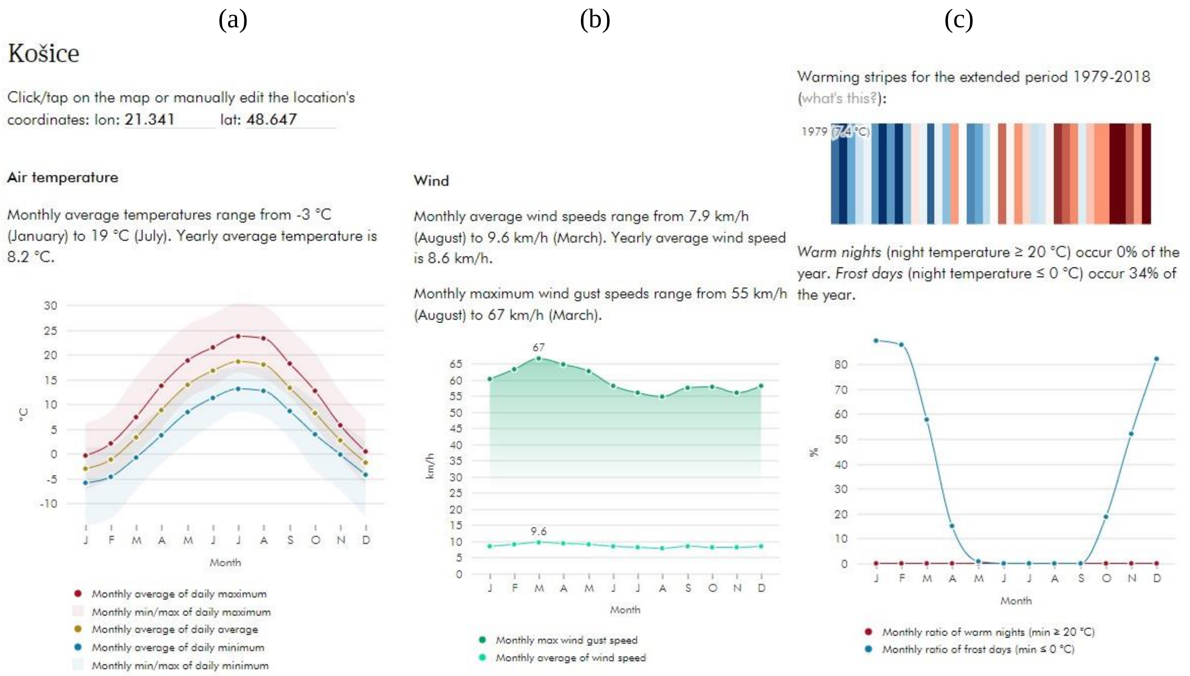

Figure 1: Lobelia Earth average year analysis for Košice, Slovakia. (a) air temperature, (b) wind, and (c) warming trends

The virtual wind tunnel is automatically generated in Eddy3D according to best-practice guidelines [13]. The case study urban area measures 375 x 450 meters.

2.2 Eddy3D CFD Simulations

The boundary conditions and the simulation settings are specified in Table 1.

Table 1: Boundary conditions and simulation settings in the Košice case study

Boundary conditions			**Simulation settings**			
Wind direction (°)	**Reference wind velocity *U* (m/s)**	**Orography factor z_0 (-)**	**Number of iterations**	**Turbulence model**	**Relaxation factors**	**Number of CPUs**
0 (northerly)	9.6	1	2000	Realizable k-ε	Optimized (pre-defined)	6

Reynolds-Averaged Navier-Stokes (RANS) [14] CFD solver method and realizable k-ε, are used in the case study. The convergence criteria and relaxation factors are specified as optimized in Eddy3D. The convergence criteria are set as $1e^{-5}$ in the optimized setting; however, the simulations will end after reaching 2000 iterations, which naturally does not guarantee that the solution is converged. On the other hand, the converging trend is apparent.

2.3 Post-processing

Two CFD simulations were carried out for the two design alternatives: (a) with a designed 15-story building, and (b) with a designed 9-story building of a different shape at a now empty roundabout. The results are post-processed only using the environment of Grasshopper.

3 Wind Analysis Results

3.1 Status Quo

The case study site consists of two spots. The first one was examined in previous studies [5] (highlighted in blue in Figure 2) and the second one (green color in Figure 2) is investigated in this case study. In this second step of design, a high-rise building placed on a roundabout is designed. Currently, the roundabout serves only for parking, surrounded by a quite complex road network.

Figure 2: The map of the case study site in Košice (study site 1 in blue and study site 2 in green color)

The building at the roundabout is designed parametrically, in Grasshopper. Its shape is manipulated through profile curves and scaling and rotating of the curves.

3.2 Parametric AI-inspired Design

The idea of the wind-derived building came from a now-popular text-to-image AI (artificial intelligence) tool. The given text was ‘futuristic city with buildings generated through the wind forces’. The building was then parametrically modeled in Grasshopper for Rhino (Figure 3). Only one profile curve is the input, which is then copied to as many floors as desired with an adjustable floor height. The shape of the profile curves can be adjusted and then each profile curve is randomly rotated and scaled, creating the final visual (Figure 4). Two design options with different numbers of floors and variable geometry are investigated in the northerly winds.

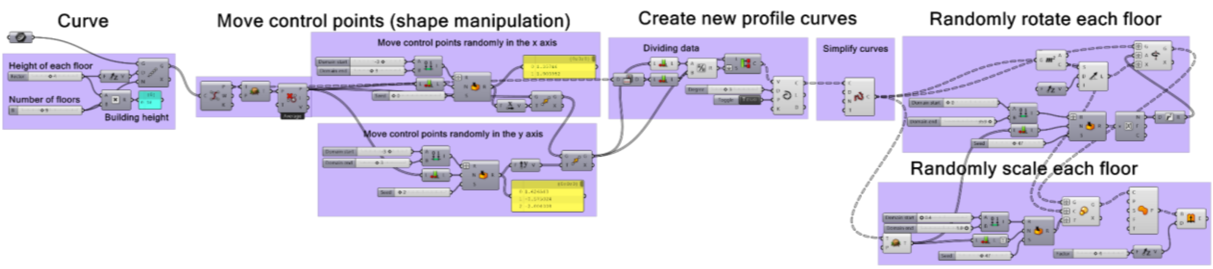

Figure 3: The algorithmic definition for the parametrically-designed building in Grasshopper

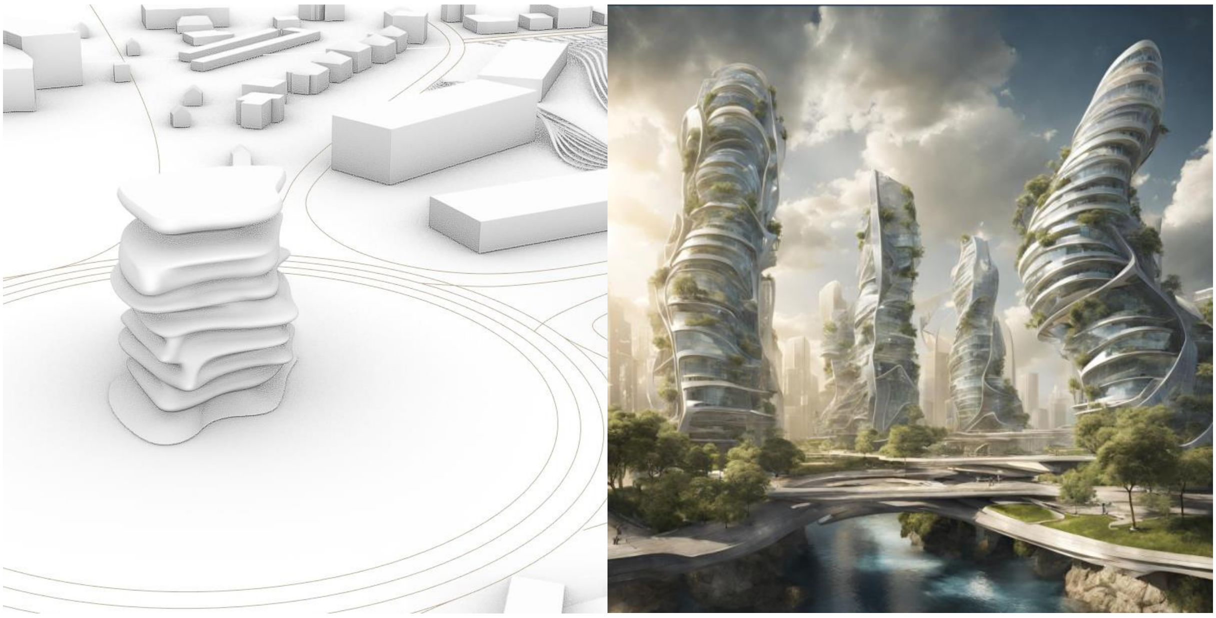

Figure 4: The idea of the wind-created building at the roundabout (the right picture is generated using AI (artificial intelligence) text to image)

3.3 Wind Analysis with Eddy3D

The wind situation is investigated at the pedestrian level, at 2 meters above the ground. The investigated geometry is simplified for a faster CFD investigation. Furthermore, in wind analyses, the incorrectly-created geometry can cause the calculations to crash. For these reasons, a simplified building is evaluated. The simulation settings, the boundary conditions, and the geometry are prepared following the settings stated in the Methods section of this paper. The results of the simulations can be observed in Figures 5-7.

(a)

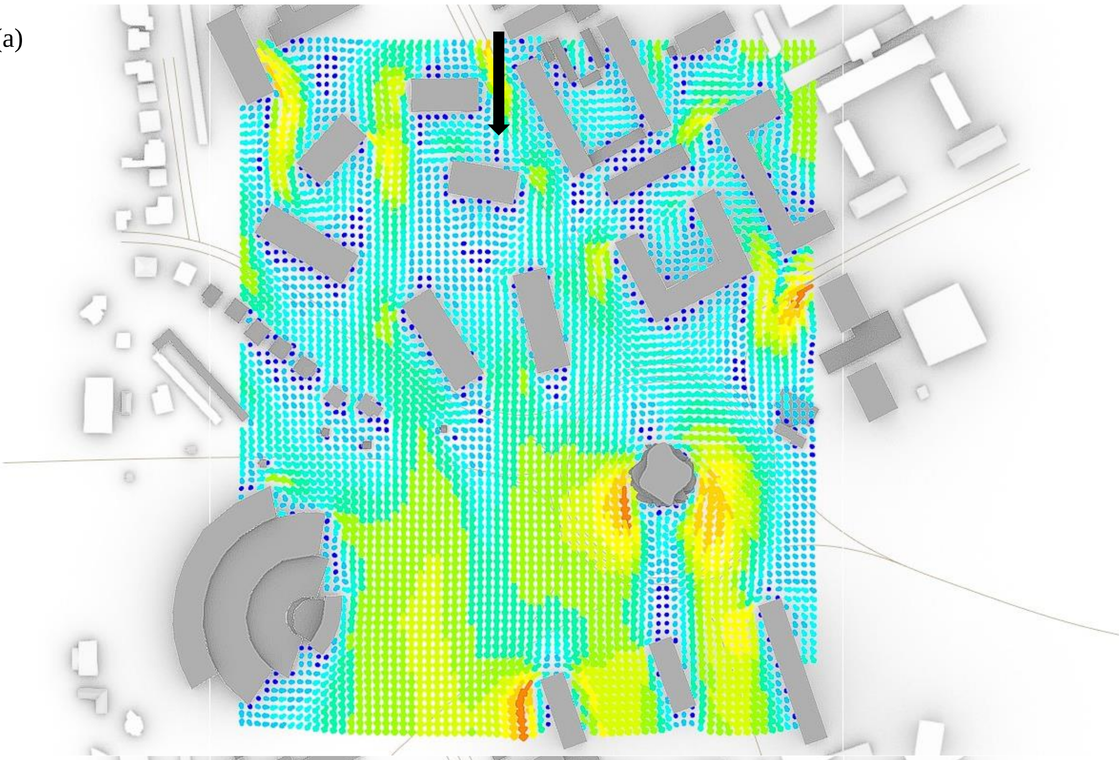

(b)

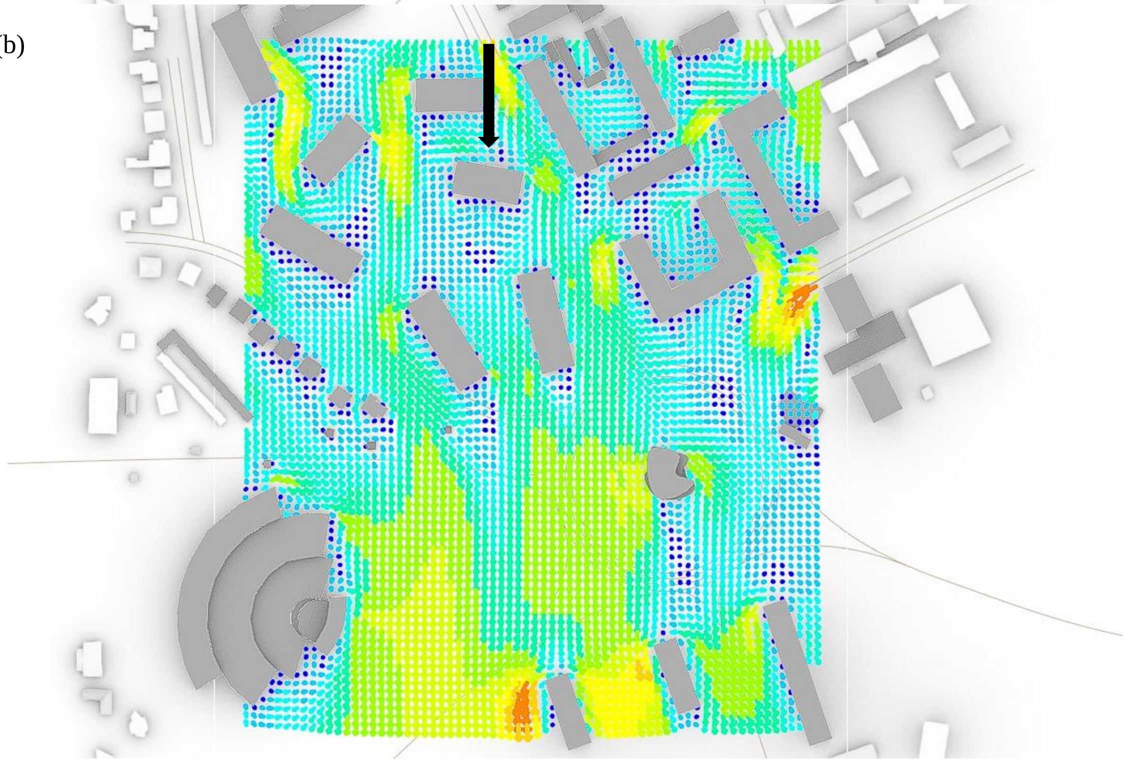

Figure 5: The results of the wind analysis in the top view. The wind speed is displayed at 2 m above the ground in the following color scheme: dark blue = 0 m/s, red = 10 m/s. (a) Design 1 with 15 floors, (b) Design 2 with 9 floors and a different shape

All the CFD analysis results are post-processed in the environment of Grasshopper. There are external software, such as Paraview that can be used for the results visualization. In this paper, however, they are not used for the early design phase investigations. In Figures 6 and 7, the color scheme used for the results visualization has a different range compared to the visualization in the top view. The reason is to first introduce the wind flowlines and speed trend in the top view and then highlight the zones uncomfortable for pedestrians in the perspective.

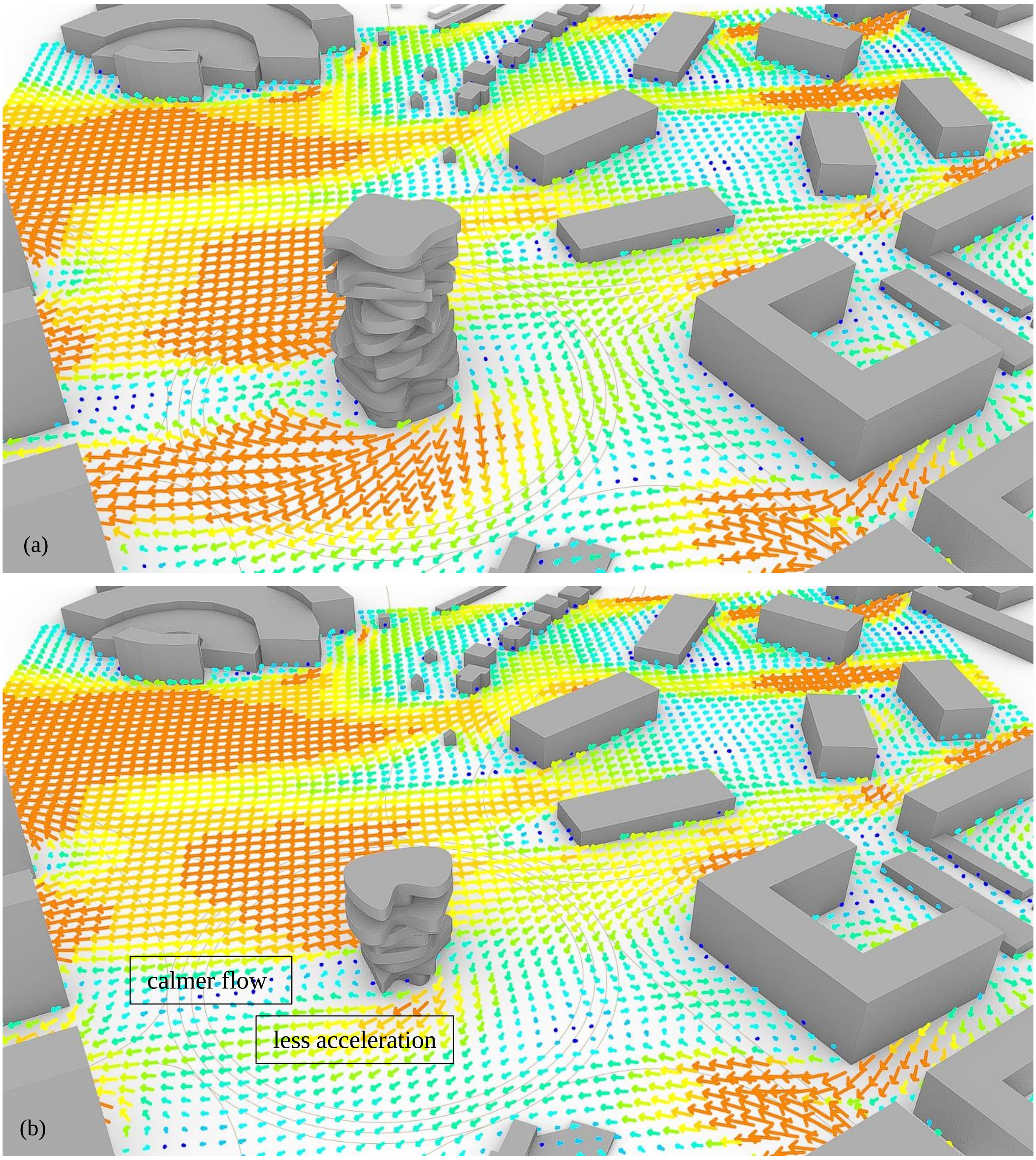

Figure 6: The results of the wind analysis in the perspective view. The wind speed is displayed at 2 m above the ground in the following color scheme: dark blue = 0 m/s, red = 6 m/s to highlight the uncomfortable areas. (a) Design 1 with 15 floors, (b) Design 2 with 9 floors

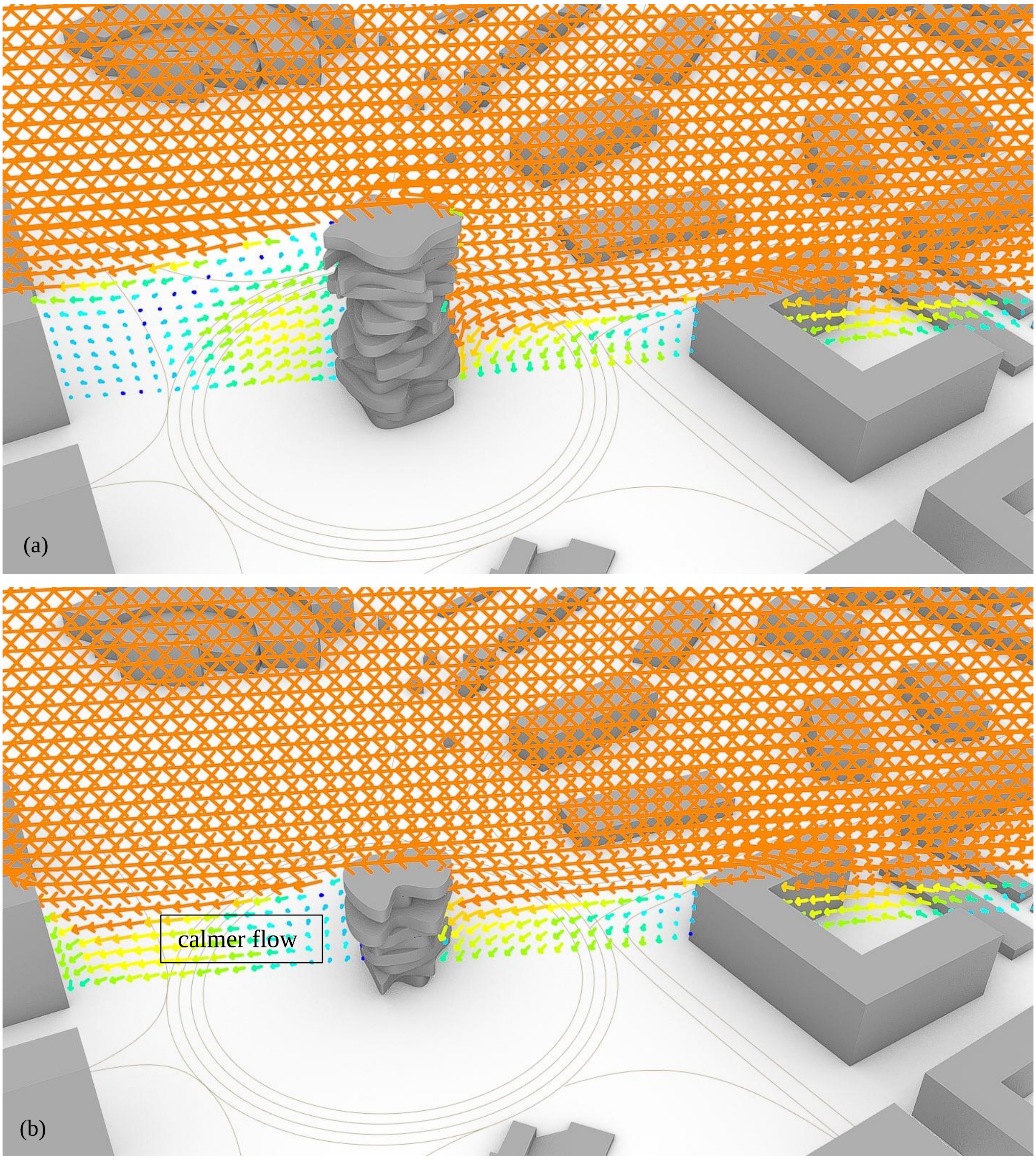

Figure 7: The results of the wind analysis in the perspective view. The wind speed is displayed at 2 m above the ground in the following color scheme: dark blue = 0 m/s, red = 6 m/s to highlight the uncomfortable areas. (a) Design 1 with 15 floors, (b) Design 2 with 9 floors

From Figures 5-7, we can observe the differences between the two parametrically-created designs. Influenced by the lower number of floors and the different shapes of the bottom floors, Design 2 fits better into the existing built context than Design 1. The designed building with 9 floors measures 34 meters. When placed on the roundabout, surrounded by the buildings on the south side, with a height of 40 meters, and buildings on the north side, measuring around 24 meters in height, this design option is preferable in the context of the comfortable wind environment for pedestrians.

4 Conclusion

This paper introduced a digital-age urban design approach considering wind comfort at the pedestrian level as the main design goal. In one working environment of Grasshopper, the geometry of a new high-rise building is designed within the urban context of the neighboring buildings, the wind analysis is then made utilizing Eddy3D (leveraging the OpenFOAM platform) directly in Grasshopper, followed by the evaluation of the results again in the same environment. For architects, this approach has benefits over the traditional methods where the wind analysis is performed in the last design stages and different software is utilized throughout the design/investigation/evaluation process. Employing the introduced approach, the architects can investigate the environmental impact of their ideas (in this case, the effects of the design on the wind flow) and, if necessary, use the parametric nature of Grasshopper to modify the design and evaluate it again. Eddy3D wind analysis tool is optimized by the developers, so with the optimized solution and algorithm control settings, the convergence criteria, and the relaxation factors, the simulations run fast enough to provide necessary feedback in a rational time frame. Two designs of a high-rise building were investigated within the case study located in Košice, Slovakia. The impact on the wind comfort within the urban context was considered with the conclusion that the 9-story building with a slightly different shape offers a better alternative when taking into account the existing neighboring buildings and the resulting wind flow and speed at the pedestrian level. Many more building designs can be investigated within the given case study situation. When aiming for the best-fitting design solution, however, faster wind analysis techniques (machine-learning-based tools, or Fast Fluid Dynamics) coupled with shape optimization are recommended.

Acknowledgments

This work was financially supported by the Grant Agency of the Slovak Republic VEGA 1/0129/20, VEGA 1/0626/22, and VEGA 1/0307/23. I wish to dedicate this paper to my mentor, S. Kmet.

References

[1] Kemp, L., Xu, C., Depledge, J., Ebi, K.L., Gibbins, G., & Kohler T.A., (2022). Climate Endgame: Exploring Catastrophic Climate Change Scenarios. *PNAS*, *119*(34), pp. 1-9.

[2] Estrado, E. (2019). Optimisation of Complex Geometry Buildings Based on Wind Load Analysis. Graduation report, TU Delft.

[3] Kabošová, L., Katunský, D., & Kmeť, S. (2023). Designing with the Wind: Climate-Derived Architecture, 1st ed., Springer.

[4] Bielik, M., Schneider, S., & König, R. (2012). Parametric Urban Patterns Exploring. Proc. 30th ECAADe Conf. 1, 701.

[5] Kabošová, L., Chronis, A., Galanos, T., Kmeť, S. & Katunský, D. (2022). Shape optimization during design for improving outdoor wind comfort and solar radiation in cities, *Build. Environ.*, *226*, 109668.

[6] Hågbo, T., Erik, K., & Giljarhus, T. (2022). Pedestrian Wind Comfort Assessment Using Computational Fluid Dynamics Simulations with Varying Number of Wind Directions. *Frontiers in Built Environment*, *8*(1), pp. 1-14.

[7] Mackey, C., Galanos, T., Norford, L. & Roudsari, M. (2017). Wind, Sun, Surface Temperature, and Heat Island: Critical Variables for High-Resolution Outdoor Thermal Comfort. In Proc. 15th IBPSA Conf., San Francisco, USA, pp. 985–993.

[8] Osintseva, I., Koenig, R., Berst, A., Bielik, M., & Schneider, S. (2020). Automated Parametric Building Volume Generation: A Case Study for Urban Blocks. SimAUD Symp. Simul. Archit. Urban Des., pp. 211-218.

[9] Chronis, A., Turner, A., & Tsigkari, M. (2011). Generative Fluid Dynamics: Integration of Fast Fluid Dynamics and Genetic Algorithms for Wind Loading Optimization of Free Form Surfaces. SimAUD2011, pp. 79-85.

[10] Weather Data. (2023). *https://energyplus.net/weather*.

[11] Past Climate Explorer (2023). *https://era5.lobelia.earth/*

[12] Moukalled, F., Mangani, L. & Darwish, M. (2016). Fluid Mechanics and Its Applications. Springer.

[13] Janssen, W., Blocken, B., & Van Hooff, T. (2013). Use of CFD Simulations to Improve the Pedestrian Wind Comfort Around a High-Rise Building in a Complex Urban Area. In 13th Conf. Int. Build. Perform. Simul. Assoc. Chambéry, Fr. August 26-28 (Chambéry, France, 2013), pp. 1918–1925.

[14] Phillips, D., & Soligo, M. (2019). Will CFD ever Replace Wind Tunnels for Building Wind Simulations? *Int. J. High-Rise Build.*, *8*, 107-116.